Synthesis of Ordered, Phase-Separated, Organic and Metal-Containing Ionic Liquid-Based Block Copolymers via Controlled Radical Polymerization

by

Zhangxing Shi

B.S., Fudan University, Shanghai, China, 2010

A thesis submitted to

the Faculty of the Graduate School of the University of Colorado in partial fulfillment of the requirements of the degree of Doctor of Philosophy

Department of Chemistry and Biochemistry

2018

This thesis entitled

"Synthesis of Ordered, Phase-Separated, Organic and Metal-Containing Ionic Liquid-Based Block Copolymers via Controlled Radical Polymerization"

written by Zhangxing Shi

has been approved for the Department of Chemistry and Biochemistry

_____

Douglas L. Gin, Ph.D.

_____

Wei Zhang, Ph.D.

Date_____

The final copy of this thesis has been examined by the signatory, and we find that both the content and the form meet acceptable presentation standards of scholarly work in the above-mentioned discipline

ABSTRACT

Zhangxing Shi

(Ph.D., Organic Chemistry, Department of Chemistry and Biochemistry)

Synthesis of Ordered, Phase-Separated, Organic and Metal-Containing Ionic Liquid-Based Block Copolymers via Controlled Radical Polymerization

Thesis directed by Prof. Douglas L. Gin

Polymerized ionic liquids (PILs) are a class of polyelectrolytes that contain an ionic liquid (IL) moiety in each monomer repeating unit that are connected through a polymeric backbone. Since ILs are small-molecule liquid materials with a unique combination of properties (e.g., negligible vapor pressure, high thermal stability, ion conductivity, high solubility for certain light gases, etc.), the development of ordered, phase-separated polymeric systems containing PIL segments has considerable implications with respect to a range of transport-dependent, energy-based technology applications. The work presented in this thesis was focused on the synthesis of two IL-based block copolymer (BCPs) platforms: (1) a new organic IL-based BCP platform (PIL-BCP) and its morphological phase behavior; and (2) the first example of metal-containing IL-based BCP (MCIL-BCP) platform that forms ordered microstructures in the neat state and has functional capabilities introduced by the incorporated metal complex.

The PIL-BCP platform was synthesized via sequential atom-transfer radical polymerization (ATRP) of styrene and styrenic imidazolium IL monomers with different side-chains on the imidazolium units (e.g., methyl, *n*-butyl, etc.). Small-angle X-ray scattering (SAXS)

analysis of these BCPs showed the formation of four classic ordered morphologies of diblock copolymer (i.e., body-centered cubic spheres (S_{BCC}), hexagonally packed cylinders (Hex), lamellae (Lam), and notably, bicontinuous gyroid (Gyr)), depending on both the volume fraction of the PIL block and the attached alkyl group on the imidazolium units.

The MCIL-BCP platform was synthesized by sequential reversible addition-fragmentation chain transfer (RAFT) polymerization of butyl methacrylate and a Co(II) bis(salicylate) anion-containing MCIL monomer. SAXS studies on MCIL-BCP samples made from these two monomers with 70 total repeat units but different block composition ratios showed the formation of ordered microstructures (i.e., S, Hex, Lam, and Gyr phases) in their neat states. This is the first example of an IL-based BCP that exhibits the Gyr phase in the neat state to our knowledge. Additionally, these MCIL-BCPs were found to have metal-induced properties such as reversible binding of small protic molecules and catalytic reactivities.

ACKNOWLEDGMENTS

First and foremost, I would like to express my sincere gratitude to my advisor, Professor Douglas L. Gin, for his guidance and mentorship throughout my Ph.D. study and dissertation writing. He has been a perfect advisor and has taught me a lot about chemistry, research strategies, and writing skills. His mentorship helped me to develop not only academic knowledge but also interpersonal skills. I would also like to thank Professor Richard D. Noble for his helpful co-advisement during my graduate career.

I would like to thank all my current and former co-workers of the GiNoble group. Thanks to Dr. Erin Wiesenauer for her mentorship in the starting stage of my research project when I joined the group. Thanks to Prof. Travis Bailey, Alyssa May, Dilanji Wijayasekara, and Brian Newell for their help and experience in block copolymer phase characterization, DSC measurements and SAXS data analysis. Thanks to Prof. Wei Zhang for sharing his GPC instrument with us. Thanks to Prof. Richard Shoemaker for his help in NMR analysis and NMR DOSY experiments. Thanks to Dr. Yuki Kohno for his collaboration in my metal-containing block copolymer project. I would also like to thank Dr. Brian Wiesenauer, Dr. Magdalene Schenkel, Dr. Blaine Carter, Dr. Lily Robertson, Dr. Will McDanel, Josh Sloan, Dr. Dylan Mori, Dr. Sarah Dischinger, Dr. Zoban Singh, Dr. Matt Cowan, Dr. Rhia Martin, Dr. Alex Lopez, Greg Dwulet, John Malecha, Mike McGrath, and Collin Dunn for their help over the years.

Finally, I would like to thank my family and friends. Thanks to my parents and my brother for supporting me throughout my Ph.D. study. Thanks to my roommate and my friends who have made my life more enjoyable during my graduate school career.

TABLE OF CONTENTS

LIST OF FIGURES

LIST OF TABLES

LIST OF EQUATIONS

CHAPTER 1

Introduction: An overview of ionic liquids and ionic-liquid-based block copolymers

1.1 Ionic liquids

Ionic liquids (ILs) are molten salts with melting point below 100 °C under ambient pressure. The liquid nature of ILs arises from the weak coordination between the oppositely charged ions, low intermolecular interaction, and the asymmetric structures of the component ions.[1] Room-temperature ionic liquids (RTILs) are a subclass of ILs that are liquid at room temperature (ca. 25 °C) and ambient pressure.[1] In 1914, Walden reported the first example of an IL, ethylammonium nitrate, that has a melting point as low as 12 °C. At that time, ILs did not attract too much scientific attention. The first generation of ILs were organic halogenoaluminates that were studied in 1970s−1980s. However, the rapid hydrolysis of these halogenoaluminate salts limited the research and application of these ILs. In 1990s, the water- and air-stable second generation of ILs (containing tetrafluoroborate (BF_4^-), hexafluorophosphate (PF_6^-), etc. as anions) were synthesized. Since then ILs have received increased interest in academia and industry because of their distinctive properties. ILs have negligible vapor pressure due to their ionic character. The vapor pressure of ILs is typically too low to be detected at room temperature. Even at high temperatures (450−530 K), the reported vapor pressures of ILs are in the order of 10^{-8} to 10^{-7} bar.[1a] At room temperature, ILs have ionic conductivities of up to 10^{-2} S cm^{-1}, which increase significantly at higher temperatures.[1a] In combination with their high electrochemical stability, ILs have been used in various electrochemical processes. ILs also have high thermal stability. The

thermal degradation temperatures of common ILs with different anions (e.g., halides, BF_4^-, PF_6^-, TfO^-, Tf_2N^-, etc.) are in the range of 225−500 °C.[2] Another attractive property of ILs is their high solubility for certain light gases such as CO_2 and SO_2.[3] Due to this unique combination of properties, IL-based materials have been used as "green" solvents,[4] paint additives,[4] metal-extracting agents,[5] catalysts,[6] explosives,[7] hypergolic fuels,[7] liquid electrolytes,[8] CO_2-capture materials,[9] and CO_2-separation membrane materials.[10]

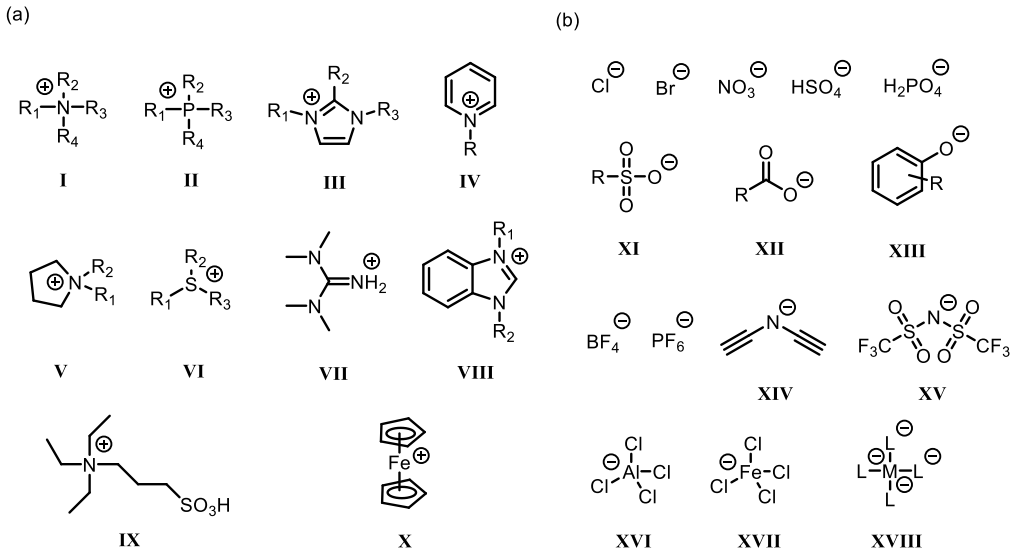

Figure 1.1. Chemicals structures of (a) cations and (b) anions of common ILs.

In addition to the properties described above, ILs also have very good synthetic versatility. The estimated number of possible different IL structures by modifying the structures of cations and anions is as high as 10^{18}.[1b] As shown in Figure 1.1, the most common cations of ILs are ammoniums (**I**), phosphoniums (**II**), imidazoliums (**III**), pyridiniums (**IV**), and pyrrolidiniums (**V**). There is also an increasing interest in synthesizing ILs containing other cations such as sulfoniums

(**VI**), guanidiniums (**VII**), and benzimidazoliums (**VIII**). The anions of ILs can be classified as hydrophilic or hydrophobic. In general, the common hydrophilic anions are halides, nitrate (NO_3^-), bisulfate (HSO_4^-), and dihydrogen phosphate ($H_2PO_4^-$). The common hydrophobic anions include tetrafluoroborate (BF_4^-), hexafluorophosphate (PF_6^-), dicyanamide (**XIV**), and bis(trifluoromethylsulfonyl)imide (Tf_2N^-, **XV**). However, this classification for some IL anions (i.e., organosulfates (**XI**), carboxylates (**XII**), and phenolates (**XIII**)) is ambiguous, since the hydrophilicity or hydrophobicity of these anions could be tuned by modifying the attached functional organic group. Among these anions, Tf_2N^- has received the most interest in recent years because of its ability to form liquid salts with low viscosity, high thermal stability, and high electrochemical stability.[1a]

ILs are usually classified based on the most important functional group contained in the cation or anion.[1b] For example, protic ILs are a subclass of ILs that have an available labile proton on the cation (e.g., **IX** in Figure 1.1).[11] Protic ILs are typically prepared through the stoichiometric neutralization reaction of certain Brønsted acids and Brønsted bases and have been used as catalysts for organic synthesis, non-aqueous amphiphile self-assembly solvents, and electrolytes for electrochemical processes.[11] Metal-containing ILs (MCILs) are a subclass of ILs that contain a metal complex as the cation or anion (e.g., metallocenes (**X**), halometallates (**XVI** and **XVII**), and metal complexes with ligands (**XVIII**)).[12] MCILs are a relative new class of functional ILs with metal-based magnetic, catalytic, optical, or molecular binding properties.[12]

1.2 Polymerized ionic liquids

Polymerized ionic liquids (PILs) are a class of polyelectrolytes that contain an IL moiety in each monomer repeating unit that are connected through a polymeric backbone to form a macromolecular architecture.[13] As a result, the ionic centers are constrained to the repeat units in the polymer chain. Although ILs are in the liquid state near room temperature, PILs are solid state material in most cases. PILs extend the properties and applications of ILs and common polyelectrolytes by combining the unique properties of ILs and macromolecules, producing new combinations of properties and functions such as tunable ionic conductivity, low glass transition temperature, and tunable solubility.[13] The major advantages of using PILs instead of ILs are the improved processability, enhanced mechanical stability, increased durability, and greater spatial controllability of the polymeric analogs over the liquid species.[13] Therefore, PILs have been successfully applied as new functional materials for use as polyelectrolyte membranes in fuel cells,[14a] solid-state electrolytes in solar cells,[14a] gel polymer electrolytes in batteries,[14a] transistors,[14b] 'smart' materials,[14b] gas separation membranes,[14b] catalysts,[14b] antimicrobial coatings,[14c] biosensors,[14c] etc.

PILs can be made by direct polymerization of reactive IL monomers or by post-polymerization modification of existing polymers containing reactive repeat units to generate the IL moieties (see Figure 1.2 for representative examples).[13] The direct polymerization of IL monomers is a straightforward strategy to prepare PILs with well-controlled structures. This strategy involves the polymerization of reactive IL monomers via free radical polymerization, atom-transfer radical polymerization (ATRP), nitroxide-mediated radical polymerization (NMP), reversible addition-fragmentation chain transfer (RAFT) polymerization, ring-opening metathesis polymerization (ROMP), polyaddition, and polycondensation.[13] On the other hand, the post-

polymerization modification approach utilizes well-defined polymer precursors carrying reactive functional groups (e.g., halides, amines, imidazoles, etc.) to form PILs afterwards. This approach is very useful when PILs with the desired architectures and functional groups are not accessible by direct polymerization of IL monomers. However, the ideal synthesis chemistry for this approach needs to be high yielding, no byproducts or only inoffensive byproducts, stereospecific, and easy to purify.

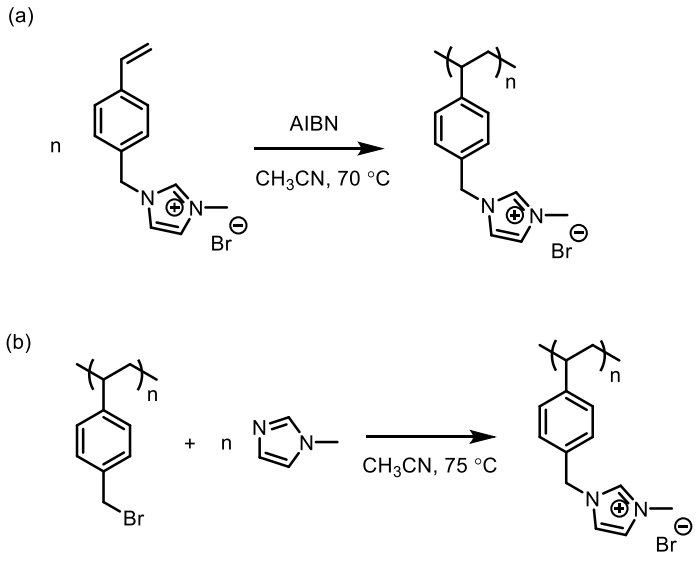

Figure 1.2. Examples of the two general methods used for the synthesis of PILs: (a) direct polymerization of an IL monomer and (b) post-polymerization modification of an existing polymer to introduce IL moieties.

1.3 Block copolymers

Homopolymers are a class of polymers that only contain chemically identical monomers, while copolymers have more than one type of monomer linked together in the same polymer chain.

Block copolymers (BCPs) are a specific subclass of copolymers in which the different monomers are not distributed within the polymer chain (random or alternating) but instead are linked as discrete homopolymer blocks.[15] In other words, BCPs can be treated as more than one homopolymers connected by covalent bonds from end to end. Depending on the number of connected distinct homopolymer blocks, BCPs can be classified as diblock, triblock, and higher multiblock copolymers. Among these types of BCPs, diblock copolymers have the simplest architecture and have attracted the most interest due to their ability to form various microstructures.[15]

In general, BCPs can be prepared using three approaches (see Figure 1.3. for representative examples): (1) sequential controlled/living polymerization of different monomers; (2) post-polymerization functionalization of an existing BCP to generate new BCP structure; and (3) connecting two or more homopolymers with reactive end groups. The first approach is widely used and has utilized living or controlled chain-addition polymerization methods such as anionic polymerization, living cationic polymerization, NMP, ATRP, RAFT polymerization, group-transfer polymerization (GTP), ROMP, and combinations of these polymerization techniques.[16] Under these controlled/living polymerization conditions, the undesired chain-transfer or termination reactions are minimized (or absent), allowing good control over the BCP architecture, molecular weight, and polydispersity. The post-polymerization functionalization of BCPs has attracted growing interest in the past decade and can be divided to two areas: covalent modification and noncovalent modification. The formation of functionalized moieties between reactive polymer side-chains and pendent reactants via covalent bonds is the most commonly used method to modify BCP structures. Hydrogenation, hydrolysis, hydrosilylation, esterification, quaternization, thiol-ene and thiol-yne chemistries, alkyne-azide cycloadditions, Michael additions, and Diels-Alder

'click' reactions have been applied to covalent post-polymerization functionalization.[17] The incorporation of functionalized moieties via noncovalent chemistry (e.g., hydrogen bonding, metal coordination, electrostatic interactions, hydrophobic interactions, π-π interactions, and inclusion complexation) into BCP architecture is an emerging area for BCP modification.[17] The modified BCP systems have distinct versatility and tunability because of the reversible side-chain functionalities. Overall, the post-polymerization functionalization approach is a powerful method to generate the desired side-chain-modified BCPs while retaining the architecture and properties of the parent BCP, especially to form functional groups that are not typically compatible with controlled/living polymerization methods. However, the chemistries used in this approach have the same limitations as described above for PIL post-polymerization functionalization. The last approach is less common and involves coupling of two appropriately end-functionalized polymer chains.[16b] One advantage of this approach is the ability of forming BCPs with homopolymer blocks made via step-growth polymerizations. However, the coupling reaction must be efficient, and usually further purification is needed to remove the remaining homopolymers from the BCP products.

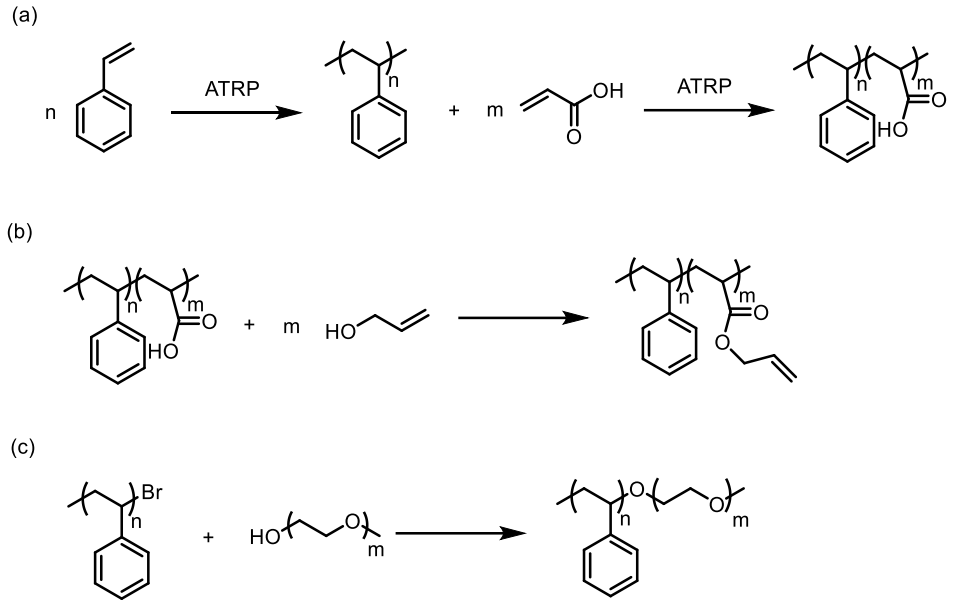

Figure 1.3. Examples of the three general methods used for the synthesis of BCPs: (a) sequential polymerization of different monomers; (b) post-polymerization functionalization of a BCP with a reactive block; and (c) reactive coupling of homopolymers.

The key feature of BCPs with immiscible blocks is their ability to phase-separate into ordered microstructures (in their neat melt state or in solution), which depends on the volume fraction (*f*) of each block and the effective degree of segregation (χN) between the blocks. As shown in Figure 1.4, varying the volume fraction of A block (f_A) and χN will generate diblock copolymers that can be disordered or phase-separated into ordered (i.e., periodic) morphologies including spheres on a body-centered-cubic lattice (S), hexagonally packed cylinders (Hex), bicontinuous cubic gyroids (Gyr), and lamellae (Lam).[18] Notably, the bicontinuous network present in the Gyr morphology has significant potential in many research areas that desire materials with domain continuity on the nanometer length scale.[18] With increasing number of blocks, the phase behavior of BCPs becomes much more complex. The phase equilibrium of multiblock

copolymers depends on the volume fractions of each block, all different χ-parameters of the blocks, the total degree of polymerization (N), and the sequences of the segments (e.g., ABC vs. ACB). For example, a wide range of ordered structures involves 30 different morphologies have been reported (experimentally or theoretically) for ABC triblock copolymers.[18a] Compared with BCP self-assembly in bulk, BCPs in solution can also self-assemble with increased complexity due to the extra interaction between each block and the solvent. The solution self-assembly of BCPs provides an important method to create soft-matter-based core−shell nanoparticles (micelles) with more than 20 morphologies such as "star-like" spherical micelles, worm-like micelles, rods, bicontinuous structures, radial or axially stacked lamellar, vesicles, tubules, pincushions, hierarchical micelles, "cross" supermicelles, etc.[19] Because of the great tunability of BCP self-assembly to form phase-separated materials with nanoscale domains, BCPs with ordered microstructures have been successfully applied as functional materials for polymer electrolytes in batteries,[20] proton-exchange membranes in fuel cells,[21], nanopattern fabrication templates,[22] photo- and thermal- responsive materials,[23] photovoltaics,[24] nanoporous membranes and coatings,[25] drug delivery platforms,[26] etc.

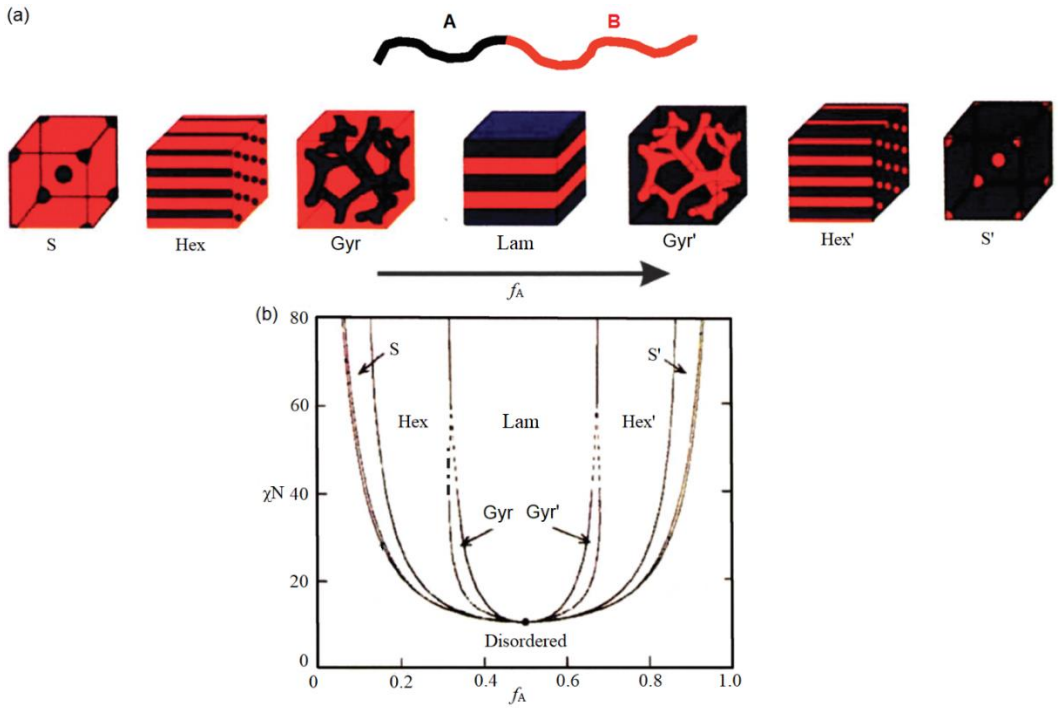

Figure 1.4. (a) Schematic representations of the classic morphologies of diblock copolymers: spheres (S), hexagonally packed cylinders (Hex), bicontinuous gyroids (Gyr), and lamellae (Lam). (b) The theoretical phase diagram of diblock copolymers that exhibit these morphologies. (reproduced from reference 18a)

1.4 Ionic liquid-based block copolymers

Ionic liquid-based block copolymers or polymerized ionic liquid-containing block copolymers (PIL-BCPs) are a subset of BCPs that contain at least one PIL as a block.[27] PIL-BCPs comprising imidazolium-, ammonium-, phosphonium-, and pyridinium-based ionic repeat units have been synthesized via three general approaches (see Figure 1.5 for representative examples): (1) sequential controlled/living polymerization of an uncharged monomer and an IL monomer; (2) controlled polymerization of an IL monomer from the end(s) of an uncharged polymer; and (3)

post-polymerization functionalization of an uncharged BCP containing reactive repeat units to generate IL moieties in situ. Research involving the first approach has utilized ATRP, RAFT polymerization, NMP, ROMP, anionic polymerization, and cobalt-mediated radical polymerization (COMP) of acrylate-, acrylamide-, styrene-, norbornene-, vinylpyridinium-, or vinyl imidazolium-based IL monomers with conventional noncharged monomers to form well defined PIL-BCPs.[13,27] Research involving the second approach has employed ATRP[28] and RAFT polymerization[29] of imidazolium-based monomers to form PIL segments off the end(s) of uncharged polymers made via step-growth polymerization. Research involving the third approach has focused on forming IL units on uncharged BCPs containing reactive side-chains, similar to the post-polymerization functionalization approach for PILs described in Section 1.2. By combining the unique properties of PILs with the mechanical strength and unique architectures of BCPs, PIL-BCPs have the ability to form ordered, phase-separated microstructures while retaining many of the desired properties of PILs. Thus, this relative new class of BCPs has been developed for use as thermoresponsive materials, precursors to carbonaceous materials, solid-state single-ion conductors, solid-state electrolytes for lithium-ion batteries, binders for lithium-ion batteries, recyclable organic catalysts, etc.[13,27]

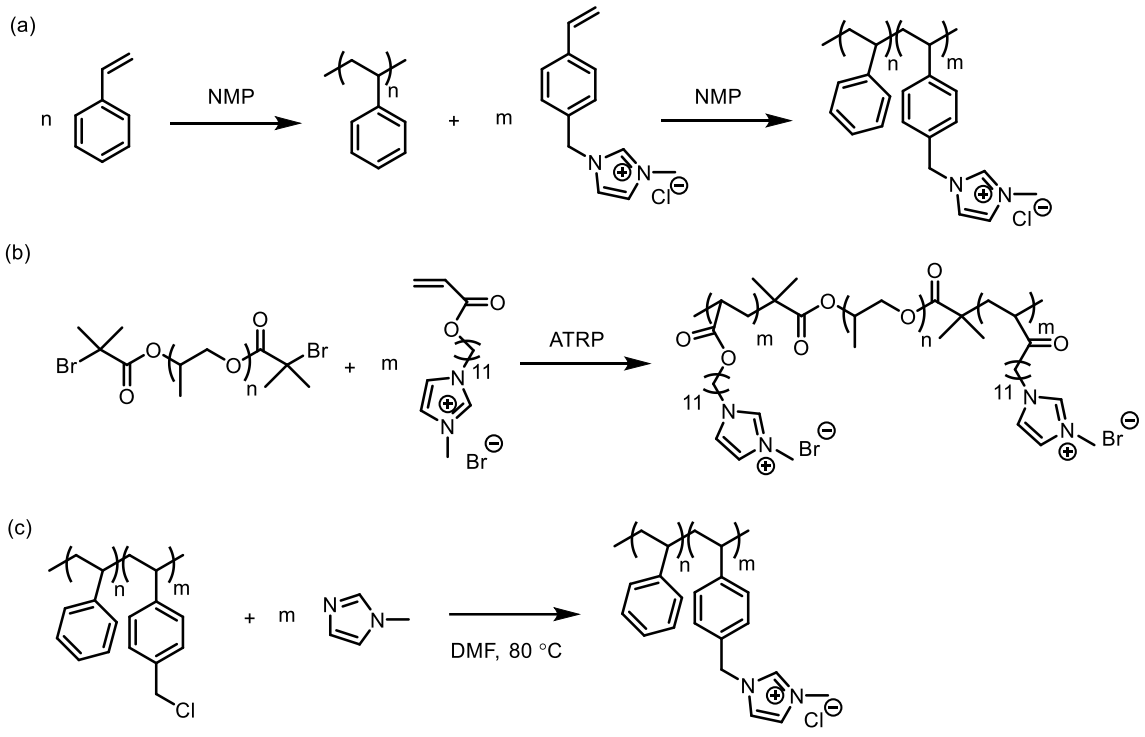

Figure 1.5. Examples of the three general methods used to synthesize PIL-BCPs: (a) sequential controlled/living polymerization of uncharged and IL monomers; (b) controlled polymerization of an IL monomer from the end(s) of an uncharged polymer; and (c) post-polymerization functionalization of an uncharged BCP.

Prior to the work described in this Ph.D. thesis, a variety of PIL-BCPs have been prepared by the approaches described above, but only a small subset of them has been reported to form ordered, phase-separated microstructures in the solvent-free melt state.[30] Notably, only two examples among these previously reported PIL-BCP systems were made via direct polymerization of an IL monomer and an uncharged monomer using ROMP[30a] or RAFT polymerization.[30d]

In 2011, our group was one of the first to show that imidazolium-based PIL-BCPs can form ordered microstructures in their neat states.[30a] Wiesenauer et al. reported the synthesis of PIL-

BCPs by sequential ROMP of a norbornene-based alkyl ester monomer and a norbornene-based imidazolium IL monomer (Figure 1.6). These PIL-BCPs with three different block ratios (noncharged-*b*-charged: 25-*b*-23, 30-*b*-20, and 35-*b*-15) all showed the formation of highly ordered Lam phases in their neat melt.

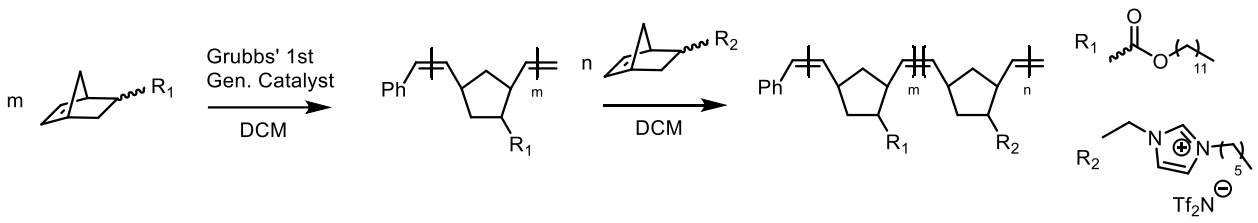

Figure 1.6. Synthesis of norbornene-based PIL-BCPs via sequential ROMP.[30a]

Mahanthappa et al. reported the synthesis of poly(styrene)-*b*-poly(4-vinylbenzyl alkylimidazolium Tf_2N^- salt) by post-polymerization functionalization around the same time in 2011.[30b] This styrene-based PIL-BCP system was made via quaternization of poly(styrene)-*b*-poly(4-vinylbenzyl chloride) with 1-alkylimidazole, followed by ion-exchange with $LiTf_2N$ (Figure 1.7). Solvent-cast or melt-pressed bulk films made from seven of these PIL-BCPs with a PIL mole fraction ranging from 2.7% to 15.6% and different alkyl groups (one methyl-, one butyl-, and five hexyl-) showed the ability to form a Lam phase and coexistent Lam phases with weakly ordered Hex phases. The ionic conductivity of the same PIL-BCP with different morphologies (ordered vs. disordered) varied by more than one order of magnitude indicating morphological defects strongly affect the observed conductivity in these materials.

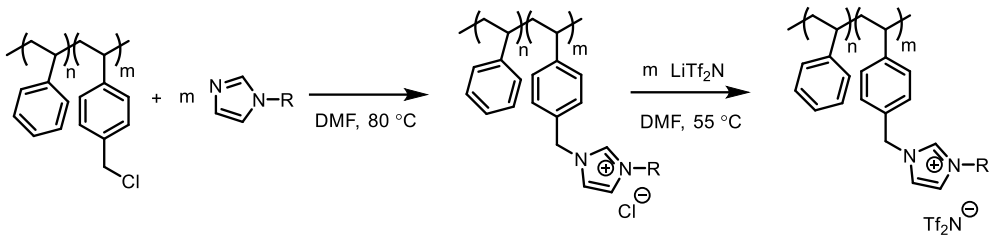

Figure 1.7. Synthesis of styrene-based PIL-BCPs via post-polymerization functionalization.[30b]

In 2013, Segalman et al. reported the synthesis of poly(styrene)-*b*-PIL BCPs via post-polymerization functionalization by reacting well defined poly(styrene)-*b*-poly(histamine methacrylamide) (PS-*b*-PHMA) BCPs with trifluoroacetic acid (Figure 1.8).[30c] Melt-pressed samples of this PIL-BCP system with five different block ratios (PIL mole fraction ranging from 8.3% to 53%) could phase-separate into different morphologies including weakly ordered Lam and weakly ordered Hex phases. The membrane samples made from these PIL-BCPs showed an order-of-magnitude higher ion conductivity compared to the PS-*b*-PHMA precursor BCP at room temperature.

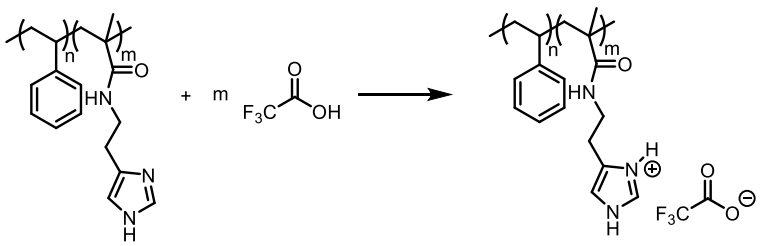

Figure 1.8. Synthesis of PIL-BCPs by post-polymerization functionalization of PS-*b*-PHMA.[30c]

As shown in Figure 1.9, Elabd et al. reported the synthesis of an acrylate-containing PIL-BCP in 2013 with 17.3 mol% of the PIL block via sequential RAFT polymerization, followed by ion-exchange with KOH solution to generate the hydroxide version of the BCP.[30d] Both BCPs showed the formation of a Lam morphology in the neat state and have increased anion conductivity (bromide or hydroxide) compared to their homopolymers or random copolymers under the same conditions. Shortly after this report, the same groups synthesized a variant PIL-BCP system contains six BCP samples (PIL mol% from 6.6% to 23.6%) using post-polymerization functionalization as shown in Figure 1.10.[30e] Thin film samples of these BCPs made by solvent casting were able to form Lam, Hex and weakly ordered phases. Interestingly, PIL-BCPs with strong microphase separation exhibited 1.5−2 orders of magnitude higher ionic conductivity than PIL-BCPs with weak microphase separation.

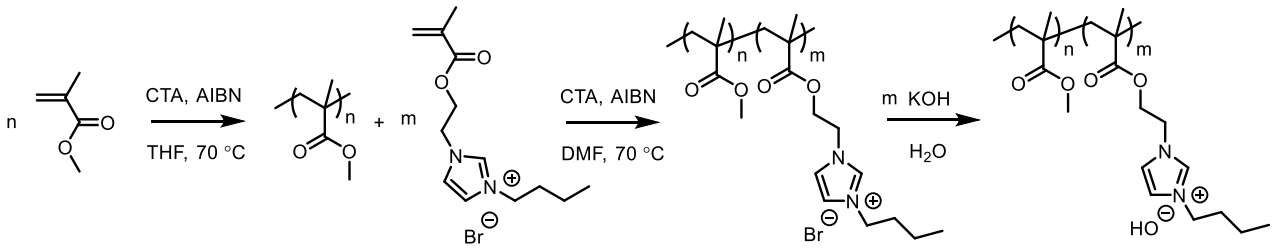

Figure 1.9. Synthesis of acrylate-based PIL-BCPs by sequential RAFT polymerization.[30d]

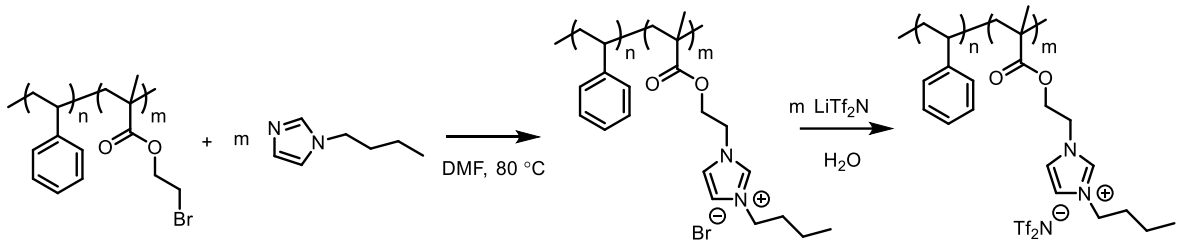

Figure 1.10. Synthesis of acrylate-based PIL-BCPs by post-polymerization functionalization. [30e]

As described in Section 1.1, MCILs expand the properties of ILs by introducing metal-based properties. Thus, MCIL-based BCPs (MCIL-BCPs) with those properties and the ability to form ordered microstructures would be promising as new functional materials. Prior to the work reported in this Ph.D. thesis, the synthesis of MCIL-BCPs was unprecedented to our knowledge. The closest reported BCPs with charged metal-containing repeat units were metallocene-based BCPs that are not true PIL-BCPs[31] because they were synthesized by copolymerization of uncharged monomers and charged metal-containing monomers that are not ILs.[31] Another close example was a paramagnetic random copolymer made via post-polymerization functionalization of an uncharged BCP to form pyridinium units that are randomly distributed in the polymer chain, then blended with $FeBr_3$ to get the metal-containing polymer (Figure 1.11).[32] However, this polymer is not a BCP and was obtained by mixing bromide polymer precursor with three equivalents (with respect to pyridinium bromide units) of $FeBr_3$ without further purification.

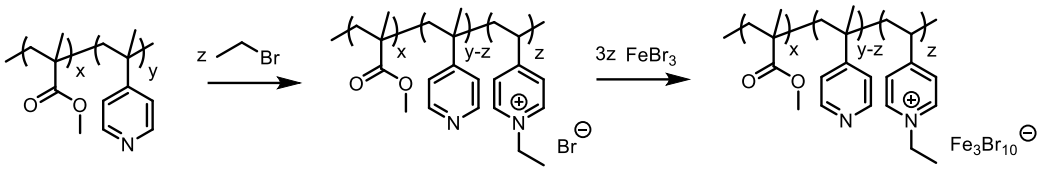

Figure 1.11. Synthesis of metal-containing random copolymers by post-polymerization functionalization.[32]

1.5 Summary

Prior to the work reported in this Ph.D. thesis, only a handful of organic-IL-based BCP systems have been reported to form ordered morphologies in their neat states. These systems had several practical limitations with respect to their synthesis and properties, and also none of these BCP systems showed the formation of a Gyr phase that we (and others) are particularly interested in for transport applications. With respect to MCIL-based polymers, to our knowledge, no MCIL-BCPs had been synthesized prior to the work described in this Ph.D. thesis.

1.6 References

(1) For recent reviews on ILs, see: (a) Weingrtner, H. *Angew. Chem. Int. Ed.* **2008**, *47*, 654−670. (b) Dong, K.; Liu, X.; Dong, H.; Zhang, X.; Zhang, S. *Chem. Rev.* **2017**, *117*, 6636−6695.

(2) For a recent review on IL thermal stability, see: Maton, C.; De Vos, N.; Stevens, C. V. *Chem. Soc. Rev.* **2013**, *42*, 5963−5977.

(3) For a recent review on IL gas solubility, see: Lei, Z.; Dai, C.; Chen, B. *Chem. Rev.* **2014**, *114*, 1289−1326.

(4) For a recent review on applications of ILs in the chemical industry, see: Plechkova, N. V.; Seddon, K. R. *Chem. Soc. Rev.* **2008**, *37*, 123−150.

(5) For a recent review on IL-based extraction, see: Sun, X.; Luo, H.; Dai, S. *Chem. Rev.* **2012**, *112*, 2100−2128.

(6) For a recent review on IL's catalytic application, see: Qiao, Y.; Ma, W.; Theyssen, N.; Chen, C.; Hou, Z. *Chem. Rev.* **2017**, *117*, 6881−6928.

(7) For a recent review on ILs as explosives and propellant fuels, see: Zhang, Q.; Shreeve, J. M. *Chem. Rev.* **2014**, *114*, 10527−10574.

(8) For a recent review on ILs for lithium and sodium batteries, see: Yang, Q.; Zhang, Z.; Sun, X.; Hu, Y.; Xing, H.; Dai, S. *Chem. Soc. Rev.* **2018**, *47*, 2020−2064.

(9) For a recent review on IL-based CO_2 capture systems, see: Zeng, S.; Zhang, X.; Bai, L.; Zhang, X.; Wang, H.; Wang, J.; Bao, D.; Li, M.; Liu, X.; Zhang, S. *Chem. Rev.* **2017**, *117*, 9625−9673.

(10) For a recent review on IL-based materials as CO_2 separation membranes, see: Tome, L. C.; Marrucho, I. M. *Chem. Soc. Rev.* **2016**, *45*, 2785−2824.

(11) For a recent review on protic ILs, see: Greaves, T. L.; Drummond, C. J. *Chem. Rev.* **2015**, *115*, 11379−11448.

(12) For recent reviews on metal-containing ILs, see: (a) Yoshida, Y.; Saito, G.; in *Ionic Liquids: Theory, Properties, New Approaches*; Kokorin, A., ed.; InTech, 2011. 723−739. (b) Estager, J.; Holbrey, J. D.; Swadz´ba-Kwas´ny, M. *Chem. Soc. Rev.* **2014**, *43*, 847−886.

(13) For recent reviews on PILs, see: (a) Yuan, J.; Antonietti, M. *Polymer* **2011**, *52*, 1469−1482. (b) Yuan, J.; Mecerreyes, D.; Antonietti, M. *Prog. Polym. Sci.* **2013**, *38*, 1009−1036.

(14) For recent reviews on the applications of PILs, see: (a) Qian, W.; Texter, J.; Yan, F. *Chem. Soc. Rev.* **2017**, *46*, 1124−1159. (b) Shaplov, A. S.; Ponkratov, D. O.; Vygodskii, Y. S. *Polym. Sci. Ser. B.* **2016**, *58*, 73−142. (c) Riduan, S. N.; Zhang, Y. *Chem. Soc. Rev.* **2013**, *42*, 9055−9070.

(15) For a recent review on BCPs, see: Kim, H.; Park, S.; Hinsberg, W. *Chem. Rev.* **2010**, *110*, 146−177.

(16) For recent reviews on the synthesis of BCPs by sequential controlled/living polymerization, see: (a) Li, X.; Iocozzia, J.; Chen, Y.; Zhao, S.; Cui, X.; Wang, W.; Yu, H.; Lin, S.; Lin, Z. *Angew. Chem. Int. Ed.* **2018**, *57*, 2046−2070. (b) Hadjichristidis, N.; Pitsikalis, M.; Iatrou, H. *Adv. Polym. Sci.* **2005**, *189*, 1−124.

(17) For a recent review on the synthesis of BCPs by post-polymerization functionalization, see: Romulus, J.; Henssler, J. T.; Weck, M. *Macromolecules* **2014**, *47*, 5437−5449.

(18) For recent reviews on the phase behavior of BCPs in their neat states, see: (a) Mai, Y.; Eisenberg, A. *Chem. Soc. Rev.* **2012**, *41*, 5969−5985. (b) Kim, J. K.; Han, C. D. *Adv. Polym. Sci.* **2010**, *231*, 77−145.

(19) For recent reviews on BCP self-assembly in solution, see: (a) Tritschler, U.; Pearce, S.; Gwyther, J.; Whittell, G. R.; Manners, I. *Macromolecules* **2017**, *50*, 3439−3463. (b) Kim, J. K.; Yang, S. Y.; Lee, Y.; Kim, Y. *Prog. Polym. Sci.* **2010**, *35*, 1325−1349.

(20) For a recent review on BCPs as polymer electrolytes, see: Young, W.; Kuan, W.; Epps, T. H. III. *J. Polym. Sci. B: Polym. Phys.* **2014**, *52*, 1−16.

(21) For a recent review on BCPs as proton-exchange membranes, see: Elabd, Y. A.; Hickner, M. A. *Macromolecules* **2011**, *44*, 1−11.

(22) For a recent review on BCPs for nanopatterning, see: Luo, M.; Epps, T. H. III. *Macromolecules* **2013**, *46*, 7567−7579.

(23) For recent reviews on BCPs as responsive materials, see: (a) Strandman, S.; Zhu, X. X. *Prog. Polym. Sci.* **2015**, *42*, 154−176. (b) Gohy, J.; Zhao, Y. *Chem. Soc. Rev.* **2013**, *42*, 7117−7129.

(24) For a recent review on BCPs as photovoltaics, see: Lee, Y.; Gomez, E. D. *Macromolecules* **2015**, *48*, 7385−7395.

(25) For a recent review on BCPs as membranes and coatings, see: Nunes, S. P. *Macromolecules* **2016**, *49*, 2905−2916.

(26) For a recent review on BCPs for nanomedicine applications, see: Cabral, H.; Miyata, K.; Osada, K.; Kataoka, K.; *Chem. Rev.* **2018**, *118*, 6844−6892.

(27) For a recent review on PIL-BCPs, see: Meek, K. M.; Elabd, Y. A. *J. Mater. Chem. A* **2015**, *3*, 24187−24194.

(28) (a) Texter, J.; Vasantha, V. A.; Crombez, R.; Maniglia, R.; Slater, L.; Mourey, T. *Macromol. Rapid Commun.* **2012**, *33*, 69−74. (b) Agudelo, N. A.; Elsen, A. M.; He, H.; López, B. L.; Matyjaszewski, K. *J. Polym. Sci. A: Polym. Chem.* **2015**, *53*, 228−238.

(29) (a) Chanthad, C.; Masser, K. A.; Xu, K.; Runt, J.; Wang, Q. *J. Mater. Chem.* **2012**, *22*, 341−344. (b) Li, J.; Liang, J.; Wu, W.; Zhang, S.; Zhang, K.; Zhou, H. *New J. Chem.* **2014**, *38*, 2508−2513.

(30) (a) Wiesenauer, E. F.; Edwards, J. P.; Scalfani, V. F.; Bailey, T. S.; Gin, D. L. *Macromolecules* **2011**, *44*, 5075−5078. (b) Weber, R. L.; Ye, Y.; Schmitt, A. L.; Banik, S. M.; Elabd, Y. A.; Mahanthappa, M. K. *Macromolecules* **2011**, *44*, 5727−5735. (c) Schneider, Y.; Modestino, M. A.; McCulloch, B. L.; Hoarfrost, M. L.; Hess, R. W.; Segalman, R. A. *Macromolecules* **2013**, *46*, 1543−1548. (d) Ye, Y.; Sharick, S.; Davis, E. M.; Winey, K. I.; Elabd, Y. A. *ACS Macro Lett.* **2013**, *2*, 575−580. (e) Choi, J.; Ye, Y.; Elabd, Y. A.; Winey, K. I. *Macromolecules* **2013**, *46*, 5290−5300.

(31) For recent reviews on metallocene-based BCPs, see: (a) Hailes, R. L. N.; Oliver, A. M.; Gwyther, J.; Whittell, G. R.; Manners, I. *Chem. Soc. Rev.* **2016**, *45*, 5358−5407. (b) Hardya, C. G.; Zhang, J.; Yan, Y.; Ren, L.; Tang, C. *Prog. Polym. Sci.* **2014**, *39*, 1742−1796. (c) Zhou, J.; Whittell, G. R.; Manners, I. *Macromolecules* **2014**, *47*, 3529−3543.

(32) Carrasco, P. M.; Tzounis, L.; Mompean, F. J.; Strati, K.; Georgopanos, P.; Garcia-Hernandez, M.; Stamm, M.; Cabanero, G.; Odriozola, I.; Avgeropoulos, A.; Garcia, I. *Macromolecules* **2013**, *46*, 1860−1867.

CHAPTER 2

Ph.D. Research Objectives

2.1 Overview of Ph.D. research

The objectives of this Ph.D. research were to develop new, ordered, phase-separated, polymerized ionic liquid-based block copolymer (PIL-BCP) systems for exploration as new functional materials, with a focus on two BCP platforms: (1) a new organic-ionic-liquid (IL)-based BCP platform that allows ease of synthesis and control over phase morphology; and (2) the first example of a metal-containing ionic liquid-based block copolymer (MCIL-BCP) platform that forms ordered nanostructures and has functional capabilities introduced by the incorporated metal complex.

As described in Chapter 1, the first generation of PIL-BCPs synthesized by our group were the norbornene-based PIL-BCPs made via living ring-opening metathesis polymerization (ROMP) (Figure 1.6). These BCPs showed the formation of Lam and weakly-ordered liquid-like packed S phases in their neat states and proved that BCP morphology had a direct impact on the gas transport properties of the material.[1] However, there were several limitations with this initial PIL-BCP system, such as the use of an expensive Ru-based ROMP catalyst, elaborate monomer syntheses, residual metal contamination (from the catalyst) in the BCP products, and poor mechanical properties due to the liquid-like nature of these BCPs. Therefore, a new styrene-based PIL-BCP platform was developed using atom-transfer radical polymerization (ATRP) (Figure 2.1) for polymer structure and molecular weight control that uses less-expensive Cu-based polymerization catalysts, easier monomer syntheses, reduced metal contamination in the final BCP material, and

easier handling of the polymer products (solid powders vs. viscous liquids). Then, the neat-state self-assembly behavior and phase diagram on the IL-rich side for this PIL-BCP system were explored by varying volume fraction of the PIL block and side group modification on the IL monomer (Figure 2.2).

In 2014, our group synthesized a new Co(II)-containing MCIL that could reversibly coordinate with H_2O and CH_3OH.[2] Since MCILs are liquid materials with IL- and metal-based properties, the ability to make processible, phase-separated, MCIL-BCPs is highly desirable for the development of new IL-based functional materials. Thus, the second objective of this Ph.D. research was to synthesize the first example of MCIL-BCPs via reversible addition-fragmentation chain-transfer (RAFT) polymerization for polymer structure and molecular weight control and explore the morphological phase behavior of these MCIL-BCPs in the neat state (Figure 2.3). Subsequently, the functional capabilities of these MCIL-BCPs as potential functional materials were investigated including the selective and reversible coordination chemistry and catalytic reactivity inherent in the transition-metal complex making up the MCIL component.

2.2 Specific research accomplishments by thesis chapter

Chapter 3 outlines the synthesis of a series of ordered, phase-separated, styrene-based PIL-BCPs (**1**) via the sequential ATRP of styrene and styrenic imidazolium bis(trifluoromethyl)sulfonamide (Tf_2N^-) monomers with different length alkyl side-chains (**2**) (Figure 2.1).[3] Studies on nine PIL-BCP samples indicated that their ability to form ordered microstructures (i.e., S, Hex, and S_{LLP} phases) depends on both the block composition and the length of the alkyl side-chain on the imidazolium-IL monomer.

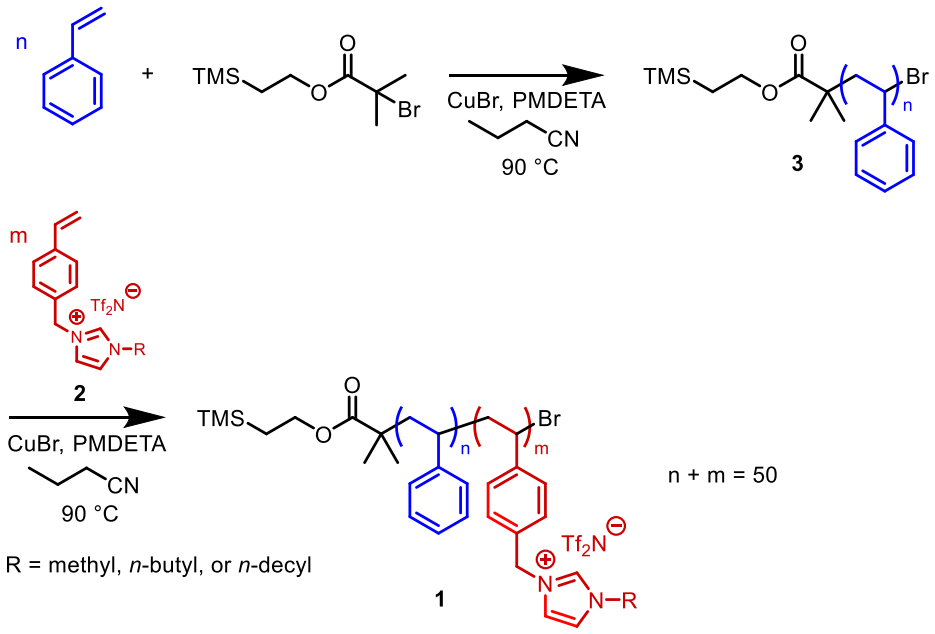

Figure 2.1. Synthesis and structures of the PIL-BCPs made via sequential ATRP in this thesis.

Chapter 4 details the synthesis and characterization of a library of thermally processable, phase-separated PIL-BCPs (**1**) using the same methods described in Chapter 3. A series of PIL-BCP variants based on **1** with various alkylimidazolium substituents (i.e., 13 methyl-, 2 *n*-propyl-, 7 *n*-butyl-, and 2 *n*-hexyl-substituted BCPs) were synthesized to cover a wide range of volume fractions of the PIL block (f_{PIL}) and tune the effective degree of segregation (χN) between the blocks. Small-angle X-ray scattering (SAXS) analysis of these BCPs (performed by collaborators at Colorado State University) showed the formation of the 4 classic ordered morphologies of diblock copolymer (i.e., S, Hex, Lam, and Gyr phases) depends on both the f_{PIL} and the attached alkyl group on the imidazolium units. Notably, simple replacement of a methyl group by the *n*-butyl group on the imidazolium IL repeat unit resulted in the emergence of the Gyr phase.

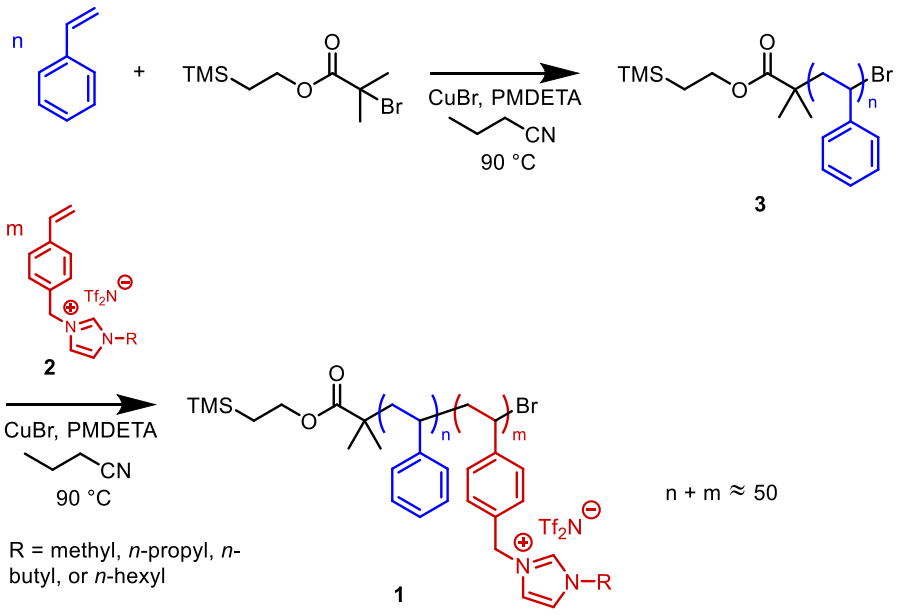

Figure 2.2. Synthesis and structures of the PS-*b*-PIL BCPs made via sequential ATRP in this thesis work.

Chapter 5 describes the synthesis and characterization of the first example of an MCIL-based, uncharged-*b*-charged diblock copolymer (**4**). This MCIL-BCP platform was made via sequential RAFT polymerization of an uncharged organic methacrylate monomer, followed by a charged MCIL monomer in which the transition-metal is contained in the anion (Figure 2.3).[4] SAXS studies on six samples of these Co(II) bis(salicylate) anion-containing BCPs all having a 70 repeat units in total but different block compositions showed the formation of ordered microstructures (i.e., S, Hex, Lam, and Gyr phases) in their neat states. To our knowledge, this is the first example of an IL-based BCP that exhibits the Gyr phase in the neat state. Additionally, these MCIL-BCPs were found to be able to reversibly bind H_2O or small alcohols with an obvious color change.

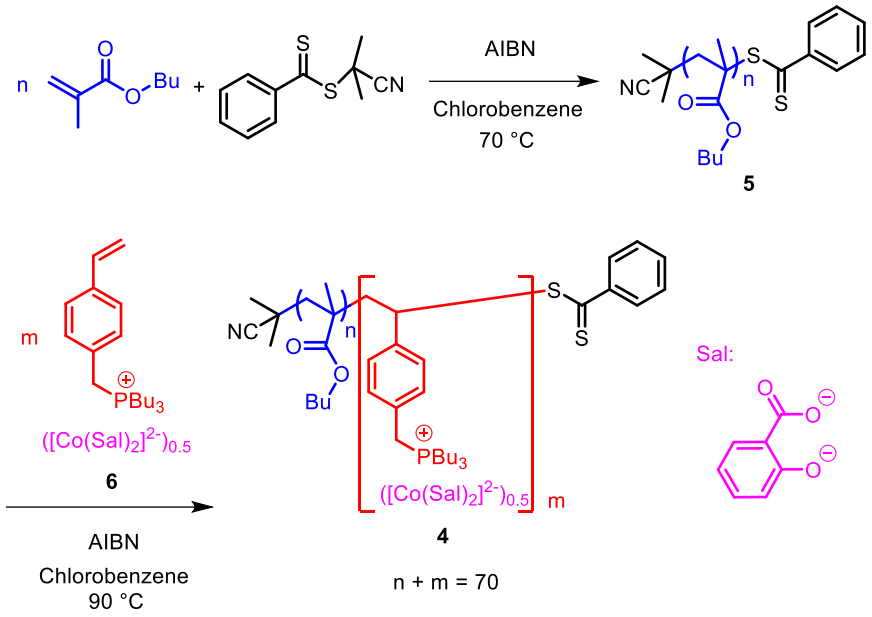

Figure 2.3. Synthesis and structures of the MCIL-BCPs made via RAFT polymerization in this thesis work.

Chapter 6 explores the reactivity of the MCIL-BCPs prepared in Chapter 5 for potential applications. First, the reversible coordination of these MCIL-BCPs with water and various hydroxyl-containing common organic solvents was further studied to understand the thermal stability and selectivity of the coordination chemistry. In addition, SAXS analysis was performed on the organic-solvent-coordinated MCIL-BCP samples to determine whether the reversible solvent coordination induces any (reversible) phase changes in the polymers. Second, the catalytic reactivity of the MCIL polymer system was also explored for known reactions that are catalyzed by Co(II) sites (e.g., autoxidation of aldehydes, epoxidation of olefins, oxidation of secondary alcohols).

2.3 References

(1) Nguyen, P. T.; Wiesenauer, E. F.; Gin, D. L.; Noble, R. D. *J. Membr. Sci.* **2013**, *430*, 312−320.

(2) Kohno, Y.; Cowan, M. G.; Masuda, M.; Bhowmick, I.; Shores, M. P.; Gin, D. L.; Noble, R. D. *Chem. Commun.* **2014**, *50*, 6633−6636.

(3) Shi, Z.; Newell, B. S.; Bailey, T. S.; Gin, D. L. *Polymer* **2014**, *55*, 6664−6671.

(4) Shi, Z.; May, A. W.; Kohno, Y.; Bailey, T. S.; Gin, D. L. *J. Polym. Sci. A: Polym. Chem.* **2017**, *55*, 2961−2965.

CHAPTER 3

Ordered, Microphase-Separated, Noncharged-Charged Diblock Copolymers via the Sequential ATRP of Styrene and Styrenic Imidazolium Monomers

(Adapted from the manuscript published under the same title in *Polymer* **2014**, *55*, 6664−6671, co-authored with Newell, B. S.; Bailey, T. S.; Gin, D. L.)

3.1 Abstract

New imidazolium ionic liquid-based noncharged-charged diblock copolymers with a total of 50 repeat units were synthesized by the direct, sequential ATRP of styrene and styrenic imidazolium bis(trifluoromethyl)sulfonamide monomers with methyl, *n*-butyl, and *n*-decyl side-chains. Small-angle X-ray scattering studies on these block copolymer samples showed that their ability to form ordered nanostructures (i.e., sphere and cylinder phases) in their neat states depends on both the styrene:imidazolium-IL ratio and the length of the alkyl side-chain on the imidazolium monomer.

3.2 Introduction

Polymerized ionic liquids (PILs) are macromolecules with charged repeat units that are prepared from or structurally related to ionic liquids (ILs).[1] Since ILs are small-molecule liquid materials with a unique combination of distinctive properties (e.g., high thermal stability,

negligible vapor pressure, ion conductivity, high solubility for certain light gases),[2] the ability to make processible, solid-state, polymeric analogs is highly desirable.[1] PILs can be made by direct polymerization of reactive IL monomers[1] or by postpolymerization modification of uncharged polymers containing reactive repeat units to generate the IL moieties.[1] Because of the synthetic versatility, ion conductivity, and high CO_2 gas solubility afforded by the imidazolium units,[1,2] imidazolium-based PILs have been successfully applied as new membrane materials for CO_2/light gas separations,[3] solid-state ion conductors,[4] specialty dispersants/surfactants,[5] and platforms for new electrochemical devices.[6]

Although imidazolium PILs have been synthesized in a number of polymer chain architectures,[1] phase-separated PIL-containing block copolymers (BCPs) has received a great deal of recent research attention. BCPs can form phase-separated nanostructures ranging from simple micelles and vesicles to ordered, periodic assemblies, making them attractive for encapsulation/release and transport applications.[7] In addition, alteration of BCP chemical composition and block ratios can be used to obtain different mechanical properties and control the phase-separated morphologies.[7] If one of these blocks contains imidazolium IL units, then nanostructured BCPs can be generated with one domain having imidazolium IL-like properties, resulting in a material with a combination of features of BCPs and PILs.

At the beginning of this work, several types of imidazolium-based BCPs containing charged and uncharged blocks have been synthesized using three general approaches: (1) sequential controlled/living polymerization of an imidazolium-based monomer with an uncharged co-monomer; (2) controlled polymerization of an imidazolium monomer from the end of an uncharged polymer; or (3) postpolymerization functionalization of an uncharged BCP containing a reactive segment to generate imidazolium units in situ. The first approach has included reversible

addition-fragmentation chain-transfer (RAFT) copolymerization of acrylate-, acrylamide-, or vinyl-substituted imidazolium monomers with conventional acrylates and acrylamides to give noncharged-charged diblock copolymers;[8–10] and sequential ring-opening metathesis polymerization (ROMP) of alkyl ester- and imidazolium-containing norbornene monomers.[11] The second approach has utilized ATRP[13,14] and RAFT[15,16] of acrylate-[13,15,16] and styrene-based[14] imidazolium monomers to form PIL segments off the end(s) of uncharged telechelic[13–15] or monofunctional[16] polymers. The third approach has involved substitution of imidazole onto uncharged BCPs containing a reactive alkyl halide block made by nitroxide-mediated polymerization (NMP),[17–19] RAFT,[20] or step-growth[21,22] polymerizations; selective quaternization of polystyrene-*b*-poly(styrene-imidazole)s formed by NMP;[23] or attachment of imidazolium groups onto uncharged thiol-acrylate-based BCPs made by RAFT.[24] One other related polymer modification approach is cation-exchange of commercial alkyl-anionic BCPs with imidazolium salts to generate BCPs with free imidazolium counterions.[25] Although many of these materials have been demonstrated to be useful in several applications,[11c,11d,16,18,20–25] only a small subset of them has been reported to form phase-separated, ordered nanostructures in the solvent-free neat state.[11,18,21c,22,23b,24] The majority of the BCPs listed above were not reported to form periodic nanostructures,[12–15,20] or they only formed micelles or non-ordered phases.[8–10,16,17,19,21a,21b,23a,25]

In 2011, our group was one of the first to show that imidazolium-based BCPs can form ordered nanostructures in their neat state by using alkyl-imidazolium BCPs made from sequential ROMP of a norbornene-based alkyl ester monomer and a norbornene-based imidazolium monomer.[11a] Supported membranes of these materials were also found to have nanostructure-dependent CO_2 transport properties, making them potential useful for gas separations.[11c,d] However, there were several limitations with our initial IL-based BCP design that hampered

preparation of substantial amounts of these materials for exploring applications (e.g., the use of an expensive Ru-based ROMP catalyst, residual metal contamination in the BCPs (from the catalyst) after isolation, and elaborate monomer syntheses).[11]

Herein, we show ordered, phase-separated, imidazolium-based noncharged-charged diblock copolymers (**1**) synthesized via the sequential ATRP of styrene and styrenic imidazolium bis(trifluoromethyl)sulfonamide (Tf_2N^-) monomers with different length alkyl side-chains (**2a–c**) (Figure 3.1). Studies on nine BCP examples of **1** with a total of 50 repeat units and styrene:imidazolium-IL repeat unit ratios of 25:25, 20:30, and 15:35 indicated that their ability to form ordered nanostructures depends on both the block ratio and the length of the alkyl chain on the imidazolium-IL monomer. Compared to our previous ROMP method, this controlled radical polymerization (CRP) approach with styrenic monomers allows the use of a less expensive catalyst system, minimum metal contamination in the BCPs formed, and more facile and scalable monomer syntheses. Although ATRP homopolymerization of imidazolium-containing monomers is well-established,[1] the direct, sequential ATRP of imidazolium and hydrophobic monomers to generate imidazolium BCPs with ordered, phase-separated nanostructures has not been reported at the beginning of this study.[8–10,12]

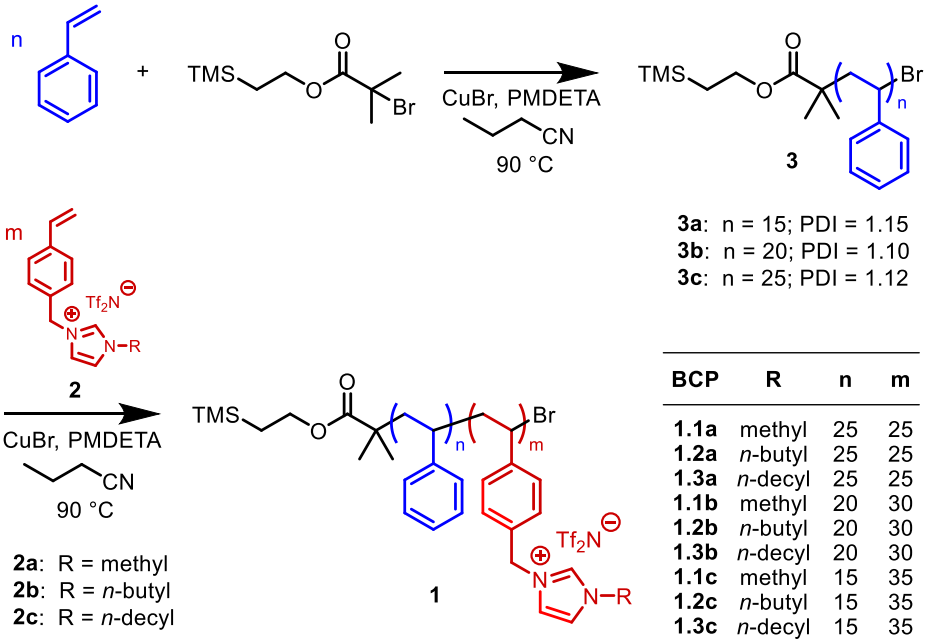

BCP	R	n	m
1.1a	methyl	25	25
1.2a	*n*-butyl	25	25
1.3a	*n*-decyl	25	25
1.1b	methyl	20	30
1.2b	*n*-butyl	20	30
1.3b	*n*-decyl	20	30
1.1c	methyl	15	35
1.2c	*n*-butyl	15	35
1.3c	*n*-decyl	15	35

Figure 3.1. Synthesis and structures of the noncharged-charged BCPs made via sequential ATRP.

3.3 Results and discussion

3.3.1 Materials synthesis

ATRP was selected as a more economical and scalable alternative to ROMP, because of its molecular weight (MW) and block ratio control, low PDI, and ability to polymerize a broad range of acrylate and styrene monomers (including ionic versions). Styrenic compounds are ideal monomers for ATRP-based BCP synthesis because of their facile synthesis and functional group attachment. Monomers **2a** and **2b** were prepared by reacting 4-vinylbenzyl chloride with the appropriate *N*-alkylimidazole, followed by ion-exchange of the Cl^- anion with Tf_2N^- according to literature procedures.[26,27a] Compound **2c** is a new monomer and was synthesized using similar methods (see Section 3.6.4).

As shown in Figure 3.1, BCPs **1** were synthesized via ATRP of first styrene and then monomers **2a**, **2b**, or **2c** using CuBr/*N,N,N′,N′,N″*-pentamethyldiethylenetriamine (PMDETA) as the catalyst system and 2-(trimethylsilyl)ethyl 2-bromo-2-methyl-propanoate as the initiator in butyronitrile solution (see Section 3.6.8 for details). Analysis of the isolated BCPs formed by this method show very little residual Cu from the polymerization catalyst (see Section 3.6.13). In our sequential copolymerizations, controlled-length, low-PDI reactive polystyrene blocks **3a–c** were first synthesized and then used as ATRP macro-initiators to form the subsequent attached imidazolium block upon addition of the appropriate amount of **2a**, **2b**, or **2c**. This polymerization sequence was important because of the lower efficiency of the initiator system with the imidazolium-IL monomers and the inconvenient purification process of the resulting ionic macro-initiator if the imidazolium blocks were synthesized first.

3.3.2 Confirmation of controlled polymerization behavior for the ATRP of styrenic imidazolium monomers 2a–c

At the start of this work, the ATRP,[27] NMP,[28] and RAFT[27b] of only two styrenic imidazolium monomers (**2b** and a chiral cyclohexanol-substituted imidazolium-styrene monomer[27f]) were reported in the literature. The controlled ATRP of **2a** and **2c** had not been reported, and the sequential ATRP of styrene and **2a–c** to generate nanostructured BCPs was also unprecedented. To confirm the controlled ATRP of **2a** and **2c** for viable BCP synthesis with styrene, the homopolymerization kinetics of **2a** and **2c** were first explored. In addition, the kinetics of the copolymerizations of styrene with **2a–c** were also studied to confirm controlled radical polymerization behavior. In these initial studies, monomer consumption and the absolute number-average MW (M_n) values of the formed polymers were calculated by ^{1}H NMR integration and end-

group analysis (see Section 3.6.10). As shown in Figure 3.2, the ATRP of **2a**, the ATRP of **2c**, and the sequential ATRP of styrene followed by **2a** (as a representative copolymerization example) all show linear, first-order monomer conversions with time and linear increases in M_n with monomer conversion. This behavior indicates that these ATRP homopolymerizations and copolymerizations are well-controlled radical polymerization. By varying the styrene and **2a–c** mole ratios in the sequential ATRP reactions, nine BCPs (**1.1a–c**, **1.2a–c**, and **1.3a–c**) were obtained with three different styrene:imidazolium-IL block ratios and three different alkyl side-chain lengths on the imidazolium-IL repeat units.

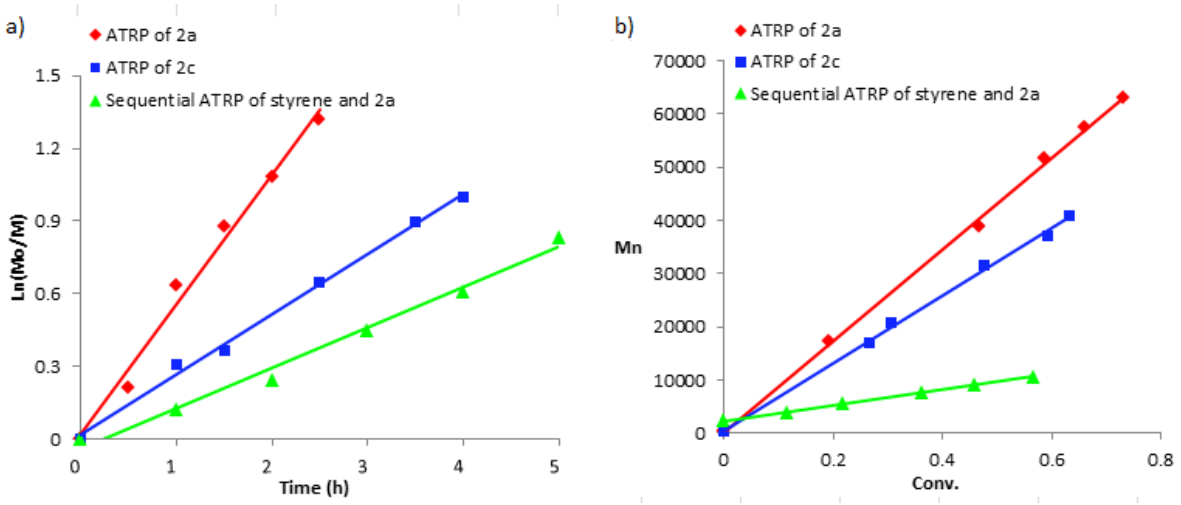

Figure 3.2. Plots confirming the controlled ATRP homopolymerization of monomers **2a** and **2c,** and the sequential ATRP of styrene and **2a** to form BCP **1.1b**.

3.3.3 Structure and molecular weight characterization of BCPs 1.1a–c, 1.2a–c, and 1.3a–c

The block composition ratios and absolute lengths of BCPs **1** (i.e., **1.1a–c**, **1.2a–c**, and **1.3a–c**) were confirmed by ^{1}H NMR analysis (see Section 3.6.9 for details): The block lengths of the polystyrene macro-initiators **3a–c** were determined by ^{1}H NMR end-group analysis using the trimethylsilyl (TMS) group on the initiator as an integration reference.[29] The styrene:imidazolium-IL block ratios for each BCP were determined by integrating and comparing distinct ^{1}H NMR signals indicative of each block. The ionic block lengths were then calculated based on the alkyl block lengths and the block composition ratios. These results were further confirmed by TMS end-group analysis[29] and the copolymerization monomer-to-initiator ratios. Consequently, the absolute M_n values for BCPs **1** could be calculated by simply multiplying the absolute block lengths (as determined by ^{1}H NMR) by the MWs of the repeat units.

Unfortunately, GPC and other conventional polymer MW determination methods (e.g., matrix-assisted laser desorption ionization time-of-flight mass spectrometry, and dynamic light scattering) could not be used to confirm the MW, PDI, or block structure of **1** because of the unusual solubility and other physical properties of these noncharged-charged BCPs, as previously reported.[11a] A modified GPC method that enables PIL MW determination was recently reported;[27c] however, we could not modify the GPC system we used in such a fashion, and the hybrid characteristics of noncharged-charged BCPs still presented solubility difficulties. Instead, a combination of alternative methods (i.e., surfactant behavior and solubility analysis, diffusion-ordered spectroscopy (DOSY), small-angle X-ray scattering (SAXS) studies) was used to verify the block architectures of **1** and to differentiate their behavior from that of a physical blend of polystyrene and poly(**2a**)–poly(**2c**) homopolymers, as described previously[11a] (see Section 3.6.11).

3.3.4 Characterization of the morphologies formed by BCPs 1

Table 3.1. Summary of the room-temperature morphologies formed by thermally annealed BCPs **1** according to SAXS analysis.

BCP	n	m	R	Morphology	Observed q/q^*_{100} values
1.1a	25	25	methyl	Hex (weakly ordered	√1, (√3), √4, √7, (√9)
1.2a	25	25	*n*-butyl	Hex (weakly ordered)	√1, (√3), √4, √7, (√9)
1.3a	25	25	*n*-decyl	Disordered	(none)
1.1b	20	30	methyl	S_{BCC}	√2, √4, √6, √8
1.2b	20	30	*n*-butyl	S_{BCC}	√2, √4, √6, √8
1.3b	20	30	*n*-decyl	Disordered	(none)
1.1c	15	35	methyl	S_{LLP} (weakly ordered)	form factor scattering
1.2c	15	35	*n*-butyl	S_{LLP} (weakly ordered)	form factor scattering
1.3c	15	35	*n*-decyl	Disordered	(none)

The room-temperature (25 °C) morphological phase behavior of BCPs **1** (following melt-phase annealing at 175 °C for 30 min) from SAXS analysis is summarized in Table 3.1. The SAXS profiles of these samples at room-temperature after annealing are shown in Figure 3.3. The data confirm microphase separation for all BCP samples containing methyl or *n*-butyl substituents on

the imidazolium ring (i.e., **1.1a, 1.1b, 1.1c, 1.2a, 1.2b,** and **1.2c**), regardless of the styrene:imidazolium-IL block ratios tested. In contrast, the BCPs with the longer *n*-decyl substituent on the imidazolium block show no evidence of microphase separation. We speculate that by increasing the non-ionic character of the imidazolium substituent opposite the phenyl linker, the ability of the system to separate the charged units and create a thermodynamic advantage through microphase separation is becoming severely diminished. Differential scanning calorimetry (DSC) measurements revealed no evidence of any observable thermal transitions between –40 and 180 °C, and thus provided no additional insight into the microphase-separated state of the systems beyond that provided by SAXS. That is, neither glass transitions for the polymer blocks nor melt transitions associated with the alkyl side-chains on the imidazolium units could be detected in these samples. Details describing the DSC measurements and representative DSC data can be found in Section 3.6.12.

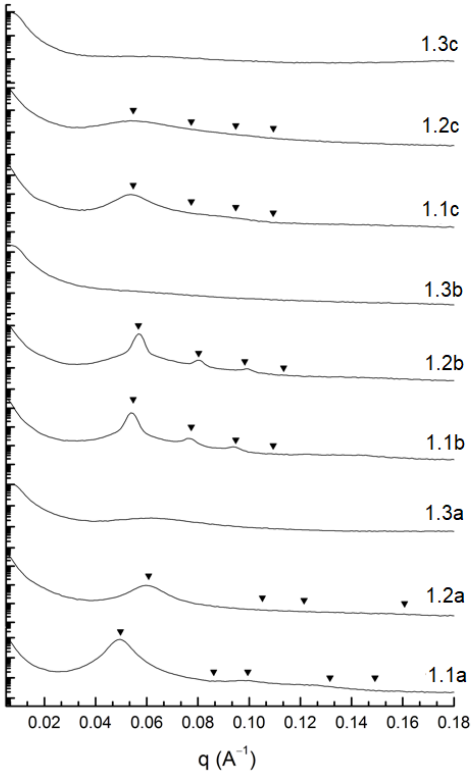

Figure 3.3. SAXS profiles of BCPs **1** at 25 °C after annealing at 175 °C for 30 min. The inverted triangles indicate the expected SAXS reflection positions for spheres ordered in a BCC lattice (**1.1b**, **1.2b**, **1.1c**, **1.2c**) and hexagonally packed cylinders (**1.1a**, **1.2a**).

The microphase-separated methyl and *n*-butyl BCP samples with the styrene:imidazolium-IL block ratios at 20:30 (**1.1b**, **1.2b**) exhibit a particularly high degree of order. In fact, both the methyl and *n*-butyl BCPs at this composition produce clear diffraction peaks consistent with the symmetry of spheres on a body-centered-cubic (S_{BCC}) lattice, with the expected q/q^* ratios of $\sqrt{2}$ (q_{110}), $\sqrt{4}$, $\sqrt{6}$, $\sqrt{8}$, etc. Here, $q^* = q_{100}$ is absent due to the reflection conditions associated with the BCC symmetry. Importantly, the q_{110} interplanar spacings at 25 °C imply cubic unit cell lattice constants of 16.6 and 15.5 nm for the methyl and *n*-butyl substituted samples, respectively. Such large lattice constants suggest chain stretching in these systems is significant, given the small

degrees of polymerization (DPs) used in this initial study. Mahanthappa and coworkers saw similar evidence of chain stretching in analogous noncharged-charged BCPs prepared by postpolymerization modification;[18] however, their studies were limited to compositions in which the charged imidazolium blocks comprised only the minority component (i.e., ≤17 mol% of the total number of repeat units). This was largely a constraint of the limited DPs and MW control that they could achieve using a creative multi-step, postpolymerization modification strategy to produce the charged imidazolium block. In their case, they used NMP of styrene and 4-vinylbenzyl chloride to produce modifiable polymeric precursors that were then quaternized with various *N*-alkylimidazoles, followed by anion-exchange with Tf_2N^-.[18] In contrast, our sequential ATRP of styrene and monomers **2a–c** reported here enables these imidazolium-containing BCPs to be produced more directly/easily and at compositions spanning the entire mole fraction spectrum.

It is significant that the sphere morphology is present in BCP **1** homologs in which the charged imidazolium block comprises just 60 mol% of the repeat units in the chain. For BCPs in which the repeat units of the two blocks are of similar volumes, such compositions would sit at the edge of the lamellar phase boundary. This suggests the volume increase associated with adding the charged imidazolium substituent to the phenyl ring in the polystyrene backbone is substantial, and creates significant packing differences between the ionic and nonionic blocks in the system. Mahanthappa and coworkers actually saw lamellar morphologies forming at imidazolium repeat unit compositions as low as 8 mol%.[18] Their results, taken together with ours, emphasize the rather extreme asymmetry in packing introduced when one block carries the charged imidazolium species.

Based on these observations, one would expect BCPs **1.1a** (methyl) and **1.2a** (*n*-butyl) with noncharged:charged block ratios fixed at 25:25 to exhibit phase behavior bounded by lamellae and sphere phases. However, the broadness evident in the scattering peaks (even after annealing at

175 °C) suggests that while these samples clearly phase-separate, they are challenged to find a well-ordered morphology at these compositions. In Figure 3.3, inverted triangular markers above the SAXS profiles of BCPs **1.1a** and **1.2a** indicate the positions of expected reflections for cylinders on a hexagonal lattice (i.e., at q/q^* ratios of $\sqrt{1}$ (q_{100}), $\sqrt{3}$, $\sqrt{4}$, $\sqrt{7}$, $\sqrt{9}$, etc.). At this point, a definitive assignment of the formed phase is not possible based on scattering data alone.

The most asymmetric BCP samples (**1.1c** and **1.2c**) with styrene:imidazolium-IL block ratios at 15:35 are also only weakly ordered. Based on the propensity of samples **1.1b** and **1.2b** to adopt the S_{BCC} lattice, the volume fraction of the styrene block in **1.1c** and **1.2c** may be significantly lower than the 0.10–0.14% range associated with the S_{BCC} phase. Samples in which the volume fraction of one block approaches values less than 10% have been found in many instances to adopt a liquid-like packing of spherical domains (S_{LLP}).[11b,30] The scattering signature for these systems is entirely consistent with that observed for **1.1c** and **1.2c**, with characteristic shoulder adjacent to a broad primary peak associated with form factor oscillations. Notably, these same scattering signatures were also characteristic of the S_{BCC}-forming samples (**1.1b** and **1.2b)** prior to annealing (c.f., Figure 3.4).

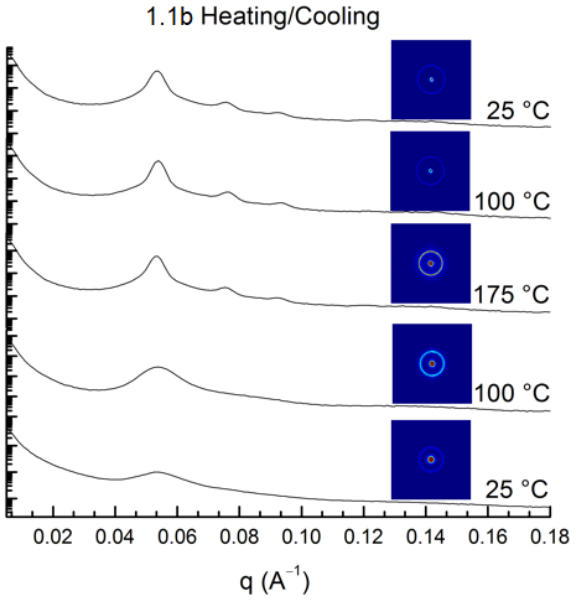

Figure 3.4. SAXS profiles of BCP **1.1b** throughout the thermal annealing procedure. Peak positions are consistent with those for spheres packed in a BCC lattice.

Inspection of each series of samples organized by fixed styrene:imidazolium-IL block ratios reveals that an increase in the alkyl substituent chain length on the imidazolium ring produces a decrease in the principle domain spacing for the system. This seemingly counter-intuitive result supports the argument that adding nonionic character (via choice of alkyl chain length) to the ionic block reduces the degree of segregation in the system, and helps relieve the high degree of chain stretching required to reach a free energy minimum. This shift towards decreased segregation levels supports the argument that the *n*-decyl substituent on the imidazolium ring is indeed acting to compatibilize the system. These data also suggest that a judicious choice of alkyl substituent on the imidazolium-IL monomer provides a discrete method for tuning the Flory interaction parameter for such systems. If true, one might be able to control the ability of the

system to adopt phases like bicontinuous gyroid, which have demonstrated a clear preference to form under weakly segregated conditions.[11b,18]

Similar to other imidazolium-based noncharged-charged BCPs we produced in the past,[11] many of the samples produced here required an initial heating step to achieve their highest level of order. For example, Figure 3.4 shows that there is a sufficient delay in obtaining highly ordered BCC spheres in the first heating cycle. The gradual ordering process, evident by an evolution of the diffraction pattern from one with broad, form-factor oscillations at room temperature, to one with multiple, easily resolved diffraction peaks at 175 °C and above. As mentioned previously, this type of behavior in which liquid-like packing of spheres (S_{LLP}) often exists prior to development of the fully organized S_{BCC} lattice is fairly common in other BCP systems.[11b,30] As shown in Figure 3.4, the highly ordered structure established during the initial heating remains preserved during subsequent cooling, with no evidence of any return to the initial, less ordered state.

3.4 Summary

We have shown that imidazolium-based noncharged-charged diblock copolymers (**1**) capable of forming ordered, phase-separated nanostructures can be synthesized by the direct, sequential ATRP of styrene and styrenic imidazolium bis(trifluoromethyl)sulfonamide monomers containing different-length alkyl side-chains. SAXS studies on thermally annealed samples of **1** with a total of 50 repeat units and styrene:imidazolium-IL repeat unit ratios of 25:25, 20:30, and 15:35 showed that their ability to form ordered nanostructures in their neat states depends on both the block ratio and the length of the alkyl side-chain on the imidazolium monomer. It was found

that only the BCP samples with the two short alkyl chains (methyl and *n*-butyl) on the imidazolium monomer could form ordered nanostructures over the range of compositions tested: The methyl- and *n*-butyl-substituted BCPs with the most symmetric noncharged:charged repeat unit ratio (25:25) exhibited scattering signatures for weakly-ordered cylinders (hexagonal lattice), while the methyl- and *n*-butyl- substituted BCPs with progressively more asymmetric block ratios (20:30 and 15:35) formed spheres in a body-centered cubic lattice or with more disordered liquid-like packing character. In contrast, none of the BCPs containing the longer imidazolium side-chain (*n*-decyl) exhibited any ordered phase-separated structures regardless of block composition. This result suggests that overly long alkyl chains on the ionic imidazolium block can make it more miscible with the hydrophobic styrene block and less conducive to mutual phase separation. Collectively, these initial results with this directly polymerized IL-based BCP system show that it may be able to target the formation of specific phase-separated morphologies via judicious choice of styrene:imidazolium-IL block ratio and the nature of the substituent(s) on the imidazolium-styrene monomer. One specific objective in these structure-morphology investigations is to obtain a bicontinuous cubic/gyroid phase, which has so far been elusive in imidazolium-based noncharged-charged BCPs. The ability to directly synthesize the target BCPs via sequential ATRP of styrene and a selected imidazolium-IL monomer allows ready access to the desired BCPs.

3.5 Acknowledgments

Financial support for the work performed at CU Boulder was provided by the Department of Energy ARPA-e program (grant: DE-AR0000098) and matching funds from Total, S.A. (France). Financial support for the work performed at CSU was provided by the National Science Foundation (grant: CBET-1160026) and the ACS Petroleum Research Fund (grant: 52018-ND7).

SAXS studies were performed at CSU using a regional instrument supported by the National Science Foundation MRI Program (grant: DMR-0821799).

3.6 Supporting information

3.6.1 Materials and general procedures

1-Bromodecane, sodium hydride, imidazole, 1-methylimidazole, 1-butylimidazole, 4-vinylbenzyl chloride, 2-(trimethylsilyl)ethanol, α-bromoisobutyryl bromide, triethylamine, copper(I) bromide, Dowex 50Wx4 ion-exchange resin, benzoyl peroxide, *N,N,N′,N′,N″*-pentamethyldiethylenetriamine (PMDETA), butyronitrile, and TEMPO were all purchased from the Sigma-Aldrich Co., and used as received. Styrene was purchased from the Sigma-Aldrich Co. and purified by passage over a column of basic alumina to remove the added radical inhibitor. Lithium bis(trifluoromethylsulfonyl)amide ($LiTf_2N$) was purchased as Fluorad™ Lithium Trifluoromethane Sulfonimide from the 3M Company. All solvents were purchased from Sigma-Aldrich or Mallinckrodt, Inc., and purified/dehydrated via N_2-pressurized activated alumina columns, and de-gassed. The H_2O used for synthesis was purified and deionized, with resistivity greater than 12 MΩ/cm. All polymerizations were carried out in a dry Ar atmosphere using standard Schlenk line techniques.

3.6.2 Instrumentation

^1H and ^{13}C NMR spectra were obtained using a Bruker 300 Ultrashield™ (300 MHz for ^1H) spectrometer. Chemical shifts are reported in ppm relative to residual non-deuterated solvent.

HRMS (ES) analysis was performed by the Central Analytical Facility in the Dept. of Chemistry and Biochemistry at the University of Colorado, Boulder. Gel permeation chromatography (GPC) was performed using a Viscotek GPC-Max chromatography system outfitted with three 7.5 x 340 mm Polypore™ (Polymer Laboratories) columns in series, a Viscotek differential refractive index (RI) detector, and an Alltech column oven (mobile phase THF, 40 °C, 1 mL min^{-1} flow rate). Molecular weight data obtained on this GPC system were referenced to polystyrene molecular weight standards. NMR diffusion ordered spectroscopy (DOSY) experiments were performed using a Varian Inova-400NMR spectrometer. Small-angle X-ray scattering (SAXS) data were collected using a Rigaku SMax3000 High Brilliance three-pinhole SAXS system outfitted with a MicroMax-007HFM rotating anode (Cu K_α), a Confocal Max-Flux Optic, a Gabriel-type multi-wire area detector, and a Linkam thermal stage. Differential scanning calorimetry (DSC) measurements were performed using a Mettler Toledo DSC823^e and a Julabo FT100 Intracooler. Energy-dispersive X-ray spectroscopy (EDS) was performed using a JEOL JSM-6480 scanning electron microscope with an elemental detection lower limit of carbon.

3.6.3 Synthesis of 1-decylimidazole

This compound was synthesized using a variation of the procedure previously reported.[31] Sodium hydride (60% dispersion in mineral oil, 1.56 g, 39.0 mmol) was suspended in dry THF (50 mL) under Ar at 0 °C. Imidazole (2.16 g, 31.7 mmol) was dissolved in dry THF (20 mL) and added drop-wise. After 30 min, 1-bromodecane (5.41 g, 24.5 mmol) was added. The resulting reaction mixture was then stirred at room temperature overnight. After careful addition of a few drops of water to quench the remaining sodium hydride, the organic solvent was removed in vacuo, and diethyl ether (50 mL) was added. This solution was then washed with water (3 x 50 mL), dried

over anhydrous $MgSO_4$, filtered, concentrated, and then purified by flash chromatography (ethyl acetate/hexanes = 10/1 (v/v)) to give the product as a light yellow oil (yield: 4.38 g, 86%). Spectroscopic and purity data matched those reported for this compound.[31]

3.6.4 Synthesis of 1-(4-vinylbenzyl)-3-alkylimidazolium bis(trifluoromethylsulfonyl)amide monomers (2)

These compounds were synthesized using a variation of the procedures previously reported.[27a,32] The methods below detail the synthesis of styrenic imidazolium monomer **2a–c**.

(a) Synthesis of 1-(4-Vinylbenzyl)-3-methylimidazolium bis(trifluoromethylsulfonyl)amide (2a). (Note: This monomer has been reported in the literature, but the complete synthesis and characterization data for only its chloride derivative has been provided,[32] not the Tf_2N^- analog **2a**). 4-Vinylbenzyl chloride (2.50 g, 16.4 mmol) and 1-methylimidazole (1.48 g, 18.0 mmol) were stirred in acetonitrile (100 mL) at reflux for 18 h. Upon cooling, the reaction mixture was concentrated to form a yellow viscous oil and washed with Et_2O (3 x 100 mL). The resulting oil was then dissolved in H_2O (100 mL), $LiTf_2N$ (5.17 g, 18.0 mmol) was added, and then the mixture stirred at room temperature for 12 h. A yellow oil was then extracted from this aqueous mixture with CH_2Cl_2 (3 x 50 mL). The CH_2Cl_2 layer was then washed with H_2O (3 x 100 mL), dried over anhydrous $MgSO_4$, filtered, and concentrated to give monomer **2a** as light-yellow oil (yield: 6.83 g, 87%). ^{1}H NMR (300 MHz, $CDCl_3$): δ8.77 (s, 1H), 7.43 (d, *J* = 8.2 Hz, 2H), 7.32 (d, *J* = 8.2 Hz, 2H), 7.21 (dt, *J* = 18.0, 1.8 Hz, 2H), 6.69 (dd, *J* = 17.6, 10.9 Hz, 1H), 5.77 (d, *J* = 17.6, 1H), 5.31 (d, *J* = 10.9, 1H), 5.28 (s, 2H), 3.90 (s, 3H). ^{13}C NMR (75 MHz, $CDCl_3$): δ139.06, 135.92, 135.80, 131.69, 129.24, 127.30, 123.96, 122.21, 122.01, 117.76,

115.64, 53.29, 36.39. IR (neat): 3153.53, 1562.40, 1347.39, 1329.23, 1178.28, 1132.72, 1051.69, 994.24, 920.00, 830.65, 789.12, 739.18, 715.92, 635.47. HRMS (ES) calcd. for $C_{15}H_{15}F_6N_3O_4S_2$ (M^+ Tf_2N^-): 479.0408; observed: 479.0424. Since imidazolium-based ionic liquid compounds are known in the literature to have combustion issues for C, H, and N elemental analysis,[33] the ^1H and ^{13}C NMR spectra for isolated **2a** are provided below to help confirm its purity.

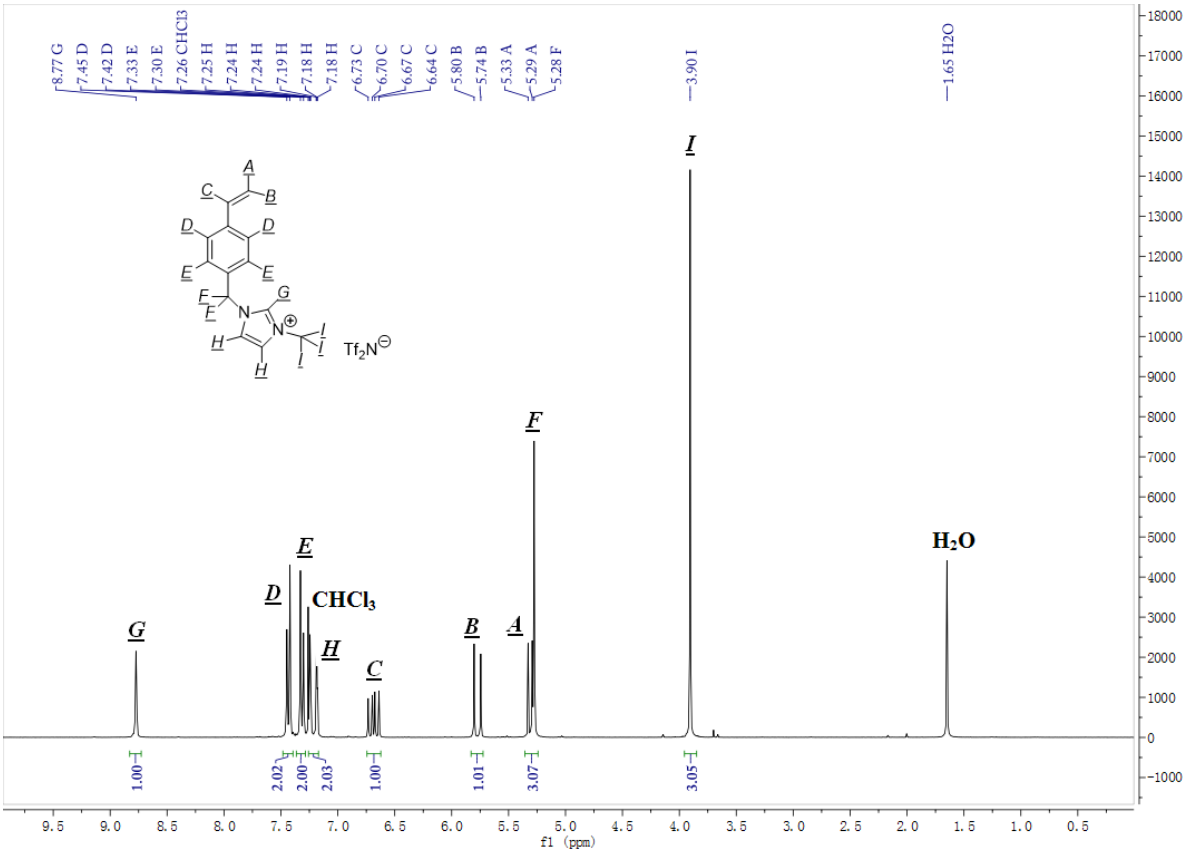

Figure 3.S1. ^1H NMR spectrum and peak assignments for **2a**.

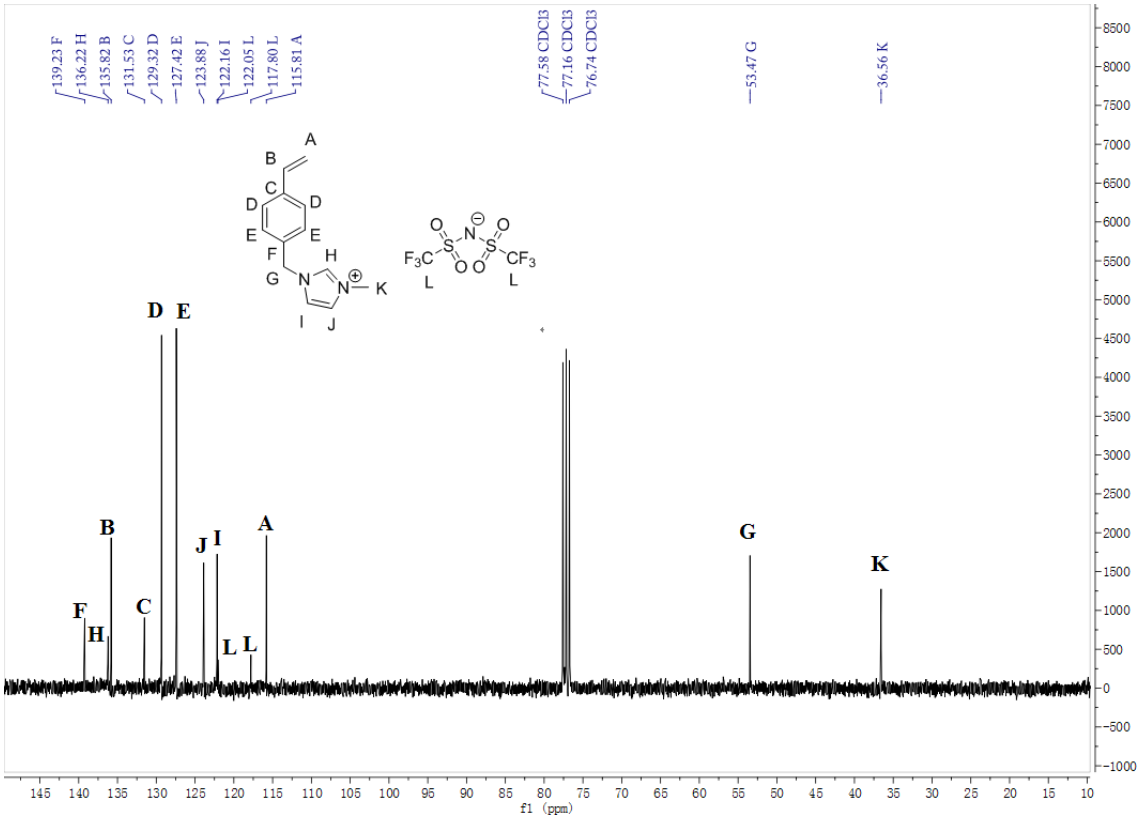

Figure 3.S2. ^{13}C NMR spectrum and peak assignments for **2a**.

(b) Synthesis of 1-(4-Vinylbenzyl)-3-butyl-imidazolium bis(trifluoromethylsulfonyl)amide (2b).[27a] 4-Vinylbenzyl chloride (2.00 g, 13.1 mmol) and 1-butylimidazole (1.79 g, 14.4 mmol) were stirred in acetonitrile (80 mL) at reflux for 18 h. Upon cooling, the reaction mixture was concentrated to form a yellow viscous oil and washed with Et_2O (3 x 80 mL). The resulting oil was then dissolved in H_2O (80 mL). $LiTf_2N$ (4.51 g, 15.7 mmol) was added, and then the mixture stirred at room temperature for 12 h. A yellow oil was then extracted from this aqueous mixture with CH_2Cl_2 (3 x 50 mL). The CH_2Cl_2 layer was then washed with H_2O (3 x 100 mL), dried over anhydrous $MgSO_4$, filtered, and concentrated to give monomer

2b as light-yellow oil (yield: 5.81 g, 85%). Spectroscopic and purity data matched those reported for this compound.[27a]

(c) Synthesis of 1-(4-Vinylbenzyl)-3-decyl-imidazolium bis(trifluoromethylsulfonyl)amide (2c). 4-Vinylbenzyl chloride (1.00 g, 6.55 mmol) and 1-decylimidazole (1.50 g, 7.20 mmol) were stirred in acetonitrile (40 mL) at reflux for 18 h. Upon cooling, the reaction mixture was concentrated to form a yellow viscous oil and washed with Et_2O (3 x 40 mL). The resulting oil was then dissolved in H_2O (40 mL). $LiTf_2N$ (2.26 g, 7.87 mmol) was added, and then the resulting mixture stirred at room temperature for 12 h. A yellow oil was then extracted from this aqueous mixture with CH_2Cl_2 (3 x 50 mL). The CH_2Cl_2 layer was then washed with H_2O (3 x 100 mL), dried over anhydrous $MgSO_4$, filtered, and concentrated to give monomer **2c** as light-yellow oil (yield: 3.49 g, 88%). ^{1}H NMR (300 MHz, $CDCl_3$): δ8.88 (s, 1H), 7.44 (d, *J* = 8.2 Hz, 2H), 7.33 (d, *J* = 8.2 Hz, 2H), 7.24 (dt, *J* = 12.0, 2.0 Hz, 2H), 6.69 (dd, *J* = 17.6, 10.9 Hz, 1H), 5.78 (d, *J* = 17.6, 1H), 5.31 (d, *J* = 10.8, 1H), 5.31 (s, 2H), 4.16 (t, *J* = 7.4 Hz, 2H), 1.93 – 1.76 (m, 2H), 1.39 – 1.17 (m, 14H), 0.87 (t, *J* = 7.0 Hz, 3H). ^{13}C NMR (75 MHz, $CDCl_3$): δ139.19, 135.83, 135.58, 131.69, 129.29, 127.41, 122.45, 122.24, 122.08, 117.82, 115.76, 53.46, 50.49, 31.95, 30.18, 29.51, 29.40, 29.34, 28.96, 26.24, 22.77, 14.21. IR (neat): 3146.88, 2927.24, 2856.85, 1560.77, 1456.43, 1348.21, 1182.03, 1133.87, 1053.89, 990.02, 914.86, 830.80, 788.70, 739.55, 653.29. HRMS (ES) calcd. for $C_{24}H_{33}F_6N_3O_4S_2$ (M^+ Tf_2N^-): 605.1817; observed: 605.2435. Since imidazolium-based ionic liquid compounds are known in the literature to have combustion issues for C, H, and N elemental analysis,[33] the ^{1}H and ^{13}C NMR spectra for isolated **2c** are provided below to help confirm its purity.

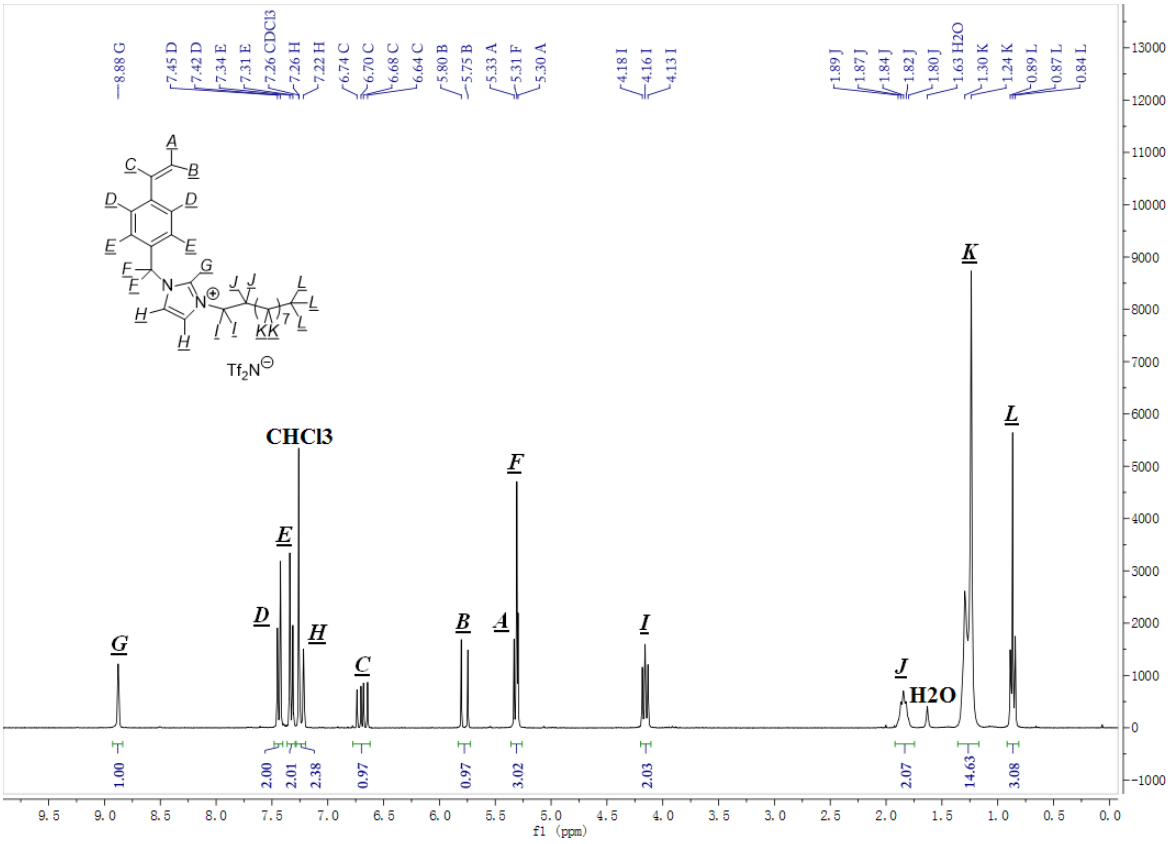

Figure 3.S3. ^{1}H NMR spectrum and peak assignments for **2c**.

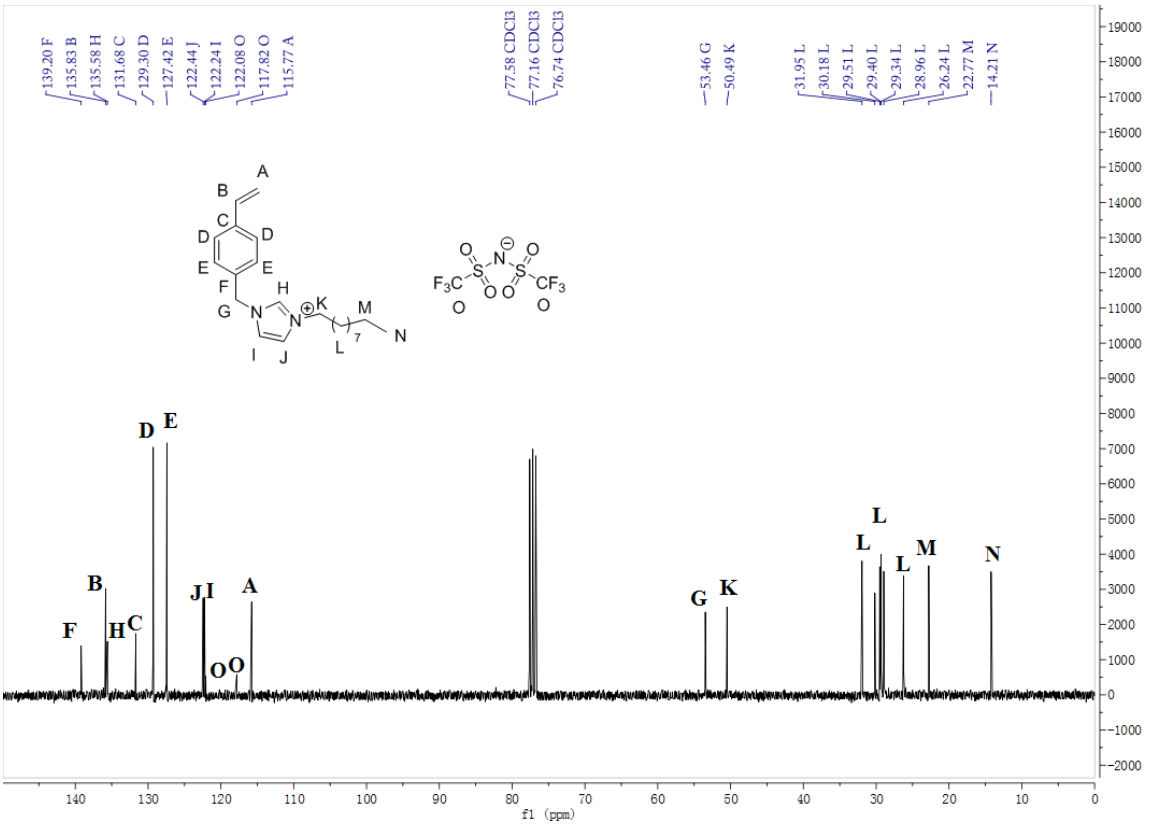

Figure 3.S4. ^{13}C NMR spectrum and peak assignments for **2c**.

3.6.5 Synthesis of 2-(trimethylsilyl)ethyl 2-bromo-2-methylpropanoate (TMS-EBMP)

This compound was synthesized using the previously reported procedure.[27c] Spectroscopic and purity data matched those reported for this compound.[27c]

3.6.6 Synthesis of polystyrene macro-initiators 3a–c via ATRP

These compounds were synthesized using a variation of the procedures previously reported.[34] ^{1}H NMR analysis of **3a–c** confirmed the absence of unreacted styrene monomer. The DP and M_n values of **3a–c** were calculated based on the ^{1}H NMR end-group analysis (Table 3.S1).

Table 3.S1. The DP, M_n, and PDI values for the ATRP-synthesized polystyrene macro-initiators **3a–c**.

Polystyrene Macro-initiator	DP	M_n (g/mol)	PDI
3a	25	2,871	1.12
3b	20	2,350	1.10
3c	15	1,829	1.15

(a) synthesis of polystyrene macro-initiator 3a. Styrene (2.50 g, 24.0 mmol) and PMDETA (22.3 mg, 0.129 mmol) were added to a flame-dried Schlenk flask and degassed by three freeze-pump-thaw cycles. The flask was then allowed to warm to room temperature, back filled with argon, and CuBr (18.4 mg, 0.128 mmol) was added. The resulting mixture was stirred at room temperature for 30 minutes and TMS-EBMP (229 mg, 0.857 mmol) was added. The flask was then place in an oil bath at 90 °C for 22 h. The content of the flask was purified as described in general procedures to give **3a** as white solid (yield: 2.25 g, 82%). DP = 25; PDI = 1.12; M_n = 2,871 g/mol (calculated using ^{1}H NMR polymer end-group analysis. See Section 3.6.7 for details).

(b) synthesis of polystyrene macro-initiator 3b. Styrene (2.50 g, 24.0 mmol) and PMDETA (28.4 mg, 0.164 mmol) were added to a flame-dried Schlenk flask and degassed by three freeze-pump-thaw cycles. The flask was then warmed to room temperature, back-filled with

Ar, and CuBr (23.4 mg, 0.163 mmol) was added. The resulting mixture was stirred at room temperature for 30 minutes and TMS-EBMP (292 mg, 1.06 mmol) was added. The flask was then place in an oil bath at 90 °C for 22 h. The content of the flask was purified as described in general procedure in Experimental Section to give **3b** as white solid (yield: 2.18 g, 78%). DP = 20; PDI = 1.10; M_n = 2,350 g/mol (calculated using ^{1}H NMR polymer end-group analysis. See Section 3.6.7 for details).

(c) synthesis of polystyrene macro-initiator 3c. Styrene (2.50 g, 24.0 mmol) and PMDETA (37.5 mg, 0.216 mmol) were added to a flame-dried Schlenk flask and degassed by three freeze-pump-thaw cycles. After the flask was allowed to warm to room temperature and back-filled with Ar, CuBr (31.4 mg, 0.218 mmol) was added. The resulting mixture was stirred at room temperature for 30 minutes and TMS-EBMP (389 mg, 1.46 mmol) was added. The flask was then place in an oil bath at 90 °C for 22 h. The content of the flask was purified as described in general procedure in Experimental Section to give **3c** as white solid (yield: 1.88 g, 65%). DP = 15; PDI = 1.15; M_n = 1,829 g/mol (calculated using ^{1}H NMR polymer end-group analysis. See Section 3.6.7 for details).

3.6.7 Determination of the DP and M_n values of polystyrene macro-initiators 3a–c[29]

The ATRP of styrene to make macro-initiators **3a–c** has been established in the literature to have controlled polymerization character.[34] The DP and M_n values of synthesized polystyrene macro-initiators **3a–c** were calculated based on the ^{1}H NMR peak integral of protons (*D*) on the TMS end-group relative to that of the protons (*E*) on the benzene ring for these polymers (Eqs. 3.1 and 3.2).[29] See Figure 3.S5 below for example data used to calculate these values for **3b**.

$$DP = \frac{\mathrm{E_{1H\ NMR\ Integration}} \times 9}{\mathrm{D_{1H\ NMR\ Integration}} \times 5} \qquad \text{(Eq. 3.1)}$$

$$M_{\mathrm{n}} = (\mathrm{DP} \times M_{\mathrm{monomer}}) + M_{\mathrm{TMS\text{-}EBMP}} \qquad \text{(Eq. 3.2)}$$

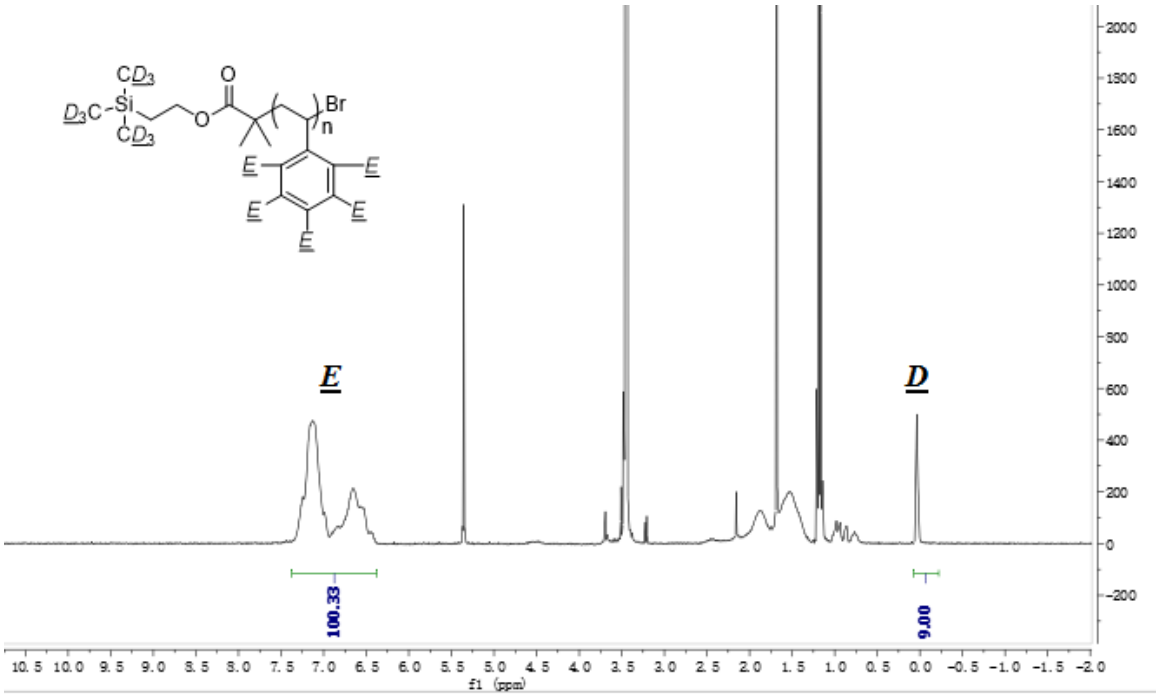

Figure 3.S5. Example ^{1}H NMR spectrum of **3b**, and the ^{1}H NMR peak assignments used for calculating the DP and M_{n} value. Calculated DP = 20.07 ≅ 20, M_{n} = 2,350 g/mol.

3.6.8 Synthesis of BCPs 1 via ATRP of imidazolium-IL monomers 2a–c from the polystyrene macro-initiators 3a–c

The calculated block compositions and M_{n} values of **1** are shown in Table 3.S2 below:

Table 3.S2. The calculated block compositions and M_n values of BCPs **1a–i** from ^{1}H NMR analysis.

BCP	n	m	M_n (g/mol)
1.1a	25	25	14,856
1.2a	25	25	15,908
1.3a	25	25	18,012
1.1b	20	30	16,733
1.2b	20	30	17,995
1.3b	20	30	20,520
1.1c	15	35	18,609
1.2c	15	35	20,082
1.3c	15	35	23,028

(a) Synthesis of BCP 1.1a. Imidazolium monomer **2a** (418 mg, 0.871 mmol), PMDETA (24.0 mg, 0.139 mmol), and butyronitrile (1 mL) were added to a flame-dried Schlenk flask and degassed by three freeze-pump-thaw cycles. After the flask was allowed to warm to room temperature and back-filled with Ar, CuBr (20.0 mg, 0.139 mmol) was added. The resulting mixture was stirred at room temperature for 30 min, and macro-initiator **3a** (100 mg, 0.0348 mmol)

was added. The flask was then placed in a 90 °C oil bath and stirred. Upon complete consumption of monomer **2a** (as verified by ^{1}H NMR analysis), the resulting reaction mixture was purified as described in the general procedure above to give BCP **1.1a** as a white solid (yield: 0.303 g, 58%). Block repeat unit molar ratio = 1:1 (styrene:imidazolium-IL); block length composition = 25-*b*-25 (styrene-*b*-imidazolium-IL); M_n = 14,856 g/mol (calculated based on ^{1}H NMR analysis. See Section 3.6.9 for details).

(b) Synthesis of BCP 1.2a. Imidazolium monomer **2b** (454 mg, 0.871 mmol), PMDETA (24.0 mg, 0.139 mmol), and butyronitrile (1 mL) were added to a flame-dried Schlenk flask and degassed by three freeze-pump-thaw cycles. After the flask was allowed to warm to room temperature and back-filled with Ar, CuBr (20.0 mg, 0.139 mmol) was added. The resulting mixture was stirred at room temperature for 30 min, and macro-initiator **3a** (100.0 mg, 0.0348 mmol) was added. The flask was then placed in a 90 °C oil bath and stirred. Upon complete consumption of monomer **2b** (as verified by ^{1}H NMR analysis), the resulting reaction mixture was purified as described in the general procedure in the Experimental Section to give BCP **1.2a** as a white solid (yield: 0.330 g, 60%). Block repeat unit molar ratio = 1:1 (styrene:imidazolium-IL); block length composition = 25-*b*-25 (styrene-*b*-imidazolium-IL); M_n= 15,908 g mol^{-1} (calculated based on ^{1}H NMR analysis. See Section 3.6.9 for details).

(c) Synthesis of BCP 1.3a. Imidazolium monomer **2c** (448 mg, 0.740 mmol), PMDETA (20.5 mg, 0.118 mmol), and butyronitrile (1 mL) were added to a flame-dried Schlenk flask and degassed by three freeze-pump-thaw cycles. After the flask was allowed to warm to room temperature and back-filled with Ar, CuBr (17.0 mg, 0.118 mmol) was added. The resulting mixture was stirred at room temperature for 30 min, and macro-initiator **3a** (85.0 mg, 0.0296 mmol) was added. The flask was then placed in a 90 °C oil bath and stirred. Upon complete consumption

of monomer **2c** (as verified by ^{1}H NMR analysis), the resulting reaction mixture was purified as described in the general procedure in the Experimental Section to give BCP **1.3a** as a white solid (yield: 0.384 g, 72%). Block repeat unit molar ratio = 1:1 (styrene:imidazolium-IL); block length composition = 25-*b*-25 (styrene-*b*-imidazolium-IL); M_n = 18,012 g mol^{-1} (calculated based on ^{1}H NMR analysis. See Section 3.6.9 for details).

(d) Synthesis of BCP 1.1b. Imidazolium monomer **2a** (490 mg, 1.02 mmol), PMDETA (23.6 mg, 0.136 mmol), and butyronitrile (1 mL) were added to a flame-dried Schlenk flask and degassed by three freeze-pump-thaw cycles. After the flask was allowed to warm to room temperature and back-filled with Ar, CuBr (19.5 mg, 0.136 mmol) was added. The resulting mixture was stirred at room temperature for 30 min, and macro-initiator **3b** (80.0 mg, 0.0340 mmol) was added. The flask was then placed in a 90 °C oil bath and stirred. Upon complete consumption of monomer **2a** (as verified by ^{1}H NMR analysis), the resulting reaction mixture was purified as described in the general procedure in the Experimental Section to give BCP **1.1b** as a white solid (yield: 0.353 g, 62%). Block repeat unit molar ratio = 1:1.5 (styrene:imidazolium-IL); block length composition = 20-*b*-30 (styrene-*b*-imidazolium-IL); M_n = 16,733 g mol^{-1} (calculated based on ^{1}H NMR analysis. See Section 3.6.9 for details).

(e) Synthesis of BCP 1.2b. Imidazolium monomer **2b** (532 mg, 1.02 mmol), PMDETA (23.6 mg, 0.136 mmol), and butyronitrile (1 mL) were added to a flame-dried Schlenk flask and degassed by three freeze-pump-thaw cycles. After the flask was allowed to warm to room temperature and back-filled with Ar, CuBr (19.5 mg, 0.136 mmol) was added. The resulting mixture was stirred at room temperature for 30 min, and macro-initiator **3b** (80.0 mg, 0.0340 mmol) was added. The flask was then placed in a 90 °C oil bath and stirred. Upon complete consumption of monomer **2b** (as verified by ^{1}H NMR analysis), the resulting reaction mixture was purified as

described in the general procedure in the Experimental Section to give BCP **1.2b** as a white solid (yield: 0.398 g, 65%). Block repeat unit molar ratio = 1:1.5 (styrene:imidazolium-IL); block length composition = 20-*b*-30 (styrene-*b*-imidazolium-IL); M_n = 17,995 g mol^{-1} (calculated based on ^{1}H NMR analysis. See Section 3.6.9 for details).

(f) Synthesis of BCP 1.3b. Imidazolium monomer **2c** (464 mg, 0.766 mmol), PMDETA (17.7 mg, 0.102 mmol), and butyronitrile (1 mL) were added to a flame-dried Schlenk flask and degassed by three freeze-pump-thaw cycles. After the flask was allowed to warm to room temperature and back-filled with Ar, CuBr (14.6 mg, 0.102 mmol) was added. The resulting mixture was stirred at room temperature for 30 min, and macro-initiator **3b** (60.0 mg, 0.0255 mmol) was added. The flask was then placed in a 90 °C oil bath and stirred. Upon complete consumption of monomer **2c** (as verified by ^{1}H NMR analysis), the resulting reaction mixture was purified as described in the general procedure in the Experimental Section to give BCP **1.3b** as a white solid (yield: 0.288 g, 55%). Block repeat unit molar ratio = 1:1.5 (styrene:imidazolium-IL); block length composition = 20-*b*-30 (styrene-*b*-imidazolium-IL); M_n = 20,520 g mol^{-1} (calculated based on ^{1}H NMR analysis. See Section 3.6.9 for details).

(g) Synthesis of BCP 1.1c. Imidazolium monomer **2a** (459 mg, 0.957 mmol), PMDETA (18.9 mg, 0.109 mmol), and butyronitrile (0.8 mL) were added to a flame-dried Schlenk flask and degassed by three freeze-pump-thaw cycles. After the flask was allowed to warm to room temperature and back-filled with Ar, CuBr (15.7 mg, 0.109 mmol) was added. The resulting mixture was stirred at room temperature for 30 min, and macro-initiator **3c** (50.0 mg, 0.0273 mmol) was added. The flask was then placed in a 90 °C oil bath and stirred. Upon complete consumption of monomer **2a** (as verified by ^{1}H NMR analysis), the resulting reaction mixture was purified as described in the general procedure in the Experimental Section to give BCP **1.1c** as white solid

(yield: 0.305 g, 60%). Block repeat unit molar ratio = 1:2.33 (styrene:imidazolium-IL); block length composition = 15-*b*-35 (styrene-*b*-imidazolium-IL); M_n = 18,609 g mol^{-1} (calculated based on ^{1}H NMR analysis. See Section 3.6.9 for details).

(h) Synthesis of BCP 1.2c. Imidazolium monomer **2b** (499 mg, 0.956 mmol), PMDETA (18.9 mg, 0.109 mmol), and butyronitrile (0.8 mL) were added to a flame-dried Schlenk flask and degassed by three freeze-pump-thaw cycles. After the flask was allowed to warm to room temperature and back-filled with Ar, CuBr (15.7 mg, 0.109 mmol) was added. The resulting mixture was stirred at room temperature for 30 min, and macro-initiator **3c** (50.0 mg, 0.0273 mmol) was added. The flask was then placed in a 90 °C oil bath and stirred. Upon complete consumption of monomer **2b** (as verified by ^{1}H NMR analysis), the resulting reaction mixture was purified as described in the general procedure in the Experimental Section to give BCP **1.2c** as a white solid (yield: 0.357 g, 65%). Block repeat unit molar ratio = 1:2.33 (styrene:imidazolium-IL); block length composition = 15-*b*-35 (styrene-*b*-imidazolium-IL); M_n = 20,082 g mol^{-1} (calculated based on ^{1}H NMR analysis. See Section 3.6.9 for details).

(i) Synthesis of BCP 1.3c. Imidazolium monomer **2c** (464 mg, 0.765 mmol), PMDETA (15.2 mg, 0.0877 mmol), and butyronitrile (0.8 mL) were added to a flame-dried Schlenk flask and degassed by three freeze-pump-thaw cycles. After the flask was allowed to warm to room temperature and back-filled with Ar, CuBr (12.6 mg, 0.0877 mmol) was added. The resulting mixture was stirred at room temperature for 30 min, and macro-initiator **3c** (40.0 mg, 0.0219 mmol) was added. The flask was then placed in a 90 °C oil bath and stirred. Upon complete consumption of monomer **2c** (as verified by ^{1}H NMR analysis), the resulting reaction mixture was purified as described in the general procedure in the Experimental Section to give BCP **1.3c** as a white solid (yield: 0.317 g, 63%). Block repeat unit molar ratio = 1:2.33 (styrene:imidazolium-IL); block

length composition = 15-*b*-35 (styrene-*b*-imidazolium-IL); M_n = 23,028 g mol^{-1} (calculated based on ^{1}H NMR analysis. See Section 3.6.9 for details).

3.6.9 Determination of BCP compositions and molecular weights

The block composition ratios, overall lengths, and M_n values of BCPs **1** were determined via ^{1}H NMR analysis. For example, see Figure 3.S6 for ^{1}H NMR peaks assignments and an example spectrum used for these calculations: The signals of protons *B* on the imidazolium ring of **1.1b** overlap to create a broad peak between 8.25–9.25 ppm (signal *B*). The signals of the other two protons on the imidazolium ring and all the protons on the benzene ring overlap to create a broad peak between 6.20–7.55 ppm (signal *F*). The signals of benzylic protons overlap to create a broad peak between 4.90–5.52 ppm (signal *G*). The signals of protons of TMS end-group overlap to create a broad peak between 0.1–0.12 ppm (signal *D*). So the styrene:imidazolium-styrene ratio can be calculated by Eq. 3.3. The length of ionic block can be calculated by Eq. 3.4 and confirmed by end-group analysis[29] (Eq. 3.5) and conversion (Eq. 3.6). The M_n of BCPs can be calculated by Eq. 3.7.

$$\text{Styrene:imidazolium-styrene ratio} = \frac{[F_{^1\text{H NMR Integration}} - (6 \times B_{^1\text{H NMR Integration}})]}{B_{^1\text{H NMR Integration}} \times 5} \quad \text{(Eq. 3.3)}$$

$$\text{Ionic block length m} = \frac{n}{\text{Styrene:imidazolium-styrene ratio}} \quad \text{(Eq. 3.4)}$$

$$\text{Ionic block length m} = \frac{B_{1H\ NMR\ Integration} \times 9}{D_{1H\ NMR\ Integration}} \quad \text{(Eq. 3.5)}$$

$$\text{Ionic block length m} = (\text{monomer: initiator ratio}) \times \text{conversion} \quad \text{(Eq. 3.6)}$$

$$M_n = (n \times M_{styrene}) + (m \times M_{monomer\ 2}) + M_{TMS\text{-}EBMP} \quad \text{(Eq. 3.7)}$$

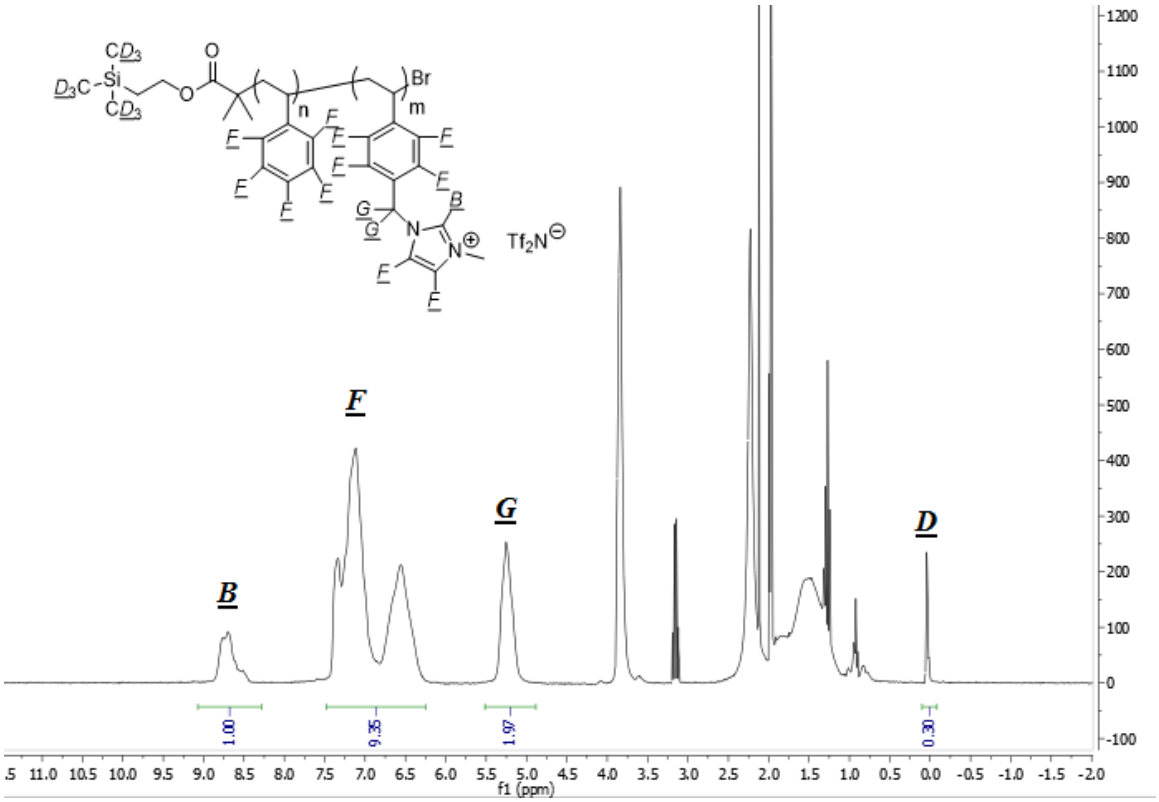

Figure 3.S6. Example: The ^{1}H NMR spectrum of BCP **1.1b**, and the ^{1}H NMR peak assignments used for calculating the block composition ratio, overall length, and M_n value. The calculated styrene:imidazolium-IL ratio is 0.67, m = 29.85 ≅ 30, M_n = 16,733 g/mol.

3.6.10 Verification of the controlled polymerization character for the ATRP of imidazolium monomers 2a–c

(a) Verification of controlled polymerization behavior for the ATRP homopolymerizations of monomers 2a–c. The degree of conversion was calculated based on the ^{1}H NMR peaks integrals of proton (*A*) on the double bonds relative to the peak of the protons (*B*) on the imidazolium ring (N-C<u>H</u>-N) for these homopolymers of **2a–c** (Eqs. 3.8 and 3.9). See Figure 3.S7 below for ^{1}H NMR assignments and example data used to calculate the degree of monomer conversion for the ATRP of monomer **2a** to generate poly(**2a**).

$$ln\,\frac{[M]_0}{[M]} = ln\,\frac{B_{1H\ NMR\ Integration}}{A_{1H\ NMR\ Integration}} \qquad \text{(Eq. 3.8)}$$

$$\text{Conversion} = \frac{B_{1H\ NMR\ Integration} - A_{1H\ NMR\ Integration}}{B_{1H\ NMR\ Integration}} \qquad \text{(Eq. 3.9)}$$

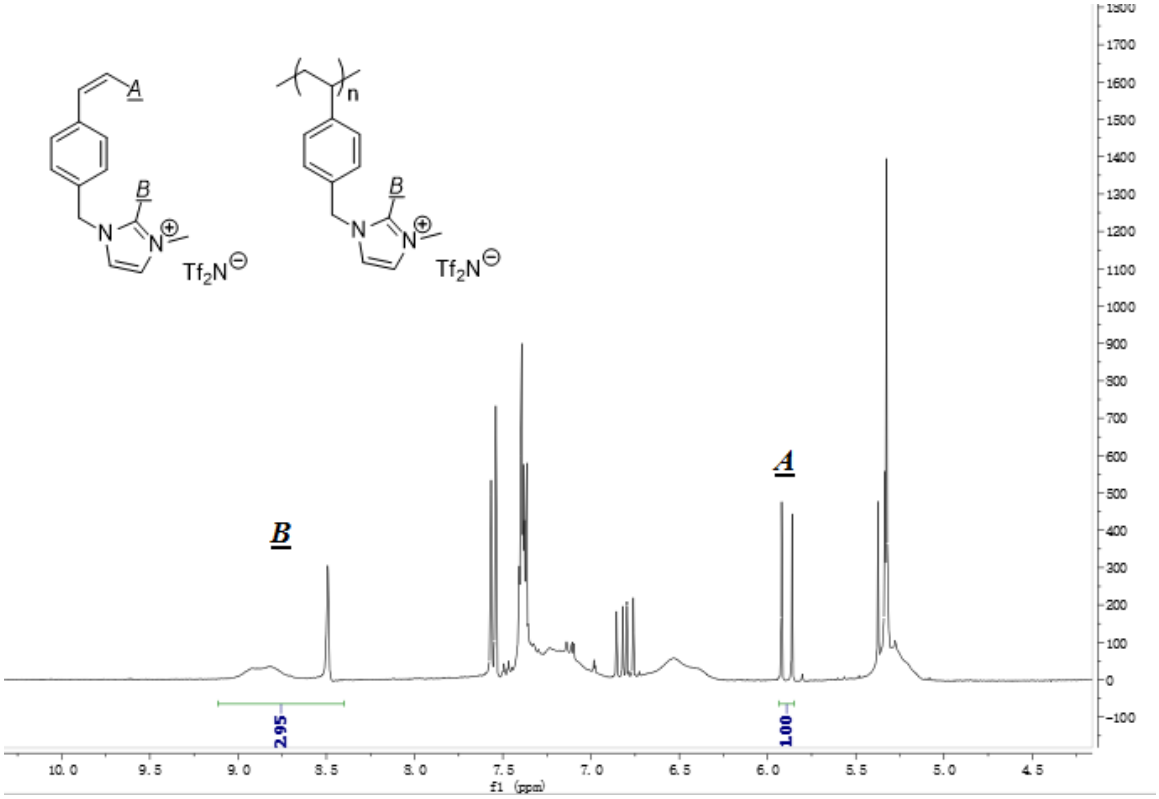

Figure 3.S7 An example ^{1}H NMR spectrum of the reaction mixture for the ATRP of monomer **2a**, and the ^{1}H NMR peak assignments used for calculating the degree of monomer conversion. The calculated conversion is 66.1%.

The M_n values for the homopolymers of **2a–c** were calculated based on the ^{1}H NMR peaks integrals of the protons (*D*) on the TMS end-group of the polymer relative to that due to proton (*B*) on the imidazolium ring C(2) position (i.e., N-C<u>H</u>-N) (Eq. 3.10).[29] See Figure 3.S8 below for ^{1}H NMR assignments and example data used to calculate M_n for poly(**2a**).

$$M_n = \frac{B_{1H\ NMR\ Integration} \times 9 \times M_{monomer}}{D_{1H\ NMR\ Integration}} + M_{TMS\text{-}EBMP} \qquad \text{(Eq. 3.10)}$$

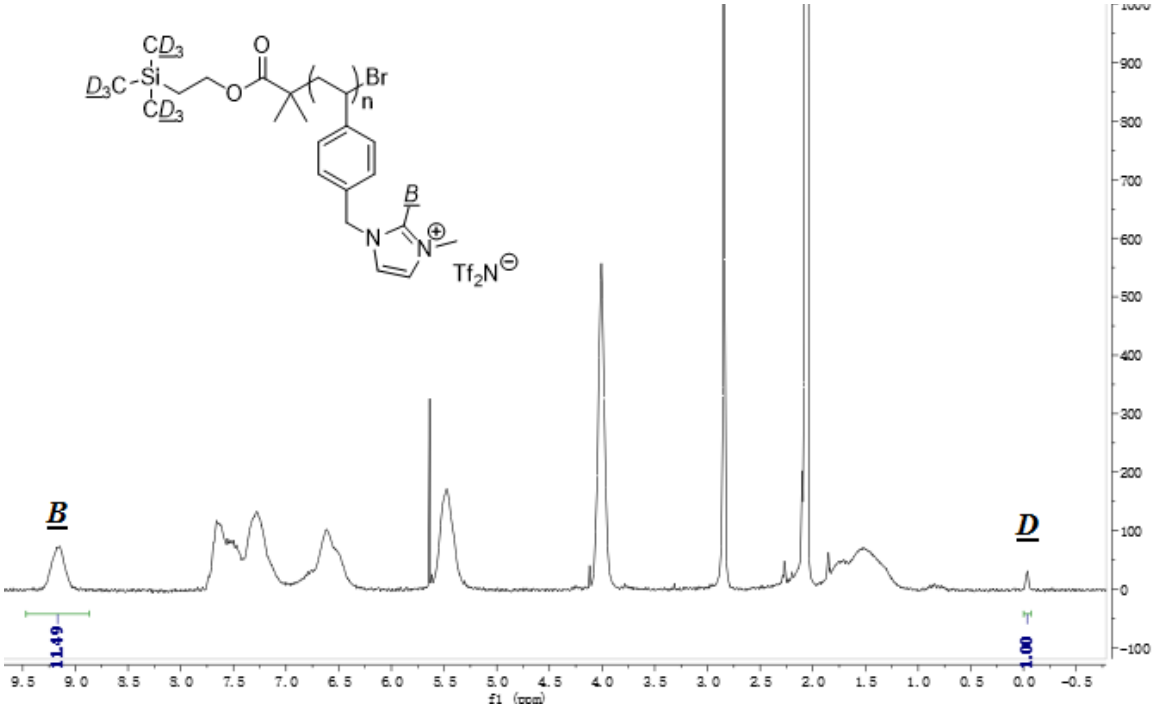

Figure 3.S8. Example ^{1}H NMR spectra of the precipitated poly(**2a**), and the ^{1}H NMR peak assignments used for calculating the M_n value. The calculated M_n is 49,843 g/mol.

To confirm the controlled ATRP of imidazolium monomers **2a–c** (with MW control, etc.), the kinetics plots of the ATRP homopolymerizations of monomers **2a** and **2c** are shown in Figures 3.S9 and 3.S10, respectively, as representative data.

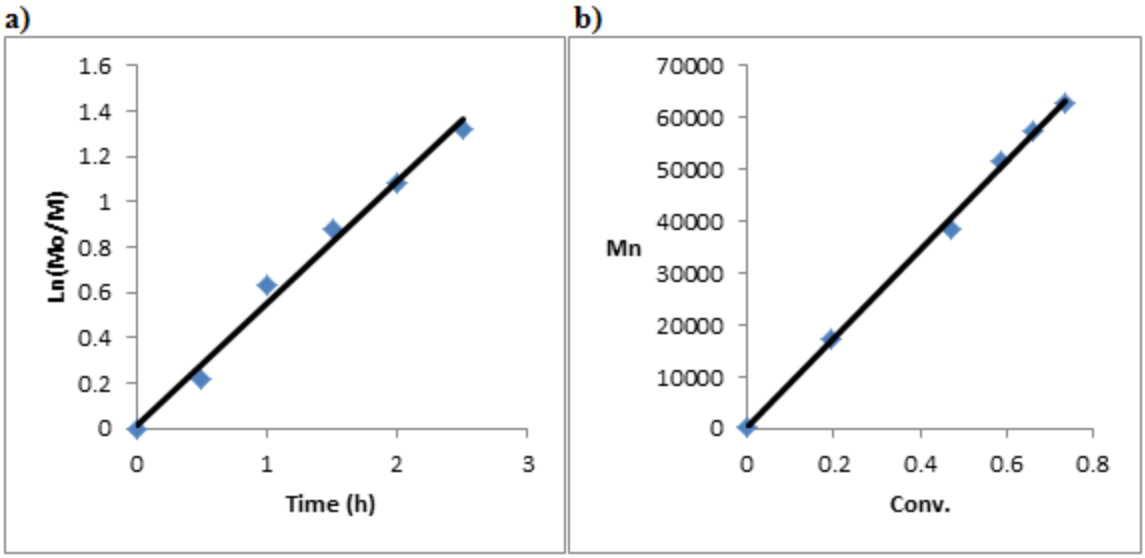

Figure 3.S9. System used for monitoring the kinetics of the ATRP homopolymerization of **2a**: [**2a**/TMS-EBMP/CuBr/PMDETA] = 100/1/4/4 (mol/mol/mol/mol). (a) Plot of the calculated $ln([M]_0/[M])$ vs. reaction time (R^2 = 0.9873). (b) Plot of the calculated M_n vs. calculated degree of monomer conversion (R^2 = 0.9985).

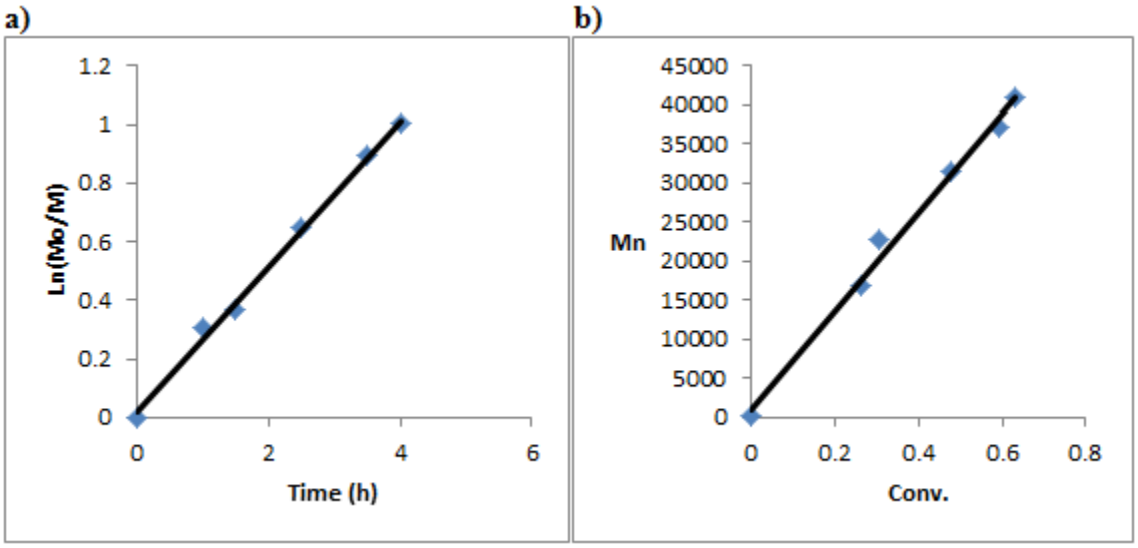

Figure 3.S10. System used for monitoring the kinetics of the ATRP homopolymerization of **2c**: [**2c**/TMS-EBMP/CuBr/PMDETA] = 100/1/4/4 (mol/mol/mol/mol). (a)Plot of the calculated $ln([M]_0/[M])$ vs. reaction time ($R^2 = 0.9959$). (b)Plot of the calculated M_n vs. calculated conversion ($R^2 = 0.9919$).

(b) Verification of controlled polymerization behavior for the ATRP polymerizations of monomers 2a–c from the polystyrene macro-initiators 3a–c to form BCPs 1. To confirm the controlled ATRP of monomers **2a–c** from the polystyrene macro-initiators **3a–c**, the kinetics plots of the ATRP reaction of monomer **2a** from macro-initiator **3b** are shown in Figure 3.S11 below, as representative example data. The degrees of conversion, DP, and M_n of each polymer block were determined as mentioned in the prior sections.

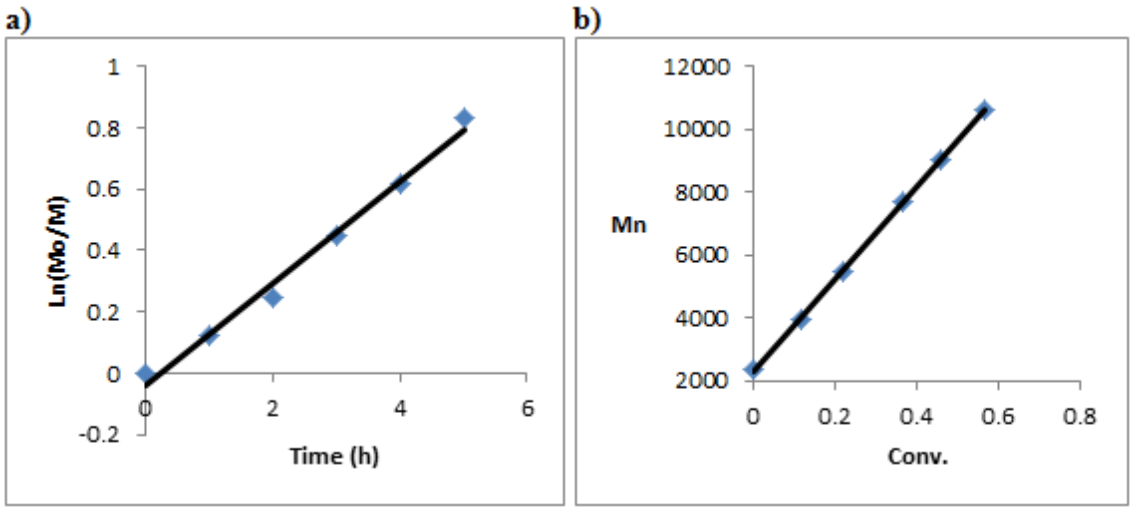

Figure 3.S11. System used for monitoring the kinetics of the ATRP polymerization of **2a** from polystyrene macro-initiator **3b** to form **BCP 1.1b**: [**2a**/**3b**/CuBr/PMDETA] = 30/1/4/4

(mol/mol/mol/mol). (a) Plot of the calculated $ln([M]_0/[M])$ vs. reaction time ($R^2 = 0.9888$). (b) Plot of the calculated M_n vs. calculated degree of monomer conversion ($R^2 = 0.9989$).

3.6.11 Verification of the block copolymer architecture for BCPs 1

The block architecture of BCPs **1** were verified by a combination of surfactant behavior and solubility analysis, diffusion-ordered spectroscopy (DOSY), and small-angle X-ray scattering (SAXS) studies, as described previously in an earlier publication on alkyl:imidazolium BCPs prepared by ROMP from our groups.[11a]

(a) Surfactant behavior and solubility analysis.[11a] Block copolymers **1** all showed surfactant behavior (i.e., extensive foaming when agitated) when mixed in CH_2Cl_2, THF, MeOH, and EtOAc, as would be expected from amphiphilic BCPs. Control experiments with physical blends of polystyrene and poly(**2**) of the same length as blocks in the BCPs did not show this behavior. BCPs **1** also showed very different solubility behavior compared to physical blends of the two homopolymers, polystyrene and poly(**2**). For example, when mixed with MeOH (10 mg/mL) **1.1b** forms a clear solution, whereas the physical blend yields a white solid within a clear solution on top (i.e., polystyrene is insoluble in MeOH while ionic poly(**2**) is soluble). Similar results were observed when comparing samples **1** to their physical blends in CH_2Cl_2, where polystyrene is soluble and ionic poly(**2**) is insoluble.

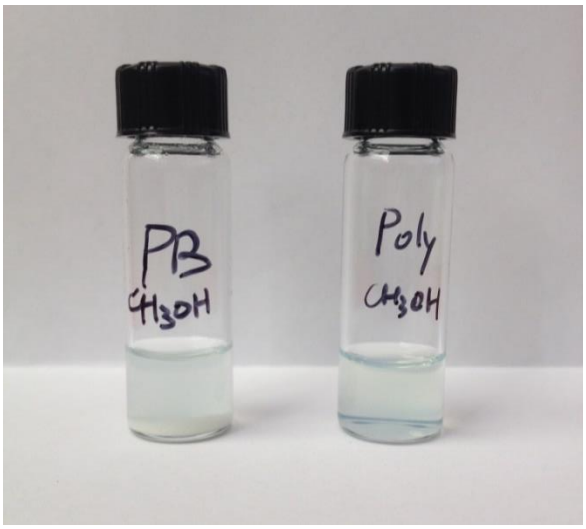

Figure 3.S12. Picture showing different solubilities of BCP **1.1b** (vial: **Poly, CH_3OH**) and a physical blend (vial: **PB, CH_3OH**) of polystyrene + poly(**2a**) in MeOH at room temperature.

(b) NMR DOSY studies.[11a] In the room-temperature NMR DOSY spectrum of BCP **1.1b** in $(CD_3)CO$ (10 mg/mL) (Figure 3.S13), all peaks corresponding to both the styrene and imidazolium blocks exhibited the same diffusion constant (1.55×10^{-10} m^2 s^{-1}). This result indicates that **1.1b** consists of only one macromolecular species (as expected for a BCP) and is different with a physical blend of two distinct homopolymer species (Figure 3.S14). Collectively, the results of these comparative studies are consistent with a covalently linked BCP architecture for **1**, instead of a physical blend of the two homopolymers[11a] (i.e., polystyrene + poly(**2a**)).

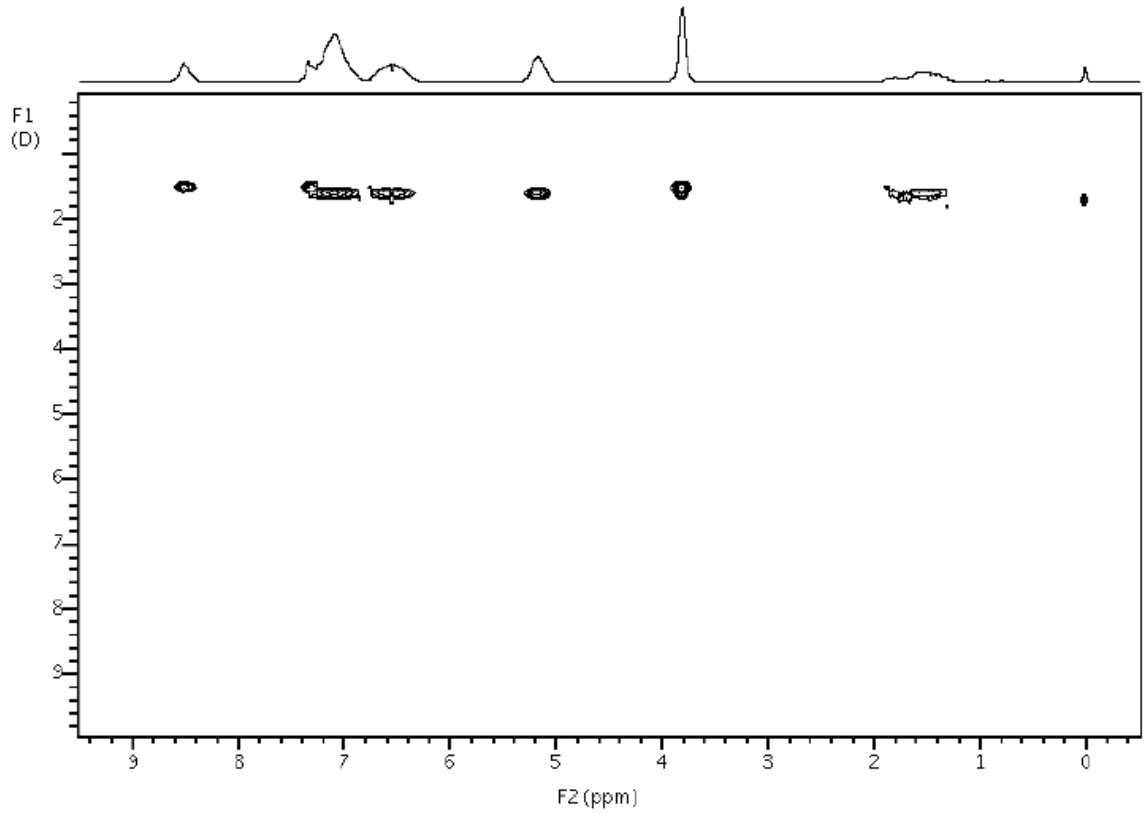

Figure 3.S13. An example NMR DOSY spectrum of BCP **1.1b** in $(CD_3)CO$ at room temperature showing only one diffusion constant: $D = 1.55 \times 10^{-10}$ m^2/s. The total gradient time (δ) used was 2.5 ms, and the diffusion delay (Δ) was 150 ms.

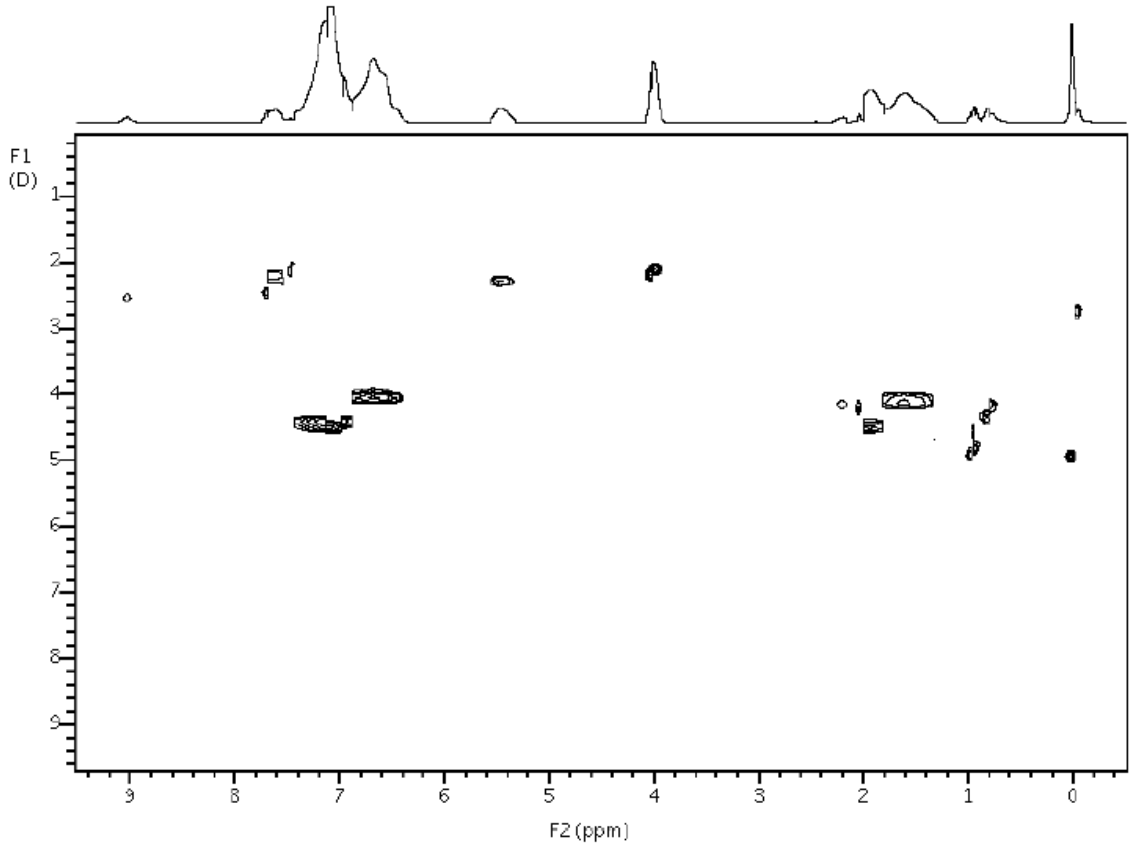

Figure 3.S14. An example NMR DOSY spectrum of a physical blend of polystyrene and poly(**2a**) in $(CD_3)CO$ at room temperature showing two diffusion constants: $D_1 = 2.24 \times 10^{-10}$ m^2/s and $D_2 = 4.20 \times 10^{-10}$ m^2/s. The peaks do not perfectly correspond to the two components due to the overlap of the broad peaks. The total gradient time (δ) used was 2.5 ms, and the diffusion delay (Δ) was 60 ms.

(c) Small-angle X-ray scattering analysis.[11a] Small-angle X-ray scattering (SAXS) data were collected using a Rigaku S-Max 3000 High Brilliance three-pinhole SAXS system outfitted with a MicroMax-007HFM rotating anode (Cu K_α, λ = 1.54 Å), sample-to-detector distance of 2.19 m, Confocal Max-Flux Optics, Gabriel multiwire area detector (1024 × 1024 pixel resolution),

and a Linkam thermal stage. Copolymer samples were sandwiched between Kapton windows (0.05 mm thick × 10 mm diameter). Before collection of temperature-dependent SAXS data, the sample stage temperature was allowed to equilibrate for 5 min under vacuum, unless otherwise stated. Data were collected under vacuum (~100 mtorr) with exposure times of 1200 s for all samples. SAXS data were azimuthally integrated from the 2D detector patterns and plotted as logarithmic intensity vs. the scattering wave vector, q, defined as $q = (4\pi/\lambda) \sin(2\theta_B/2)$, where $2\theta_B$ is the angle between the incident and scattered waves. SAXS data of BCP **1** were collected, together with data collected for the physical blends of the two homopolymers (polystyrene + ionic poly(**2**)) with the same lengths as the BCP blocks for comparison. For example, BCP **1.1b** forms the S_{BCC} phase after annealing, whereas the physical blend yields a disordered phase under the same conditions. Similar results were observed when comparing the other BCPs to their analogous physical blends.

3.6.12 Differential scanning calorimetry (DSC)

DSC studies on BCPs **1** revealed no evidence of any observable thermal transitions between –40 and 180 °C. The DSC profile of BCP **1.1b** is shown in Figure 3.S15 as an example of what was observed for **1**.

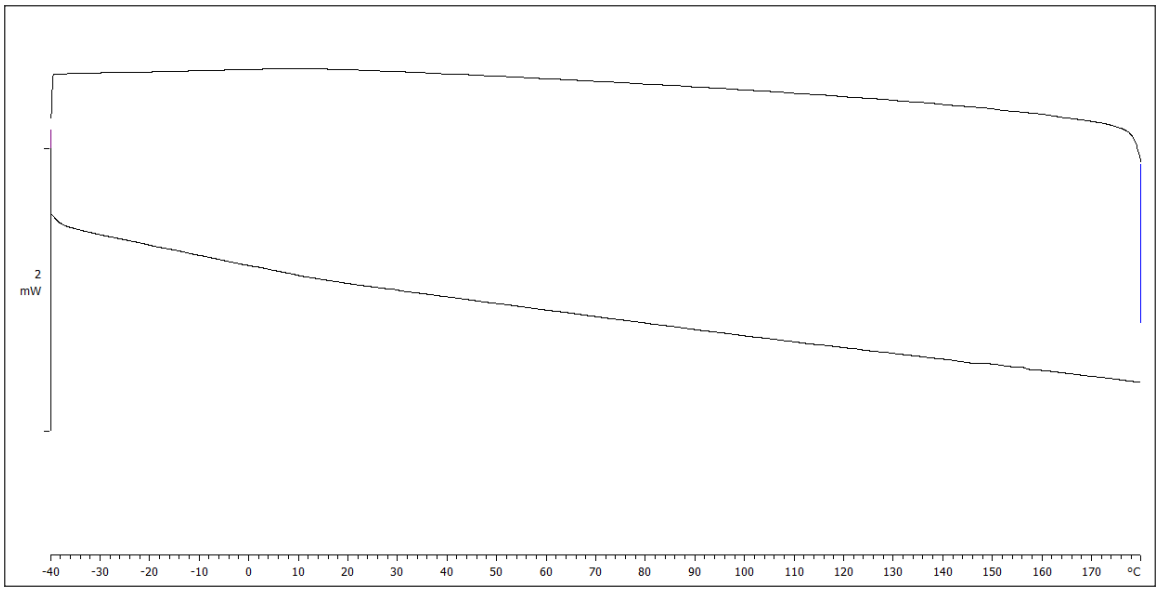

Figure 3.S15. DSC profile of BCP **1.1b** performed at heating and cooling rates of 5 °C min^{-1}.

3.6.13 Energy-dispersive X-ray spectroscopy (EDS)

EDS studies were performed to help confirm the residual metal content (Cu from the ATRP catalyst) in the isolated BCPs **1**, since good elemental analysis of imidazolium IL-based materials is known to be problematic.[33] For example, the EDS spectrum of BCP **1.1b** (Figure 3.S16) shows the absence of a Cu peak. This result indicates that the Cu content in BCP **1.1b** is below the detection limit of the EDS instrument. Similar results were observed for the other BCPs in the series.

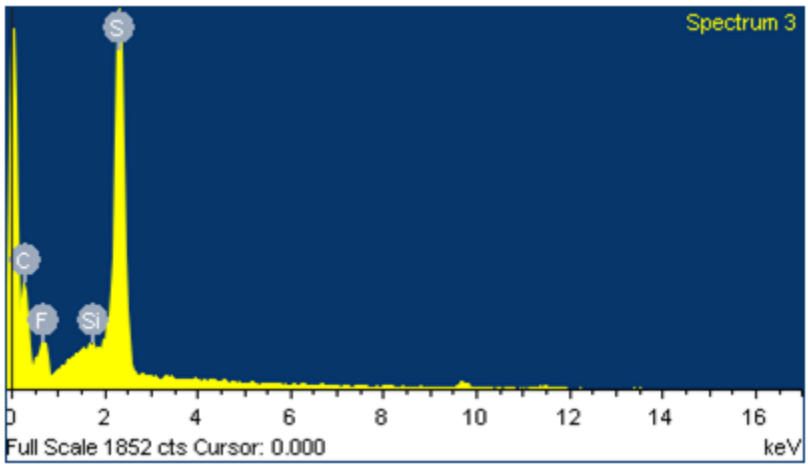

Figure 3.S16. An example EDS spectrum of BCP **1.1b** showing that the amount of residual Cu in the sample from the ATRP catalyst is below the detection limit of the instrument.

3.7 References

(1) For recent reviews on PILs, see: (a) Green, O.; Grubjesic, S.; Lee, S.; Firestone, M. A. *J. Macromol. Sci. C: Polym. Rev.* **2009**, *49*, 339−360. (b) Yuan, J.; Mecerreyes, D.; Antonietti, M. *Prog. Polym. Sci.* **2013**, *38*, 1009−1036. (c) Lu, J.; Yan, F.; Texter, J. *Prog. Polym. Sci.* **2009**, *34*, 431−448. (d) Anderson, E.; Long, T. *Polymer* **2010**, *51*, 2447−2454. (e) Jaeger, W.; Bohrisch, J.; Laschewsky, A. *Prog. Polym. Sci.* **2010**, *35*, 511−577.

(2) For a recent review on IL and IL monomer design, see: Green, M. D.; Long, T. E. *J. Macromol. Sci. C: Polym. Rev.* **2009**, *49*, 291−314.

(3) (a) Ding, S.; Tang, H.; Radosz, M.; Shen, Y. *J. Polym. Sci. A: Polym. Chem.* **2004**, *42*, 5794−5801. (b) Bara, J. E.; Lessmann, S.; Gabriel, C. J.; Hatakeyama, E. S.; Noble, R. D.; Gin, D. L. *Ind. Eng. Chem. Res.* **2007**, *46*, 5397−55404.

(4) (a) Ohno, H., Ito, K. *Chem. Lett.* **1998**, *27*, 751−752. (b) Ohno, H., Yoshizawa, M., Ogihara, W. *Electrochim. Acta* **2004**, *50*, 255−261. (c) Vygodskii, Y.; Shaplov, A.; Lozinskaya, E.; Lyssenko, K.; Golovanov, D.; Malyshkina, I.; Gavrilova, N.; Buchmeiser, M. *Macromol. Chem. Phys.* **2008**, *209*, 40−51.

(5) (a) Marcilla, R.; Curri, M. L.; Cozzoli, P. D.; Mart´ınez, M. T.; Loinaz, I.; Grande, H.; Pomposo, J. A.; Mecerreyes, D. *Small* **2006**, *2*, 507−512. (b) Fukushima, T.; Kosaka, A.; Yamamoto, Y.; Aimiya, T.; Notazawa, S.; Takigawa, T.; Inabe, T.; Aida, T. *Small* **2006**, *2*, 554−560.

(6) (a) Ho, H. A.; Leclerc, M. *J. Am. Chem. Soc.* **2003**, *125*, 4412−4413. (b) Ricks-Laskoski, H. L.; Snow, A. W. *J. Am. Chem. Soc.* **2006**, *128*, 12402−12403.

(7) For a recent review on morphologies of BCPs, see: Mai, Y.; Eisenberg, A. *Chem. Soc. Rev.* **2012**, *41*, 5969−5985.

(8) Vijayakrishna, K.; Jewrajka, S. K.; Ruiz, A.; Marcilla, R.; Pomposo, J. A.; Mecerreyes, D.; Taton, D.; Gnanou, Y. *Macromolecules* **2008**, *41*, 6299−6308**.**

(9) Mori, H.; Yahagi, M.; Endo, T. *Macromolecules* **2009**, *42*, 8082−8092.

(10) Karjalainen, E.; Chenna, N.; Laurinm¨aki, P.; Butcher, S. J.; Tenhu, H. *Polym. Chem.* **2013**, *4*, 1014−1024.

(11) (a) Wiesenauer, E. F.; Edwards, J. P.; Scalfani, V. F.; Bailey, T. S.; Gin, D. L. *Macromolecules* **2011**, *44*, 5075−5078. (b) Scalfani, V. F.; Wiesenauer, E. F.; Ekblad, J. R.; Edwards, J. P.; Gin, D. L.; Bailey, T. S. *Macromolecules* **2012**, *45*, 4262−4276. (c) Nguyen, P. T.; Wiesenauer, E. F.; Gin, D. L.; Noble, R. D. *J. Membr. Sci.* **2013**, *430*, 312−320. (d) Wiesenauer,

E. F.; Nguyen, P. T.; Newell, B. S.; Bailey, T. S.; Noble, R. D.; Gin, D. L. *Soft Matter* **2013**, *9*, 7923−7927.

(12) He, H.; Luebke, D.; Nulwala, H.; Matyjaszewski, K. *Macromolecules* **2014**, *47*, 6601−6609.

(13) Texter, J.; Vasantha, V. A.; Crombez, R.; Maniglia, R.; Slater, L.; Mourey, T. *Macromol. Rapid Commun.* **2012**, *33*, 69−74.

(14) Agudelo, N. A.; Elsen, A. M.; He, H.; López, B. L.; Matyjaszewski, K. *J. Polym. Sci. A: Polym. Chem.* **2015**, *53*, 228−238.

(15) Chanthad, C.; Masser, K. A.; Xu, K.; Runt, J.; Wang, Q. *J. Mater. Chem.* **2012**, *22*, 341−344.

(16) Li, J.; Liang, J.; Wu, W.; Zhang, S.; Zhang, K.; Zhou, H. *New J. Chem.* **2014**, *38*, 2508−2513.

(17) (a) Stancik, C. M.; Lavoie, A. R.; Schutz, J.; Achurra, P. A.; Lindner, P.; Gast, A. P.; Waymouth, R. M. *Langmuir* **2004**, *20*, 596−605. (b) Stancik, C. M.; Lavoie, A. R.; Achurra, P. A.; Waymouth, R. M.; Gast, A. P. *Langmuir* **2004**, *20*, 8975−8987.

(18) Weber, R. L.; Ye, Y.; Schmitt, A. L.; Banik, S. M.; Elabd, Y. A.; Mahanthappa, M. K. *Macromolecules* **2011**, *44*, 5727−5735.

(19) Green, M. D.; Choi, J.-H.; Winey, K. I.; Long, T. E. *Macromolecules* **2012**, *45*, 4749−4757.

(20) Gu, Y.; Timothy P. Lodge, T. P. *Macromolecules* **2011**, *44*, 1732−1736.

(21) (a) Rao, A. H. N.; Thankamony, R. L.; Kim, H.-J.; Namb, S.; Kim, T.-H. *Polymer* **2013**, *54*, 111−119. (b)Rao, A. H. N.; Kim, H.-J.; Namb, S.; Kim, T.-H. *Polymer* **2013**, *54*. 6918−6928. (c) Rao, A. H. N.; Kim, H.-J.; Namb, S.; Kim, T.-H. *Int. J. Hydrogen Energy* **2014**, *39*, 5919−5930.

(22) Han, G. L.; Xu, P. Y.; Zhou, K.; Zhang, Q. G.; Zhu, A. M.; Liu. Q. L. *J. Membr. Sci.* **2014**, *464*, 72−79.

(23) (a) Green, M. D.; Wan, D.; Hemp, S. T.; Choi, J.-H.; Winey, K. I.; Heflin, J. R.; Long, T. E. *Polymer* **2012**, *53*, 3677−3686. (b) Jangu, C.; Wang, J.-H. H.; Wang, D.; Sharick, S.; Heflin, J. R.; Winey, K. I.; Colby, R. H.; Long, T. E. *Macromol. Chem. Phys.* **2014**, *215*, 1319−1331.

(24) Adzima, B. J.; Venna, S. R.; Klara, S. S.; He, H.; Zhong, M.; Luebke, D. R.; Mauter, M. S.; Matyjaszewski, K.; Nulwala, H. B. *J. Mater. Chem. A* **2014**, *2*, 7967−7972.

(25) Gao, R.; Wang, D.; Heflin, J. R.; Long, T. E. *J. Mater. Chem.* **2012**, *22*, 13473−13476.

(26) Bara, J. E.; Lessmann, S.; Gabriel, C. J.; Hatakeyama, E. S.; Noble, R. D.; Gin, D. L. *Ind. Eng. Chem.Res.* **2007**, *46*, 5397−5404.

(27) (a) Tang, J.; Tang, H.; Sun, W.; Radosz, M.; Shen, Y. *J. Polym. Sci. A: Polym. Chem.* **2005**, *43*, 5477−5489. (b) He, X.; Yang, W.; Pei, X. *Macromolecules* **2008**, *41*, 4615−4621. (c) He, H.; Zhong, M.; Adzima, B.; Luebke, D.; Nulwala, H.; Matyjaszewski, K. *J. Am. Chem. Soc.* **2013**, *135*, 4227−4230. (d) Oh, J. Y.; Chi, W. S.; Lee, J. H.; Kim, J. H.; Kang, S. W. *Ind. Eng. Chem. Res.* **2013**, *52*, 9607−9611. (e) Chi, W. S.; Hong, S. U.; Jung, B.; Kang. S. W.; Kang, Y. S.; Kim, J. H. *J. Membr. Sci.* **2013**, *443*, 54−61. (f) Karjalainen, E.; Izquierdo, D. F.; Marti-Centelles, V.; Luis, S. V.; Tenhu, H.; Garcia-Verdugo. E. *Polym. Chem.* **2014**, *5*, 1437−1446. (g) Hu, H.; Yuan, W.; Zhao, H.; Baker, G. L. *J. Polym. Sci. A: Polym. Chem.* **2014**, *52*, 121−127. (h) He, H.; Averick, S.; Roth, E.; Luebke, D.; Nulwala, H.; Matyjaszewski, K. *Polymer* **2014**, *55*, 3330−3338. (i) He,

H.; Zhong, M.; Luebke, D.; Nulwala, H.; Matyjaszewski, K. *J. Polym. Sci. A: Polym. Chem.* **2014**, *52*, 2175−2184.

(28) Long, S.; Wan, F.; Yang, W.; Guo, H.; He, X.; Ren, J.; Gao, J. *J. Appl. Polym. Sci.* **2013**, *130*, 2680−2687.

(29) Päch, M.; Zehm, D.; Lange, M.; Dambowsky, I.; Weiss, J.; Laschewsky, A. *J. Am. Chem. Soc.* **2010**, *132*, 8757−8765.

(30) (a) Guo, C.; Bailey, T. S. *Soft Matter* **2010,** *6*, 4807−4818. (b) Scalfani, V. F.; Bailey, T. S. *Macromolecules* **2011,** *44*, 6557−6567.

(31) Zhao, H.; Foss, F. W. Jr.; Breslow, R. *J. Am. Chem. Soc.* **2013**, *130*, 12590−12591.

(32) Zhao, D.; Fei, Z.; Ang, W. H.; Dyson, P. J. *Small* **2006**, *2*, 879−883.

(33) Schenkel, M. R.; Zhao, R.; Robertson, L. A.; Wiesenauer, B. R.; Clark, N. A.; Gin, D. L. *Liq. Cryst.* **2013**, *40*, 1067−1081.

(34) Xia, J.; Matyjaszewski, K. *Macromolecules* **2011**, *30*, 7697−7700.

CHAPTER 4

Phase Behavior of Highly Asymmetric, Poly(Ionic Liquid)-Rich Diblock Copolymers and the Effects of Simple Structural Modification on Phase Behavior

(Adapted from a manuscript initially submitted to *Macromolecules* under the same title, co-authored with May, A. W.; Wijayasekara, D. B.; Gin, D. L.; Bailey, T. S. My contribution to this work was the synthesis and structural characterization of the block copolymers; the morphological characterization of the polymers was performed by our collaborators at Colorado State University.)

4.1 Abstract

A series of thermally processable, phase separated diblock copolymers made via sequential ATRP of styrene and styrenic ionic liquid (IL) monomers with various alkyl imidazolium substituents were synthesized to cover a wide range of volume fractions, most notably those on the IL-rich side of the phase diagram. Small-angle X-ray scattering (SAXS) analysis was used to confirm melt-state (and glassy state) phase behavior. All four classic diblock copolymer morphologies (e.g. body-centered cubic spheres (S_{BCC}), hexagonally packed cylinders (Hex), lamellae (Lam), and notably, bicontinuous gyroid (Gyr)) were observed. These PS-*b*-PIL diblock copolymers were found to have a high degree of conformational asymmetry, highlighted by the shift of the Lam phase window with boundaries falling between f_{PIL} = 0.31 and 0.55. Variation of

the alkyl group appeared to influence the strength of the Flory-like interaction parameter of the system, $\chi_{PS/PIL}$. Therefore, simple substitution of methyl by *n*-butyl on the imidazolium IL resulted in the emergence of the (notoriously segregation-sensitive) Gyr phase, superseding the persistent coexistence of Lam and Hex in the methyl-substituted imidazolium diblock copolymer.

4.2 Introduction

Ionic liquids (ILs) have been a major focal point in many areas of chemistry and engineering due to their favorable properties and emerging capabilities. ILs are frequently used as green solvents due to their near-zero vapor pressure and negligible flammability. The high ionic conductivity, thermal stability, and sorption selectivity for certain light gases make ILs attractive for use in energy applications[1] (i.e., as battery materials[2] and post-combustion gas separation membranes[3]). In circumstances where the mechanical properties of a polymer are more desirable, researchers have developed polymerized ionic liquids (PILs), or polymers that incorporate the typically ionic portion of the ILs as part of each repeat unit.[4,5] The counter-anions remain separate and weakly coordinated to the polymer backbone, which allows the PILs to maintain high ionic conductivity.

Due to the liquid-like nature of many PIL homopolymers of interest, the ability to tune the mechanical and other properties of PILs can be limited. One strategy to mitigate this problem has been to incorporate PIL into block copolymer (BCP) architectures to generate BCPs containing a PIL block (PIL-BCPs) with the tunability of glass transition temperature and BCP morphologies. PIL-BCPs have one block dedicated to providing mechanical integrity while allowing the PIL block to retain many of the desirable qualities of the ILs.[1,6] To produce PIL-BCPs, incorporating

IL functional units (e.g. imidazolium, ammonium, phosphonium, etc.) into a monomer structure (which are frequently styrene-, acrylate-, vinyl-, or norbornene-based) has been a commonly used strategy in recent years.[1,4–7] Diblock copolymer (AB) architectures are typically the most widely synthesized; however, Matyjaszewski and co-workers recently reported several interesting BCP architectures including ABA or BCB triblock copolymers in which B is the charged IL block.[8]

Generally, there have been three strategies employed to synthesize PIL-BCPs.[1,6] These include (1) the post-polymerization modification of reactive groups on an uncharged BCPs to generate the IL moiety, (2) the growth of PIL blocks on an uncharged polymer, and (3) the sequential copolymerization of neutral and IL monomers. A multitude of polymerization techniques[1,6] have been used to achieve this, including the earliest examples of PIL-BCPs synthesized via nitroxide-mediated polymerization (NMP),[7,9,10] reversible addition-fragmentation chain-transfer (RAFT) polymerization,[11] atom-transfer radical polymerization (ATRP),[8,12,13] ring-opening metathesis polymerization (ROMP),[14] and anionic polymerization[1].

While the synthetic development of novel PIL-BCPs continues to be a major research focus, it is also crucial that the self-assembly thermodynamics of this relatively new class of materials be fully understood and characterized. For example, Mahanthappa and coworkers showed that the conductivity of various styrene/styrenic imidazolium BCPs varied widely depending on morphology, long-range order, and preparation of the polymer film.[9] Additionally, for polymers intended as gas separation membranes, Drzal et al. and Nguyen et al. both showed that BCP morphology had a direct impact on the gas transport properties of the material.[15,16] Therefore, we have focused on applying polymerization techniques for IL monomers that allow the precise control over block ratios and molecular weights, as an approach to understand the comprehensive phase separation behavior of various PIL-BCP systems. We previously published the phase

behavior of a series of alkyl-imidazolium norbornene block copolymers synthesized via ROMP.[14,17] In fact, this was one of the earliest studies to show that imidazolium-based PIL-BCPs are capable of forming ordered nanostructures in their neat melt. Some significant drawbacks to this norbornene system include the need for expensive ROMP catalysts, lengthy monomer synthesis, and poor mechanical properties due to the liquid-like[17] nature of this BCP led to the exploration of more convenient polymerization techniques and monomers.

As shown in Chapter 3, we performed a preliminary study[13] investigating the morphology of several styrene/styrenic alkyl-imidazolium BCPs. These PIL-BCP system synthesized via ATRP has several advantages over the norbornene/ROMP system including lower cost, easier synthesis, reduced metal contamination, easier handling and storage (solid powders vs. viscous liquids), and thermal processability. While Mahanthappa and coworkers prepared similar BCPs by post-polymerization modification of styrene/4-vinylbenzyl chloride BCPs, our groups and the Matyjaszewski group showed that imidazolium-based PIL-BCPs can be made by direct ATRP of uncharged monomers and IL monomers in scalable quantities with excellent molecular weight (MW) control and purity. Since then, we started to further explore the self-assembly behavior and expand the known phase diagram for the linear diblock copolymer architecture of this PIL-BCP system. We believe a detailed understanding of how the densely charged PIL block influences BCP phase behavior will create a foundation from which more complex BCP phase behavior can be investigated, such as higher-order, linear BCPs (ABA, ABC, ABAC, etc.),[18–21] small molecule-doped BCPs,[22] pom-pom BCPs,[23] or BCPs incorporated into unusual matrices.[24] Thus, we expand the phase diagram to the PIL-rich region ($f_{PIL} > 0.5$). Herein, we present the melt-state phase behavior of these alkyl-imidazolium-containing styrenic diblock BCPs made by sequential ATRP

as function of (a) PIL block volume fraction and (b) different alkyl groups on the imidazolium repeat unit.

4.3 Results and discussion

4.3.1 Synthesis and characterization of PS-PIL BCPs

Polystyrene-*b*-poly(1-(4-vinylbenzyl)-3-alkyl imidazolium bis(trifluoromethanesulfonyl)-imide) (PS-*b*-PIL) BCPs (**1**) were synthesized via the sequential ATRP procedures as described in Chapter 3 (Figure 4.1).[13] In this two-step sequential copolymerization, polystyrene homopolymers (**3**) with controlled MW and low polydispersity index (PDI) was first synthesized and used as macroinitiators. The imidazolium-based PIL block was then formed upon addition of the appropriate amount and type of IL monomers (**2**). The BCPs synthesized were targeted to contain approximately 50 total repeat units while varying the relative volume fraction of the PIL block. The block composition ratio and molecular weight of each PS-*b*-PIL BCP (**1**) were confirmed by ^{1}H NMR analysis (see Section 4.6.12 for details).[13] The degree of polymerization (DP) and number average molecular weight (M_n) of the PS blocks were determined by end-group analysis using the TMS group on the initiator as a ^{1}H NMR reference. The PS:PIL block ratios for each BCP were calculated by integrating and comparing distinct ^{1}H NMR signals indicative of each block. The DP of the PIL block was then determined based on the calculated block composition ratios and DP of the PS block. Consequently, the M_n values for BCPs **1** could be calculated by multiplying the DP of each block by the MWs of the respective repeat units (see Table 4.1).

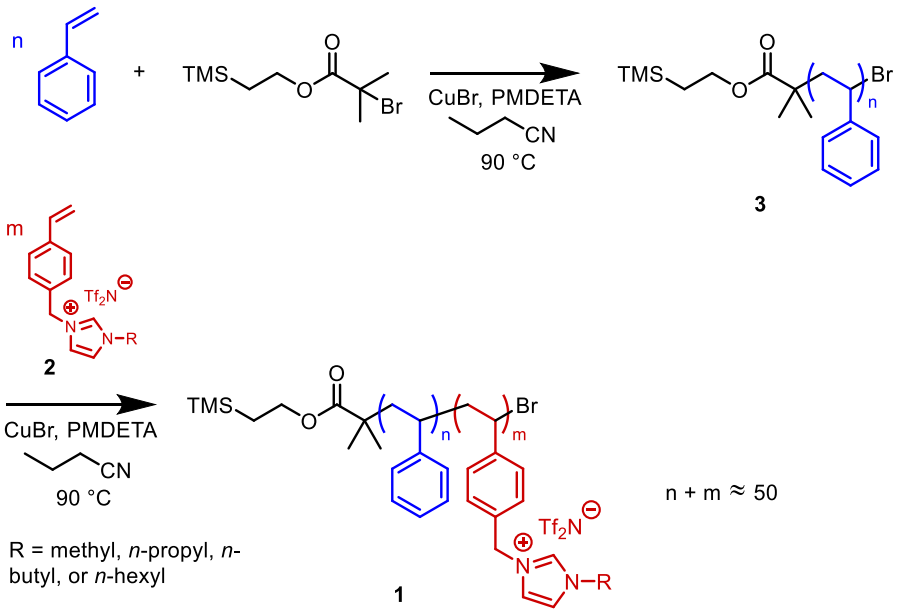

Figure 4.3. Synthesis and structures of the PS-*b*-PIL BCPs made via sequential ATRP.

Table 4.2. Morphological characteristics of PS-*b*-PIL BCPs **1** at room temperature after thermal annealing.

BCP	n	m	f_{PIL}[a]	M_n[b] (g mol^{-1})	d_{100}* (nm)	Morphology	Observed q*/q_{100}[c]
R = methyl							
1.1c[d]	15	35	0.89	18600	16.6[e]	S_{LLP}	form scattering
1.1b[d]	20	30	0.85	16700	16.5[e]	S_{BCC}	√2, √4, √6, √8, √10, √12, √14, (√16)
1.1a[d]	25	25	0.79	14900	12.7	Hex (weakly ordered)	√1, (√3), √4, √7, (√9), (√12), (√13)
1.1d	30	18	0.70	12000	14.8	Hex (weakly ordered)	√1, √3, √4, √7, (√9), (√12), (√13)
1.1e	34	15	0.64	11000	16.7	Hex	√1, √3, √4, √7, (√9), √12, √13
1.1f	36	14	0.61	10800	16.7	Hex	√1, √3, √4, √7, (√9), √12, √13

1.1g	37	13	0.58	10400	15.5	Hex (weakly ordered)	√1, √3, √4, √7, (√9), (√12), (√13)
1.1h	40	12	0.55	10200	14.2	Lam (weakly ordered)	√1, √4, √9
					15.7	Hex (weakly ordered)	√1, √3, √4, (√7), (√9), (√12), (√13)
1.1i	34	10	0.54	8600	13.8	Lam	√1, √4, √9
					15.7	Hex	√1, √3, √4, (√7), (√9), √12, (√13)
1.1j	40	10	0.50	9200	13.0	Lam	√1, √4, √9
1.1k	40	9	0.48	8700	12.5	Lam	√1, √4, √9
1.1l	40	8	0.45	8300	12.3	Lam	√1, √4, √9
1.1m	45	5	0.31	7400	11.7	Lam	√1, √4, √9
					11.0	Hex	√1, √3, √4, (√7), (√9)
R = *n*-butyl							
1.2c[d]	15	35	0.90	20100	16.3[e]	S_{LLP}	form scattering
1.2b[d]	20	30	0.86	18000	15.6e	S_{BCC}	√2, √4, √6, (√8)
1.2a[d]	25	25	0.80	15900	11.3	Hex (weakly ordered)	√1, (√3), (√4), (√7), (√9),
1.2d	30	18	0.71	12800	14.5	Hex	√1, (√3), √4, √7, (√9),
1.2e	34	14	0.63	11100	15.0	Hex	√1, √3, √4, √7, √9, √12, √13
					15.3 (d_{211})	Gyr	√6, √8, (√14), (√16), √20, √22, √24, √26, (√30), (√32), (√38), (√40), √42, √46, (√48), (√50)
1.2f	40	9	0.49	9100	12.0	Lam	√1, √4, √9
1.2g	45	5	0.33	7600	12.1	Lam	√1, √4, (√9)
R = *n*-propyl							
1.4a	35	15	0.65	11500	15.4	Hex	√1, (√3), √4, √7, (√9), (√12), √13
1.4b	40	10	0.52	9500	13.2	Lam	√1, √4, √9

					14.0	Hex	√1, √3, √4, √7, (√9), (√12), (√13)
R = *n*-hexyl							
1.5a	20	30	0.86	18800	13.9	none	none observed
1.5b	25	25	0.80	16600	10.6	none	none observed

[a] f_{PIL} determined by $f_{PIL} = (M_{n,PIL}*\rho_{PIL}^{-1})/([M_{n,PIL}*\rho_{PIL}^{-1}]+[M_{n,PS}*\rho_{PS}^{-1}])$ where ρ_{PS} (0.969 g cm^{-3}) and ρ_{PIL} (1.06 g cm^{-3}, calculated from SAXS data of sample **1.1j**) are taken as nominal densities at 140 °C.[25] [b] Calculated based on n and m values obtained from ^{1}H NMR analysis and rounded down to nearest hundred g mol^{-1}.[13] [c] Permitted reflections for the specified morphology; those not observed are listed in parentheses. [d] Data integrated from previous work[13] [e] Calculated from d_{110} based on data from previous work.[13]

4.3.2 Overview of phase behavior

As shown in Chapter 3, we developed the synthesis of imidazolium-based PS-*b*-PIL BCPs with different R-group functionality (methyl, *n*-butyl, *n*-decyl) on the imidazolium block, and we included a preliminary assessment of the role of the R group on the ability of these BCPs to phase separate. Depending on the R group, molar ratios of the PIL block between 50–70% were observed to form spherical or cylindrical morphologies (methyl and *n*-butyl), or failed to phase separate (*n*-decyl). This revealed several intriguing characteristics about this BCP system. Specifically, R-group length significantly affected the ability of the PS-*b*-PIL BCPs to phase separate, and a much wider compositional range of samples would be desired to understand the phase behavior of these polymers. Due to the lack of observable phase separation with the series of *n*-decyl-substituted BCPs, the focus of our phase behavior investigation was narrowed to BCPs with R-groups containing up to six carbons, with an emphasis on those with methyl and *n*-butyl groups.

Gel permeation chromatography (GPC) data of the PS macroinitiators (see Section 4.6.11) show narrow PDIs (1.08 to 1.15). The ionic nature of the PIL block prevented the use of conventional GPC to characterize the MWs of the PIL-BCPs without significant modification to the GPC system.[13] While the PDIs of our final BCPs were unable to be measured, one of the many reasons ATRP was chosen as the synthetic method is its ability to produce relatively narrow PDIs in polymers, PILs included.[8,12,13,26,27]

Small-angle X-ray scattering (SAXS) was used as the primary characterization method to describe the phase behavior of various alkyl-substituted (methyl, *n*-propyl, *n*-butyl, *n*-hexyl) PS-*b*-PIL BCPs (PS-*b*-MePIL, PS-*b*-PrPIL, PS-*b*-BuPIL, PS-*b*-HxPIL). All samples were thermally annealed in the bulk under vacuum in the sample chamber of the SAXS instrument, with data collection typically taken every 50 °C, starting at room temperature. All samples were stepped to 175 °C, subjected to an annealing period between 30 min and 2 h, and then stepped back down to room temperature. A maximum temperature of 175 °C was chosen as a compromise between providing the polymer chains sufficient mobility to achieve at/near equilibrium phase behavior in a short amount of time (~15 min for most samples) and limiting the potential for thermal degradation. Some of the samples showed ordered phases emerging at lower temperatures such as 100 °C or 125 °C, but all samples were annealed at 175 °C for consistency and efficiency.

Polymer phase behavior is best described by three fundamental parameters: (1) the volume fraction of one of the blocks (f), (2) the effective degree of segregation (χN), and (3) the conformational asymmetry (ϵ). Conformational asymmetry, while not shown explicitly in the phase diagram, accounts for the space-filling differences in the blocks of a BCP and routinely manifests itself as a shift in the phase boundaries of the phase diagram (such that symmetry around $f = 0.5$ is lost).[28,29] In general, a BCP phase diagram maps out the specific equilibrium morphology

at each composition and segregation strength for which the overall free energy of the BCP is minimized.[30] Generally, f would be calculated using bulk homopolymer densities to determine the relative ratio of block volumes, but in our case the bulk homopolymer density of the alkyl-PIL blocks were unknown. However, it was possible to estimate the PIL block densities using characteristics of the SAXS diffraction data (see Section 4.3.3 for further explanation), allowing volume fractions to be determined. χN is the product of χ (a Flory-like interaction parameter) and N (the degree of polymerization). χ represents the free energy penalty (i.e. energy increase) associated with the interaction energy produced upon mixing of dissimilar repeat units.[30] While a typical phase diagram will present phase behavior data as χN versus f, several factors that we, and others, have encountered with other PIL-BCPs (e.g., an inability to disorder even for low molecular weight PS-*b*-PIL BCPs at experimentally feasible temperatures) precluded simple determination of the value of $\chi_{PS/PIL}$ for these systems.[9,14] Despite being unknown, the value of χ is largely considered to be independent of f for any A/B BCP pair. Additionally, as χ is inversely related to temperature, and all samples have a similar value of N (~50 repeat units) by synthetic design, reporting phase behavior as a function of temperature (T) vs. f achieves a similar outcome as using a traditional χN vs. f plot.

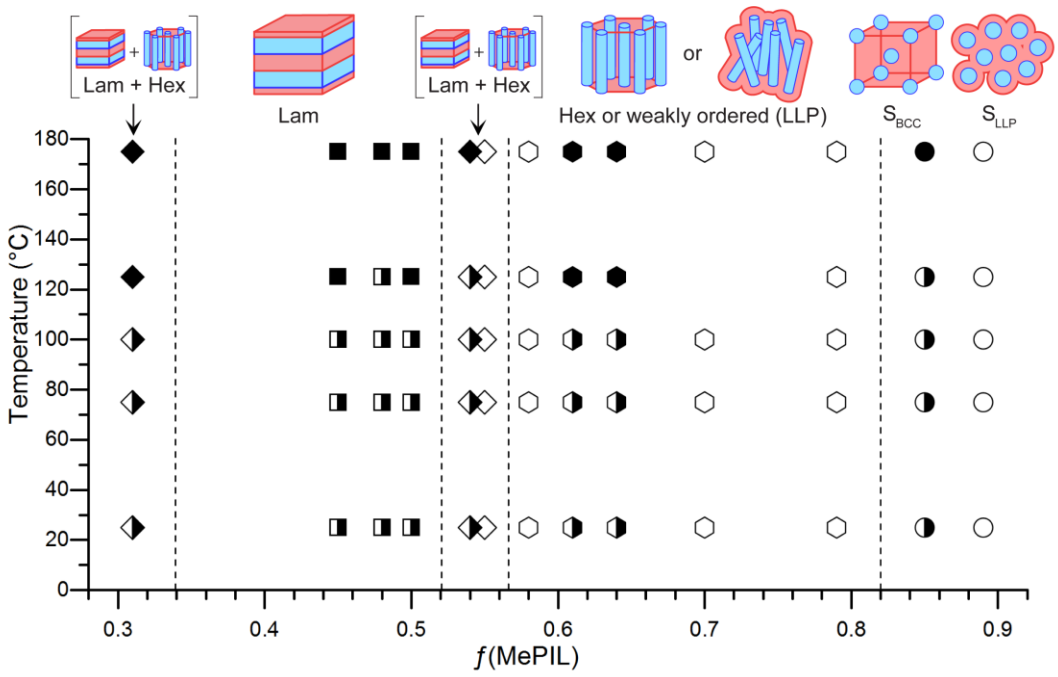

Figure 4.4. Phase diagram for methyl-substituted PS-*b*-PIL BCPs **1.1a–m** as a function of volume fraction of the PIL component. Open data points represent weakly ordered samples, filled data points represent highly ordered samples, and half-filled data points represent samples that ordered upon reaching an appropriate annealing temperature and remained ordered in that phase upon cooling.

The summary of phase behavior results of the methyl-functionalized series of PS-*b*-MePIL BCPs is shown in Figure 4.2, in which we were able to observe three out of the four classical diblock copolymer morphologies: Lam (data represented as square symbols in Figure 4.2), Hex (hexagon symbols), and S_{BCC} (circle symbols). Samples that never achieved any high degree of order (or adopted a liquid-like packing rather than an organized lattice) are represented as open circle symbols; and samples that were initially weakly ordered but became well-ordered upon thermal annealing (and remained ordered during cooling) are represented as half-filled symbols.

In the two areas where the Gyr morphology would traditionally appear for a diblock copolymer,[28,31–33] a persistent coexistence of Lam and Hex (diamonds in Figure 4.2) was observed instead. More asymmetric samples adopting a liquid-like packing of either cylinders or spheres provided the general location for the order-to-order (Hex to S_{BCC}) and order-to-disorder (S_{BCC} to S_{LLP}) phase boundaries on the high f_{PIL} side of the phase diagram. However, we were unable to observe any of the samples in this series in a completely disordered state.

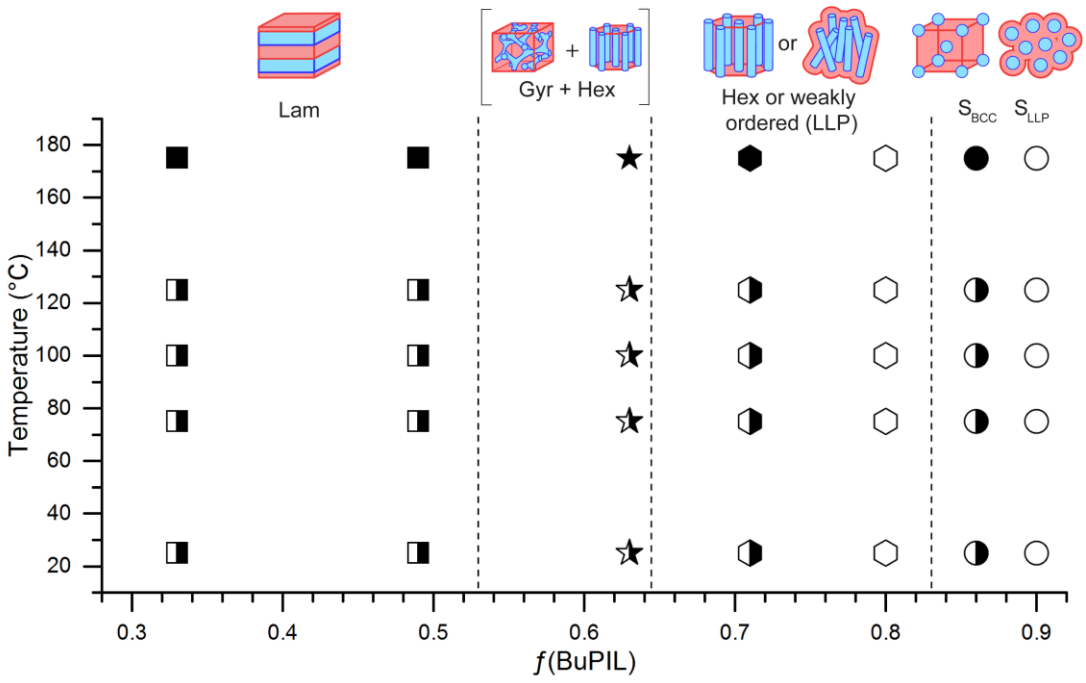

Figure 4.3. Phase Diagram of phase separating, *n*-butyl-substituted PS-*b*-PIL BCPs **1.2a–g** with respect to volume fraction of the PIL component. Open data points represent weakly ordered samples, filled data points represent highly ordered samples, and half-filled data points represent samples that ordered upon reaching an appropriate annealing temperature and remained as such upon cooling. Data for samples with f_{BuPIL} greater than 0.8 are integrated from previous work.[13]

Figure 4.3 shows the effect of modifying the R-group functionality of the imidazolium unit (from methyl to *n*-butyl) on phase behavior, and consequently, on decreasing the segregation strength between blocks. The absence of Gyr phase in the PS-*b*-MePIL BCPs was likely symptomatic of the high degree of segregation intrinsic to the system, notorious for thwarting gyroid formation.[34] However, by substitution of the methyl substituent with an *n*-butyl group, we found strong evidence for the emergence of a Gyr phase (in coexistence with cylinders) in PS-*b*-PIL BCP **1.2e**. The full phase behavior of the *n*-butyl series is discussed in detail in later sections.

For all samples that formed ordered morphologies upon thermal annealing, no ordered-phase to ordered-phase transitions (OOTs) within any single sample were observed throughout the experimentally accessible range of temperatures examined (from room temperature to as high as 240 °C). That is, only one morphology (or persistent coexistence of morphologies) was observed for each individual sample. All morphologies developed through annealing at high temperature remained unchanged once cooled, even when annealed at lower temperatures just above the T_g of the PS block. In addition, the inability of these BCPs to disorder prior to thermal decomposition made it difficult to definitively classify any observed morphologies as true equilibrium phases, or directly determine the value of $\chi_{PS/PIL}$ from SAXS alone.[14,35,36] However, given the extremely large temperature window in which they persisted once ordered, it is likely that most of the morphologies observed are in their equilibrium state, and for those that are in a persistent metastable state the kinetics of any OOT are too prohibitively slow for the timescale of this study.

While analyzing our earlier norbornene PIL-BCP system, we surmised that the inability to disorder most of these polymer samples without inducing decomposition provided strong evidence for an extremely high segregation strength (χN) between the blocks, despite the low degrees of

polymerization (where N, or n+m ≤ 50). It is possible that χ is even higher in this PS-*b*-PIL system, as none of the BCPs studied showed any evidence of disordering, while two samples in the norbornene system either approached or even achieved disorder. Below, we present a more detailed analysis of each morphology identified using SAXS data as a function of temperature for every PIL-BCP.

4.3.3 Lam morphologies of PS-*b*-MePILs

SAXS analysis of BCP samples **1.1j–l**, from 45 to 50% by volume of PIL, exhibited evidence of the Lam morphology, as shown in Figure 4.4. Upon thermal annealing, all of these samples showed higher-ordered SAXS diffraction reflections at q/q^* ratios of √1, √4, and √9 (where q^* is the position of the primary scattering wave vector, q_{100}), consistent with the calculated allowed reflections[37] for this classic diblock copolymer morphology (solid inverted triangle symbols in Figure 4.4). These three samples, with approximate M_n values ranging from 8300 g mol^{-1} (**1.1l**) to 9300 g mol^{-1} (**1.1j**) were found to have small but steadily increasing domain spacings (d_{100} increasing from 12.3 to 13.0 nm, respectively) due to the MW increase and the shift to higher PIL block volume. Notably, when compared with non-ionic LAM-forming diblock copolymer analogous like polystyrene-*b*-poly(vinylpyridine), nearly double DP (N ~ 95–105) are required to achieve similar domain spacing values.[38] This behavior underscores the very extended nature of the ionic PIL block in the melt and its strong predilection for adopting a stretched chain conformation during self-assembly.

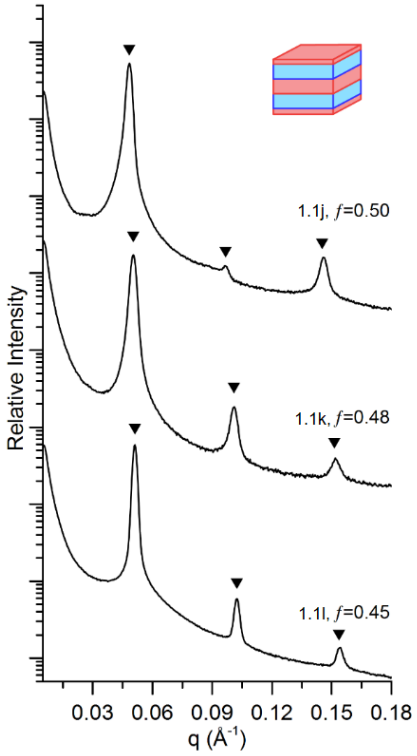

Figure 4.4. Room temperature (25 °C) SAXS data collected post-annealing for Lam PS-*b*-MePIL BCPs **1.1j-l**. Each sample was subjected to a two-hour annealing (in vacuo) at 175 °C. Solid inverted triangles represent the calculated values of allowed SAXS reflections (based on q*) for a Lam morphology, found at q/q^* ratios of √1, √4, and √9 (where q^*, the primary scattering wave vector, is q_{100}). Volume fractions were calculated from sample **1.1j**, where nearly complete suppression of the even-order reflection at $q/q^* = \sqrt{4}$ indicates equal volumes of either block ($f_{PIL} \approx 0.5$)[9,14] and allowed for estimation of the bulk homopolymer density of MePIL.

The near extinction of the even-order reflection $q/q^* = \sqrt{4}$ in sample **1.1j** suggests nearly symmetrical block volumes, a phenomenon observed previously with our norbornene-based PIL-BCPs and with the *n*-hexyl-functionalized styrene-imidazolium BCPs studied by Mahanthappa and coworkers.[9,14] Using the bulk homopolymer density of polystyrene (0.969 g cm^{-3} at 140 °C)[39]

and setting the relative volumes of the two blocks to 0.50, we were able to calculate an approximate density for the MePIL block as 1.06 g cm^{-3}. This value was then used in conjunction with experimentally determined block ratios (calculated from ^{1}H NMR analysis) to estimate the volume fraction of PIL block for each PIL-BCP. Interestingly, the difference between samples **1.1j** and **1.1k** (in which the $q/q^* = \sqrt{4}$ peak is suppressed, and clearly present, respectively) is only a single added MePIL repeat unit on average. Thus, even though suppression of the $q/q^* = \sqrt{4}$ is not absolute in **1.1j**, our estimation of the PIL block density is believed to be reasonably accurate given the apparent sensitivity of the $q/q^* = \sqrt{4}$ peak extinction to very small changes in BCP composition.

4.3.4 Hex morphologies of PS-*b*-MePILs

In the region spanning f_{PIL} = 0.58 to 0.79, SAXS data of samples **1.1c–g** with M_n values ranging from 10400 to 14900 g mol[1] showed evidence of the Hex morphology with all samples exhibiting multiple higher order SAXS reflections at allowed q/q^* ratios of $\sqrt{1}$, $\sqrt{3}$, $\sqrt{4}$, $\sqrt{7}$, $\sqrt{9}$, $\sqrt{12}$, and $\sqrt{13}$ (shown as hollow inverted triangle symbols in Figure 4.5). This transition in phase behavior in the PIL-rich region from a Lam to Hex phase just beyond f_{PIL} = 0.5 leads to the construction of a highly asymmetrical phase diagram. In the PS-rich region, however, we do not observe a Hex phase emerging until f_{PIL} = 0.31 (see next section for discussion of these coexistence regions). One way to quantify the asymmetry is with the conformational symmetry ratio, ϵ, which describes the inequality in space-filling characteristics of each block, where an $\epsilon \neq 1$ indicates a conformationally asymmetric polymer. A significant shift in the phase boundaries here suggests that the ϵ value of this BCP is significant. However, we are unable to calculate its value without the statistical segment length (b) of each block, which, to our knowledge, has not been determined for any styrenic imidazolium-based PILs.[28,32,36,40] We assume a much larger statistical segment

length in the MePIL block due to an extended conformation of the main chain associated with both steric and electrostatic repulsion among the bulkier cationic imidazolium side groups.[36] When the PIL block occupies the majority of the volume, it encourages the interface between the PS and MePIL blocks to curve towards the PS domain, initiating a shift towards the PS cylinder phase at lower volume fractions of PIL.[28,32] This effect is reminiscent of phase diagrams of other highly asymmetric block copolymers with an $\epsilon > 2$, such as poly(ethylene oxide-*b*-isoprene)[40] and the "brush-like" diblock copolymer poly(1,2-octylene oxide)-*b*-poly(ethylene oxide)[31].

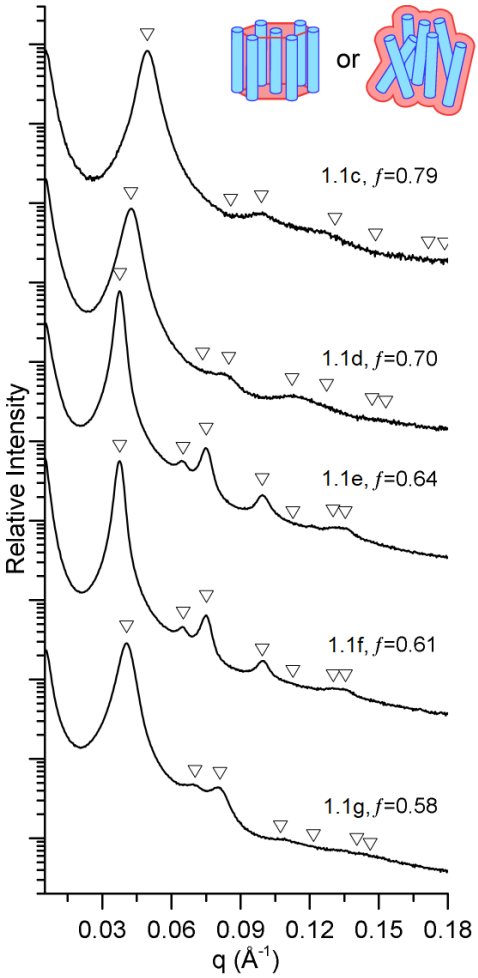

Figure 4.5. Room-temperature SAXS profiles (25 °C) collected post-anneal for Hex-forming PS-*b*-MePIL BCPs **1.1c–g**. Samples **1.1d–g** were subject to a two-hour annealing (in vacuo) at 175 °C, while sample **1.1c** was annealed for 30 min. Open inverted triangle symbols represent the calculated values of allowed SAXS reflections for a Hex morphology, at q/q^* ratios of $\sqrt{1}$, $\sqrt{3}$, $\sqrt{4}$, $\sqrt{7}$, $\sqrt{9}$, $\sqrt{12}$, and $\sqrt{13}$ (where $q^* = q_{100}$). Samples **1.1e** and **1.1f** exhibit a high degree of order, while the rest, **1.1c**, **1.1d**, and **1.1g** more closely match a liquid-like packing of cylinders phase.

In this region of the phase diagram, we observed samples (**1.1c, 1.1d, 1.1g**) that experienced some difficulty in forming a highly ordered hexagonal packing, instead exhibiting more of a liquid-like packing of cylinders, even after two full hours of annealing at 175 °C (Figure 4.6). In the norbornene-imidazolium system previously studied, this weakly ordered morphology was easily transformed into a Hex phase through thermal annealing.[14] Because there is nothing thermodynamically favorable about weakly ordered cylinders, we expect that the observed lack of periodicity in samples **1.1c**, **1.1d**, and **1.1g** stems from extremely slow ordering kinetics as a result of presumably high values of χ. Additionally, their location in regions of f_{PIL} close to the Hex/S_{BCC} or Hex/Lam phase boundaries, may also be influencing their driving force to exhibit a strong degree of order.[41]

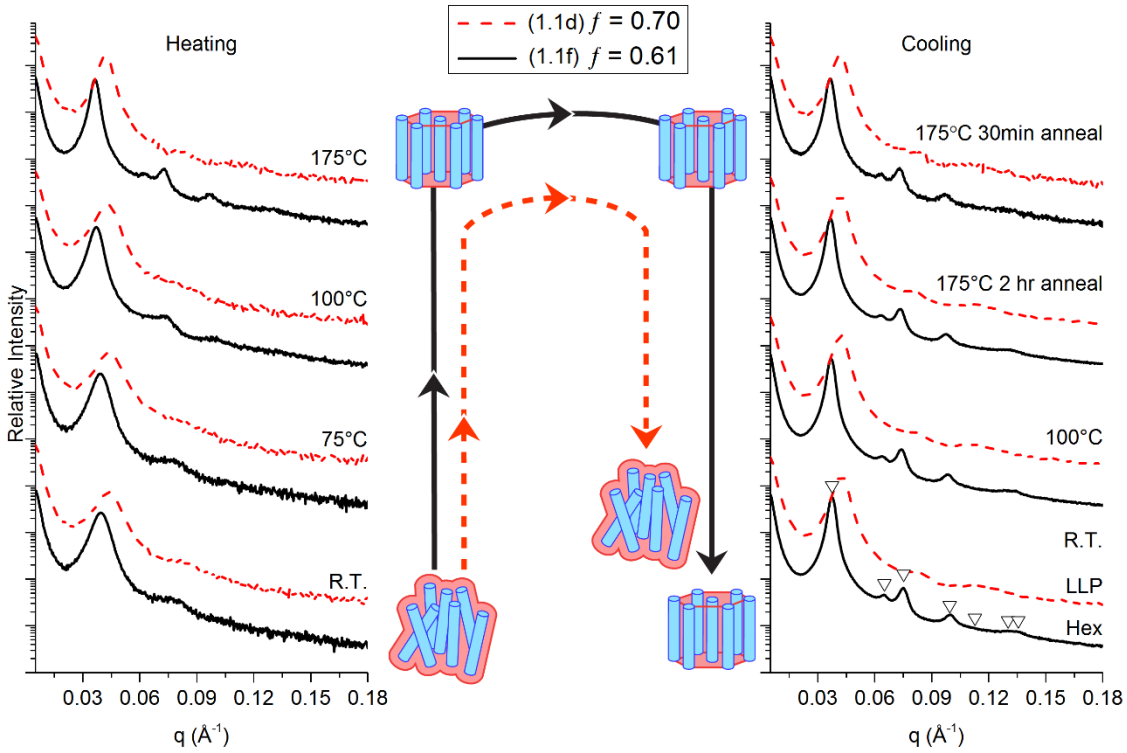

Figure 4.6. Temperature-dependent SAXS profiles for cylinder-forming samples **1.1d** and **1.1f** illustrating the difference in scattering profiles for a sample that formed highly-ordered, periodic hexagonal nanostructure very rapidly (**1.1f**), and a sample that phase separated rapidly but remained weakly ordered even after extended thermal annealing (**1.1d**).

4.3.5 Coexistence of Lam and Hex morphologies of PS-*b*-MePILs

Three BCP samples (**1.1h**, **1.1i**, and **1.1m**) with f_{PIL} of 0.55, 0.54, and 0.31 (and M_n values of 10300, 8700 and 7400 g mol^{-1}) respectively, exhibited coexistence of Lam and Hex phases that persisted throughout the thermal annealing process. In addition to two distinct q^* values (where q^*, the primary scattering wave vector, is q_{100} for both Lam and Hex phases), all samples showed

at least one uniquely identifiable higher-order SAXS reflection for each morphology. Specifically, scattering peaks at q/q^* ratios of √1, √4, and √9 for the Lam phases, and √1, √3, and √4 for the Hex phase (Figure 4.7).

Another interesting effect of the conformational asymmetry of these PIL-BCPs appears to manifest itself in the relative positions of q_{Hex}^* and q_{Lam}^* in the two coexistence regions on either side of the Lam phase window. That is, while q_{Hex}^* is less than q_{Lam}^* for coexistence samples in the PIL-rich region of the phase diagram, q_{Hex}^* is greater than q_{Lam}^* in the PS-rich region. The latter is consistent with the positioning of q_{Hex}^* and q_{Lam}^* in our previous study of norbornene based PIL-BCPs, where the focus was limited to the investigation of BCPs with the non-ionic block comprising the majority component. It is not clear whether the inversion in q^* position between the two coexistence regions that span opposite sides of the Lam window constitutes a general phenomenon in strongly segregated conformationally asymmetric systems showing coexistent phases.

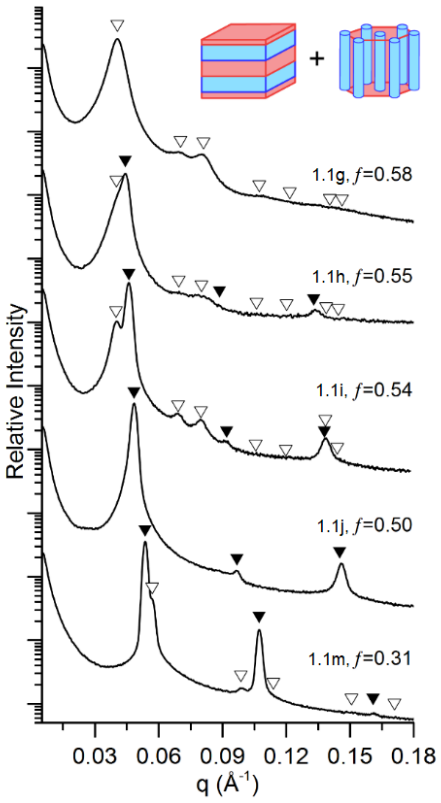

Figure 4.7. Post-annealing SAXS data collected at room temperature (25 °C) for PS-*b*-MePIL BCPs **1.1h, 1.1i** and **1.1m** showing a persistent coexistence of the Lam and Hex phases. Samples **1.1g** and **1.1j** are included in this plot as BCPs that exhibit purely Hex and Lam morphologies, respectively, near the phase border. Samples **1.1h** and **1.1i** were subject to a 2 h annealing period (*in vacuo*) at 175 °C, while sample **1.1m** was annealed for 8 h. Solid inverted triangle symbols represent the calculated positions of allowed SAXS reflections for a Lam morphology, at q/q^* ratios of √1, √4, and √9, and open inverted triangles represent the calculated positions of allowed SAXS reflections for a Hex morphology, at q/q^* ratios of √1, √3, √4, √7, √9, √12, and √13 (where $q^* = q_{100}$).

For all diblock copolymer morphologies except for Lam (which has both uniform domain thickness and constant mean curvature), there is a struggle between the need to have constant mean curvature to minimize interfacial tension between the blocks, and uniform domain thickness to maximize the entropic nature of chain stretching. This is known as packing frustration, because it is impossible to satisfy both requirements completely when there is enough asymmetry to cause interfacial curvature.[42–44] In our PIL-BCP system, the bulky, space filling nature of the PIL block forces interfacial curvature towards the PS domains almost immediately after the PIL block becomes the majority component by volume ($f_{PIL} > 0.5$). Early adoption of curvature appears to be in response to a need to relieve packing frustration felt particularly by the relatively short and bulky PIL blocks. Even though the stretching entropy is slightly reduced when the PS domains are forced to stretch to fill the center of the relatively large cylindrical domains, entropy gains are made in the relaxation of the PIL chains through their larger interfacial area per chain. The opposite is true when PS is the majority component. PS does not experience space constraints the way the PIL block does, so we observe the Lam phase over a wider range of f and smaller spacing between PIL cylinders on this side of the phase diagram.[45]

None of the SAXS patterns of these three BCP samples fit to any of the complex morphologies such as Gyr or the metastable hexagonally perforated lamellae. Given the apparent stability and small window of this coexistence between the Lam and Hex phases, it is probable that a complex morphology does not experimentally exist for this system. If this is the case, the most reasonable explanation is the ostensibly large χN values, even at high temperature. Polymers with low χN can adopt a Gyr morphology because the penalty for non-constant mean curvature is still more favorable relative to the entropic advantage of having a minority component with nearly uniform domain thickness.[25,43,44] For a diblock copolymer with larger χN values, morphologies in

which the mean curvature must deviate significantly from a single constant value (characteristic of the Gyr phase) experience an increase in packing frustration that challenges the ability of these phases to remain experimentally stable.[45]

While conformational asymmetry has been shown to affect the locations of phase boundaries, conformationally asymmetric BCPs have been observed to adopt the Gyr morphology, even in the strongly segregated regime around $\chi N \approx 50$, so conformational asymmetry alone cannot account for the absence of this phase.[28,31,40] In fact, Cochran et al. showed that conformational asymmetry actually increased the width of the theoretical Gyr phase window at high segregations (χN = 40, 80), albeit the phase window was still extremely narrow.[46] Davidock et al. produced several examples of highly segregated polymers that formed the gyroid phase with χN values up to 120. However, these polymers were synthesized with anionic polymerization and therefore had very narrow PDI values.[34] Polydispersity has been shown to have significant effects on the phase diagram of BCP morphologies,[47] but also does not inherently discourage the formation of complex morphologies. Self-consistent field theory (SCFT) predicts the existence of a gyroid phase window for AB diblock copolymers (with PDIs of the Ablock between 1.0 and 2.0, and a monodisperse B block). But as polydispersity increases, that phase window narrows significantly. Above $\chi N \approx 20$, the Gyr phase window is virtually non-existent on the more asymmetrical side of the predicted phase diagram for the most polydisperse model.[42] In 2005, Lynd and Hillmyer concluded that introducing polydispersity into a diblock copolymer melt causes it to relieve packing frustration much in the same way that conformational asymmetry does. That is, increased polydispersity in the minority component will encourage transitions to higher mean curvature (Lam → Hex), while increased polydispersity in the majority component will push the system to adopt decreased overall curvature (Hex → Lam). Indeed, they were able to observe the gyroid morphology in

poly(ethylene-*alt*-propylene)-*b*-polylactide BCPs in the weakly segregated regime (χN ≈ 10 to 20) with PDIs of the respective blocks as large as 1.36 and 1.67.[48] Conversely, Bendejacq et al. studied a series of highly segregated (χN > 50) BCPs and BCP/homopolymer blends with high PDIs that exhibited persistent coexistence of Lam and Hex phase in lieu of a Gyr phase.[49] Although we suspect that the polydispersity of this series of PIL-BCPs is not as significant as those mentioned previously, the compounded effect of some polydispersity and substantial conformational asymmetry is playing a major role in the observed morphology in the region of extremely high χN that our methyl-functionalized PIL-BCPs appear to populate.

Even with a small amount of polydispersity within a polymer sample, self-fractionation during phase separation allows us to explain how a persistent coexistence of two very different morphologies lowers the free energy of the system enough to be preferable to the formation of Lam, Hex, Gyr phases or any metastable complex morphology. During the annealing process, more compositionally symmetric chains separate from more compositionally asymmetric chains to form Lam or Hex domains, respectively. SCFT models that allow distinct population distributions for each morphology have accounted for such behavior.[42] This phenomenon is only advantageous for a highly-segregated sample. Fractionation into discrete domains causes a significant reduction in system entropy, but this effect is negated by the overwhelming relief of packing frustration achieved through Lam and Hex phase coexistence.[42] This is a plausible explanation for the difference in primary scattering peak (q^*) resolution between samples **1.1h** and **1.1i**, which have nearly identical volume fractions. **1.1h**, which is about 20% longer than **1.1i**, appears to have a compositional makeup (e.g., compositional polydispersity) or reduced mobility[41] that produces a diminished desire or ability to fractionate. This would lead to a smaller difference in domain spacing, less distinction between coexisting domains, and more weakly defined

scattering patterns of both morphologies. Additionally, fractionation accounts for the structure factor extinction of the √4 Lam peak seen in sample **1.1i**, particularly in Figure 4.8 after extended annealing. The average volume fraction of PIL for **1.1i** is 0.54, but if the more symmetrical chains that separate to form the Lam domain were much closer to 0.50 then the √4 peak would disappear accordingly, as seen with sample **1.1j**.

Sample **1.1i** was subject to extended thermal annealing between 125 °C and 175 °C in a vacuum-sealed ampule and placed in an oil bath for a total of one month, as a means to investigate the stability and equilibrium nature of this phase coexistence (Figure 4.8). Within the first several hours of annealing, a shift in the prevalence for the Hex phase is apparent by the increase in intensity of q^*_{Hex} and the peaks at $q/q^*_{Hex} = \sqrt{3}$ and $\sqrt{4}$, coupled with a slight decrease in the $q/q^*_{Lam} = \sqrt{4}$ and $\sqrt{9}$ peaks shown by comparing Figures 4.8a and 4.8b. Beyond 6 h of annealing, the differences from 6 h to 1 month (Figures 4.8b and 4.8c) are very subtle, if not negligible, suggesting that at- or near-equilibrium phase behavior is achieved within the first day of annealing, and the coexistence phase is persistent.

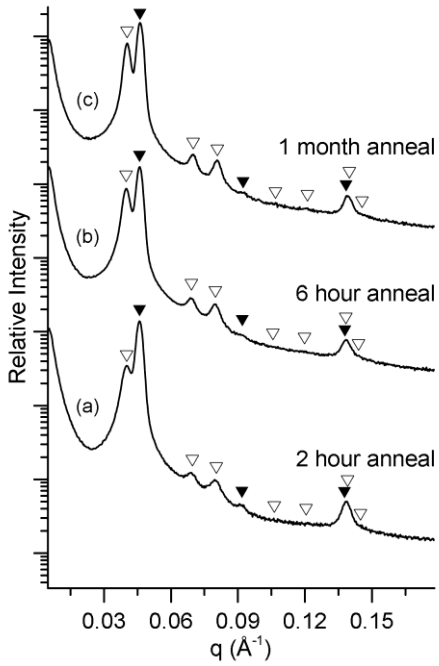

Figure 4.8. Room-temperature SAXS data for sample **1.1i** showing persistent coexistence of lamellae (solid inverted triangle symbols) and hexagonally packed cylinders (open inverted triangle symbols) after extended thermal annealing. Initially, the Lam phase dominates, but after 6 hours of annealing at 175 °C, the Hex phase become more prevalent. After 1 month of thermal annealing under vacuum between 125 °C and 160 °C, a further shift toward the Hex phase is minimal, indicating that coexistence in this sample is persistent.

4.3.6 S_{BCC} morphologies of PS-*b*-MePILs

In the most compositionally asymmetric region of the phase diagram ($f_{PIL} \geq 0.85$), two samples[13] showed SAXS patterns indicative of a sphere-based morphology. Upon thermal annealing, sample **1.1b** developed multiple higher-order SAXS reflections at q/q^* ratios (indicated as inverted triangle symbols with a strikethrough in Figure 4.9) of $\sqrt{2}$, $\sqrt{4}$, $\sqrt{6}$, etc., where q^* is the

primary scattering wave vector, q_{100}, that are consistent with S_{BCC} morphology.[14] As expected with S_{BCC}, q_{100} is absent due to the reflection conditions of the *Im3m* space group. The lattice constant ($a = d_{100}$) for samples **1.1a** and **1.1b** can be easily calculated from the first observed q value (q_{110}) giving values of 16.6 and 16.5 nm, respectively. The broad, form-factor scattering seen with sample **1.1a** (and with **1.1b** prior to annealing at 175 °C) is routinely observed for spherical micelles that persist with a liquid-like disordered packing (LLP), or S_{LLP}. The inability of spherical domains to order on a BCC lattice is typically due to compositional fluctuations near the ODT, sphere polydispersity, and limited chain mobility due to chain entanglements and slow chain diffusion kinetics.[14] As a result, S_{LLP} is often observed in samples with volume fractions that theoretically fall in the BCC range.[50,51] The persistence of liquid-like spherical domains in sample **1.1a** across the full experimental temperature range might imply that an f_{PIL} of 0.89 approaches the ODT but we are unable to pinpoint an actual disorder transition for this system.

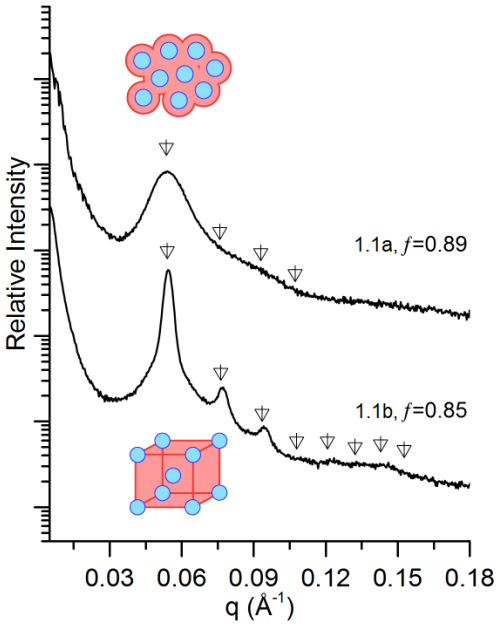

Figure 4.9. Post-annealing SAXS data at room temperature (25 °C) for S_{BCC} forming PS-*b*-MePIL BCPs **1.1a** and **1.1b**. Samples **1.1a** and **1.1b** were subject to a 30-min annealing period (in vacuo) at 175 °C. Open inverted triangles with a strikethrough represent the calculated allowed SAXS reflections for S_{BCC}, at q/q^* ratios of √2, √4, √6, √8, √10, √12, √14 and √16 (where q^*, the primary scattering wave vector, is q_{100}). Sample **1.1a** exhibits a more liquid-like packing of spheres (S_{LLP}), as opposed to the BCC lattice observed for **1.1b**.

4.3.7 R-group modification of PS-*b*-PIL BCPs

In a preliminary study, we indirectly determined that R-group modification had a sizable impact on interaction parameter (χ) between the PS and PIL blocks based on two observations: (1) samples with *n*-butyl functionality but comparable block ratios had smaller *d*-spacings than their methyl counterparts; (2) the *n*-decyl-substituted blocks appeared to be miscible enough with the

PS blocks to prevent phase separation altogether.[13] To investigate this effect further, we have prepared four additional *n*-butyl-functionalized BCPs (PS-*b*-BuPIL). The post-annealing room-temperature SAXS data for all seven samples are summarized in Figure 4.10. In this series we observe all four classic diblock copolymer morphologies; S_{BCC} (**1.2b**), Hex (**1.2d** and **1.2e**), Gyr (**1.2e**, in coexistence with cylinders, represented as stars in Figure 4.3), and Lam (**1.2f** and **1.2g**), as well as two samples (**1.2a** and **1.2c**) that showed no higher order SAXS reflections but we suspect have adopted a liquid-packing of spheres and cylinders, respectively, based on their relative positions in the phase diagram (Figure 4.3).

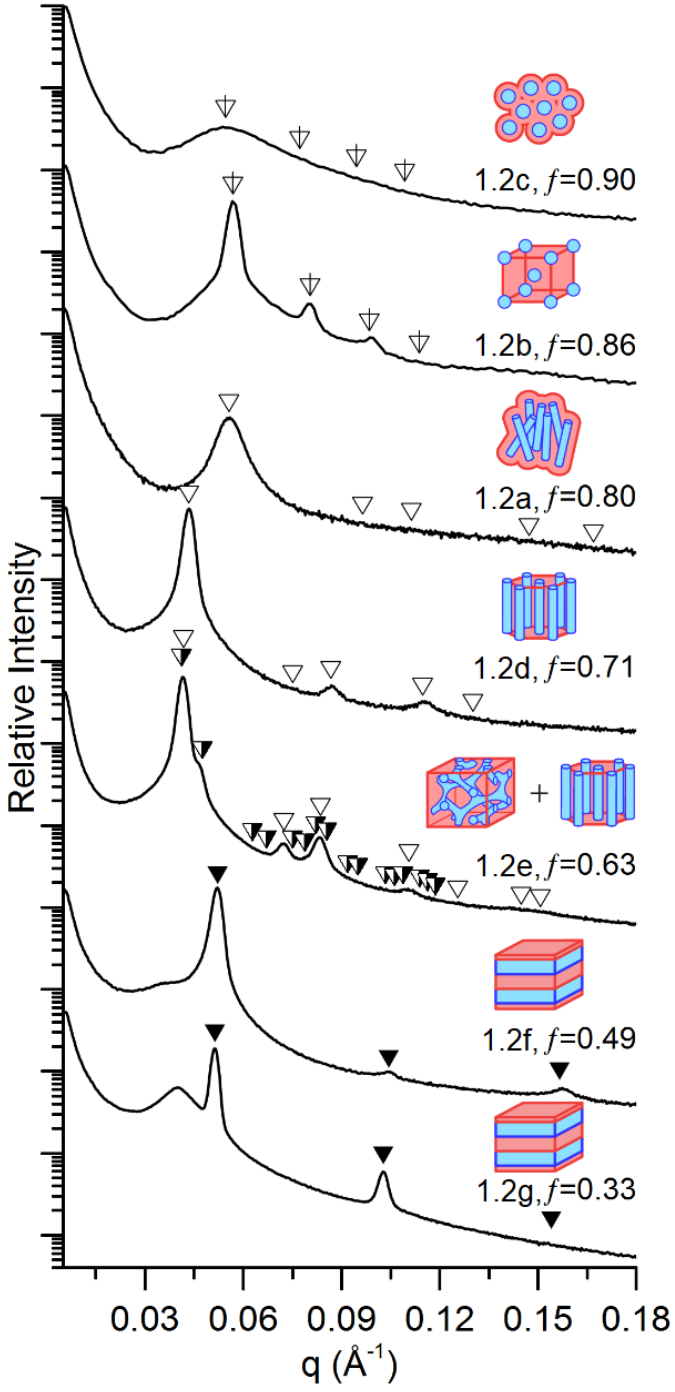

Figure 4.10. Post-annealing, room temperature SAXS profiles for *n*-butyl-substituted PS-*b*-PIL BCPs **1.2a–g**. The allowed reflections for each morphology shown are represented as inverted triangles, including the possible emergence of the Gyr morphology (with expected peak locations

denoted by half-filled triangle symbols above **1.2e** at q/q^* ratios of √6, √8, √14, √16, √20, etc. where q^*, the primary scattering wave vector, is q_{100}). The possible emergence of the Gyr morphology suggests a lower interaction parameter (χ) in the *n*-butyl-substituted PS-*b*-PIL BCPs than that associated with the methyl-substituted PS-*b*-PIL BCPs.

We were unable to observe any structure factor extinction of the even-ordered reflections (such as the elimination of the $q/q^* = \sqrt{4}$ peak in sample **1.1j**) for the series of *n*-butyl-functionalized PIL-BCPs, and therefore unable to estimate the density of the BuPIL block based purely on SAXS evidence. To build a phase diagram using the volume fraction of the BuPIL block then, it was necessary to estimate the PIL block density using some known density values of similar block architectures, namely our density value of 1.06 g cm^{-3} for the MePIL block and Mahanthappa and coworkers' value of 1.096 g cm^{-3} for the HxPIL block.[9] It is reasonable to assume that our PIL block with *n*-butyl functionality would have a density falling between that of the methyl- and *n*-hexyl-functionalized polymers; and therefore, we estimate the block density of the BuPIL at 1.08 g cm^{-3}. This value was used to calculate the f_{PIL} values (listed in Table 4.1) for Figure 4.3.

Even though we were unable to determine a quantitative value for χ, we believe we observe a significant enough shift with *n*-butyl R-group modification such that the Gyr morphology is able to emerge in coexistence with Hex in sample **1.2e** after extended thermal annealing (see Section 4.6.13). This also affirms that χ (and consequently position within the phase diagram) is indeed tunable using the precisely controlled synthetic methods and selection of R groups. In this case, by adding a less polar group (i.e., *n*-butyl) to the end of the PIL repeat unit, we have achieved greater miscibility between the PS and PIL block. This effectively lowers the mixing penalty of

the two blocks, relieving packing frustration within the system, and allowing the complex bicontinuous Gyr morphology to form.[48]

Additionally, we prepared two *n*-propyl-functionalized samples, **1.4a** and **1.4b** (see Table 4.1) which exhibited phase behavior similar to the PS-MePIL series. We also prepared two *n*-hexyl-functionalized samples, **1.5a** and **1.5b** (see Table 4.1) that showed phase separation but no higher-order SAXS reflections. Mahanthappa and co-workers investigated *n*-hexyl functionalized polymers with identical structure that formed ordered nanostructures. However, they had significantly higher MW, and therefore much higher χN values.[9] Those samples were also on the PIL-lean side of the phase diagram (in contrast to the PIL-rich region on which we have focused). These differences make it difficult to glean any morphological insight about samples **1.5a** and **1.5b** from their work. But coupled with the observed shift in χN from the methyl to the *n*-butyl series discussed earlier, it is reasonable to infer that χN is lowered sufficiently in our *n*-hexyl series of polymers that these systems remain only weakly segregated and have difficulty establishing long-range periodic order.

4.4 Summary

We used SAXS data to show that a series of 13 methyl-, 2 *n*-propyl-, 7 *n*-butyl-, and 2 *n*-hexyl- functionalized PIL-BCPs synthesized via direct, sequential ATRP of styrene and styrenic imidazolium IL monomers can form ordered, phase separated nanostructures that encompass the entirety of the classic diblock copolymer phase diagram. These ordered nanostructures, once formed through moderate annealing, were shown to remain well-ordered even upon cooling to room temperature. The ability of these PIL-BCPs to remain ordered at ambient temperature,

coupled with their easy handling, thermally processable nature, and intrinsic ionic conductivity,[9] suggests a potential future in solid-state polymer electrolyte membrane technologies.[1,52]

We were able to observe well-ordered samples forming S_{BCC}, Hex, and Lam morphologies, and notably, one example of a Gyr phase in coexistence with the Hex phase. A Lam-forming sample exhibiting near structure factor extinction of the even-ordered SAXS reflection at a q/q^* ratio of $\sqrt{4}$ provided the means to estimate MePIL block density and consequently volume fraction of the MePIL block. The compilation of these data was used to build two phase diagrams (one for the methyl and one for the *n*-butyl series) detailing their phase behavior with respect to f_{PIL} and temperature. Temperature was used as a proxy for χN, due to a limited means to quantify χ in this study. Regardless, we believe the χN values for the methyl series of PIL BCPs to be substantial based on an observed persistent coexistence of Lam and Hex phases in two separate samples where the Gyr morphology was anticipated. It was also noted that both phase diagrams showed a high degree of conformational asymmetry (ϵ) between the charged and uncharged blocks, likely due to a combination of steric bulk and stiffness associated with highly coordinated Tf_2N^- counter ions in the PIL blocks, in many ways reminiscent of the increased stiffness experienced in "bottle-brush" type polymers.[31]

We also demonstrated the apparent ability to tune χ through modification of pendant alkyl groups on the imidazolium block by showing that the *n*-butyl-functionalized PIL-BCPs are capable of forming complex morphologies that are not present in the more highly segregated methyl-functionalized system. The bicontinuous network present in the Gyr morphology holds significant potential in many research areas that desire an ability to achieve charge transport in systems with domain continuity on the nanometer length scale, including conductive thin films,[53] transport applications,[54] solid-state batteries,[52] and organic photovoltaics[55].

4.5 Acknowledgments

Financial support for the work performed at CSU was provided by the National Science Foundation under grant numbers CBET-1160026 and DMR-1808824. Financial support for the work performed at CU Boulder was provided by the U.S. Dept of Energy ARPA-E program (grants: DE-AR0000343 and DE-AR0000770). The SAXS instrument used in this work is supported by the Central Instrument Facility of the Department of Chemistry at CSU and by the National Science Foundation under grant DMR-0821799.

4.6 Supporting information

4.6.1 Materials and methods

1-Bromopropane, 1-bromohexane, sodium hydride, imidazole, 1-methylimidazole, 1-butylimidazole, 4-vinylbenzyl chloride, 2-(trimethylsilyl)ethanol, α-bromoisobutyryl bromide, triethylamine, copper(I) bromide, butyronitrile, Dowex 50Wx4 ion-exchange resin, benzoyl peroxide, and *N,N,N′,N′,N″*-pentamethyldiethylenetriamine (PMDETA) were all purchased from the Sigma-Aldrich Co., and used as received. Styrene was purchased from the Sigma-Aldrich Co. and purified by passage through a column of neutral alumina to remove the added radical inhibitor. Lithium bis(trifluoromethylsulfonyl)amide ($LiTf_2N$) was purchased as Fluorad™ Lithium Trifluoromethane Sulfonimide from the 3M Company. All solvents were purchased from Sigma-Aldrich or Mallinckrodt, Inc. and purified/dehydrated via N_2-pressurized activated alumina columns, and de-gassed. The H_2O used for synthesis was purified and deionized, with resistivity greater than 12 MΩ/cm. All polymerizations were carried out in a dry Ar atmosphere using standard Schlenk line techniques.

4.6.2 Instrumentation

^{1}H and ^{13}C NMR spectra were obtained using a Bruker 300 Ultrashield™ (300 MHz for ^{1}H) spectrometer. Chemical shifts are reported in ppm relative to residual non-deuterated solvent. HRMS (ES) analysis was performed by the Central Analytical Facility in the Dept. of Chemistry and Biochemistry at the University of Colorado, Boulder. Gel permeation chromatography (GPC) was performed using a Viscotek GPC-Max chromatography system outfitted with three 7.5 x 340 mm Polypore™ (Polymer Laboratories) columns in series, a Viscotek differential refractive index (RI) detector, and an Alltech column oven (mobile phase THF, 40 °C, 1 mL min^{-1} flow rate). Molecular weight data obtained on this GPC system were referenced to polystyrene molecular weight standards. SAXS data were collected using a Rigaku SMax3000 High Brilliance three-pinhole SAXS system outfitted with a MicroMax-007HFM rotating anode (Cu K_{α}), a Confocal Max-Flux Optic, a Gabriel-type multi-wire area detector, and a Linkam thermal stage. Differential scanning calorimetry (DSC) measurements were performed using a TA Instruments DSC 2500 with an RCS90 cooling system.

4.6.3 Synthesis of 1-propylimidazole

Synthesized as previously reported.[56] Characterization data matched those reported.[56]

4.6.4 Synthesis of 1-hexylimidazole

Synthesized as previously reported.[56] Characterization data matched those reported.[56]

4.6.5 Synthesis of 1-(4-vinylbenzyl)-3-alkylimidazolium bis(trifluoromethylsulfonyl)amide monomers (2)

These compounds were synthesized using the procedures previously reported.[13] The characterization data of monomers **2** matched those reported.[13,57,58]

4.6.6 Synthesis of 2-(Trimethylsilyl)ethyl 2-bromo-2-methylpropanoate (TMS-EBMP)

Synthesized as previously reported.[27] Characterization data matched those reported.[27]

4.6.7 Synthesis of polystyrene macro-initiators 3

These compounds were synthesized using the procedures previously reported.[13] In a typical procedure, the desired amount of purified styrene and PMDETA were added to a flame-dried Schlenk flask and degassed by three freeze-pump-thaw cycles. The flask was warmed to room temperature and back-filled with Ar, the desired amount of CuBr was then added. The resulting mixture was stirred at room temperature for 30 min, and TMS-EBMP was then injected. The flask was then stirred at 90 °C for 22 h. The contents of the flask were cooled to room temperature, dissolved in acetone, stirred with Dowex 50Wx4 ion-exchange resin for 30 min, and filtered through a short plug of neutral alumina. The resulting solution was then concentrated, diluted with Et_2O, precipitated by adding into MeOH, and filtered to give the desired PS macro-initiator **3** as a white solid. The DP and M_n values of BCPs **3** were calculated based on the ^{1}H NMR end-group analysis (see Section 4.6.11).

4.6.8 Synthesis of PS-PIL BCPs 1

These compounds were synthesized using the procedures previously reported.[13] In a typical procedure, the appropriate amount of the desired imidazolium monomer **2**, PMDETA, and butyronitrile were added to a flame-dried Schlenk flask and degassed by three freeze-pump-thaw cycles. The flask was warmed to room temperature and back-filled with Ar, the appropriate amount of CuBr was then added. The resulting mixture was then stirred at room temperature for 30 min, and the appropriate amount of the desired PS macro-initiator **3** was added. The flask was then stirred at 90 °C for 24 h. The contents of the flask were cooled to room temperature, diluted with acetone, stirred with Dowex 50Wx4 ion-exchange resin for 15 min, and then filtered through a short plug of neutral alumina. The resulting solution was then concentrated, diluted with acetone, precipitated by adding into a MeOH/H_2O (3/1 (v/v)) mixture, and filtered. The resulting precipitate was then dissolved in acetone, re-precipitated by adding into hexanes, and filtered to give the desired BCP **1** as a white solid. The synthesis of **1.1j** is shown below as a representative example. The block compositions and M_n values of PS-*b*-PIL BCPs **1** were calculated based on the ^{1}H NMR analysis (see Section 4.6.12).

4.6.9 Example: Synthesis of PS-*b*-PIL BCP 1.1j

1-(4-Vinylbenzyl)-3-methylimidazolium bis(trifluoromethylsulfonyl)amide (303 mg, 0.632 mmol), PMDETA (31.3 mg, 0.181 mmol), and butyronitrile (1.70 mL) were added to a flame-dried Schlenk flask and degassed by three freeze-pump-thaw cycles. The flask was warmed to room temperature and back-filled with Ar, CuBr (25.9 mg, 0.181 mmol) was added. The resulting mixture was stirred at room temperature for 30 min, and macroinitiator **3** (n = 40, 200

mg, 0.0451 mmol) was added. The flask was then stirred at 90 °C for 24 h. The resulting reaction mixture was purified as described in the general procedure above to give **1.1j** as a white solid (yield: 0.342 g, 82%). Block repeat unit molar ratio = 4:1 (PS:PIL); block length composition = 40-*b*-10 (PS-*b*-PIL); M_n = 9,227 ≅ 9200 g/mol (calculated based on ^{1}H NMR analysis, see Section 4.6.12).

4.6.10 Small-angle X-ray scattering (SAXS)

SAXS data were collected using a Rigaku S-Max 3000 High Brilliance three-pinhole SAXS system outfitted with a MicroMax-007HFM rotating anode (Cu K_α, λ = 1.54 Å), sample-to-detector distance of 2.19 m, Confocal Max-Flux Optics, Gabriel multiwire area detector (1024 × 1024 pixel resolution), and a Linkam thermal stage. Copolymer samples were sandwiched between Kapton windows (0.06 mm thick × 10 mm diameter). Before collection of temperature-dependent SAXS data, the sample stage temperature was equilibrated for 5 min under vacuum, unless otherwise stated. Data were collected under vacuum (~100 mtorr) with exposure times ranging from 60 to 3600 s for all samples. SAXS data were azimuthally integrated from the 2D detector patterns and plotted as logarithmic intensity vs. the scattering wave vector, q, defined as $q = (4\pi/\lambda) \sin(2\theta_B/2)$, where $2\theta_B$ is the angle between the incident and scattered waves.

4.6.11 Determination of the DP and M_n values of the series of PS macro-initiators 3

Table 4.S1. DP, M_n, and PDI values of the PS macro-initiators **3**. The M_n values are rounded down to nearest hundred g/mol.

BCP	DP	M_n (g/mol)	PDI
3a	15	1,800	1.15
3b	20	2,400	1.10
3c	25	2,900	1.12
3d	30	3,400	1.08
3e	34	3,800	1.12
3f	36	4,000	1.13
3g	37	4,100	1.13
3h	40	4,400	1.11
3i	45	5,000	1.13

The PS macro-initiators **3a–i** were synthesized using the procedures previously reported.[13] The DP and M_n values of the synthesized PS macro-initiators **3a–i** were calculated based on the ^{1}H NMR peak integral of protons (*D*) on the TMS end-group relative to that of the protons (*E*) on

the benzene ring for these polymers (Eqs. 4.1 and 4.2).[13] See Figure 4.S1 below for example data used to calculate these values for **3h**.

$$\mathrm{DP} = \frac{\mathrm{E}_{1\mathrm{H\ NMR\ Integration}} \times 9}{\mathrm{D}_{1\mathrm{H\ NMR\ Integration}} \times 5} \qquad \text{(Eq. 4.1)}$$

$$M_{\mathrm{n}} = (\mathrm{DP} \times M_{\mathrm{monomer}}) + M_{\mathrm{TMS\text{-}EBMP}} \qquad \text{(Eq. 4.2)}$$

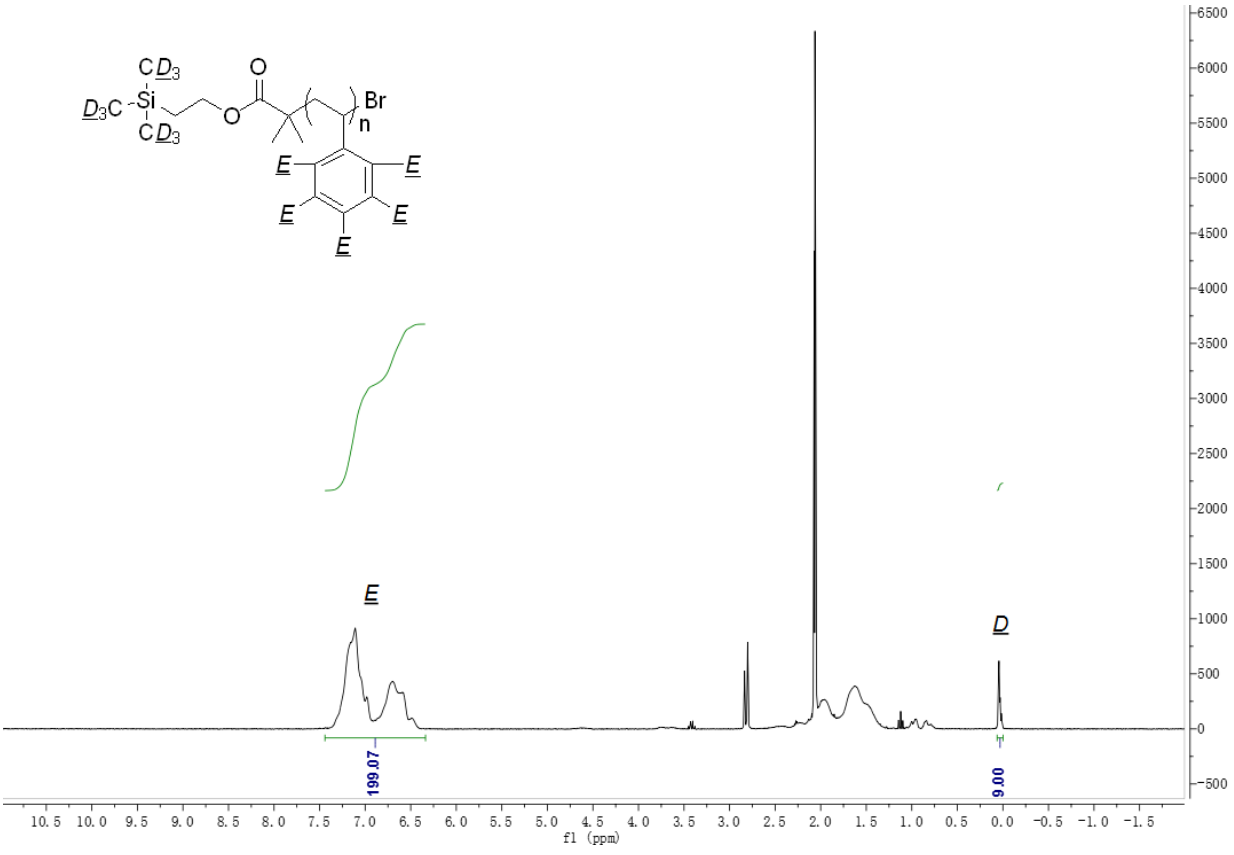

Figure 4.S1. Example ^{1}H NMR spectrum of **3h**, and the ^{1}H NMR peak assignments used for calculating the DP and M_{n} value. Calculated DP = 39.8 ≅ 40, M_{n} = 4,433 ≅ 4,400 g/mol.

4.6.12 Determination of the block composition ratio and M_n values of the series of PS-*b*-PIL BCPs 1

Table 4.S2. Block composition ratios and M_n values of PS-*b*-PIL BCPs **1**. The M_n values are rounded down to nearest hundred g/mol.

BCP	n	m	M_n (g/mol)
1.1c	15	35	18,600
1.1b	20	30	16,700
1.1a	25	25	14,900
1.1d	30	18	12,000
1.1e	34	15	11,000
1.1f	36	14	10,800
1.1g	37	13	10,400
1.1h	40	12	10,200
1.1i	34	10	8,600
1.1j	40	10	9,200
1.1k	40	9	8,700
1.1l	40	8	8,300

1.1m	45	5	7,400
1.2c	15	35	20,100
1.2b	20	30	18,000
1.2a	25	25	15,900
1.2d	30	18	12,800
1.2e	34	14	11,100
1.2f	40	9	9,100
1.2g	45	5	7,600
1.4a	35	15	11,500
1.4b	40	10	9,500
1.5a	20	30	18,800
1.5b	25	25	16,600

The block composition ratios and M_n values of PS-*b*-PIL BCPs **1** were determined via ^{1}H NMR analysis.[13] See Figure 4.S2 for an example spectrum and ^{1}H NMR peaks assignments used for these calculations. The PS:PIL ratio can be calculated by Eq. 4.3. The length of PIL block can be calculated by Eq. 4.4 and confirmed by end-group analysis (Eq. 4.5). The M_n of PS-*b*-PIL BCPs can be calculated by Eq. 4.6.

$$\text{PS:PIL ratio} = \frac{[F_{1H\ NMR\ Integration} - (6 \times B_{1H\ NMR\ Integration})]}{B_{1H\ NMR\ Integration} \times 5} \quad \text{(Eq. 4.3)}$$

$$\text{PS block length m} = \frac{n}{\text{Styrene:imidazolium} - \text{styrene ratio}} \quad \text{(Eq. 4.4)}$$

$$\text{PIL length m} = \frac{B_{1H\ NMR\ Integration} \times 9}{D_{1H\ NMR\ Integration}} \quad \text{(Eq. 4.5)}$$

$$M_n = (n \times M_{styrene}) + (m \times M_{monomer\ 2}) + M_{TMS\text{-}EBMP} \quad \text{(Eq. 4.6)}$$

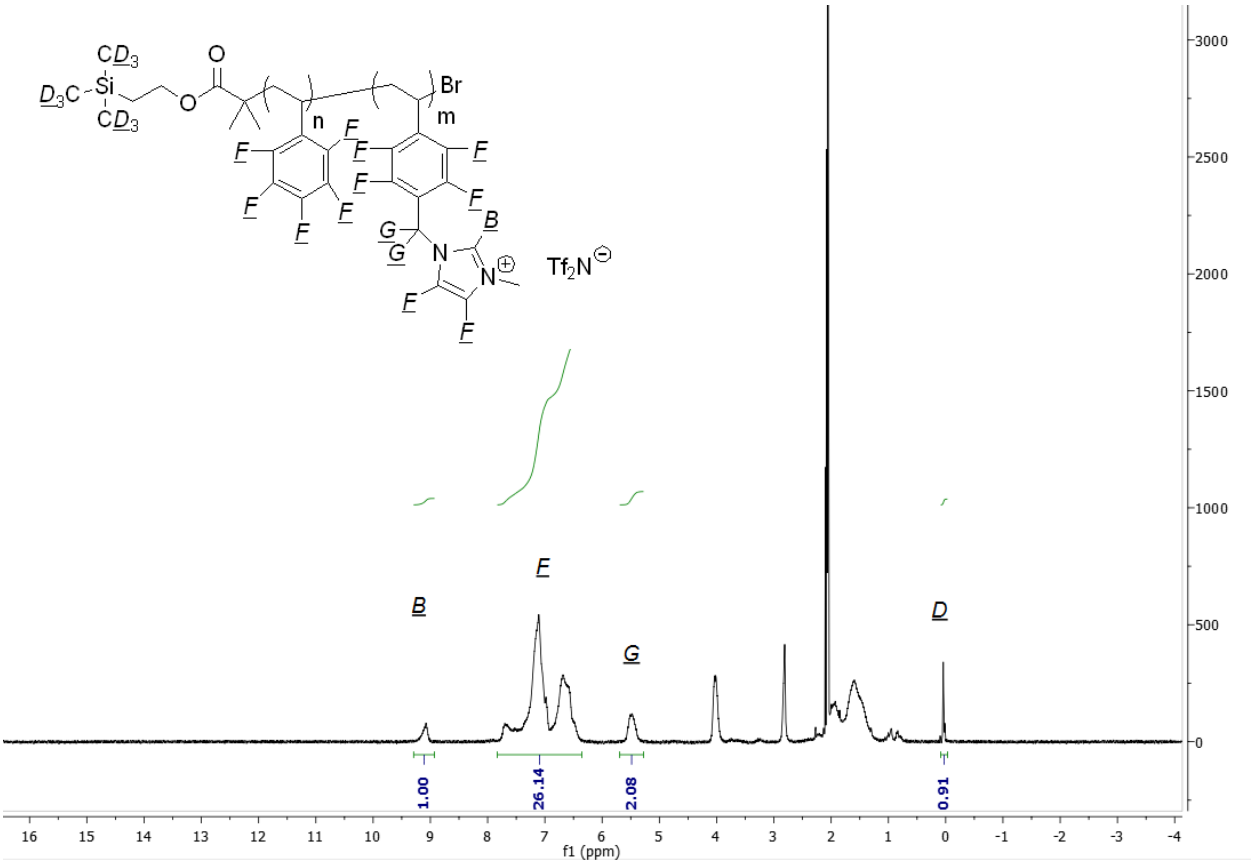

Figure 4.S2. Example ^{1}H NMR spectrum of PS-*b*-PIL BCP **1.1j**, and the ^{1}H NMR peak assignments used for calculating the block composition ratio and M_n value. The calculated PS:PIL is 4.02, m = 9.93 ≅ 10, M_n = 9,227 ≅ 9,200 g/mol.

4.6.13 Extended thermal annealing of PS-b-PIL BCP 1.2e

The SAXS profile for BCP **1.2e** with extended thermal annealing is shown is Figure 4.S3. The Gyr morphology is able to emerge in coexistence with Hex with *n*-butyl R-group modification.

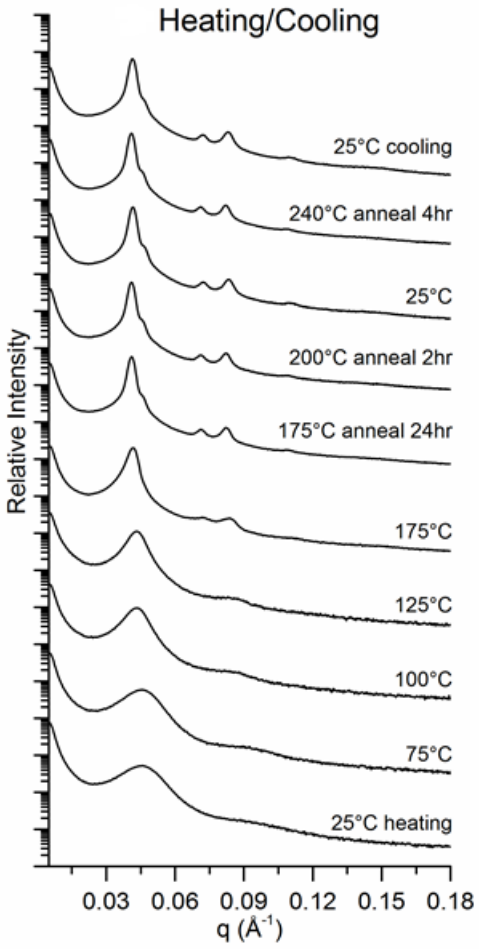

Figure 4.S3. SAXS profile for the extended thermal annealing of BCP **1.2e**.

4.6.14 Differential scanning calorimetry (DSC)

DSC was run on three PS-*b*-PIL BCPs (**1.1d**, **1.1g**, and **1.1k**) as representative samples using a heat-cool-heat-cool method at 10 °C min^{-1} from −40 °C to 180 °C. Weak transitions around 37 °C and 85 °C were observed for these three BCP samples.

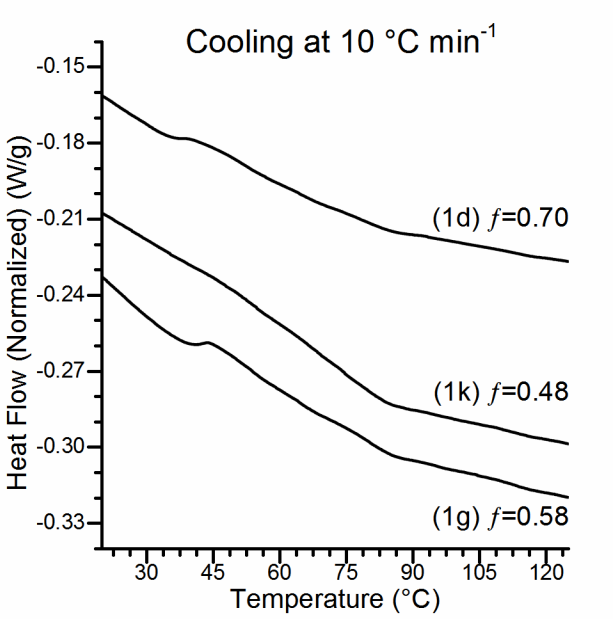

Figure 4.S4. Differential scanning calorimetry data for samples **1.1d**, **1.1g**, and **1.1k.**

4.7 References

(1) Meek, K. M.; Elabd, Y. A. *J. Mater. Chem. A* **2015**, *3*, 24187−24194.

(2) Osada, I.; de Vries, H.; Scrosati, B.; Passerini, S. *Angew. Chem. Int. Ed.* **2016**, *55*, 500−513.

(3) Wijayasekara, D. B.; Cowan, M. G.; Lewis, J. T.; Gin, D. L.; Noble, R. D.; Bailey, T. S. *J. Membr. Sci.* **2016**, *511*, 170−179.

(4) Nishimura, N.; Ohno, H. *Polymer* **2014**, *55*, 3289−3297.

(5) Mecerreyes, D. *Prog. Polym. Sci.* **2011**, *36*, 1629−1648.

(6) Yuan, J.; Mecerreyes, D.; Antonietti, M. *Prog. Polym. Sci.* **2013**, *38*, 1009−1036.

(7) Sudre, G.; Inceoglu, S.; Cotanda, P.; Balsara, N. P. *Macromolecules* **2013**, *46*, 1519−1527.

(8) He, H.; Luebke, D.; Nulwala, H.; Matyjaszewski, K. *Macromolecules* **2014**, *47*, 6601−6609.

(9) Weber, R. L.; Ye, Y.; Schmitt, A. L.; Banik, S. M.; Elabd, Y. A.; Mahanthappa, M. K. *Macromolecules* **2011**, *44*, 5727−5735.

(10) Stancik, C. M.; Lavoie, A. R.; Schütz, J.; Achurra, P. A.; Lindner, P.; Gast, A. P.; Waymouth, R. M. *Langmuir* **2004**, *20*, 596−605.

(11) Shi, Z.; May, A. W.; Kohno, Y.; Bailey, T. S.; Gin, D. L. *J. Polym. Sci. A Polym. Chem.* **2017**, *55*, 2961−2965.

(12) Agudelo, N. A.; Elsen, A. M.; He, H.; López, B. L.; Matyjaszewski, K. *J. Polym. Sci. A Polym. Chem.* **2015**, *53*, 228−238.

(13) Shi, Z.; Newell, B. S.; Bailey, T. S.; Gin, D. L. *Polymer* **2014**, *55*, 6664−6671.

(14) Scalfani, V. F.; Wiesenauer, E. F.; Ekblad, J. R.; Edwards, J. P.; Gin, D. L.; Bailey, T. S. *Macromolecules* **2012**, *45*, 4262−4276.

(15) Drzal, P. L.; Halasa, A. F.; Kofinas, P. *Polymer* **2000**, *41*, 4671−4677.

(16) Nguyen, P. T.; Wiesenauer, E. F.; Gin, D. L.; Noble, R. D. *J. Memb. Sci.* **2013**, *430*, 312−320.

(17) Wiesenauer, E. F.; Edwards, J. P.; Scalfani, V. F.; Bailey, T. S.; Gin, D. L. *Macromolecules* **2011**, *44*, 5075−5078.

(18) Bailey, T. S.; Hardy, C. M.; Epps, T. H.; Bates, F. S. *Macromolecules* **2002**, *35*, 7007−7017.

(19) Epps, T. H.; Cochran, E. W.; Bailey, T. S.; Waletzko, R. S.; Hardy, C. M.; Bates, F. S. *Macromolecules* **2004**, *37*, 8325−8341.

(20) Wiesenauer, E. F.; Nguyen, P. T.; Newell, B. S.; Bailey, T. S.; Noble, R. D.; Gin, D. L. *Soft Matter* **2013**, *9*, 7923−7927.

(21) Lee, S.; Bluemle, M. J.; Bates, F. S. *Science* **2010**, *330*, 349−353.

(22) Epps, T. H.; Bailey, T. S.; Waletzko, R.; Bates, F. S. *Macromolecules* **2003**, *36*, 2873−2881.

(23) Wijayasekara, D. B.; Huang, T.; Richardson, J. M.; Knauss, D. M.; Bailey, T. S. *Macromolecules* **2016**, *49*, 595−608.

(24) Fan, W.; Wang, L.; Zheng, S. *Macromolecules* **2009**, *42*, 327−336.

(25) Hajduk, D. A.; Harper, P. E.; Gruner, S. M.; Honeker, C. C.; Kim, G.; Thomas, E. L.; *Macromolecules* **1994**, *27*, 4063−4075.

(26) Oh, J.; Kuk, J.; Lee, T.; Ye, J.; Paik, H.-J.; Lee, H. W.; Chang, T. *ACS Macro Lett.* **2017**, *6*, 758−761.

(27) He, H.; Zhong, M.; Adzima, B.; Luebke, D.; Nulwala, H.; Matyjaszewski, K. *J. Am. Chem. Soc.* **2013**, *135*, 4227−4230.

(28) Matsen, M. W.; Bates, F. S. *J. Polym. Sci. B Polym. Phys.* **1997**, *35*, 945−952.

(29) Hajduk, D. A.; Takenouchi, H.; Hillmyer, M. A.; Bates, F. S.; Vigild, M. E.; Almdal, K. *Macromolecules* **1997**, *30*, 3788−3795.

(30) Bates, F. S. *Science* **1991**, *251*, 898−905.

(31) Hamley, I. W.; O'Driscoll, B. M. D.; Lotze, G.; Moulton, C.; Allgaier, J.; Frielinghaus, H. *Macromol. Rapid Commun.* **2009**, *30*, 2141−2146.

(32) Bates, F. S.; Schulz, M. F.; Khandpur, A. K.; Förster, S.; Rosedale, J. H.; Almdal, K.; Mortensen, K. *Faraday Discuss.* **1994**, *98*, 7−18.

(33) Bates, F. S.; Fredrickson, G. H. *Phys. Today* **1999**, *52*, 32−38.

(34) Davidock, D. A.; Hillmyer, M. A.; Lodge, T. P. *Macromolecules* **2003**, *36*, 4682−4685.

(35) Hajduk, D. A.; Gruner, S. M.; Rangarajan, P.; Register, R. A.; Fetters, L. J.; Honeker, C.; Albalak, R. J.; Thomas, E. L. *Macromolecules* **1994**, *27*, 490−501.

(36) Chu, J. H.; Rangarajan, P.; Adams, J. L.; Register, R. A. *Polymer* **1995**, *36*, 1569−1575.

(37) Förster, S.; Timmann, A.; Konrad, M.; Schellbach, C.; Meyer, A.; Funari, S. S.; Mulvaney, P.; Knott, R. *J. Phys. Chem. B* **2005**, *109*, 1347−1360.

(38) Matsushita, Y.; Mori, K.; Saguchi, R.; Nakao, Y.; Noda, I.; Nagasawaid, M. *Macromolecules* **1990**, *23*, 4313−4316.

(39) Fetters, L. J.; Lohse, D. J.; Richter, D.; Witten, T. A.; Zirkel, A. *Macromolecules* **1994**, *27*, 4639−4647.

(40) Floudas, G.; Vazaiou, B.; Schipper, F.; Ulrich, R.; Wiesner, U.; Iatrou, H.; Hadjichristidis, N. *Macromolecules* **2001**, *34*, 2947−2957.

(41) Lipic, P. M.; Bates, F. S.; Matsen, M. W. *J. Polym. Sci. B Polym. Phys.* **1999**, *37*, 2229−2238.

(42) Matsen, M. W. *Phys. Rev. Lett.* **2007**, *99*, 148304-1−148304-4.

(43) Matsen, M. W.; Bates, F. S. *Macromolecules* **1996**, *29*, 7641−7644.

(44) Matsen, M. W.; Bates, F. S. *J. Chem. Phys.* **1997**, *106*, 2436−2448.

(45) Matsen, M. W. *J. Phys. Condens. Matter* **2002**, *14*, R21−R47.

(46) Cochran, E. W.; Garcia-Cervera, C. J.; Fredrickson, G. H. *Macromolecules* **2006**, *39*, 2449−2451.

(47) Widin, J. M.; Kim, M.; Schmitt, A. K.; Han, E.; Gopalan, P.; Mahanthappa, M. K. *Macromolecules* **2013**, *46*, 4472−4480.

(48) Lynd, N. A.; Hillmyer, M. A. *Macromolecules* **2005**, *38*, 8803−8810.

(49) Bendejacq, D.; Ponsinet, V.; Joanicot, M.; Loo, Y. L.; Register, R. A. *Macromolecules* **2002**, *35*, 6645−6649.

(50) Guo, C.; Bailey, T. S. *Soft Matter* **2010**, *6*, 4807−4818.

(51) Kinning, D. J.; Thomas, E. L. *Macromolecules* **1984**, *17*, 1712−1718.

(52) Zekoll, S.; Marriner-Edwards, C.; Hekselman, A. K. O.; Kasemchainan, J.; Kuss, C.; Armstrong, D. E. J.; Cai, D.; Wallace, R. J.; Richter, F. H.; Thijssen, J. H. J.; Bruce, P. G. *Energy Environ. Sci.* **2018**, *11*, 185−201.

(53) Ryu, I. H.; Kim, Y. J.; Jung, Y. S.; Lim, J. S.; Ross, C. A.; Son, J. G. *ACS Appl. Mater. Interfaces* **2017**, *9*, 17427−17434.

(54) Li, L.; Schulte, L.; Clausen, L. D.; Hansen, K. M.; Jonsson, G. E.; Ndoni, S. *ACS Nano* **2011**, *5*, 7754−7766.

(55) Crossland, E. J. W.; Nedelcu, M.; Ducati, C.; Ludwigs, S.; Hillmyer, M. A.; Steiner, U.; Snaith, H. J. *Nano Lett.* **2009**, *9*, 2813−2819.

(56) Serpell, C. J.; Cookson, J.; Thompson, A. L.; Brown, C. M.; Beer, P. D. *Dalton Trans.* **2013**, *42*, 1385−1393.

(57) Bara, J. E.; Hatakeyama, E. S.; Gin, D. L.; Noble, R. D. *Polym. Adv. Technol.* **2008**, *19*, 1415−1420.

(58) Bara, J. E.; Lessmann, S.; Gabriel, C. J.; Hatakeyama, E. S.; Noble, R. D.; Gin, D. L. *Ind. Eng. Chem. Res.* **2007**, *46*, 5397−5404.

CHAPTER 5

Metal-Containing Ionic Liquid-Based, Uncharged-Charged Diblock Copolymers that Form Ordered, Phase-Separated Microstructures and Reversibly Coordinate Small Protic Molecules

(Adapted from the manuscript published under the same title in *J. Polym. Sci. A: Polym. Chem.* **2017**, *55*, 2961−2965, co-authored with May, A. W.; Kohno, Y.; Bailey, T. S.; Gin, D. L.)

5.1 Abstract

A series of metal-containing ionic liquid-based, uncharged-charged block copolymers (BCPs) with total repeat units of 70 was synthesized via reversible addition-fragmentation chain-transfer polymerization. Small-angle X-ray scattering studies show these Co(II) bis(salicylate) anion-containing BCPs can form ordered microstructures (including a gyroid phase) in their neat states. Additionally, these BCPs can reversibly coordinate H_2O or small alcohols with a noticeable color change.

5.2 Introduction

Polymerized ionic liquids (PILs) are intrinsically charged polymers prepared from or structurally related to ionic liquids (ILs, i.e., molten salts at ≤100 °C and ambient pressure).[1,2] Since PILs have the combined properties of polymer architectures and many of the desired properties of ILs (e.g., negligible vapor pressure, ion conductivity, high solubility for certain light

gases), PILs have been used as functional materials for many applications such as responsive materials, gas separation membranes, solid-state ion conductors, etc.[1,2]

IL-based block copolymers (BCPs) are a distinct and relatively new class of BCPs that contain at least one PIL segment.[2] By combining the unique properties of PILs with the ability of BCPs to phase-separate into ordered microstructures, IL-based BCPs have shown promise as new functional materials as carbonaceous materials, electrolytes for supercapacitors, binders for lithium ion batteries, recyclable organic catalysts, etc.[2] Over the past few years, a variety of IL-based BCPs have been prepared by either sequential controlled/living polymerization of an IL monomer and an uncharged co-monomer; or by post-polymerization functionalization of uncharged BCPs containing reactive repeat units to generate charged moieties on the polymer.[2] Although many IL-based BCPs have been studied as functional materials,[2] only a small subset of them has been reported to form ordered, phase-separated nanostructures in the solvent-free melt state.[3]

One recent method for introducing new functional properties into ILs has been to incorporate a metal complex in the IL. These metal-containing ILs (MCILs) are a relative new class of functional ILs with metal-based magnetic,[4] optical,[4,5] catalytic,[4,6] or molecular binding properties.[4,7] Consequently, MCIL-based BCPs (MCIL-BCPs) with such properties and the ability to form ordered microstructures would be desirable as new functional materials. However, before this work, MCIL-based PIL homopolymers are rare,[8] and MCIL-BCPs are unprecedented to our knowledge. The closest reported materials with charged blocks are metallocene-based BCPs that are not true IL-based BCPs.[9] These BCPs were made by copolymerizing uncharged monomers and charged metal-containing monomers that are not molten salts and do not have typical IL structures.[9]

Herein, we present the first example of a MCIL-based, noncharged-charged BCP platform (**4**) that exhibits ordered, phase-separated microstructures in the neat state and can reversibly coordinate protic small molecules with an accompanying color change. This MCIL-BCP system was made by reversible addition-fragmentation chain-transfer (RAFT) polymerization of first butyl methacrylate to form uncharged poly(butyl methacrylate) (PBMA) macro-chain-transfer agents (macroCTAs) of controlled length (**5**), and then co-polymerization of a styrenic phosphonium IL monomer with a cobalt(II) bis(salicylate) anion (**6**) (Figure 5.1). Short MCIL-BCPs of this system (**4a–f**) ranging from 35-*b*-35 to 60-*b*-10 (noncharged-*b*-charged block ratios) show a range of ordered nanostructures (i.e., weakly ordered spheres (S), lamellar (Lam), columnar hexagonal (Hex), and gyroid (Gyr)) by small-angle X-ray scattering (SAXS) after annealing in their neat states. These MCIL-BCPs were also found to reversibly coordinate to the vapor of protic small molecules (e.g., H_2O and small alcohols) with a noticeable color change. This combination of properties makes this new BCP platform unique and potentially useful for applications development.

5.3 Results and discussion

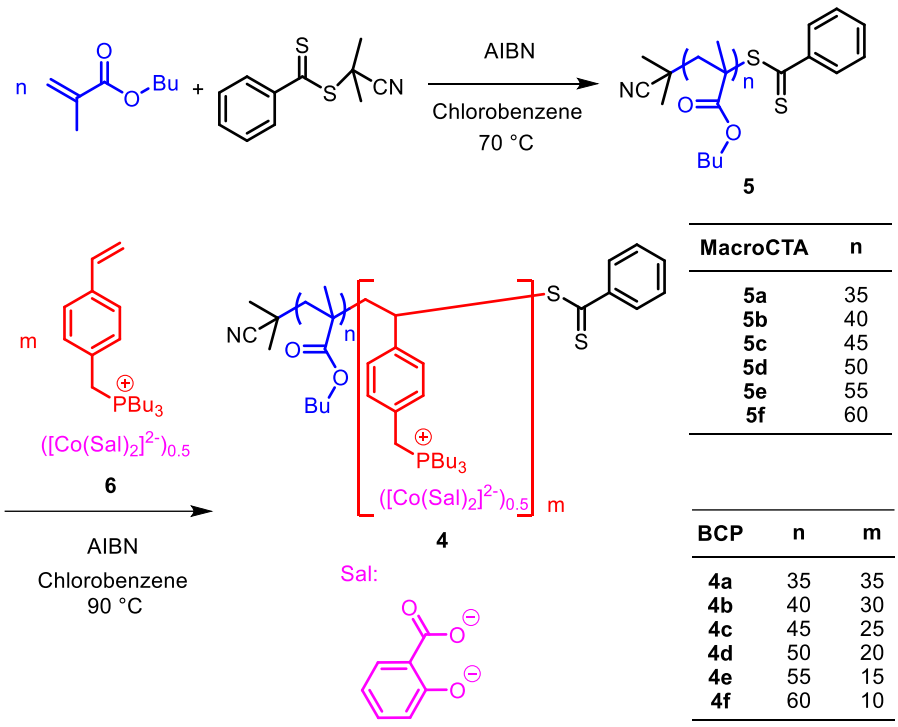

MacroCTA	n
5a	35
5b	40
5c	45
5d	50
5e	55
5f	60

BCP	n	m
4a	35	35
4b	40	30
4c	45	25
4d	50	20
4e	55	15
4f	60	10

Figure 5.1. Synthesis and structures of the MCIL-BCPs **4a–f** in this study.

As shown in Figure 5.1, MCIL-BCPs **4a–f** were synthesized via sequential RAFT polymerization of butyl methacrylate and MCIL monomer **6** using 2-cyano-2-propyl benzodithioate (CPBD) as the chain-transfer agent, azobis(isobutyronitrile) (AIBN) as the radical initiator, and chlorobenzene as the polymerization solvent (see Section 5.6.7 for details). MCIL monomer **6** is a new compound that was synthesized using a procedure based on one previously reported by our group.[7] In our sequential RAFT copolymerization, reactive PBMA blocks **5** with controlled lengths and low PDI values were first synthesized and then used as RAFT macroCTAs to attach the subsequent poly(MCIL) block via addition of the appropriate amount of monomer **6**. This polymerization sequence was chosen because BCPs made via RAFT are typically synthesized

by polymerizing the monomer with the better propagating radical leaving group (i.e., arylates) first.[10] RAFT polymerizations of methacrylates and styrenic monomers are well established in literature,[11] but RAFT polymerization of monomers containing a Co(II) bis(salicylate) anion complex is unprecedented. Consequently, kinetics studies of the copolymerization of butyl methacrylate and **6** were performed to confirm controlled polymerization (see Section 5.6.9).

The absolute lengths and block composition ratios of MCIL-BCPs **4a–f** were confirmed by ^{1}H NMR analysis: The block lengths of the PBMA macroCTAs **5a–f** were determined by ^{1}H NMR end-group analysis using the aromatic protons on the CPBD as an integration reference.[12] The PBMA:poly(MCIL) block ratios for each BCP were determined by integrating and comparing distinct ^{1}H NMR signals indicative of each block. The poly(MCIL) block lengths were then calculated based on the PBMA block lengths and the block composition ratios.[12] These results were further confirmed by monitoring the degree of conversion and monomer-to-initiator ratios. Then, the absolute M_n values for **4a–f** were calculated by multiplying the absolute block lengths (from ^{1}H NMR spectroscopy) by the molecular weights (MWs) of the repeat units (see Section 5.6.8 for details).

Unfortunately, GPC[13] and other conventional polymer MW determination techniques could not be used to confirm the MW, PDI, or blocky structure of **4a–f** because of the unusual solubility and other physical properties of these noncharged-charged MCIL-BCPs.[3h] Instead, a combination of alternative methods (i.e., surfactant behavior and solubility analysis, diffusion-ordered NMR spectroscopy, SAXS studies) was used to verify the block architectures of **4a–f** and differentiate their behavior from that of a physical blend of PBMA and poly(**6**) homopolymers, as described previously for characterizing IL-based BCPs[3h] (see Section 5.6.10).

SAXS was particularly effective in demonstrating the block connectivity, as well as the MW and composition control, afforded by the CPBD chain-transfer agent. As depicted in Figure 5.2 and summarized in Table 5.1, precise control of the relative sizes of each block in **4a–f** permitted synthesis of a series of macromolecules collectively displaying characteristics representative of each of the classic BCP morphologies (Lam, Gyr, Hex, and a weakly-ordered sphere phase (S)). Notably, sample **4d** may be the very first example of an IL-based BCP exhibiting the Gyr phase. In previous investigations of imidazolium-based IL-BCPs based on styrenic[3f,3g] and norbornene[3h,3i] monomer derivatives, the Gyr phase was noticeably absent, with systems preferring to produce (presumably metastable but persistent) regions of Lam/Hex coexistence. MCIL-BCP **4d** exhibited behavior prototypical of many non-ionic BCPs, quickly transitioning from a metastable Hex phase to a persistent Gyr phase with minimal thermal annealing.[14–16] SAXS data for **4a–f** as a function of temperature during heating, annealing, and cooling are provided in Section 5.6.13.

Table 5.1. Morphological characteristics of MCIL-BCPs **4a–f**.

BCP	*n*	*m*	d* / {*hkl*}* (nm)	Morphology	Observed q*/q_{100}
4a	35	35	14.8 / {110}	(S)	weakly-ordered spheres
4b	40	30	14.8 / {100}	Hex	√1, (√3), √4, √7
4c	45	25	14.2 / {100}	Hex	√1, √3, √4, √7
4d	50	20	14.4 / {211}	Gyr (Hex)	√6, √8, √14, √16, (√20), √22, √24, √26)
4e	55	15	13.5 / {100}	Lam	√1, √4, √9
4f	60	10	12.8 / {100}	Lam	√1, √4, (√9)

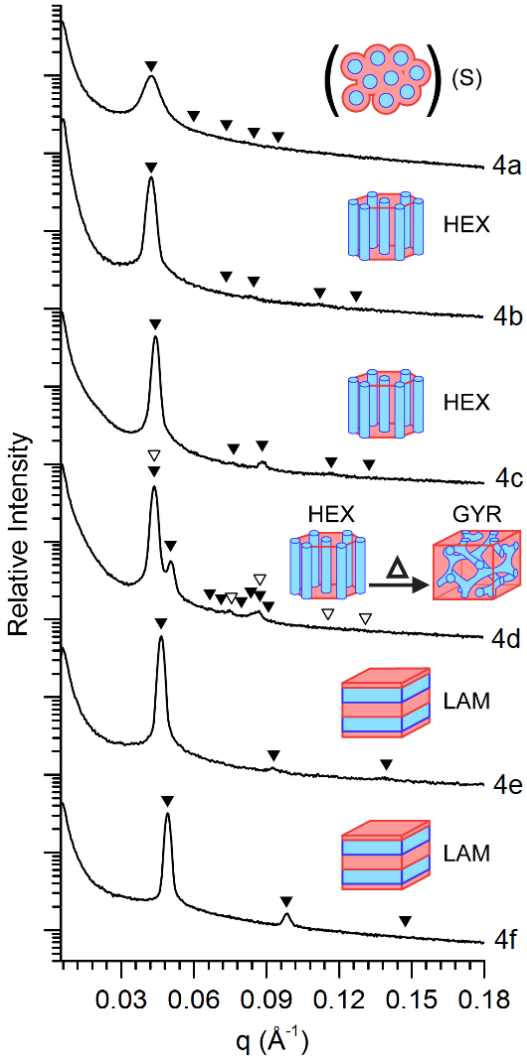

Figure 5.2 SAXS patterns (175 ˚C) for MCIL-BCPs **4a–f** after annealing for 2 h. Inverted triangles designate the expected reflection locations for the indicated morphologies based on the position of q^*.

Notably, the sequence of morphologies and their compositional distribution with respect to volume fraction in IL-BCPs has proven to mimic that of traditional uncharged BCP systems.[3] However, one unique trait exhibited by these charged MCIL-BCPs and shared with the previously

studied styrenic-[3f,3g] and norbornene-[3h,3i] based PIL-BCP systems is a clear disparity in repeat unit volumes and its role in determining the selection of morphology. The data in Table 5.1 reveal that even at noncharged-to-charged repeat unit ratios as high as 60:10 (**4f**), the relative volumes occupied by each block are likely similar, promoting the adoption of a Lam phase. As this ratio decreases toward unity (**4a**), the charged block continues to occupy greater fractions of the overall BCP volume, and the adopted phases follow the prototypical path toward morphologies with increasing average mean curvature.[17] Under that observation, we suspect that **4a**, for which no higher order reflections are observed, is likely adopting a weakly-ordered sphere or micelle-like phase. Such phases tend to persist at the edges of the phase diagram, with the evolution of a more ordered lattice often constrained kinetically.[3i,18] Finally, it is notable that these MCIL-BCPs are able to adopt ordered morphologies at such small numbers of repeat units. Clearly, the Flory-like interaction parameter, χ, for this combination of blocks is significant; however, direct χ measurement was beyond the scope of this initial work.

MCIL-BCPs **4a–f** were also found to selectively and reversibly coordinate small protic molecules (e.g., H_2O, small alcohols such as MeOH, EtOH, etc.) with a distinct color change. After exposure to the vapor of these small protic molecules, **4a–f** undergo a color change from dark blue to light purple. The original dark blue color can be restored by mild heating or in vacuo treatment of the coordinated BCPs (see Figure 5.3 for an example). This reversible colorimetric coordination behavior has been observed previously with MCILs containing the same Co(II) bis(salicylate) anion upon exposure to H_2O or alcohols.[7] However, the vapor of aprotic small molecules (e.g., Et_2O, acetone, ethyl acetate, etc.) will not trigger the reversible color change described above, indicating no coordination between **4a–f** and these aprotic molecules (see Section 5.6.15).

Interestingly, preliminary SAXS of **4d** suggests that water vapor coordination does not appear to affect its Gyr morphology but may slightly increase domain spacing (see Section 5.6.14).

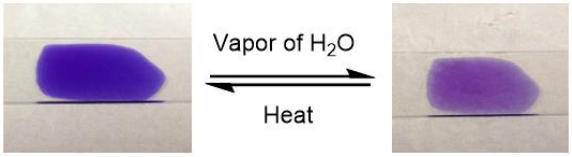

Figure 5.3. Reversible color change of **4d** upon coordination with H_2O vapor.

5.4 Summary

In summary, new MCIL-based BCPs **4a–f** have been made via RAFT polymerization that are capable of forming ordered nanostructures (including the Gyr phase) in their neat states and can also reversibly coordinate with H_2O and small alcohols with an associated color change. We are currently investigating the morphological behavior and phase stability of this MCIL-BCP system as a function of the extent of H_2O and small alcohol coordination. We are also exploring on whether phase changes can be induced upon reversible water or alcohol coordination to allow these MCIL-based BCPs to be used in responsive or transport applications.

5.5 Acknowledgments

Financial support for the work performed at CU Boulder was provided by the U.S. Dept. of Energy ARPA-E program (grant: DE-AR0000343) and matching funds from Total, S.A.

Financial support for the work performed at CSU was provided by the CSU Energy Institute and the OVPR Catalyst for Innovative Partnerships Program.

5.6 Supporting information

5.6.1 Materials

Tributylphosphine, 4-vinylbenzyl chloride, cobalt(II) chloride hexahydrate, lithium salicylate, 2-cyano-2-propyl benzodithioate (CPBD), and chlorobenzene were all purchased from Sigma-Aldrich and used as received. Butyl methacrylate was purchased from Sigma-Aldrich and purified by passage over a column of basic alumina to remove the added radical inhibitor. Azobis(isobutyronitrile) (AIBN) was purchased from the Sigma-Aldrich Co. and recrystallized from methanol. All solvents were purchased from Sigma-Aldrich or Mallinckrodt, Inc., and purified/dehydrated via N_2-pressurized activated alumina columns, and de-gassed. The H_2O used for synthesis was purified and de-ionized, with a resistivity value greater than 12 MΩ/cm. All polymerizations were carried out in a dry Ar atmosphere using standard Schlenk line techniques.

5.6.2 Instrumentation

^{1}H and ^{13}C NMR spectra were obtained using a Bruker 300 Ultrashield™ (300 MHz for ^{1}H) spectrometer. Chemical shifts are reported in ppm relative to residual non-deuterated solvent. Gel permeation chromatography (GPC) was performed using a Viscotek GPC-Max chromatography system outfitted with three 7.5 x 340 mm Polypore™ (Polymer Laboratories) columns in series, a Viscotek differential refractive index (RI) detector, and an Alltech column

oven (mobile phase THF, 40 °C, 1 mL min^{-1} flow rate). MW data obtained on this GPC system were referenced to polystyrene MWstandards. Elemental analysis was performed with a Vario EL III (Elementar) instrument at the Tokyo University of Agriculture and Technology. Small-angle X-ray scattering (SAXS) data were collected using a Rigaku SMax3000 High Brilliance three-pinhole SAXS system outfitted with a MicroMax-007HFM rotating anode (Cu K_α), a Confocal Max-Flux Optic, a Gabriel-type multi-wire area detector, and a Linkam thermal stage. Differential scanning calorimetry (DSC) measurements were performed using a Mettler Toledo DSC823^e and a Julabo FT100 Intracooler. UV-visible spectroscopy was performed using a UV-2450 instrument (SHIMADZU).

5.6.3 Synthesis of tributyl(4-vinylbenzyl)phosphonium chloride[19]

Synthesized as previously reported.[1] Characterization data matched those reported.[19]

5.6.4 Synthesis of bis[tributyl(4-vinylbenzyl)phosphonium] [cobalt(II) bis(salicylate)] (6)

Tributyl(4-vinylbenzyl)phosphonium chloride (1.000 g, 2.82 mmol) was dissolved in H_2O (5 mL). Subsequently, individual aq. aliquots (2.5 mL) of lithium salicylate (0.812 g, 5.64 mmol) and cobalt(II) chloride hexahydrate (0.335 g, 1.41 mmol) were prepared and then added dropwise. A deep purple liquid formed immediately and was extracted using CH_2Cl_2. The CH_2Cl_2 layer was then repeatedly washed with water until no halides were detected by the silver nitrate test. This solution was then dried over anhydrous Na_2SO_4, filtered, and then concentrated. The resulting liquid was dissolved in MeOH, stirred at R.T. for 24 h, filtered, and finally concentrated in vacuo to give **9** as a deep blue liquid (yield: 1.24 g, 91%). ^{1}H NMR (300 MHz, CD_3OD): δ 8.04 (s, 1H),

7.44 (d, *J* = 8.0 Hz, 2H), 7.33–7.17 (m, 4H), 7.10 (s, 1H), 6.69 (dd, *J* = 17.6, 10.9 Hz, 1H), 5.77 (dt, *J* = 17.6, 0.9 Hz, 1H), 5.23 (dt, *J* = 10.9, 1.0 Hz, 1H), 3.65 (d, *J* = 14.8 Hz, 2H), 2.17–1.98 (m, 6H), 1.51–1.33 (m, 12H), 1.00–0.82 (m, 9H). ^{13}C NMR (75 MHz, CD_3OD): δ 138.00 (d, *J* = 3.9 Hz), 135.64 (d, *J* = 2.2 Hz), 133.06, 129.80 (d, *J* = 5.1 Hz), 127.59 (d, *J* = 8.9 Hz), 126.84 (d, *J* = 3.3 Hz), 120.78, 118.86, 113.95 (d, *J* = 1.8 Hz), 25.41 (d, *J* = 45.4 Hz), 23.45 (d, *J* = 15.7 Hz), 22.77 (d, *J* = 4.7 Hz), 17.56 (d, *J* = 47.3 Hz), 12.15 (d, *J* = 0.9 Hz). The ^{13}C signals of the phosphonium cation were split into doublets by the ^{31}P nucleus. The number of ^{13}C signals for the cobalt anion is less than expected due to the interference of the paramagnetic Co(II) center.[7] Anal. calcd. for $C_{56}H_{80}CoO_6P_2$: C 69.33, H 8.31, N 0; found: C 69.34, H 8.02, N 0.

When monomer **6** is dissolved in common non- or weakly coordinating NMR solvents (i.e., $CDCl_3$, CD_2Cl_2, $(CD_3)_2CO$), its ^{1}H and ^{13}C signals are broad peaks due to the paramagnetism of the Co(II) ion present in the anion. However, the ^{1}H and ^{13}C signals of the phosphonium cation of **6** are sharp peaks when dissolved in CD_3OD because of the combined effects of coordination of CD_3OD to the Co(II) anion and good solvent separation of the phosphonium cation from the paramagnetic Co(II) anion.

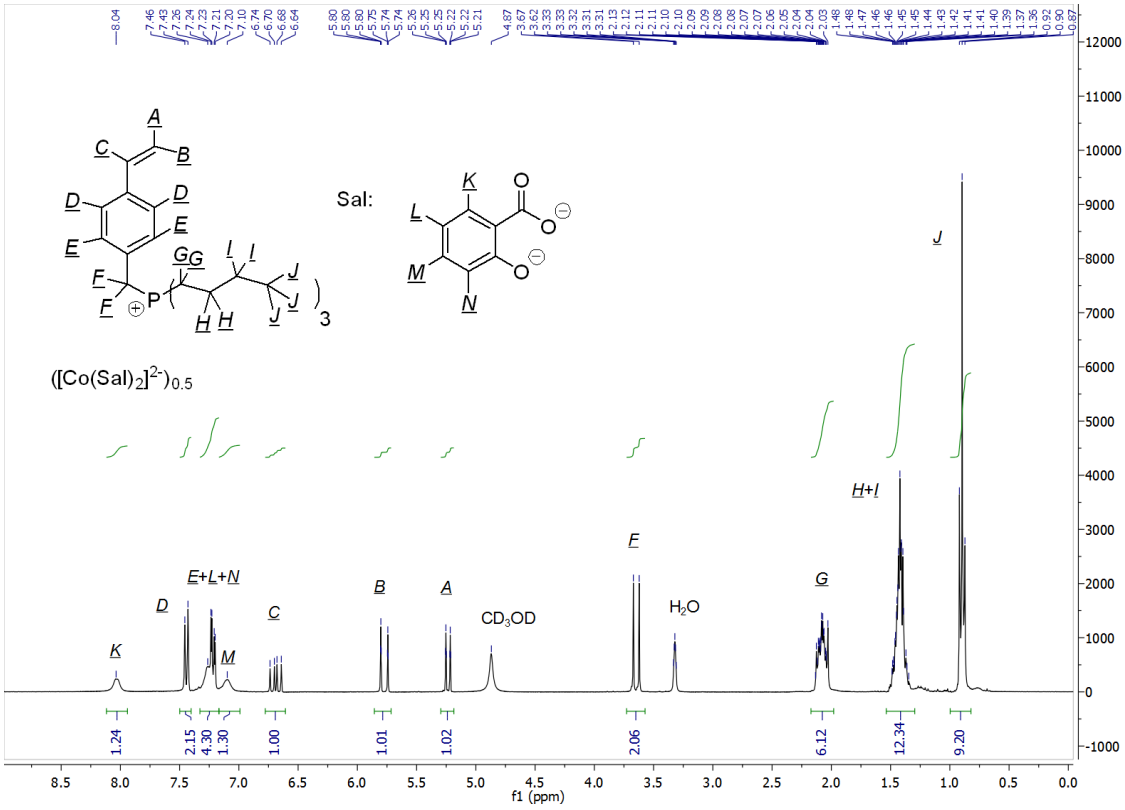

Figure 5.S1. ^{1}H NMR spectrum and peak assignments for monomer **6**.

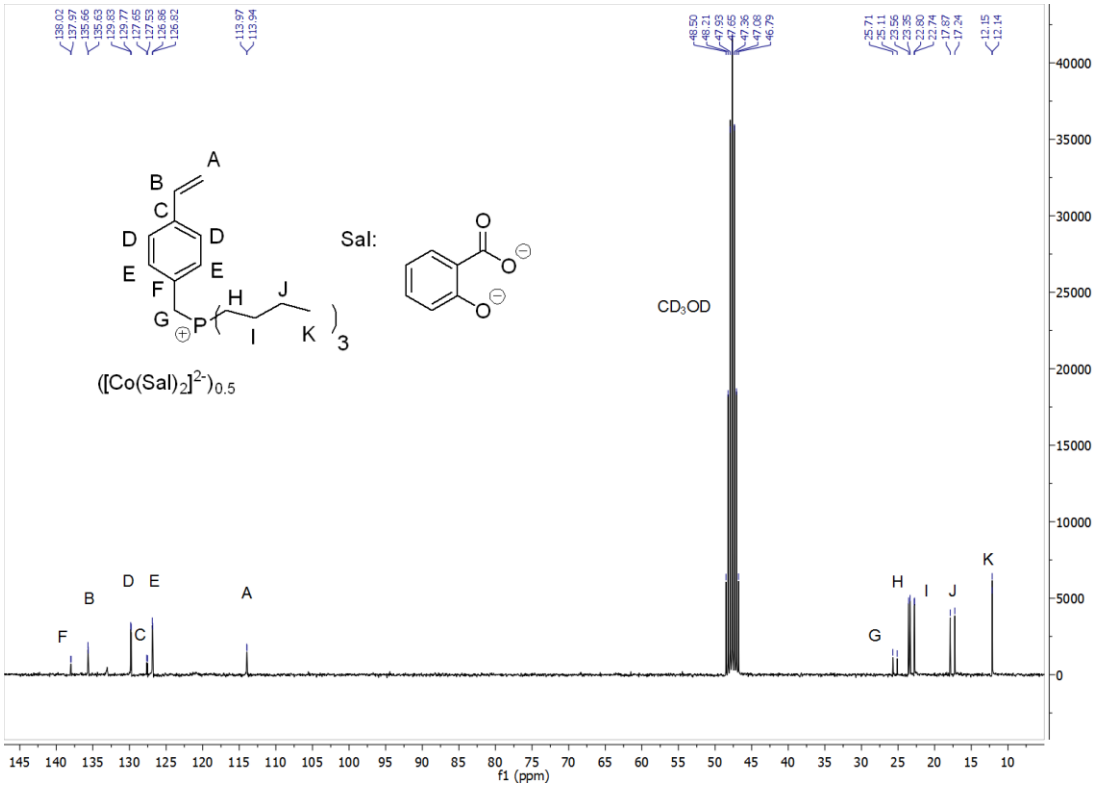

Figure 5.S2. ^{13}C NMR spectrum and peak assignments for monomer **6**. As mentioned before, the carbon signals of Co(II) anion is hard to interpret due to the paramagnetic effect of Co(II).

5.6.5 Synthesis of PBMA macro-chain-transfer agents (macroCTAs) 5a–f[10]

The DP, M_n, and PDI values of **5a–f** are shown in Table 5.S1 below.

Table 5.S1. The DP, M_n, and PDI values for PBMA macroCTAs **5a–f**.

PBMA MacroCTA	DP	M_n (g/mol)	PDI
5a	35	5,198	1.08
5b	40	5,909	1.06
5c	45	6,620	1.10
5d	50	7,331	1.04
5e	55	8,042	1.07
5f	60	8,753	1.10

(a) Synthesis of PBMA macroCTA 5a. Butyl methacrylate (1.50 g, 10.5 mmol), CPBD (66.7 mg, 0.301 mmol), chlorobenzene (1.2 mL) and AIBN (5.00 mg, 0.0304 mmol) were added to a flame-dried Schlenk flask and degassed by three freeze-pump-thaw cycles. The flask was then allowed to warm to room temperature and back-filled with Ar. The resulting mixture was then stirred at 70 °C for 24 h. Upon complete consumption of the butyl methacrylate (as verified by ^{1}H NMR analysis), the contents of the flask were cooled to room temperature, diluted with THF, precipitated by adding into MeOH, and the precipitate recovered by filtration to give the desired PBMA macroCTA **5a** as a pink solid (yield: 1.32 g, 84%). DP = 35; PDI = 1.08; M_n = 5198 g/mol (calculated using ^{1}H NMR polymer end-group analysis. See the following sections for details on how the DP and absolute M_n were determined using ^{1}H NMR analysis).

(b) Synthesis of PBMA macroCTA 5b. Butyl methacrylate (1.50 g, 10.5 mmol), CPBD (58.4 mg, 0.264 mmol), chlorobenzene (1.2 mL) and AIBN (4.30 mg, 0.0264 mmol) were added to a flame-dried Schlenk flask and degassed by three freeze-pump-thaw cycles. The flask was then allowed to warm to room temperature and back-filled with Ar. The resulting mixture was then stirred at 70 °C for 24 h. Upon complete consumption of the butyl methacrylate (as verified by ^{1}H NMR analysis), the contents of the flask were cooled to room temperature, diluted with THF, precipitated by adding into MeOH, and the precipitate recovered by filtration to give the desired PBMA macroCTA **5b** as a pink solid (yield: 1.27 g, 82%). DP = 40; PDI = 1.06; M_n = 5909 g/mol (calculated using ^{1}H NMR polymer end-group analysis. See the following sections for details on how the DP and absolute M_n were determined using ^{1}H NMR analysis).

(c) Synthesis of PBMA macroCTA 5c. Butyl methacrylate (1.50 g, 10.5 mmol), CPBD (51.9 mg, 0.234 mmol), chlorobenzene (1.2 mL) and AIBN (3.80 mg, 0.0231 mmol) were added to a flame-dried Schlenk flask and degassed by three freeze-pump-thaw cycles. The flask was then allowed to warm to room temperature and back-filled with Ar. The resulting mixture was then stirred at 70 °C for 24 h. Upon complete consumption of the butyl methacrylate (as verified by ^{1}H NMR analysis), the contents of the flask were cooled to room temperature, diluted with THF, precipitated by adding into MeOH, and the precipitate recovered by filtration to give the desired PBMA macroCTA **5c** as a pink solid (yield: 1.15 g, 74%). DP = 45; PDI = 1.10; M_n = 6620 g/mol (calculated using ^{1}H NMR polymer end-group analysis. See the following sections for details on how the DP and absolute M_n were determined using ^{1}H NMR analysis).

(d) Synthesis of PBMA macroCTA 5d. Butyl methacrylate (1.50 g, 10.5 mmol), CPBD (46.7 mg, 0.211 mmol), chlorobenzene (1.2 mL) and AIBN (3.50 mg, 0.0213 mmol) were added to a flame-dried Schlenk flask and degassed by 3 freeze-pump-thaw cycles. The flask was then

allowed to warm to room temperature and back-filled with Ar. The resulting mixture was then stirred at 70 °C for 24 h. Upon complete consumption of butyl methacrylate (as verified by ^{1}H NMR analysis), the contents of the flask were cooled to room temperature, diluted with THF, precipitated by adding into MeOH, and the precipitate recovered by filtration to give the desired PBMA macroCTA **5d** as a pink solid (yield: 1.24 g, 80%). DP = 50; PDI = 1.04; M_n = 7331 g/mol (calculated using ^{1}H NMR polymer end-group analysis. See the following sections for details on how the DP and absolute M_n were determined using ^{1}H NMR analysis).

(e) Synthesis of PBMA macroCTA 5e. Butyl methacrylate (1.50 g, 10.5 mmol), CPBD (42.5 mg, 0.192 mmol), chlorobenzene (1.2 mL) and AIBN (3.2 mg, 0.0194 mmol) were added to a flame-dried Schlenk flask and degassed by three freeze-pump-thaw cycles. The flask was then allowed to warm to room temperature and back-filled with Ar. The resulting mixture was then stirred at 70 °C for 24 h. Upon complete consumption of the butyl methacrylate (as verified by ^{1}H NMR analysis), the contents of the flask were cooled to room temperature, diluted with THF, precipitated by adding into MeOH, and the precipitate recovered by filtration to give the desired PBMA macroCTA **5e** as a pink solid (yield: 1.18 g, 76%). DP = 55; PDI = 1.07; M_n = 8042 g/mol (calculated using ^{1}H NMR polymer end-group analysis. See the following sections for details on how the DP and absolute M_n were determined using ^{1}H NMR analysis).

(f) Synthesis of PBMA macroCTA 5f. Butyl methacrylate (1.50 g, 10.5 mmol), CPBD (38.9 mg, 0.176 mmol), chlorobenzene (1.2 mL) and AIBN (2.9 mg, 0.0176 mmol) were added to a flame-dried Schlenk flask and degassed by three freeze-pump-thaw cycles. The flask was then allowed to warm to room temperature and back-filled with Ar. The resulting mixture was then stirred at 70 °C for 24 h. Upon complete consumption of the butyl methacrylate (as verified by ^{1}H NMR analysis), the contents of the flask were cooled to room temperature, diluted with THF,

precipitated by adding into MeOH, and the precipitate recovered by filtration to give the desired PBMA macroCTA **5f** as a pink solid (yield: 1.21 g, 79%). DP = 60; PDI = 1.10; M_n = 8753 g/mol (calculated using ^{1}H NMR polymer end-group analysis. See the following sections for details on how the DP and absolute M_n were determined using ^{1}H NMR analysis).

5.6.6 Determination of the DP and M_n values of PBMA macroCTAs 5a–f[12]

The RAFT of butyl methacrylate to make macroCTAs has been established in the literature to have controlled polymerization character.[10] The DP and M_n values of synthesized PBMA macroCTAs **5a–f** were calculated based on the ^{1}H NMR peak integral of aromatic protons (*A*) on the CPBD end-group relative to that of the protons (*B*) on the ester group for these polymers (Eqs. 5.1 and 5.2).[12] See Figure 5.S3 below for example data used to calculate these values for **5d**.

$$DP = \frac{\mathrm{B}_{\text{1H NMR Integration}}}{\mathrm{A}_{\text{1H NMR Integration}}} \qquad \text{(Eq. 5.1)}$$

$$M_n = (\mathrm{DP} \times M_{\mathrm{monomer}}) + M_{\mathrm{CPBD}} \qquad \text{(Eq. 5.2)}$$

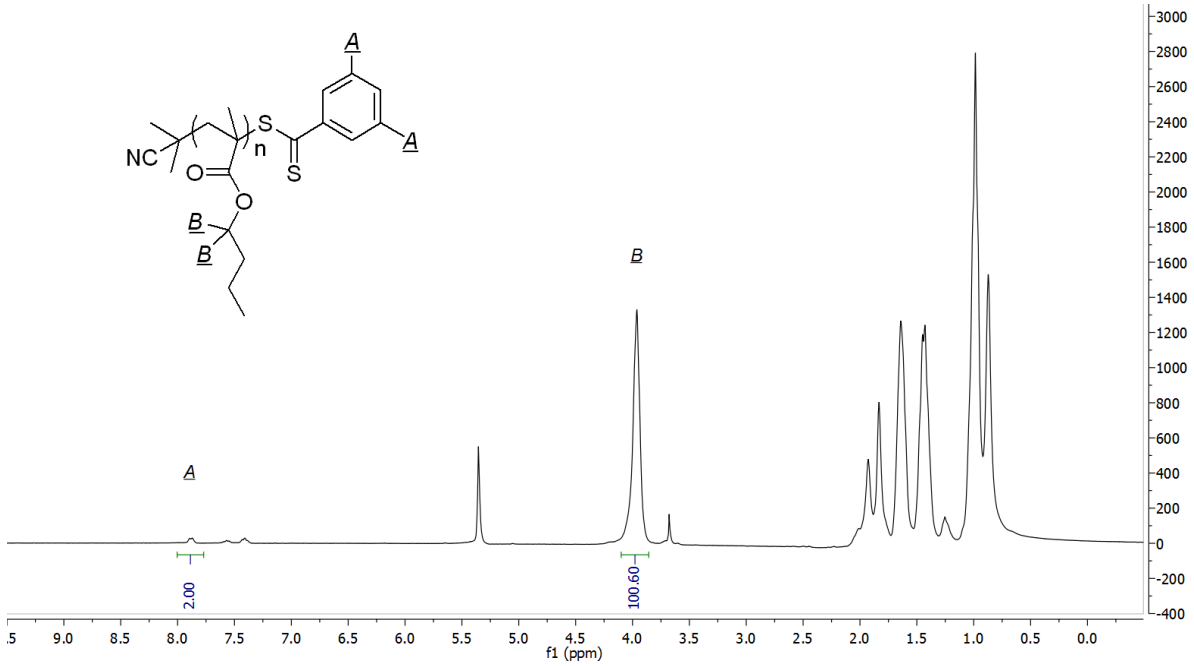

Figure 5.S3. Example ^{1}H NMR spectrum of **5d**, and the ^{1}H NMR peak assignments used for calculating the DP and M_n value. Calculated DP = 50.3 (≅ 50), M_n = 7,331 g/mol.

5.6.7 Synthesis of MCIL-BCPs 4a–f

The calculated block compositions and M_n values of MCIL-BCPs **4a–f** are shown in Table 5.S2 below:

Table 5.S2. The calculated block compositions and M_n values of MCIL-BCPs **4a–f** from ^{1}H NMR analysis.

BCP	n	m	M_n (g/mol)
4a	35	35	22,175
4b	40	30	20,461
4c	45	25	18,747
4d	50	20	17,033
4e	55	15	15,318
4f	60	10	13,604

(a) Synthesis of MCIL-BCP 4a. Monomer **6** (235 mg, 0.484 mmol), **5a** (72.0 mg, 0.0139 mmol), chlorobenzene (1.00 mL) and AIBN (0.500 mg, 0.00304 mmol) were added to a flame-dried Schlenk flask and degassed by three freeze-pump-thaw cycles. The flask was then allowed to warm to room temperature and back-filled with Ar. The resulting mixture was then stirred at 90 °C for 48 h. Upon complete consumption of monomer **6** (as verified by ^{1}H NMR analysis), the contents of the flask were cooled to room temperature, diluted with ethyl acetate, precipitated by adding into hexane/ethyl acetate (4/1 (v/v)) mixture. The resulting precipitate was recovered by filtration to give the MCIL-BCP **4a** as a dark blue solid (yield: 220 mg, 72%). Block repeat unit molar ratio = 1:1 (butyl methacrylate:monomer **6**); block length composition = 35-*b*-35 (PBMA-

b-poly(**6**)); M_n = 22,175 g/mol (calculated based on ^{1}H NMR analysis. See following sections for details on how the copolymer block composition, block lengths, and M_n were determined).

(b) Synthesis of MCIL-BCP 4b. Monomer **6** (246 mg, 0.507 mmol), **5b** (99.9 mg, 0.0169 mmol), chlorobenzene (1.20 mL) and AIBN (0.600 mg, 0.00365 mmol) were added to a flame-dried Schlenk flask and degassed by three freeze-pump-thaw cycles. The flask was then allowed to warm to room temperature and back-filled with Ar. The resulting mixture was then stirred at 90 °C for 48 h. Upon complete consumption of monomer **6** (as verified by ^{1}H NMR analysis), the contents of the flask were cooled to room temperature, diluted with ethyl acetate, precipitated by adding into hexane/ethyl acetate (4/1 (v/v)) mixture. The resulting precipitate was recovered by filtration to give the MCIL-BCP **4b** as a dark blue solid (yield: 286 mg, 83%). Block repeat unit molar ratio = 1.33:1 (butyl methacrylate:monomer **6**); block length composition = 40-*b*-30 (PBMA-*b*-poly(**6**)); M_n = 20,461 g/mol (calculated based on ^{1}H NMR analysis. See following sections for details on how the copolymer block composition, block lengths, and M_n were determined).

(c) Synthesis of MCIL-BCP 4c. Monomer **6** (266 mg, 0.548 mmol), **5c** (145 mg, 0.0219 mmol), chlorobenzene (1.20 mL) and AIBN (0.700 mg, 0.00426 mmol) were added to a flame-dried Schlenk flask and degassed by three freeze-pump-thaw cycles. The flask was then allowed to warm to room temperature and back-filled with Ar. The resulting mixture was then stirred at 90 °C for 48 h. Upon complete consumption of monomer **6** (as verified by ^{1}H NMR analysis), the contents of the flask were cooled to room temperature, diluted with ethyl acetate, precipitated by adding into hexane/ethyl acetate (4/1 (v/v)) mixture. The resulting precipitate was recovered by filtration to give the MCIL-BCP **4c** as a dark blue solid (yield: 322 mg, 78%). Block repeat unit molar ratio = 1.8:1 (butyl methacrylate: monomer **6**); block length composition = 45-*b*-25 (PBMA-

b-poly(**6**)); M_n = 18,747 g/mol (calculated based on ^{1}H NMR analysis. See following sections for details on how the copolymer block composition, block lengths, and M_n were determined).

(d) Synthesis of MCIL-BCP 4d. Monomer **6** (274 mg, 0.565 mmol), **5d** (207 mg, 0.0282 mmol), chlorobenzene (1.5 mL) and AIBN (0.930 mg, 0.00566 mmol) were added to a flame-dried Schlenk flask and degassed by three freeze-pump-thaw cycles. The flask was then allowed to warm to room temperature and back-filled with Ar. The resulting mixture was then stirred at 90 °C for 48 h. Upon complete consumption of **6** (as verified by ^{1}H NMR analysis), the contents of the flask were cooled to R.T., diluted with ethyl acetate, precipitated by adding into hexane/ethyl acetate (4/1 (v/v)) mixture. The resulting precipitate was recovered by filtration to give the MCIL-BCP **4d** as a dark blue solid (yield: 300 mg, 62%). Block repeat unit molar ratio = 2.5:1 (butyl methacrylate:monomer **6**); block length composition = 50-*b*-20 (PBMA-*b*-poly(**6**)); M_n = 17,032 g/mol (calculated based on ^{1}H NMR analysis. See following sections for details on how the copolymer block composition, block lengths, and M_n were determined).

(e) Synthesis of MCIL-BCP 4e. Monomer **6** (214 mg, 0.441 mmol), **5e** (236 mg, 0.0294 mmol), chlorobenzene (2.40 mL) and AIBN (1.00 mg, 0.00609 mmol) were added to a flame-dried Schlenk flask and degassed by three freeze-pump-thaw cycles. The flask was then allowed to warm to room temperature and back-filled with Ar. The resulting mixture was then stirred at 90 °C for 48 h. Upon complete consumption of monomer **6** (as verified by ^{1}H NMR analysis), the contents of the flask were cooled to room temperature, diluted with ethyl acetate, precipitated by adding into hexane/ethyl acetate (4/1 (v/v)) mixture. The resulting precipitate was recovered by filtration to give the MCIL-BCP **4e** as a dark blue solid (yield: 338 mg, 75%). Block repeat unit molar ratio = 3.67:1 (butyl methacrylate:monomer **6**); block length composition = 55-*b*-15 (PBMA-*b*-poly(**6**));

M_n = 15,318 g/mol (calculated based on ^{1}H NMR analysis. See following sections for details on how the copolymer block composition, block lengths, and M_n were determined).

(f) Synthesis of MCIL-BCP 4f. Monomer **6** (256 mg, 0.528 mmol), **5f** (462 mg, 0.0528 mmol), chlorobenzene (3.00 mL) and AIBN (1.70 mg, 0.0104 mmol) were added to a flame-dried Schlenk flask and degassed by three freeze-pump-thaw cycles. The flask was then allowed to warm to room temperature and back-filled with Ar. The resulting mixture was then stirred at 90 °C for 48 h. Upon complete consumption of monomer **6** (as verified by ^{1}H NMR analysis), the contents of the flask were cooled to room temperature, diluted with ethyl acetate, precipitated by adding into hexane/ethyl acetate (4/1 (v/v)) mixture. The resulting precipitate was recovered by filtration to give the MCIL-BCP **4f** as a dark blue solid (yield: 512 mg, 71%). Block repeat unit molar ratio = 6:1 (butyl methacrylate:monomer **6**); block length composition = 60-*b*-10 (PBMA-*b*-poly(**6**)); M_n = 13,604 g/mol (calculated based on ^{1}H NMR analysis. See following sections for details on how the copolymer block composition, block lengths, and M_n were determined).

5.6.8 Determination of BCP Compositions and Molecular Weights

The block composition ratios, overall lengths, and M_n values of MCIL-BCPs **4a–f** were determined via ^{1}H NMR analysis. For example, see Figure 5.S4 for ^{1}H NMR peak assignments and an example spectrum used for these calculations: The signals of protons *D* on the butyl ester of **4d** overlap to create a broad peak between 3.89–4.09 ppm (signal *D*). The signals of the benzylic protons (protons *E*) on phosphonium overlap to create a broad peak between 3.54–3.88 ppm (signal *E*). So the PBMA:poly(**6**) ratio can be calculated by Eq. 5.3. The length of the poly(**6**) block can

be calculated by Eq. 5.4 and confirmed by conversion (Eq. 5.5). The M_n of BCPs can be calculated by Eq. 5.6.

$$\text{PBMA:poly(}\mathbf{6}\text{) ratio} = \frac{D_{^1H\ NMR\ Integration}}{E_{^1H\ NMR\ Integration}} \quad \text{(Eq. 5.3)}$$

$$\text{Poly(}\mathbf{6}\text{) block length, m} = \frac{n}{\text{PBMA:poly(}\mathbf{6}\text{) ratio}} \quad \text{(Eq. 5.4)}$$

$$\text{Poly(}\mathbf{6}\text{) block length, m} = (\text{monomer: macroCTA ratio}) \times \text{conversion} \quad \text{(Eq. 5.5)}$$

$$M_n = (n \times M_{BMA}) + (m \times M_{monomer\ \mathbf{6}}) + M_{CPBD} \quad \text{(Eq. 5.6)}$$

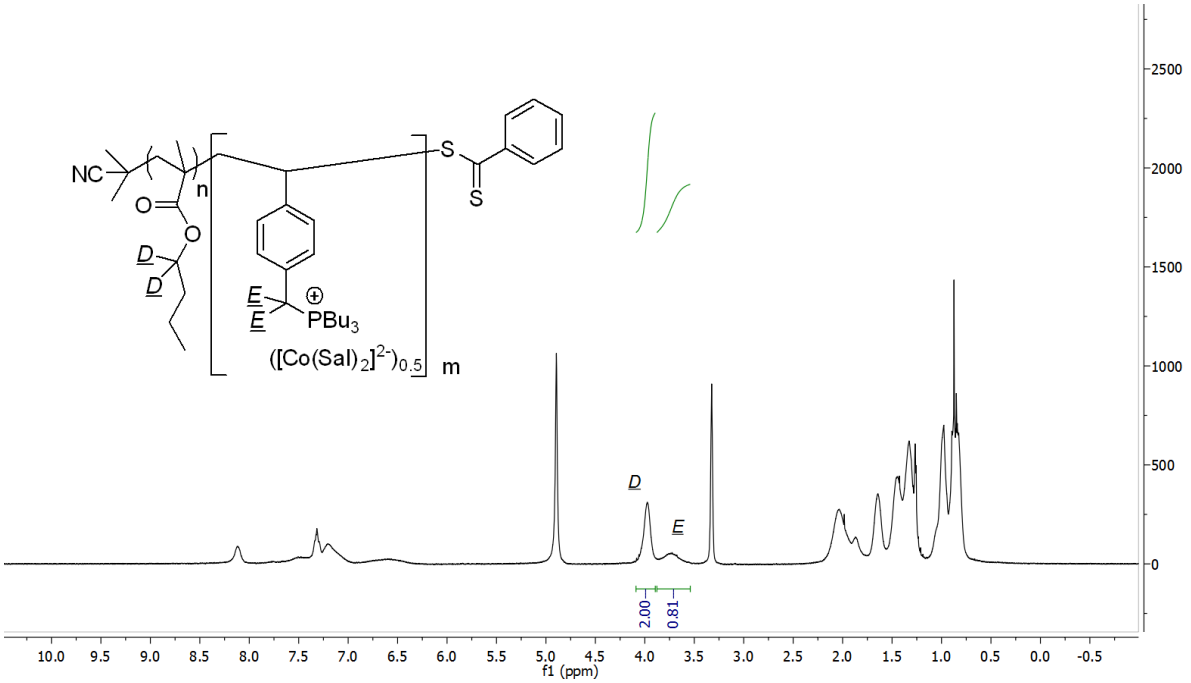

Figure 5.S4. Example ^{1}H NMR spectrum of MCIL-BCP **4d**, and the ^{1}H NMR peak assignments used for calculating the block composition ratio, overall length, and M_n value. The calculated PBMA:poly(**6**) ratio is 2.47, m = 20.24 (≅ 20), M_n = 17,033 g/mol.

5.6.9 Polymerization kinetics experiments

To confirm the controlled RAFT polymerization of monomer **6** from the PBMA macroCTAs, the kinetics plots of the RAFT reaction of **6** from PBMA macroCTA **5d** are shown in Figure 5.S5 below, as representative example data. The degree of conversion was calculated based on the ^{1}H NMR peaks integrals of proton (*A*) on the styrene unit double bond relative to the peak of the benzylic protons (*B*) next to the phosphonium group on monomer **6** (Eqs. 5.7 and 5.8). See Figure 5.S6 below for ^{1}H NMR assignments and example data used to calculate the degree of monomer conversion for the RAFT of monomer **6** to generate MCIL-BCP **4d**. The DP and M_n of each block copolymer were determined as mentioned in the prior sections.

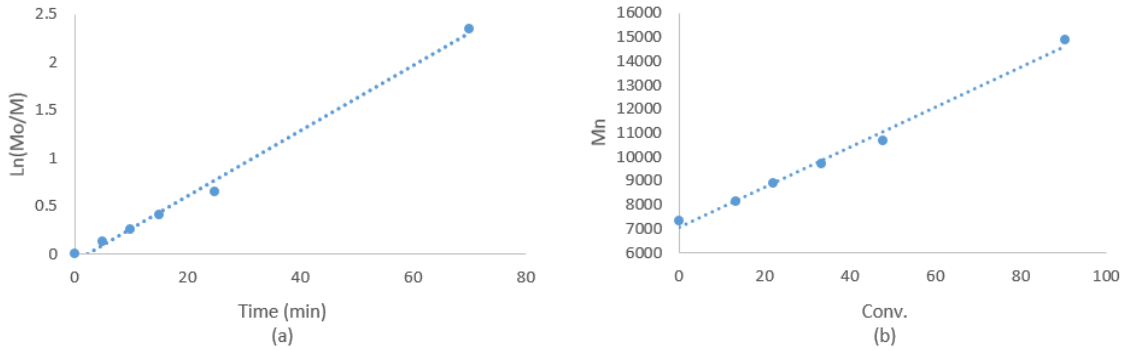

Figure 5.S5. System used for monitoring the kinetics of the RAFT polymerization of **6** from PBMA macroCTA **5d** to form MCIL-BCP **4d**: (a) Plot of the calculated $ln([M]_0/[M])$ vs. reaction time ($R^2 = 0.9933$). (b) Plot of the calculated M_n vs. calculated degree of monomer conversion ($R^2 = 0.9915$).

$$ln\frac{[M]_0}{[M]} = ln\left[\frac{B_{1H\ NMR\ Integration}}{A_{1H\ NMR\ Integration} \times 2}\right] \quad \text{(Eq. 5.7)}$$

$$\text{Conversion} = \frac{B_{1H\ NMR\ Integration} - A_{1H\ NMR\ Integration} \times 2}{B_{1H\ NMR\ Integration}} \quad \text{(Eq. 5.8)}$$

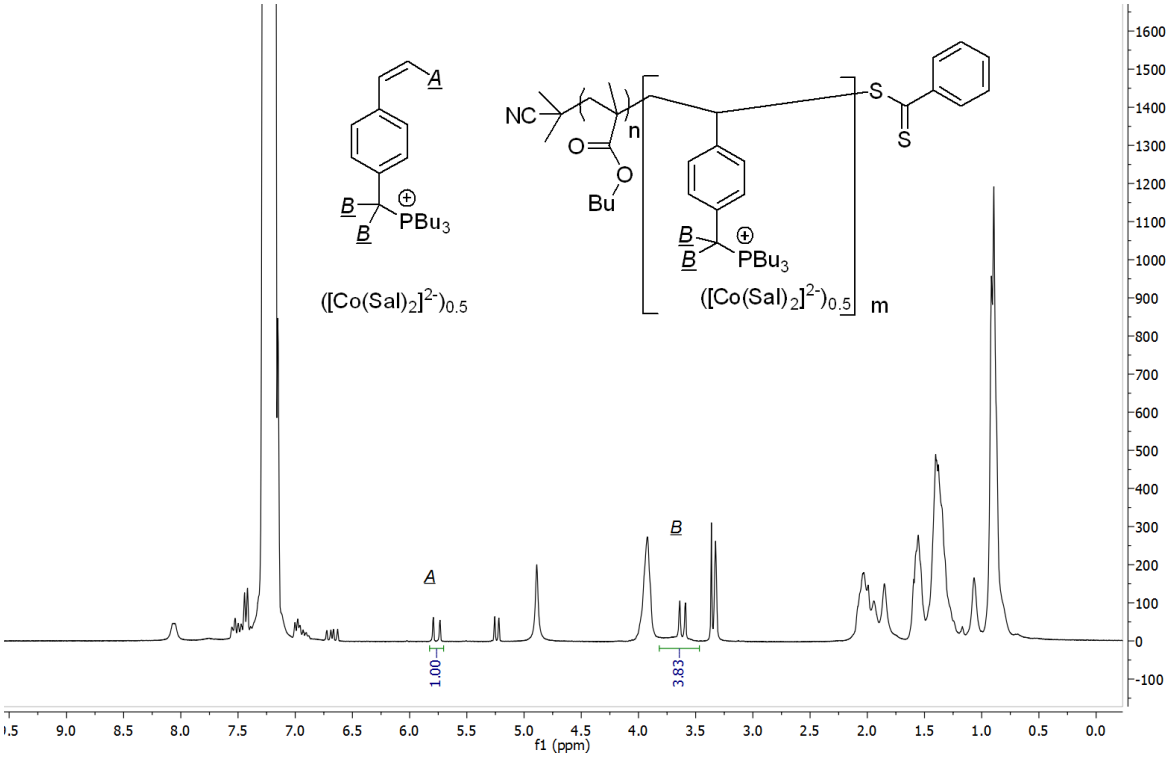

Figure 5.S6. An example ^{1}H NMR spectrum of the reaction mixture for the RAFT of monomer **6** from PBMA macroCTA **5d**, and the ^{1}H NMR peak assignments used for calculating the degree of monomer conversion. The calculated conversion is 47.8%.

5.6.10 Verification of the BCP architecture for MCIL-BCPs 4a–f

The block architecture of MCIL-BCPs **4a–f** were verified by a combination of surfactant behavior and solubility analysis, diffusion-ordered spectroscopy (DOSY) and small-angle X-ray scattering (SAXS) studies, as described previously in an earlier publication on IL-based BCPs prepared by ROMP from our research groups.[3p]

(a) Surfactant behavior and solubility analysis.[3p] MCIL-based BCPs **4a–f** all showed surfactant behavior (i.e., extensive foaming when agitated) when mixed in CH_2Cl_2, THF, acetone,

and EtOAc, as would be expected from amphiphilic BCPs. Control experiments with physical blends of PBMA and poly(**6**) of the same length as blocks in the BCPs did not show this behavior. MCIL-BCPs **4a–f** also showed very different solubility behavior compared to physical blends of the two homopolymers, PBMA and poly(**6**). For example, when mixed with EtOAc (10 mg/mL) **4d** forms a clear solution, whereas the physical blend yields a dark blue solid within a clear solution on top (i.e., PBMA is soluble in EtOAc while poly(**6**) is insoluble).

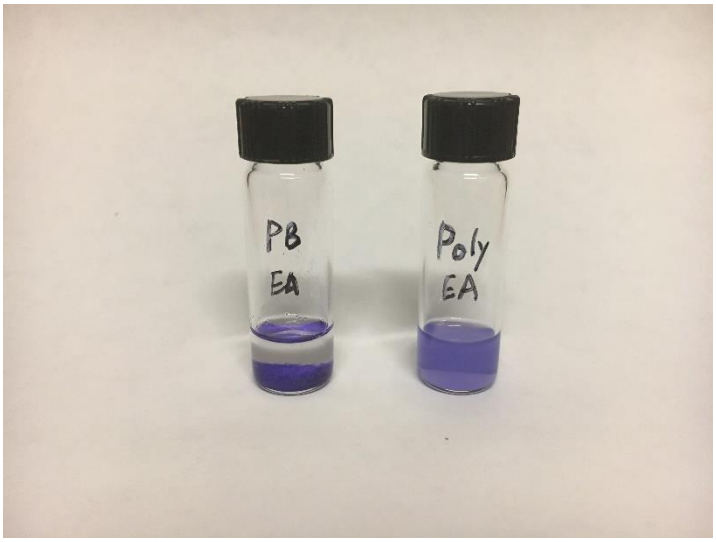

Figure 5.S7. Picture showing different solubilities of BCP **4d** in EtAcO (vial labelled: **Poly, EA**) and a physical blend of PBMA + poly(**6**) in in EtOAc (vial labelled: **PB, EA**) at room temperature.

(b) NMR DOSY studies.[3p] In the room-temperature NMR DOSY spectrum of BCP **4d** in CD_3OD (10 mg/mL) (Figure 5.S8), all peaks corresponding to both the PBMA and poly(**6**) blocks exhibited the same diffusion constant (1.50×10^{-6} m^2 s^{-1}). This result indicates that **4d** consists of only one macromolecular species (as expected for a BCP) and is different with a physical blend of

two distinct homopolymer species (Figure 5.S9). Collectively, the results of these comparative studies are consistent with a covalently linked BCP architecture for **4a–f**, instead of a physical blend of the two homopolymers[3p] (i.e., PBMA + poly(**6**)).

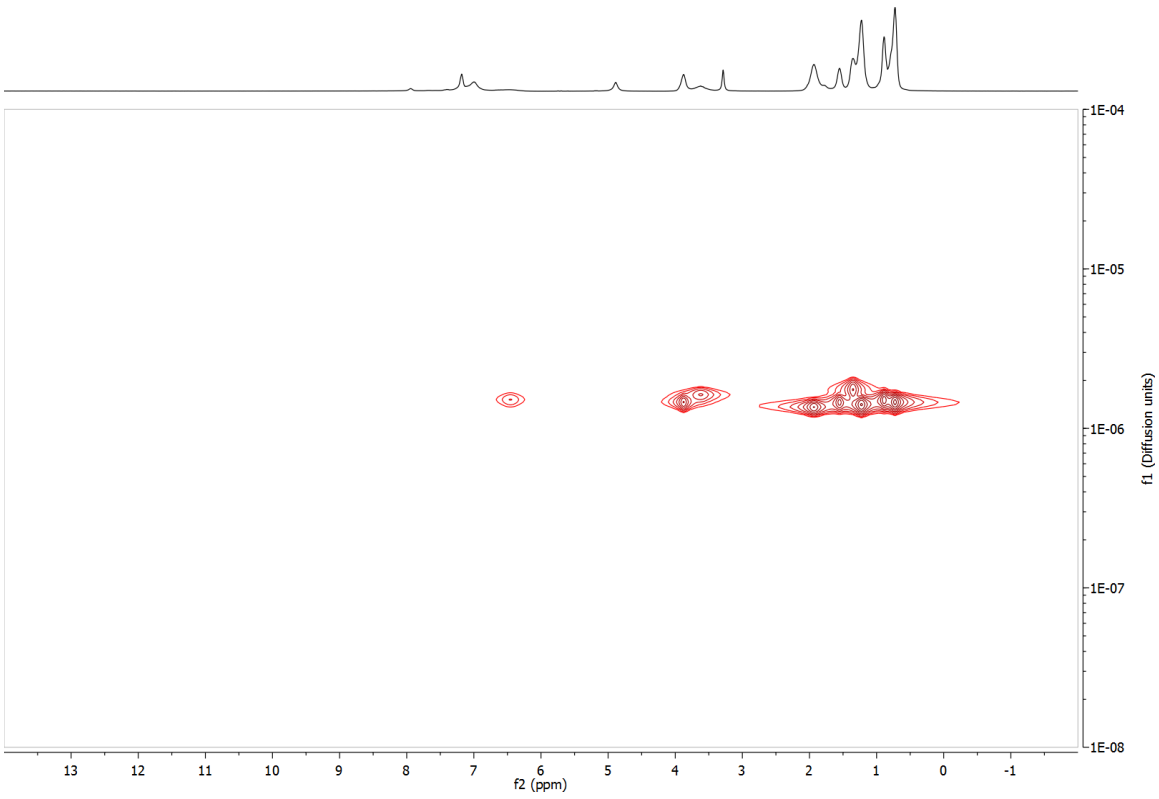

Figure 5.S8. An example NMR DOSY spectrum of BCP **4d** in CD_3OD at room temperature showing only one diffusion constant: D = 1.50 x 10^{-6} m^2 s^{-1}. The total gradient time (δ) used was 2.5 ms, and the diffusion delay (Δ) was 170 ms.

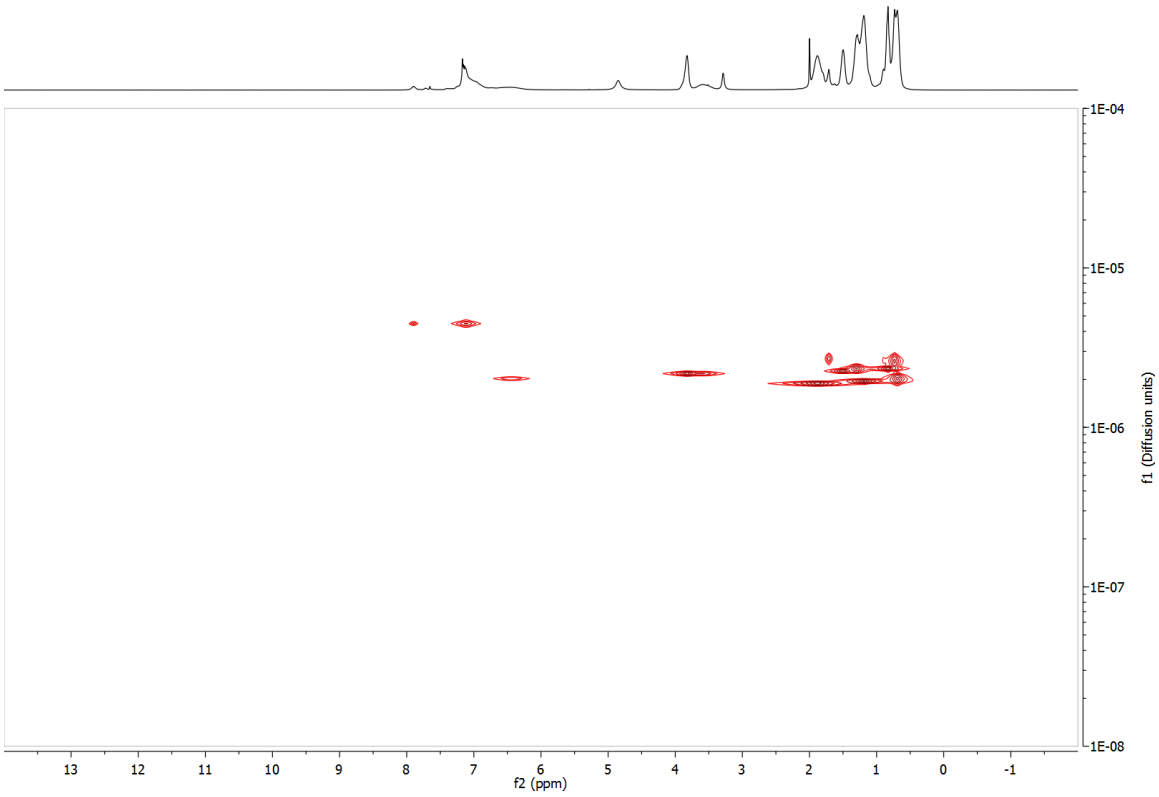

Figure 5.S9. An example NMR DOSY spectrum of a physical blend of PBMA and poly(**6**) in CD_3OD at room temperature showing two diffusion constants: D_1 = 4.47 x 10^{-6} m^2 s^{-1} and D_2 = 2.10 x 10^{-6} m^2 s^{-1}. The peaks do not perfectly correspond to the two components due to the overlap of the broad peaks. The total gradient time (δ) used was 2.5 ms, and the diffusion delay (Δ) was 80 ms.

(c) SAXS analysis.[3p] SAXS data of MCIL-BCPs **4a–f** were collected, together with data collected for the physical blends of the two homopolymers (i.e., PBMA + poly(**6**)) with the same lengths as the BCP blocks for comparison. For example, MCIL-BCP **4d** forms the gyroid (Gyr) phase after annealing, whereas the physical blend yields a disordered phase under the same

conditions (Figure 5.S10). Similar results were observed when comparing the other BCPs to their analogous physical blends.

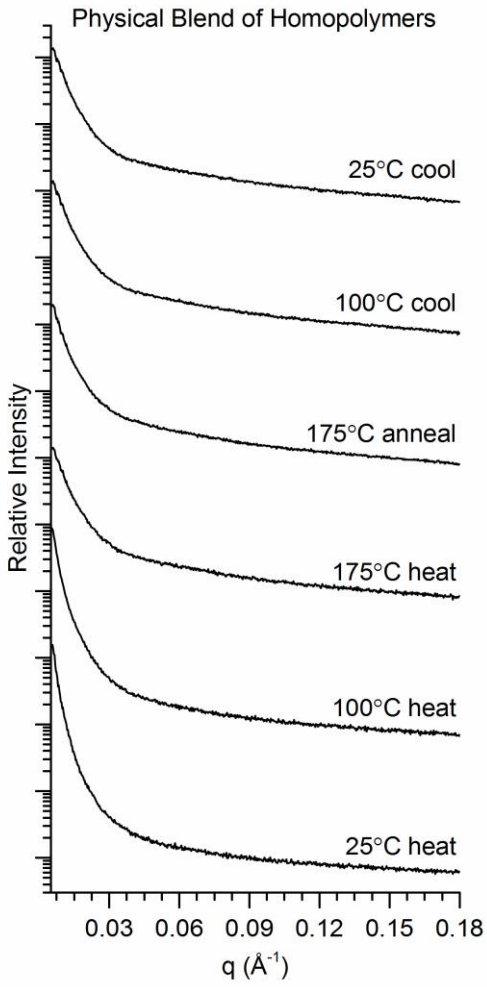

Figure 5.S10. SAXS profiles of physical blends of the two homopolymers (PBMA + poly(**6**)) at different temperatures during annealing.

5.6.11 Differential Scanning Calorimetry (DSC)

The DSC studies on MCIL-BCPs **4a–f** (see Figure 5.S11 for representative DSC profiles) only revealed evidence of a single glass transition falling consistently between 20 and 40 °C, typical of PBMA homopolymer. During the DSC studies on MCIL-based homopolymer poly(**6**), a typical glass transition peak was observed at 55 °C (Figure 5.S11). However, this transition was not detected in any of the DSC profiles of the MCIL-BCPs **4a–f**. Given the clear evidence of phase separation established by the SAXS data, it appears the limited domain sizes for these small overall molecular weights strongly inhibits the ability of the MCIL-based block to undergo the same thermal transitions as the bulk homopolymer poly(**6**).

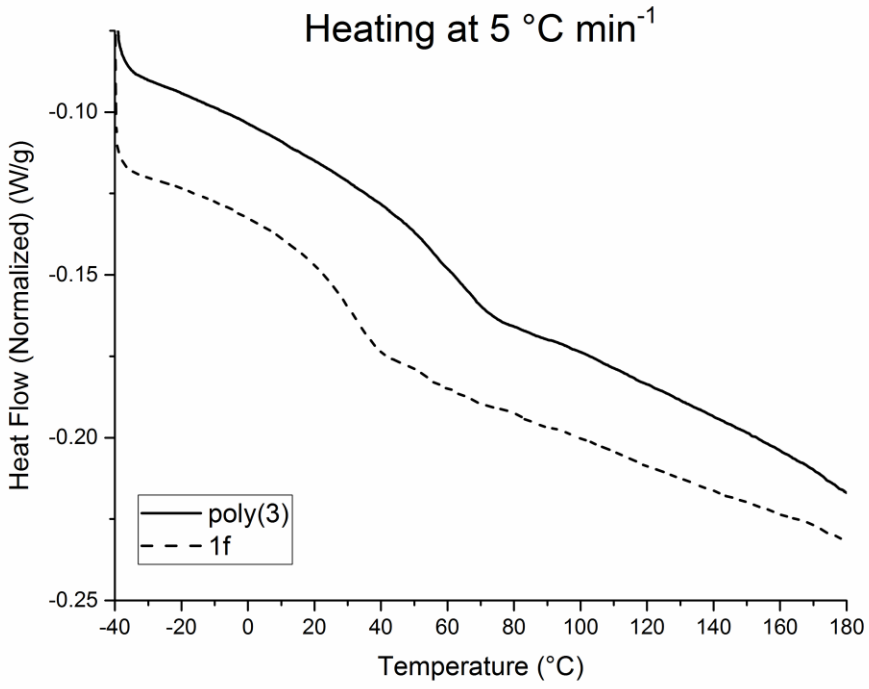

Figure 5.S11. DSC profiles of poly(**6**) and a representative MCIL-BCP **4f** at heating and cooling rates of 5 °C min^{-1}.

5.6.12 Ultraviolet–visible (UV-vis) spectroscopy analysis of the MCIL-BCPs

UV-vis studies were performed to help confirm that the Co(II) bis(salicylate) anion was unchanged during the RAFT polymerization process. The UV-vis spectrum of monomer **6** and MCIL-based BCP **4d** show the same absorption bands (Figures 5.S12 and 5.S13). This result indicates that the Co(II) complex remains unchanged after the polymerization.

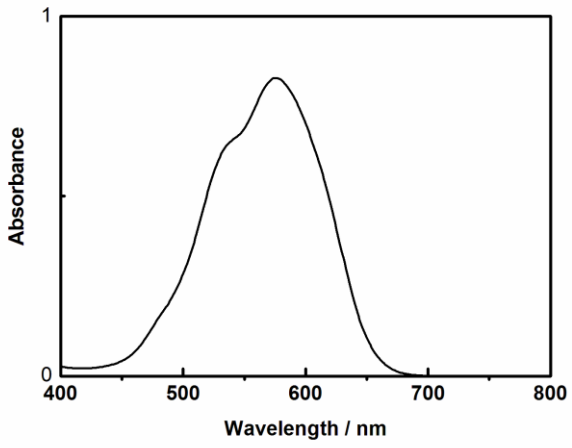

Figure 5.S12. UV-visible spectrum of monomer **6** in dichloromethane (10 mM). Two distinct bands at 533 and 573 nm were observed.

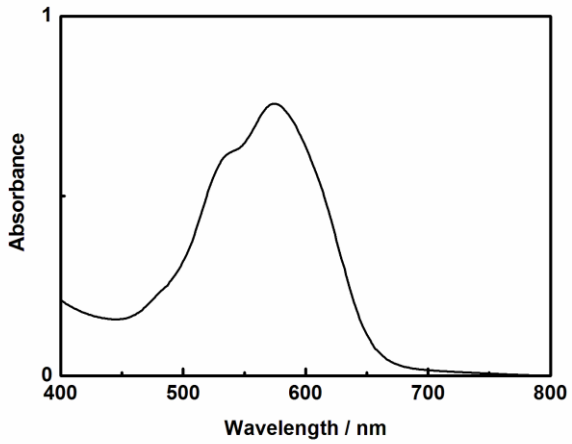

Figure 5.S13. UV-visible spectrum of **4d** in dichloromethane (10 mM). Two distinct bands at 533 and 573 nm were observed.

5.6.13 SAXS characterization of MCIL-BCPs 4a–f

1D Azimuthally integrated temperature-dependent SAXS data (heating and cooling) for MCIL-based BCPs **4a–f**: Inverted triangles represent the locations of allowed reflections (listed in Table 5.1 in Section 5.3) for the morphology depicted. Each sample was sandwiched neat between thin circular Kapton film (10 mm diameter x 0.05 mm thick) and mounted on a Linkam thermal stage. They were heated to 175 °C at a rate of 10 °C min^{-1}, annealed at 175 ºC for 2 h, and then allowed to cool to ambient temperature. For each temperature point, samples were allowed to equilibrate under vacuum for 5 min. Data were then collected for the sample under vacuum, with exposure times ranging from 600 to 3600 s.

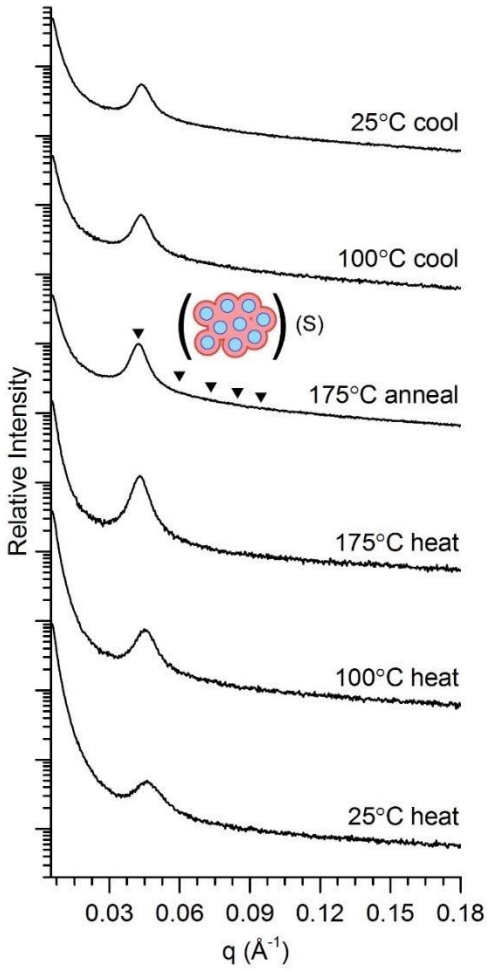

Figure 5.S14. Temperature-dependent SAXS data of MCIL-BCP **4a**.

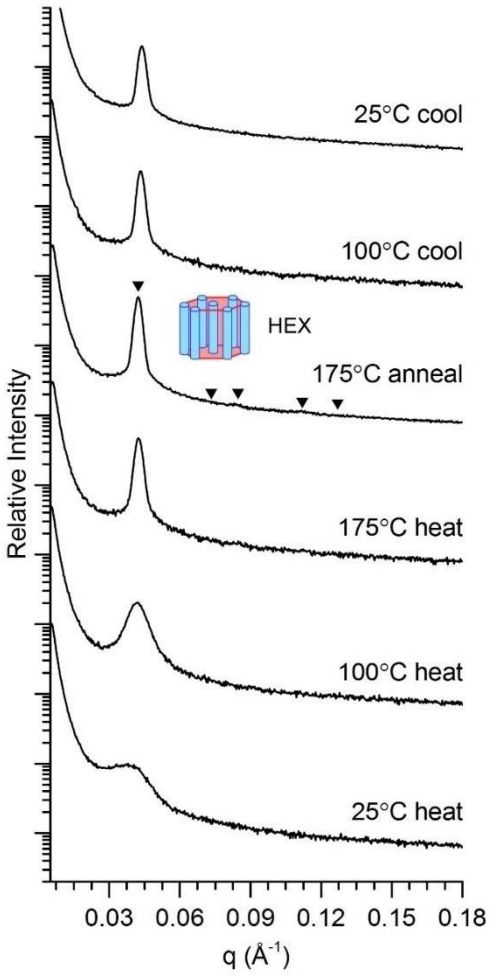

Figure 5.S15. Temperature-dependent SAXS data of MCIL-BCP **4b**.

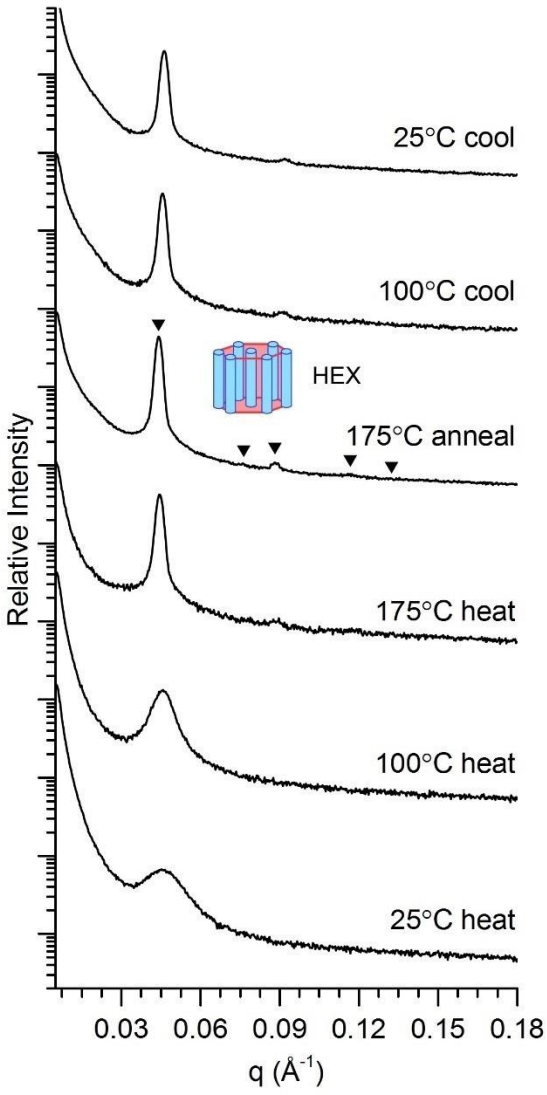

Figure 5.S16. Temperature-dependent SAXS data of MCIL-BCP **4c**.

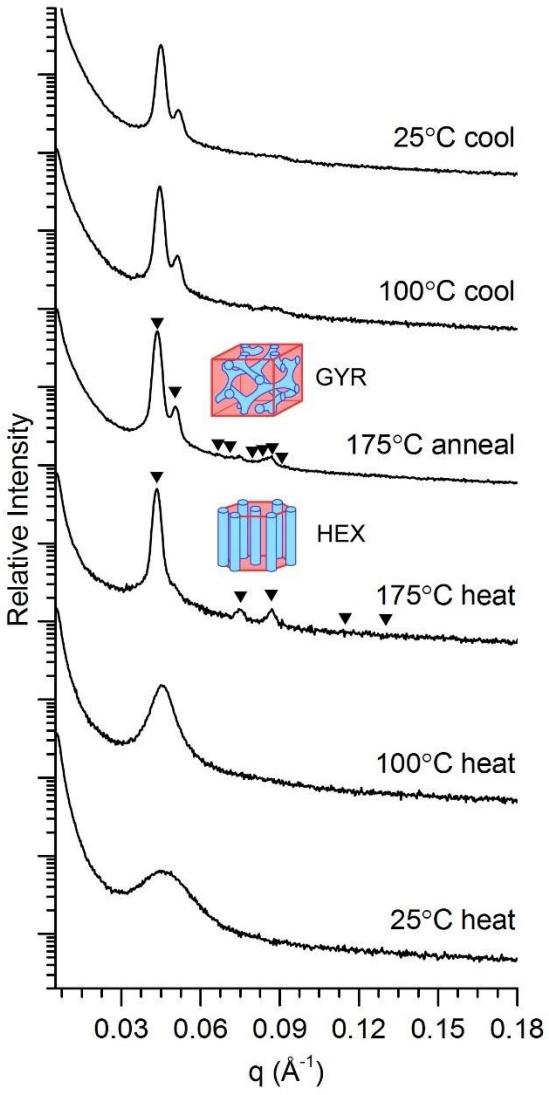

Figure 5.S17. Temperature-dependent SAXS data of MCIL-BCP **4d**.

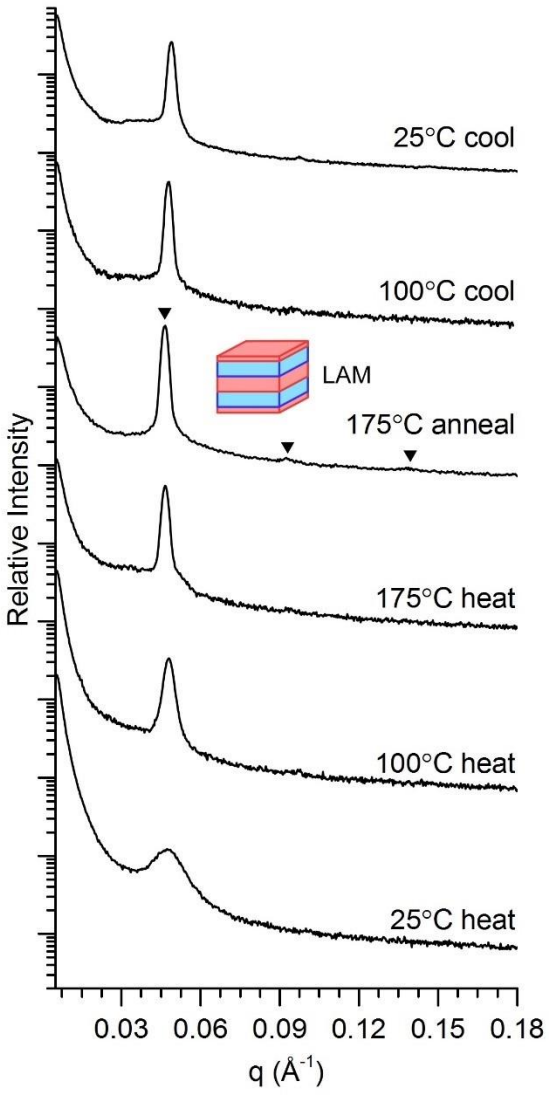

Figure 5.S18. Temperature-dependent SAXS data of MCIL-BCP **4e**.

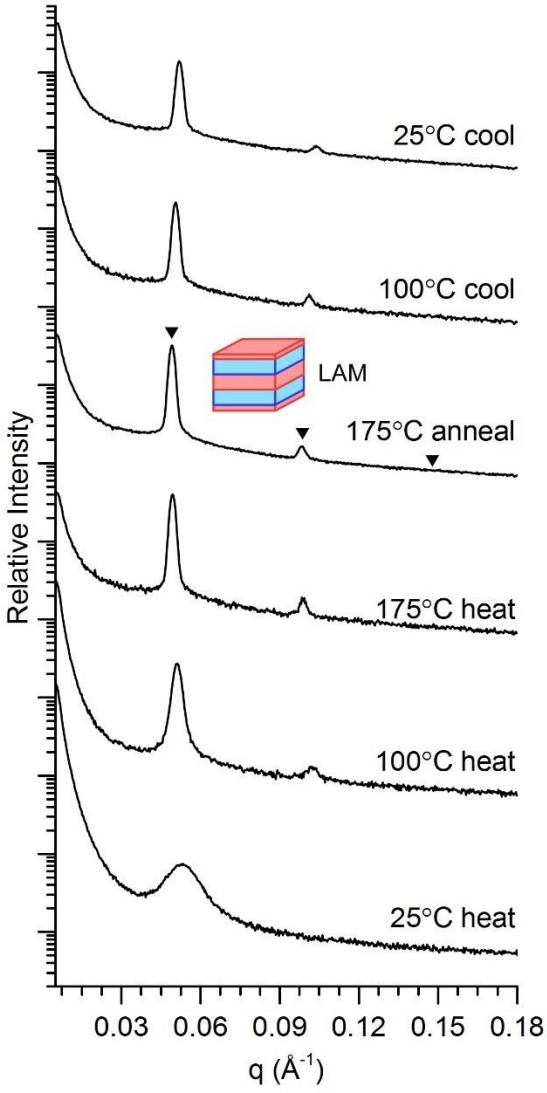

Figure 5.S19. Temperature-dependent SAXS data of MCIL-BCP **4f**.

5.6.14 SAXS characterization of hydrated and non-hydrated MCIL-based BCP 4d

1D Azimuthally integrated SAXS data at ambient temperature for **4d** before and after treatment with hydrated argon gas: The annealed SAXS sample was treated with the hydrated gas, ground into a fine powder, and sealed under air in a 1.0-mm-diameter quartz capillary. SAXS data

of both sample **4d** and background were then collected for 4500 s. Final data shown reflect sample data with background subtracted.

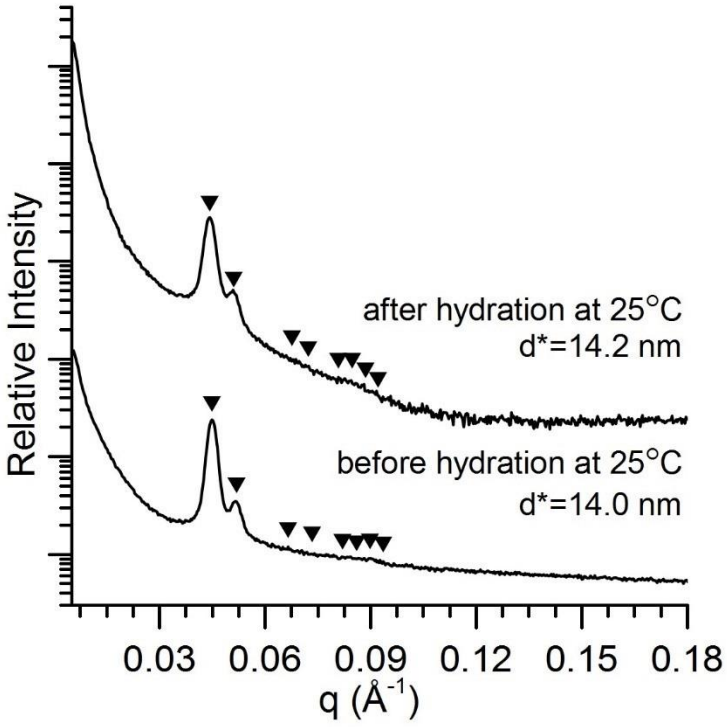

Figure 5.S20. SAXS data of MCIL-BCP **4d** before and after hydration.

5.6.15 Reversible coordination experiments of the MCIL-based BCPs 4a–f upon exposure to small alcohols and aprotic molecule vapors

MCIL-based BCPs **4a–f** undergo a color change from deep blue to light purple upon exposure to the vapor of small alcohols (e.g., methanol, ethanol, etc.). The original deep blue color can be restored by mild heating or in vacuo treatment of the coordinated BCPs (see Figure 5.S21

for an example). However, upon exposure to aprotic molecule vapors (e.g., Et_2O, acetone, ethyl acetate), no color change was observed for these MCIL-BCPs (see Figure 5.S22 for an example).

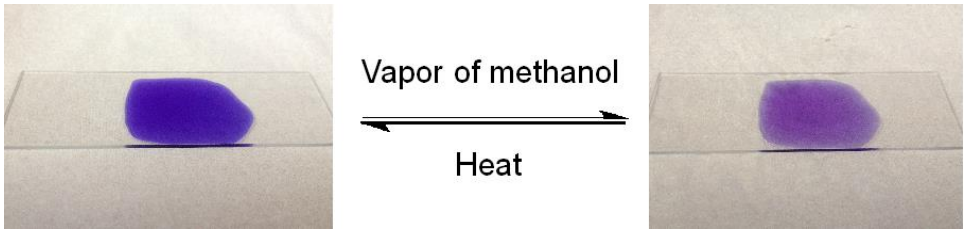

Figure 5.S21. Reversible color change of **4d** upon coordination with CH_3OH vapor.

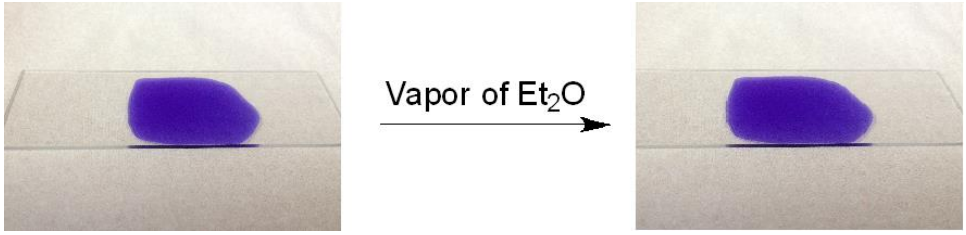

Figure 5.S22. No color change of **4d** upon exposure to Et_2O vapor.

5.6.16 Thermal stability of MCIL-BCPs 4a–f

The thermal stabilities of MCIL-BCPs **4a–f** were determined by TGA measurements using a temperature ramp rate of 10 °C $min^{-1,}$ with the samples under a dry N_2 atmosphere. Interpretation of the obtained TGA curves revealed that BCPs **4a–f** have fairly good thermal stability ($T_{decomp,}$ = 231 °C, see Figure 5.S23 for an example).

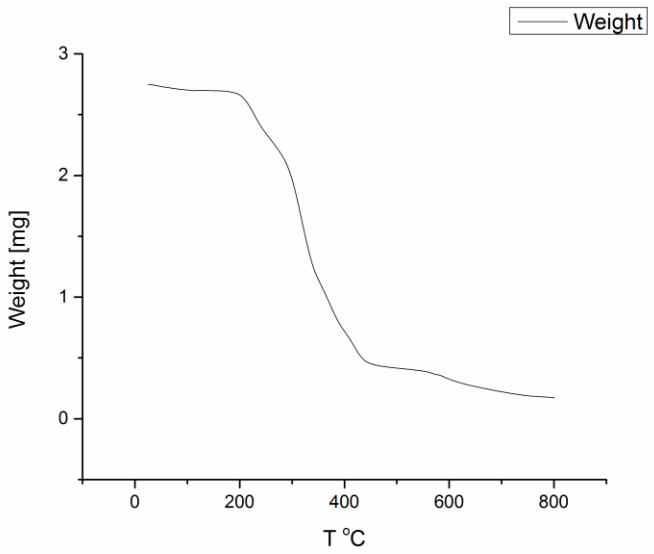

Figure 5.S23. Example TGA profile of **4d** under a dry N_2 atmosphere with a temperature ramp rate of 10 °C min^{-1}. The thermal decomposition temperature (T_{decomp}) was determined as the temperature at which 10% mass loss of the sample occurred.

5.7 References

(1) For recent reviews on poly(IL)s, see: (a) Nishimura, N.; Ohno, H. *Polymer* **2014**, *55*, 3289−3297. (b) Mecerreyes, D. *Prog. Polym. Sci.* **2011**, *36*, 1629−1648.

(2) For recent reviews on IL-based BCPs, see: (a) Meek, K. M.; Elabd, Y. A. *J. Mater. Chem. A.* **2015**, *3*, 24187−24194. (b) Yuan, J.; Mecerreyes, D.; Antonietti, M. *Prog. Polym. Sci.* **2013**, *38*, 1009−1036.

(3) For recent examples, see: (a) Liu, S.; Xu, T. *Macromolecules* **2016**, *49*, 6075−6083. (b) Sanoja, G. E.; Popere, B. C.; Beckingham, B. S.; Evans, C. M.; Lynd, N. A.; Segalman, R. A. *Macromolecules* **2016**, *49*, 2216−2223. (c) Margaretta, E.; Fahs, G. B.; Inglefield, D. L.; Jangu,

C.; Wang, D.; Heflin, J. R.; Moore, R. B.; Long, T. E. *ACS Appl. Mater. Interfaces* **2016**, *8*, 1280−1288. (d) Nykaza, J. R.; Ye, Y.; Nelson, R. L.; Jackson, A. C.; Beyer, F. L.; Davis, E. M.; Page, K.; Sharick, S.; Winey, K. I.; Elabd, Y. A. *Soft Matter* **2016**, *12*, 1133−1144. (e) Meek, K. M.; Sharick, S.; Ye, Y.; Winey, K. I.; Elabd, Y. A. *Macromolecules* **2015**, *48*, 4850−4862. (f) Jangu, C.; Wang, J. H.; Wang, D.; Fahs, G.; Heflin, J. R.; Moore, R. B.; Colby, R. H.; Long, T. E. *J. Mater. Chem. C* **2015**, *3*, 3891−3901. (g) Coupillaud, P.; Fèvre, M.; Wirotius, A.; Aissou, K.; Fleury, G.; Debuigne, A.; Detrembleur, C.; Mecerreyes, D.; Vignolle, J.; Taton, D. *Macromol. Rapid Commun.* **2014**, *35*, 422−430. (h) Shi, Z.; Newell, B. S.; Bailey, T. S.; Gin, D. L.; *Polymer* **2014**, *55*, 6664−6671. (i) Wiesenauer, E. F.; Nguyen, P. T.; Newell, B. S.; Bailey, T. S.; Noble, R. D.; Gin, D. L. *Soft Matter* **2013**, *9*, 7923−7927. (j) Choi, J. H.; Ye, Y.; Elabd, Y. A.; Winey, K. I. *Macromolecules* **2013**, *46*, 5290−5300. (k) Ye, Y.; Sharick, S.; Davis, E. M.; Winey, K. I.; Elabd, Y. A. *ACS Macro Lett.* **2013**, *2*, 575−580. (l) Nguyen, P. T.; Wiesenauer, E. F.; Gin, D. L.; Noble, R. D. *J. Membr. Sci.* **2013**, *430*, 312−320. (m) Schneider, Y.; Modestino, M. A.; McCulloch, B. L.; Hoarfrost, M. L.; Hess, R. W.; Segalman, R. A. *Macromolecules* **2013**, *46*, 1543−1548. (n) Scalfani, V. F.; Wiesenauer, E. F.; Ekblad, J. R.; Edwards, J. P.; Gin, D. L.; Bailey, T. S. *Macromolecules* **2012**, *45*, 4262−4276. (o) Weber, R. L.; Ye, Y.; Schmitt, A. L.; Banik, S. M.; Elabd, Y. A.; Mahanthappa, M. K. *Macromolecules* **2011**, *44*, 5727−5735. (p) Wiesenauer, E. F.; Edwards, J. P.; Scalfani, V. F.; Bailey, T. S.; Gin, D. L. *Macromolecules* **2011**, *44*, 5075−5078.

(4) For recent reviews on MCILs, see: (a) Santos, E.; Albo, J.; Irabien, A.; *RSC Adv.* **2014**, *4*, 40008−40018. (b) Estager, J.; Holbrey, J. D.; Swadzba-Kwasny, M. *Chem. Soc. Rev.* **2014**, *43*, 847−886.

(5) Wang, Z.; Wang, J.; Li, J.; Feng, M.; Zou, G.; Huang, X. *Chem. Commun.* **2015**, *51*, 3094−3097.

(6) (a) Patil, N. M.; Sasaki, T.; Bhanage, B. M. *ACS Sustainable Chem. Eng.* **2016**, *4*, 429−436. (b) Patil, N. M.; Sasaki, T.; Bhanage, B. M. *RSC Adv.* **2016**, *6*, 52347−52352. (c) Satapathy, A;. Gadge, S. T.; Kusumawati, E. N.; Harada, K.; Sasaki, T.; Nishio-Hamane, D.; Bhanage, B. M. *Catal. Lett.* **2015**, *145*, 824−833.

(7) Kohno, Y.; Cowan, M. G.; Masuda, M.; Bhowmick, I.; Shores, M. P.; Gin, D. L.; Noble, R. D. *Chem. Commun.* **2014**, *50*, 6633−6636.

(8) (a) Dobbelin, M.; Jovanovski, V.; Llarena, I.; Marfil, L. J. C.; Cabanero, G.; Rodriguez, J.; Mecerreyes, D. *Polym. Chem.* **2011**, *2*, 1275−1278. (b) Bonnefond, A.; Ibarra, M.; Mecerreyes, D.; Leiza, J. R. *J. Polym. Sci. A: Polym. Chem.* **2016**, *54*, 1145−1152.

(9) For recent reviews on metallocene-based BCPs, see: (a) Hailes, R. L. N.; Oliver, A. M.; Gwyther, J.; Whittell, G. R.; Manners, I. *Chem. Soc. Rev.* **2016**, *45*, 5358−5407. (b) Hardya, C. G.; Zhang, J.; Yan, Y.; Ren, L.; Tang, C. *Prog. Polym. Sci.* **2014**, *39*, 1742−1796.

(10) Mastroianni, S. E.; Patterson, J. P.; O'Reilly, R. K.; Epps, T. H. *Soft Matter*, **2013**, *9*, 10146−10154.

(11) For a recent review on RAFT polymerization, see: Moad, G. *ACS Symp. Ser.* **2015**, *1187*, 211−246.

(12) Bleach, R.; Karagoz, B.; Prakash, S. M.; Davis, T. P.; Boyer, C. *ACS Macro Lett.* **2014**, *3*, 591−596.

(13) A modified GPC method for analyzing poly(IL) MW was recently reported, but we could not modify our GPC in such a fashion: He, H.; Zhong, M.; Adzima, B.; Luebke, D.; Nulwala, H.; Matyjaszewski, K. *J. Am. Chem. Soc.* **2013**, *135*, 4227−4230.

(14) Scalfani, V. F.; Bailey, T. S. *Chem. Mater.* **2010,** *22*, 5992−6000.

(15) Floudas, G.; Vazaiou, B.; Schipper, F.; Ulrich, R.; Wiesner, U.; Iatrou, H.; Hadjichristidis, N. *Macromolecules* **2001,** *34*, 2947−2957.

(16) Hillmyer, M. A.; Bates, F. S.; Almdal, K.; Mortensen, K.; Ryan, A. J.; Fairclough, J. P. A. *Science* **1996,** *271*, 976−978.

(17) Matsen, M. W.; Bates, F. S. *Macromolecules* **1996,** *29*, 7641−7644.

(18) Scalfani, V. F.; Bailey, T. S. *Macromolecules* **2011,** *44*, 6557−6567.

(19) Cuthbert, T. J.; Harrison, T. D.; Ragogna, P. J.; Gillies, E. R. *J. Mater. Chem. B* **2016**, *4*, 4872−4883.

CHAPTER 6

Exploring the Reactivity of Co(II) Bis(salicylate)-Containing Polymers: Towards the Development of More Functional Metal-Containing Ionic Liquid-Based Block Copolymers

6.1 Abstract

The reversible coordination of Co(II) bis(salicylate)-based, metal-containing ionic liquid block copolymers (MCIL-BCPs) with common small molecules (e.g., water, alcohols, acids, ethers, etc.) was investigated. These MCIL-BCPs were found to selectively bind protic small molecules with a noticeable color change from deep blue to light purple. Room-temperature, ambient-pressure small-angle X-ray scattering (SAXS) was performed on water- or methanol-vapor-saturated MCIL-BCPs to explore any potential phase changes in the polymers induced by the small-molecule coordination. The methanol-coordinated sample showed a significant phase change from the initial gyroid (Gyr) phase to a weakly ordered liquid-like packing of spheres (S_{LLP}) morphology. The catalytic reactivity of the MCIL block of the Co(II) bis(salicylate)-based MCIL-BCP platform was also explored by investigating a cross-linked, polymerized MCIL (PMCIL) homopolymer model system as Co(II)-containing catalyst. Preliminary studies showed that this PMCIL was able to catalyze several oxidation reactions, including the autoxidation of aldehydes, epoxidation of styrene in the presence of an aldehyde substrate, and oxidation of secondary alcohols by *N*-bromosuccinimide. The crossed-linked Co(II) bis(salicylate)-based PMCIL system

showed good catalytic reactivity for the reactions tested and could be easily recovered from the reaction mixture by simple filtration.

6.2 Introduction

Metal-containing ion liquids (MCILs) are a relative new class of functional ILs that contain a metal complex as a salt component. MCILs can have interesting metal-based properties (e.g., catalytic, magnetic, optical, and molecular binding properties depending on the nature of the metal incorporated) in addition to the common properties of ILs.[1] Therefore, MCIL-based BCPs (MCIL-BCPs) with these properties and the ability to phase-separate into ordered morphologies would be desirable as new functional materials. In 2014, our group synthesized a new MCIL, tetra-*n*-butylphosphonium [cobalt(II) bis(salicylate)], that showed the ability to coordinate water and methanol molecules with a visible color change.[2] Based on this study, we synthesized and characterized the first example of a MCIL-BCP system that formed ordered microstructures in the neat state and that could reversibly coordinate protic small molecules to the Co(II) centers with an accompanying color change (see Chapter 5).[3] However, this initial work was focused on the phase tunability and microstructures of the neat MCIL-BCP system, and only limited studies on the reversible coordination was performed. Herein, in this research chapter, two aspects of reactivity for the Co(II) bis(salicylate)-based, MCIL-BCP system were investigated in terms of its interactions with small organic molecules (e.g., water, alcohols, acids, ethers, etc.): (1) phase morphology changes of the MCIL-BCP system upon reversible coordination with common small molecules; and (2) the ability of the MCIL-BCP to catalyze chemical reactions with small organic molecules.

Thus, a variety of small molecules (e.g., water, alcohols, acids, etc.) were first used to investigate the selectivity and thermal stability of the coordination chemistry based on this MCIL-BCP system. As mentioned in Chapter 1, BCP morphologies depend on the volume fraction (f) of the connected blocks and the effective degree of segregation (χN) between the blocks. Upon coordination with small molecules, both the f of the MCIL block and the χ-parameter between the two blocks could change significantly, resulting in an associated morphology change in the BCP. Therefore, the potential for a coordination-induced phase change of this MCIL-BCP system was explored by small-angle X-ray scattering (SAXS) analysis.

In addition to coordination chemistry, the possible catalytic reactivity of the MCIL-BCP introduced by the Co(II) complex was explored. Since MCILs are liquid small molecules, solid-state, phase-separated BCP analogs would be desirable for applications such as nanostructured catalytic membranes and recyclable heterogeneous catalysts. The possibility of reaction catalyzed by this MCIL-BCP system was initiated by the following observation: Upon mixing MCIL-BCPs with small aldehydes (e.g., isobutyraldehyde), an irreversible (by mild heating) color change from deep blue to brown was observed. This unusual phenomenon indicated the possible formation of Co(III) species (usually brown color) and led us to explore catalytic reactions based on Co(II) and aldehydes by this MCIL polymer material. To investigate the reactivity of the MCIL block, a cross-linked MCIL homopolymer model system was synthesized via suspension radical polymerization and explored as a heterogeneous catalyst for known reactions involving Co(II) and aldehydes (e.g., autoxidation of aldehydes[4a], epoxidation of styrene in the presence of an aldehyde[4b]).

6.3 Results and discussion

6.3.1 Reversible and selective coordination of MCIL-BCPs with small protic molecules

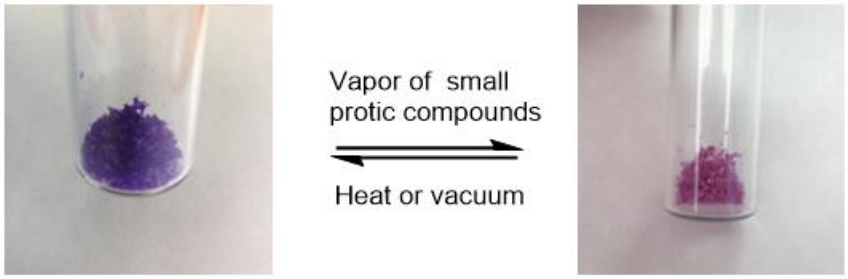

Figure 6.1. Reversible coordination of the cobalt(II) bis(salicylate)-based MCIL-BCPs with small protic molecules.

As shown in Figure 6.1, the deep blue MCIL-BCPs turned to light purple when exposed to the vapor of small protic molecules (e.g., H_2O, CH_3OH, and CH_3COOH) at room temperature and ambient pressure. The original deep blue color could be restored by mild heating or vacuum treatment of the coordinated samples. Similar reversible color change was observed when adding small protic molecules to the MCIL-BCP solution in CH_2Cl_2. Notably, no color change was observed when exposing these MCIL-BCPs under the vapor of aprotic small molecules such as diethyl ether, acetone, and ethyl acetate. Therefore, we suspect that the H-bonding between the protic molecule and the salicylate ligands of the Co(II) complex helps stabilize the coordinated structure and causes the selective binding of protic compounds over aprotic compounds. To further confirm this theory, two similar compounds (i.e., acetylacetone and ethyl acetoacetate) were used to study the selectivity of the coordination. Unlike ethyl acetoacetate, the tautomerism equilibrium

of acetylacetone favors the enol form at room temperature (Figure 6.2). Therefore, acetylacetone could be treated as protic molecule in this coordination study. The typical deep blue to light purple color change was observed when mixing the MCIL-BCP solution with acetylacetone at room temperature. In contrast, mixing the MCIL-BCP solution with ethyl acetoacetate showed no significant color change. Due to the selectivity and reversibility of the coordination chemistry described above, these MCIL-BCPs have the potential to be developed in selective separation media (i.e., sorbents, membranes) for separating small-molecule protic substrates from non-protic ones.

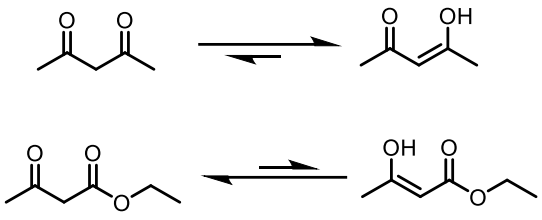

Figure 6.2. Tautomerism equilibrium of acetylacetone and ethyl acetoacetate.

As mentioned in Section 6.2, one of the goals of this MCIL-BCP system was to explore the potential phase changes induced by small-molecule coordination. Since these MCIL-BCPs were annealed at 175 °C to achieve the ordered morphologies, common small protic molecules with a broad range of boiling points were used to test the thermal stability of the coordinated MCIL-BCPs (Table 6.1). To prepare samples for thermal analysis, the MCIL-BCP and appropriate amount of the chosen small molecule were mixed in CH_2Cl_2. The CH_2Cl_2 solution was cast on a glass plate and dried in air to produce a bulk film of the small-molecule-coordinated MCIL-BCP. The glass plate was then placed on a thermal stage and heated at 5 °C/min. The thermal

decomposition temperature (T_{decomp}) of the coordinated samples was determined as the temperature at which color change of the sample occurred. Based on the T_{decomp} values of 10 coordinated MCIL-BCP samples with different small molecules, three general trends were observed for the thermal stability of these samples: (1) small molecules with higher boiling point tend to produce more thermally stable complexes (e.g., butanol vs. methanol) with the MCIL-BCP; (2) small molecules with less steric hindrance give coordinated MCIL-BCP samples with higher T_{decomp} values (e.g., benzyl alcohol vs. 2,6-dimehtylphenol); and (3) small molecules with more H-bonding donor ability increase the thermal stability of the coordinated MCIL-BCP (e.g., ethylene glycol vs. benzyl alcohol). However, even for glycerol (a non-volatile and has three H-bonding donor group) coordinated BCPs, the observed T_{decomp} of the coordinated sample is only 120 °C.

Table 6.1. Boiling points (b.p.'s) of common small protic molecules and the observed thermal decomposition temperature (T_{decomp}) of the MCIL-BCPs coordinated with these molecules. T_{decomp} was determined as the temperature at which color change of the BCP sample occurred while heating at 5 °C/min.

Small molecule coordinated	**b.p. (°C)**	$\boldsymbol{T_{decomp}}$ **(°C)**
methanol	65	30
water	100	30
acetic acid	118	40
butanol	118	50
butyric acid	164	80
ethylene glycol	197	100
2,6-dimethylphenol	203	50
benzyl alcohol	205	75
benzoic acid	249	90
glycerol	290	120

Since the decomposition temperatures of the coordinated MCIL-BCP samples are relatively low, the general thermal annealing procedure that was performed at 175 °C needed to be adjusted. Room-temperature SAXS was performed on non-coordinated MCIL-BCP samples (using MCIL-BCP **4c** as a representative example) that were annealed for 24 h at different temperatures below 120 °C. As shown in Figure 6.3, the BCP sample annealed at 80 °C showed the emergence of a cylindrical hexagonal (Hex) phase with distinct diffraction peaks, which indicated the minimum temperature required for this BCP system to form ordered morphologies within efficient annealing time. However, annealing tests of the coordinated MCIL-BCPs with T_{decomp} values above 80 °C (i.e., the butyric acid-, benzoic acid-, ethylene glycol-, and glycerol-

coordinated MCIL-BCPs) showed that the coordinated molecules were lost (partially or completely) during the 80 °C thermal annealing period.

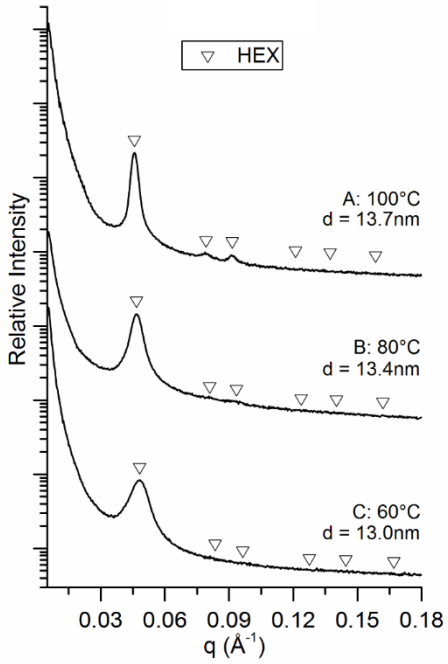

Figure 6.3. Room-temperature SAXS profiles of thermally annealed non-coordinated MCIL-BCP samples.

Due to the insufficient thermal stability of the coordinated MCIL-BCPs, room-temperature, ambient-pressure SAXS was used to investigate the phase changes of these coordinated samples instead of doing the studies at higher temperatures. For preliminary studies, samples of MCIL-BCP **4d** were first annealed at 100 °C for 24 h to form its previously reported ordered morphology (i.e., a Gyr phase) and used as a reference. The thermally annealed samples were then exposed to H_2O or CH_3OH vapor at room temperature to generate the coordinated MCIL-BCPs. SAXS

analysis of the water-coordinated samples showed no morphology changes but slightly increased domain spacing (Figure 6.4a). Interestingly, SAXS analysis of methanol-coordinated samples indicated a phase change from the initial Gyr phase to a weakly ordered, liquid-like packing of spheres (S_{LLP}) morphology (Figure 6.4b). This significant phase change could be the result of both the volume expansion of the MCIL block upon methanol coordination and the associated modified χ-parameter between the blocks.

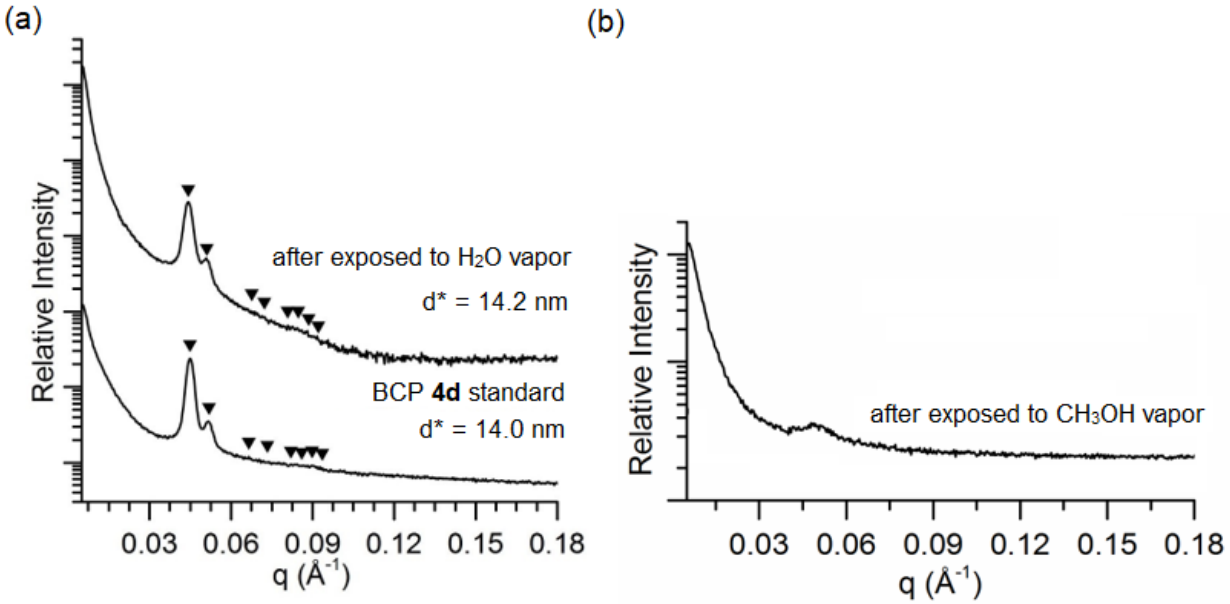

Figure 6.4. SAXS profiles of (a) thermally annealed MCIL-BCP **4d** and the water-coordinated sample after exposure to H_2O vapor at room temperature; and (b) a thermally annealed MCIL-BCP **4d** after exposure to CH_3OH vapor at room temperature.

6.3.2 Catalytic activity of a cobalt(II) bis(salicylate)-based MCIL model system

To explore the potential catalytic activity of the MCIL block, cross-linked PMCIL samples were made via modified suspension radical polymerization[5] of MCIL monomer **6** using AIBN as initiator, divinylbenzene as cross-linking agent, sodium myristate as stabilizer, and NH_4Cl as dispersing agent (Figure 6.5). In a typical suspension polymerization, MCIL monomer **6** (0.610 g, 1.26 mmol), divinylbenzene (0.0410 g, 0.315 mmol), and AIBN (2.60 mg, 0.0158 mmol) were dissolved in chlorobenzene (1 mL). Separately, sodium myristate (7.87 mg, 0.0314 mmol) and NH_4Cl (4.20 mg, 0.0314 mmol) were dissolved in H_2O (3 mL). The two solutions were combined in a round-bottom flask, degassed by three freeze-pump-thaw cycles, and back-filled with dry Ar. The resulting suspension was stirred at 80 °C for 5 h. The suspended mixture was then cooled to room temperature, filtered, washed with H_2O (3 x 10 mL) and CH_3CN (3 x 20 mL), and dried in vacuo to give the cross-linked PMCIL as a deep blue powder (yield: 0.599 g, 92%). The cross-linked PMCIL was then used as an immobilized, solid-state Co(II) catalyst to explore the catalytic reactivity inherent in the MCIL block of the cobalt(II) bis(salicylate)-based MCIL-BCP.

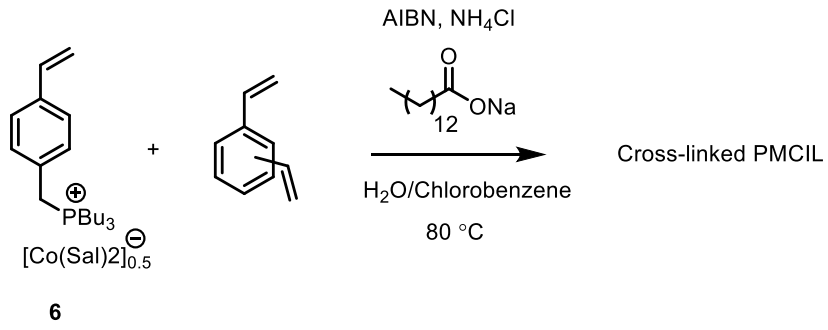

Figure 6.5. Suspension radical copolymerization of MCIL monomer **6** and divinylbenzene.

As described in Section 6.2, oxidation reactions catalyzed by Co(II) salts involving the formation of acyl radicals from aldehydes have been reported.[4] The proposed mechanisms of these reactions are summarized in Figure 6.6.[4] First, Co(II) reacts with aldehyde to form a proposed acyl-Co(III) intermediate in the presence of O_2, which could undergo hemolytic fragmentation to generate Co(II) and acyl radical. Then the acyl radical added to O_2 to produce peroxyacyl radical. Lastly, the peroxyacyl radical reacted with another aldehyde to form carboxylic acid or reacted with styrene to generate styrene oxide. Thus, the corresponding carboxylic acid is a main byproduct during the epoxidation of styrene. Therefore, the cross-linked PMCIL was tested as model polymeric catalyst for the acyl radical-mediated autoxidation of aldehyde to produce the corresponding carboxylic acid.

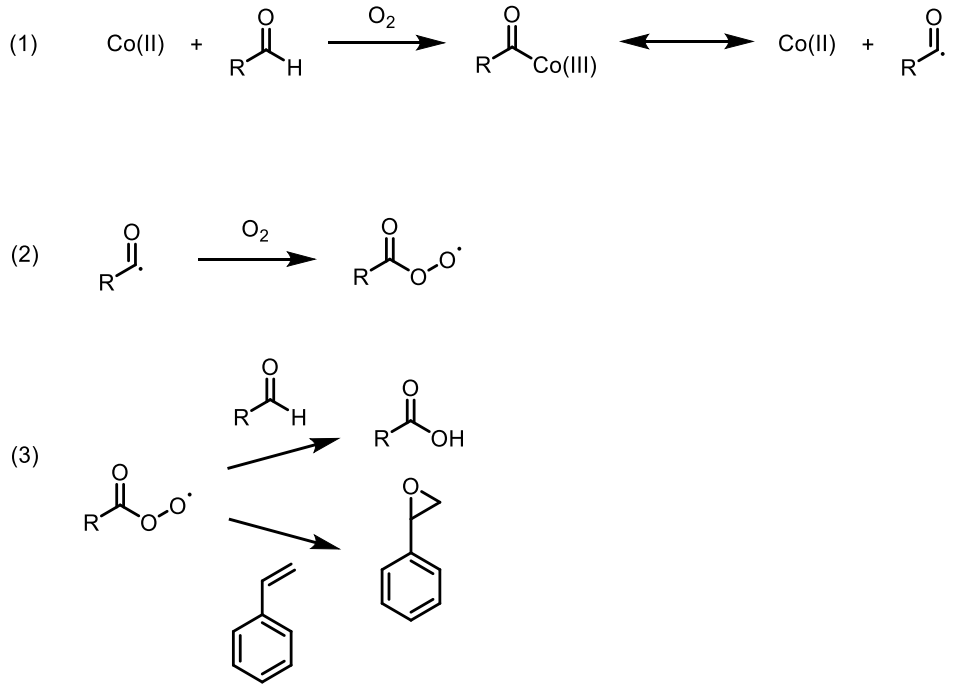

Figure 6.6. Proposed mechanism of Co(II)-catalyzed acyl radical reactions.[4]

To do this, trimethylacetaldehyde was chosen as a representative substrate for the oxidation reaction because of easy handling and the simplicity of its chemical structure (i.e., it only contains an aldehyde proton and identical methyl protons). In a typical PMCIL-catalyzed oxidation test reaction (Figure 6.7), trimethylacetaldehyde (159 mg, 1.85 mmol) and dry acetonitrile (2 mL) were added to a flame-dried Schlenk flask, degassed by three freeze-pump-thaw cycles, and back-filled with O_2. PMCIL (95.8 mg, 0.0925 mmol with respect to Co(II)) was then added. The resulting mixture was stirred at room temperature under pure O_2 (ambient pressure) for 24 h. Upon mixing PMCIL with the aldehyde solution, the deep-blue PMCIL beads turned to brown, consistent with the formation of an acyl-Co(III) intermediate. The degree of conversion of the oxidation reaction was determined by integrating and comparing distinct ^{1}H NMR signals indicative of the starting material and main product (pivalic acid). As shown in Figure 6.8, the calculated percent conversion of this catalyzed oxidation was 97.1% after 24 h. Notably, this efficient PMCIL-catalyzed oxidation also could be carried out under air at room temperature with similar conversion.

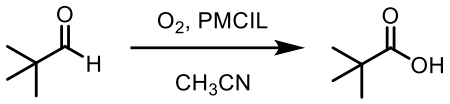

Figure 6.7. PMCIL-catalyzed aerobic oxidation of trimethylacetaldehyde.

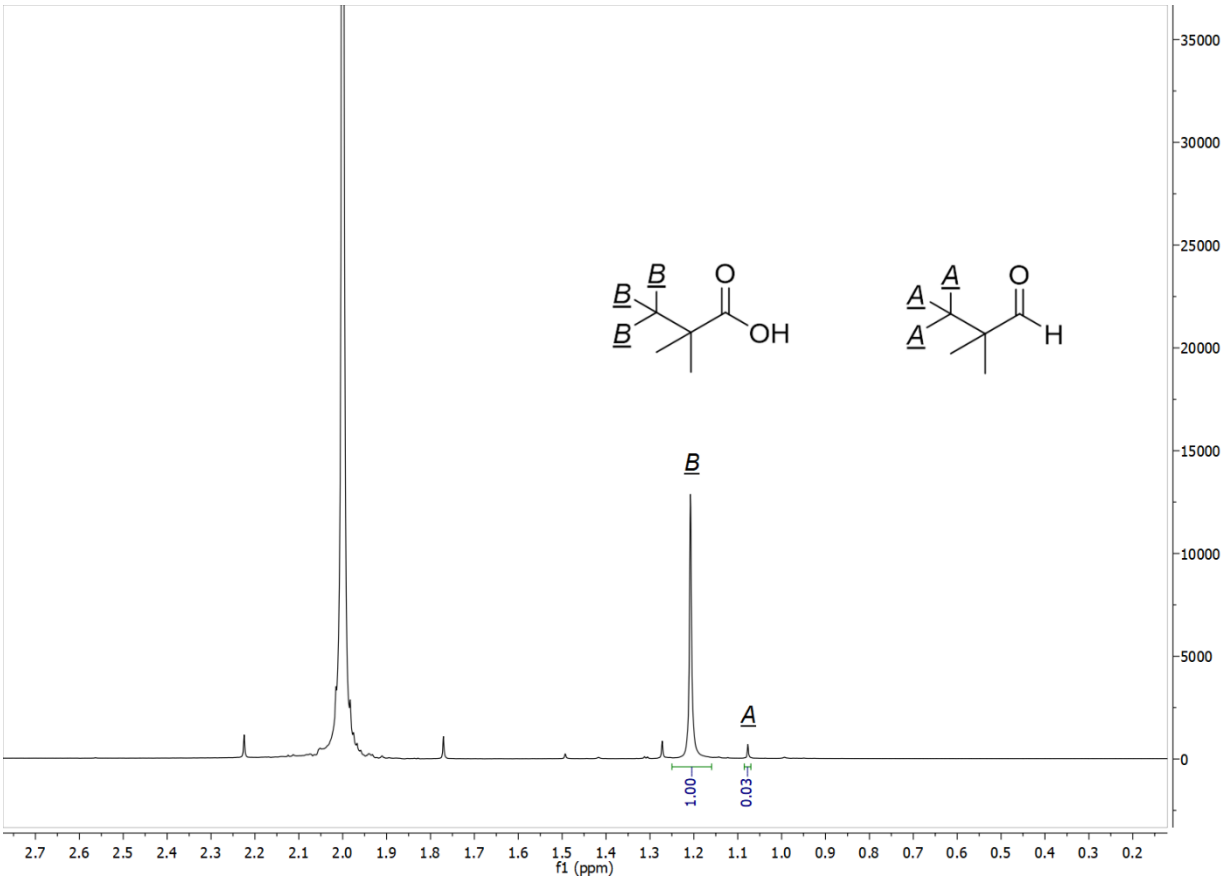

Figure 6.8. Example ^{1}H NMR spectrum of the PMCIL-catalyzed aerobic oxidation of trimethylacetaldehyde reaction mixture in CD_3CN, and the peak assignments used for calculating degree of conversion. The calculated % conversion = [1/(1 + 0.03)] x 100% = 97.1%.

As shown in Figure 6.9, the catalytic reactivity of the PMCIL catalyst system was also explored for the epoxidation of styrene in the presence of an aldehyde. In a general epoxidation reaction, styrene (107 mg, 1.03 mmol), trimethylacetaldehyde (177 mg, 2.06 mmol) and dry acetonitrile (2 mL) were added to a flame-dried Schlenk flask, degassed by three freeze-pump-thaw cycles, and back-filled with dry O_2. The PMCIL sample (100 mg, 0.103 mmol with respect to the amount of Co(II) sites) was then added. The resulting mixture was stirred at room

temperature under pure O_2 (ambient pressure) for 48 h. The conversion of the epoxidation was determined by integrating and comparing distinct ^{1}H NMR signals indicative of the styrene starting material and styrene oxide product (Figure 6.10). The calculated conversion of this PMCIL-catalyzed epoxidation was 26.5% after 24 h and 59.2% after 48 h. The degree of conversion of the epoxidation reaction is much lower compared to the aerobic oxidation of aldehydes during the same reaction time due to the slow reaction between peroxyacyl radical and styrene (Figure 6.1).[4]

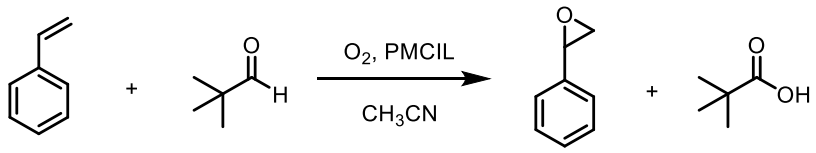

Figure 6.9. PMCIL-catalyzed epoxidation of styrene using an aldehyde as the oxidant.

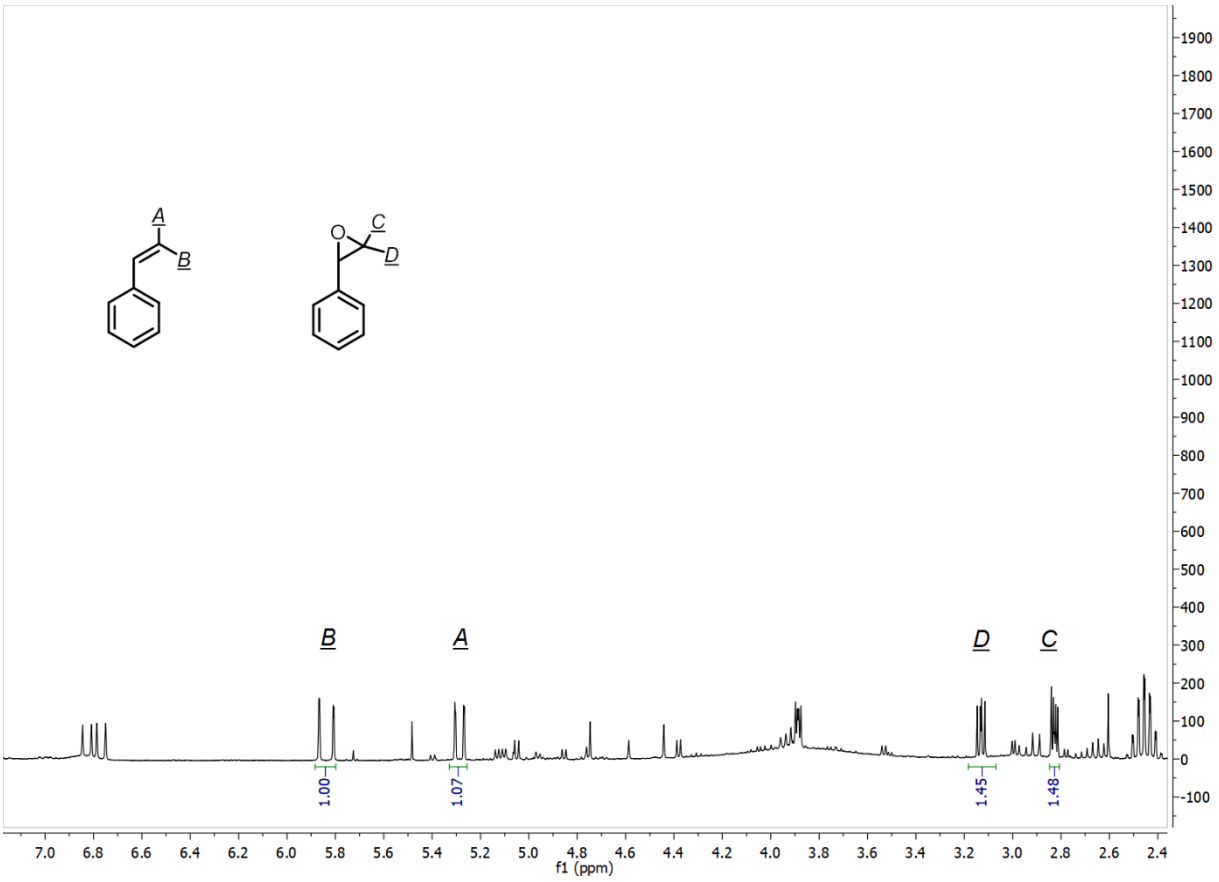

Figure 6.10. Example ^{1}H NMR spectrum of the PMCIL-catalyzed epoxidation of styrene using an aldehyde reaction mixture in CD_3CN and the peak assignments used for calculating degree of conversion. The calculated percent conversion = 1.45/(1 + 1.45) = 59.2%.

Another interesting Co(II)-catalyzed reaction reported by Sain et al. is the oxidation of secondary alcohols to ketones using *N*-bromosuccinimide (NBS) as the oxidant.[6] As shown in Figure 6.11, the proposed mechanism of this oxidation involves three steps: (1) Co(II) reacted with NBS to form Br radical and Co(III) intermediate **7**; (2) the hydrogen either form -O<u>H</u> or -C<u>H</u>-OH of the secondary alcohol was extracted by Br radical to generate intermediate **8** or **9**, respectively; and (3) these intermediates were then reacted with intermediate **7** to produce the ketone product

and regenerate the Co(II) catalyst. To investigate the reactivity of this type of oxidation using the PMCIL as catalyst, cyclohexanol was used as a representative substrate (Figure 6.12). In a typical procedure, cyclohexanol (146 mg, 1.46 mmol), NBS (260 mg, 1.46 mmol), and dry acetonitrile (3 mL) were added to a flame-dried round bottom flask equipped with a reflux condenser. The PMCIL (62 mg, 0.07 mmol with respect to Co(II) sites) was then added, and the resulting mixture was stirred at 75 °C for 2 h. The contents of the flask were cooled to room temperature, filtered, and concentrated. The resulting oil was purified by passage through a silica plug rinsed with hexanes (20 mL). The filtrate was concentrated and dried in vacuo to give cyclohexanone as a colorless liquid (yield: 93.5 mg, 65.2%).

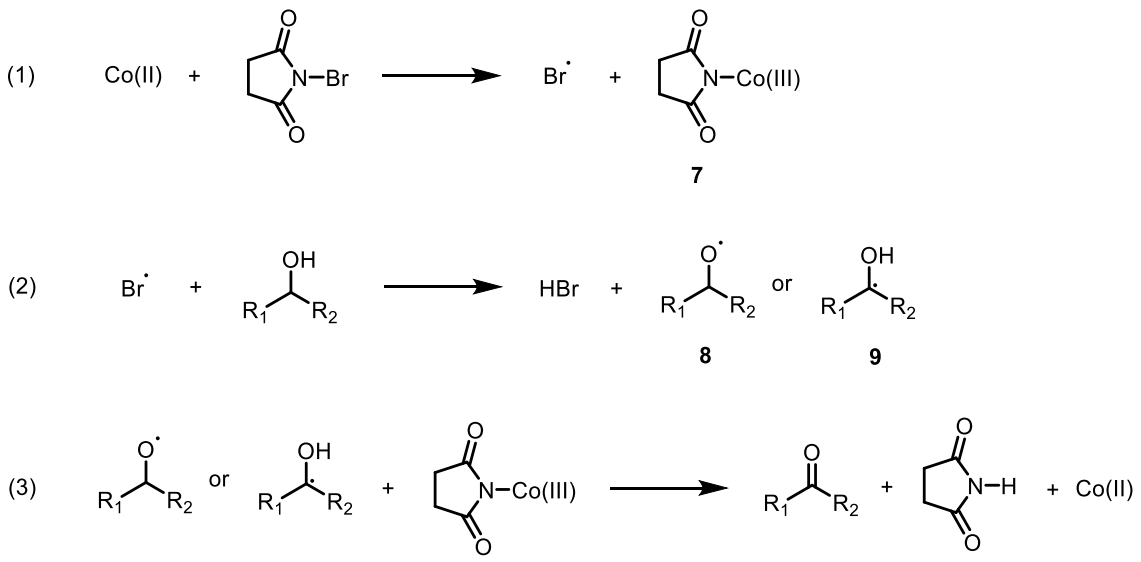

Figure 6.11. Proposed mechanism of the Co(II)-catalyzed oxidation of secondary alcohols in the presence of NBS.[6]

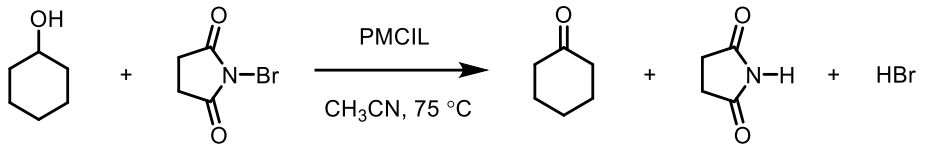

Figure 6.12. PMCIL-catalyzed oxidation of secondary alcohols in the presence of NBS.

6.4 Summary

The reactivity of the cobalt(II) bis(salicylate)-based MCIL-BCP system prepared in Chapter 5 was explored with focus on the reversible binding properties of the BCP with small molecules and its catalytic performance for several oxidation reactions. The MCIL-BCP undergoes a color change from deep blue to light purple upon exposure to the vapor of small protic molecules (e.g., H_2O, CH_3OH, etc.), while no color change was observed upon exposure to aprotic molecule vapors (e.g., Et_2O, acetone, ethyl acetate). Room-temperature, ambient-pressure SAXS analysis on thermally annealed MCIL-BCP **4d** after exposure to CH_3OH vapor showed a significant phase change from Gyr to S_{LLP}. These initial SAXS studies indicated the potential for coordination-induced phase change for this Co(II)-based MCIL-BCP system.

To explore the potential catalytic properties of the MCIL block in the cobalt(II) bis(salicylate)-based MCIL-BCP system, a cross-linked PMCIL containing the cobalt(II) bis(salicylate)-based repeat unit was explored as immobilized Co(II) catalyst for several oxidation reactions (i.e., aerobic oxidation of aldehydes, epoxidation of styrene using an aldehyde, and oxidation of secondary alcohols using NBS). For all the reactions tested, the PMCIL exhibited decent catalytic reactivity, especially for the aerobic oxidation of aldehydes (97.1% conversion). Notably, the PMCIL catalyst could be easily removed from the reaction mixture and recovered by simple filtration. Combining the catalytic reactivity with the architecture and processability of the

polymer materials, MCIL-based homopolymers and BCPs have the potential to be applied as recyclable catalysts, catalytic membranes and aldehyde decontamination materials.

6.5 References

(1) For recent reviews on metal-containing ILs, see: (a) Yoshida, Y.; Saito, G. Progress in paramagnetic ionic liquids. In *Ionic Liquids: Theory, Properties, New Approaches*; Kokorin, A., Ed.; InTech, 2011. 723−739. (b) Estager, J.; Holbrey, J. D.; Swadz´ba-Kwas´ny, M. *Chem. Soc. Rev.* **2014**, *43*, 847−886.

(2) Kohno, Y.; Cowan, M. G.; Masuda, M.; Bhowmick, I.; Shores, M. P.; Gin, D. L.; Noble, R. D. *Chem. Commun.* **2014**, *50*, 6633−6636.

(3) Shi, Z.; May, A. W.; Kohno, Y.; Bailey, T. S.; Gin, D. L. *J. Polym. Sci. A: Polym. Chem.* **2017**, *55*, 2961−2965.

(4) (a) Punniyamurthy, T.; Bhatia, B.; Iqbal, J. *J. Org. Chem.* **1994**, *59*, 850−853. (b) Nam, W.; Kim, H. J.; Kim, S. H.; Ho, R. Y. N.; Valentine, J. S. *Inorg. Chem.* **1996**, *35*, 1045−1049.

(5) Jo, Y-D.; Park, K-S.; Ahn, J-H.; Ihm, S-K. *Eur. Polym. J.* **1996,** *32*, 967−972.

(6) Sharma, V. B.; Jain, S. L.; Sain, B. *J. Mol. Catal. A: Chem.* **2005,** *227*, 47−49.

CHAPTER 7

Summary and Suggestions for Future Work

7.1 Thesis objectives

The overall objectives of this Ph.D. thesis work were to: (1) synthesize a new organic-IL-based BCP platform via ATRP and explore the morphological phase behavior of this BCP system; and (2) synthesize ordered, phase-separated, MCIL-BCPs via RAFT and investigate the reactivity of the Co(II)-containing block. The first objective was motivated by the first-generation of PIL-BCPs developed by our group that showed improved gas transport with ordered microstructures.[1] However, there were several limitations (e.g., expensive polymerization catalyst, complicated synthesis, etc.) with this initial PIL-BCP system that hampered exploration of these materials as new functional materials, and no Gyr phase was observed for this BCP system. Therefore, a new PIL-BCP system was synthesized via ATRP with good molecular-weight control and side-chain tunability. The Gyr phase was obtained by replacing the alkyl group on the imidazolium monomer from methyl to *n*-butyl. The second objective was inspired by the new Co(II)-containing MCIL synthesized by our group that showed reversible molecular binding properties for H_2O and CH_3OH.[2] The synthesis of ordered, phase-separated MCIL-BCPs was unprecedented prior to the work presented in this thesis work. Thus, new MCIL-BCPs were synthesized via RAFT polymerization and showed the formation of ordered microstructures (including Gyr phase) in their neat melt state. The reactivities of these Co(II)-containing MCIL-BCPs were explored to determine potential applications of these materials.

7.2 Summary of thesis accomplishments

As described in Chapter 3, a series of PS-*b*-PIL BCPs with 50 total repeat units and different block compositions (i.e., 25-*b*-25, 20-*b*-30, and 15-*b*-35) were synthesized via sequential ATRP of styrene and styrenic imidazolium monomers with different alkyl side chains (i.e., methyl, *n*-butyl, *n*-decyl). Kinetic studies on the block copolymerization of styrene with imidazolium monomers showed first order kinetics, which confirmed the controlled polymerization behavior of this polymerization technique. The block lengths and molecular weights of these PIL-BCPs were determined by ^{1}H NMR end-group analysis. SAXS analysis on methyl- and *n*-butyl-substituted BCPs showed the formation of ordered morphologies (i.e., S_{BCC}, Hex, and Lam) in their neat states depending on the block composition ratios, while the *n*-decyl-substituted BCPs were all disordered under the same conditions. This initial SAXS study indicated that the R group modification on the imidazolium units has a direct impact on the BCP morphology.

Following this work, the phase behavior of the PS-*b*-PIL system was further explored by tuning the volume fractions of the PIL block and the R group modification (i.e., methyl, *n*-propyl, *n*-butyl, and *n*-hexyl) on the imidazolium (Chapter 4). Methyl-substituted PIL-BCPs with PIL block volume fractions ranging from 33% to 89% were synthesized via ATRP to cover a wide range of phase diagram, especially on the IL-rich side. The volume fractions were calculated based on the BCP sample that showed nearly complete suppression of the even-order reflection at $q/q^* = \sqrt{4}$ (i.e., equal volumes of each block). SAXS studies on these methyl-substituted PIL-BCPs showed the formation of ordered morphologies including S_{LLP}, S_{BCC}, Hex, Lam phases, and persistent coexistence of Lam and Hex phases. The persistent coexistence of Lam and Hex phases indicated that the χ-parameter between the blocks was too high to form a stable Gyr phase. By replacing the methyl side-chain on the imidazolium Tf_2N^- PIL repeat units with an *n*-butyl group,

the *n*-butyl-substituted PIL-BCP showed the emergence of a Gyr phase coexisting with a Hex phase after extended thermal annealing. Additionally, the phase behavior of *n*-propyl-substituted BCPs (similar to methyl-substituted BCPs) and *n*-hexyl-substituted BCPs (only weekly ordered) were investigated. Based on these results, we have demonstrated the ability to tune χ-parameter by modification of the alkyl side-chain on the imidazolium and showed promise to obtain Gyr phase in highly segregated PIL-BCP system.

Chapter 5 detailed the synthesis of new Co(II)-containing MCIL-BCPs via sequential RAFT polymerization of butyl methacrylate and an MCIL monomer. The controlled polymerization behavior for the block copolymerization of butyl methacrylate with MCIL monomer was confirmed by kinetic studies. The absolute lengths and block composition ratios of these MCIL-BCPs were confirmed by ^{1}H NMR analysis. SAXS analysis on the MCIL-BCPs indicated their ability to form all four classic morphologies of diblock copolymers (i.e., S, Hex, Lam and notably Gyr phases). The molecular binding properties of these MCIL-BCPs were investigated by exposing the BCPs under the vapor of small molecules. The deep blue MCIL-BCPs turned to light purple upon exposure to the vapors of protic small molecules (e.g., H_2O, CH_3OH, etc.), while no color change was observed when exposed to the vapor of aprotic small molecules (e.g., diethyl ether, acetone, etc.).

Based on this study, the coordination chemistry and catalytic reactivities of the MCIL block were further explored (Chapter 6). Thermal analysis on BCP samples coordinated to protic small molecules with a broad range of boiling point showed that the decomposition temperatures of these coordinated BCPs were relatively low (below 120 °C). The potential coordination-induced phase change was investigated by comparing the room-temperature, ambient-pressure SAXS profiles of the thermally annealed BCP samples before and after exposure to H_2O or CH_3OH. The H_2O-

coordinated samples maintained the same phase with a larger domain spacing. The CH_3OH saturated samples showed significant phase change from Gyr to S_{LLP}, which provided evidence for the proposed coordination-induced phase change. The catalytic reactivates of the MCIL block were explored for three known oxidation reactions catalyzed by Co(II) (i.e., aerobic oxidation of aldehydes, epoxidation of styrene, and oxidation of secondary alcohols). Cross-linked PMCILs were synthesized by suspension polymerization and tested as Co(II)-containing catalysts. Preliminary results showed decent catalytic reactivities and easy recovery of these PMCIL catalysts.

7.3 Suggestions for future work

7.3.1 Structure modification of the neutral block in the PS-*b*-PIL system to achieve a pure gyroid phase

As described in Chapter 4, the high χ parameter between PS block and PIL block in the highly segregated PS-*b*-PIL system hindered the formation of a pure Gyr phase. To lower the χ parameter, we synthesized a series of *n*-butyl-substituted PIL-BCPs that formed Gyr morphology in the neat state. However, this Gyr phase was coexistent with Hex phase even after extended thermal annealing. Addition to the alkyl group modification on the imidazolium units, the miscibility of the two blocks also could be increased by introducing polar groups (e.g., -OH, -COOH, etc.) to the neutral block. Since these polar groups have the potential to interfere with the Cu/ligand catalyst system, metal-free controlled radical polymerization (e.g., NMP and RAFT polymerization) should be used instead of ATRP. For example, new PIL-BCPs containing hydroxy or carboxylic acid groups in the uncharged block could be synthesized via sequential RAFT

polymerization (Figure 7.1). These modified BCPs with more polar neutral block could provide another approach to achieve a pure Gyr phase for organic-IL-based BCPs.

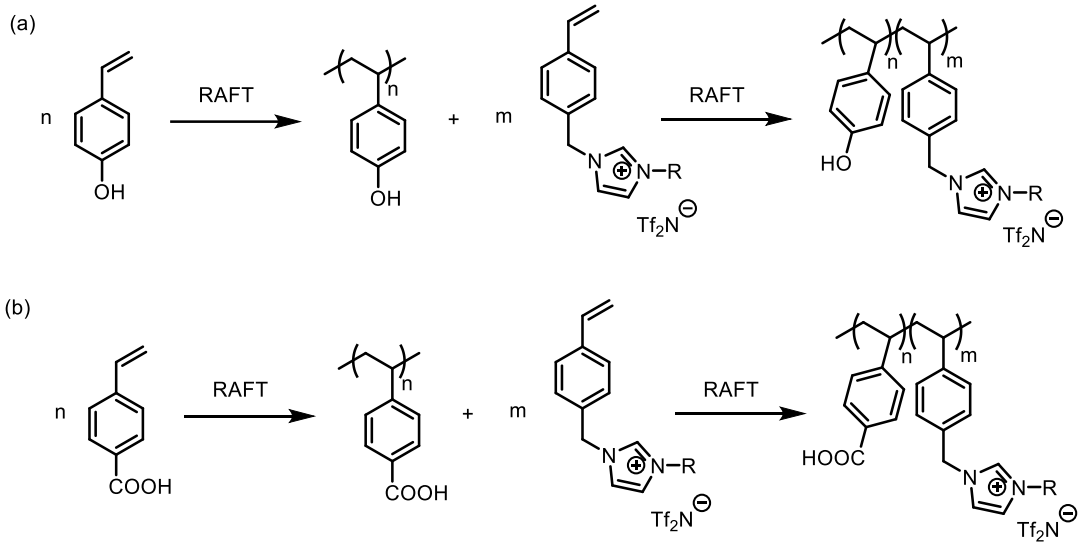

Figure 7.1. Examples of the synthesis of new PIL-BCPs containing (a) a hydroxy-substituted uncharged block and (b) a carboxylic acid-substituted uncharged block.

7.3.2 Investigate the reversible phase change of the PBMA-*b*-PMCIL system induced by small-molecule coordination

Preliminary SAXS studies on the Gyr-phase-forming MCIL-BCPs after exposure to the vapor of H_2O or CH_3OH showed the potential for coordination-induced phase change (see Chapter 6). To better understand this phase behavior, other ordered, phase-separated BCP samples (i.e., S, Hex, and Lam-phase-forming BCPs) could be tested under the same conditions. Additionally, the coordination chemistry of these MCIL-BCPs could be further explored by applying the vapor of small acids (e.g., acetic acid) and other small alcohols (e.g., ethanol, *n*-propanol, etc.). Then, the

reversibility of the coordination-induced phase changes of these MCIL-BCPs can be investigated by vacuum treatment or mild heating of the coordinated samples. If the original morphology can be restored by either method, then these materials will be promising candidates for use as responsive materials and chemical sensing materials.

7.3.3 Expand the scope of PMCIL-catalyzed oxidation reactions

As presented in Chapter 6, cross-linked PMCILs can be applied as Co(II)-containing catalysts for several oxidation reactions. However, the catalytic reactivities of the Co(II) catalyst are not limited to these types of reactions. For example, Iqbal et al. reported the synthesis of 1,2-diones from aromatic aldehydes catalyzed by Co(II) in the presence of acetic anhydride.[3a] This reaction provides a straightforward approach to make 1,2-dicarbonyl compounds in organic synthesis. Another example is the Co(II)/trifluoracetic acid-catalyzed oxidative esterification of aldehydes and alcohols reported by Zhang and co-workers.[3b] The direct formation of esters from aldehydes is a promising method in applications such as natural products synthesis. Therefore, the reactivities of the PMCIL catalyst could be explored for these two reactions to expand the functionality of the MCIL polymers (see Figure 7.2 for examples). Based on the catalytic performance of the MCIL polymers, they can be investigated as new functional materials for future applications such as recyclable catalysts, catalytic coatings, and aldehyde decontamination materials.

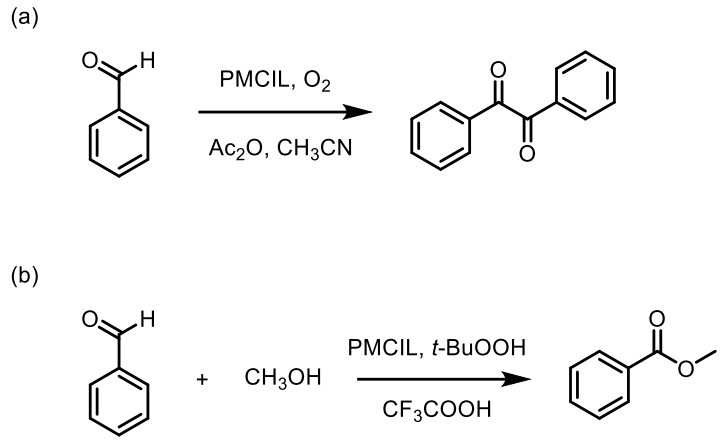

Figure 7.2. Examples of the proposed PMCIL catalyzed reactions: (a) oxidative coupling of aromatic aldehydes and (b) oxidative esterification of aldehydes.

7.4 References

(1) (a) Wiesenauer, E. F.; Edwards, J. P.; Scalfani, V. F.; Bailey, T. S.; Gin, D. L. *Macromolecules* **2011**, *44*, 5075−5078. (b) Nguyen, P. T.; Wiesenauer, E. F.; Gin, D. L.; Noble, R. D. *J. Membr. Sci.* **2013**, *430*, 312−320.

(2) Kohno, Y.; Cowan, M. G.; Masuda, M.; Bhowmick, I.; Shores, M. P.; Gin, D. L.; Noble, R. D. *Chem. Commun.* **2014**, *50*, 6633−6636.

(3) (a) Punniyamurthy, T.; Karla, S. J. S.; Iqbal, J. *Tetrahedron Lett.* **1994**, *35*, 2959−2960. (b) Mahmood, S.; Li, T.; Xu, B.; Guo, Y.; Zhang, S. *Asian J. Org. Chem.* **2017**, *6*, 768−774.

BIBLIOGRAPHY

Adzima, B. J.; Venna, S. R.; Klara, S. S.; He, H.; Zhong, M.; Luebke, D. R.; Mauter, M. S.; Matyjaszewski, K.; Nulwala, H. B. *J. Mater. Chem. A* **2014**, *2*, 7967−7972.

Agudelo, N. A.; Elsen, A. M.; He, H.; López, B. L.; Matyjaszewski, K. *J. Polym. Sci. A: Polym. Chem.* **2015**, *53*, 228−238.

Bailey, T. S.; Hardy, C. M.; Epps, T. H.; Bates, F. S. *Macromolecules* **2002**, *35*, 7007−7017.

Bara, J. E.; Hatakeyama, E. S.; Gin, D. L.; Noble, R. D. *Polym. Adv. Technol.* **2008**, *19*, 1415−1420.

Bara, J. E.; Lessmann, S.; Gabriel, C. J.; Hatakeyama, E. S.; Noble, R. D.; Gin, D. L. *Ind. Eng. Chem. Res.* **2007**, *46*, 5397−55404.

Bates, F. S. *Science* **1991**, *251*, 898−905.

Bates, F. S.; Fredrickson, G. H. *Phys. Today* **1999**, *52*, 32−38.

Bates, F. S.; Schulz, M. F.; Khandpur, A. K.; Förster, S.; Rosedale, J. H.; Almdal, K.; Mortensen, K. *Faraday Discuss.* **1994**, *98*, 7−18.

Bendejacq, D.; Ponsinet, V.; Joanicot, M.; Loo, Y. L.; Register, R. A. *Macromolecules* **2002**, *35*, 6645−6649.

Bleach, R.; Karagoz, B.; Prakash, S. M.; Davis, T. P.; Boyer, C. *ACS Macro Lett.* **2014**, *3*, 591−596.

Bonnefond, A.; Ibarra, M.; Mecerreyes, D.; Leiza, J. R. *J. Polym. Sci. A: Polym. Chem.* **2016**, *54*, 1145−1152.

Cabral, H.; Miyata, K.; Osada, K.; Kataoka, K.; *Chem. Rev.* **2018**, *118*, 6844−6892.

Carrasco, P. M.; Tzounis, L.; Mompean, F. J.; Strati, K.; Georgopanos, P.; Garcia-Hernandez, M.; Stamm, M.; Cabanero, G.; Odriozola, I.; Avgeropoulos, A.; Garcia, I. *Macromolecules* **2013**, *46*, 1860−1867.

Chanthad, C.; Masser, K. A.; Xu, K.; Runt, J.; Wang, Q. *J. Mater. Chem.* **2012**, *22*, 341−344.

Chi, W. S.; Hong, S. U.; Jung, B.; Kang. S. W.; Kang, Y. S.; Kim, J. H. *J. Membr. Sci.* **2013**, *443*, 54−61.

Choi, J.; Ye, Y.; Elabd, Y. A.; Winey, K. I. *Macromolecules* **2013**, *46*, 5290−5300.

Chu, J. H.; Rangarajan, P.; Adams, J. L.; Register, R. A. *Polymer* **1995**, *36*, 1569−1575.

Cochran, E. W.; Garcia-Cervera, C. J.; Fredrickson, G. H. *Macromolecules* **2006**, *39*, 2449−2451.

Coupillaud, P.; Fèvre, M.; Wirotius, A.; Aissou, K.; Fleury, G.; Debuigne, A.; Detrembleur, C.; Mecerreyes, D.; Vignolle, J.; Taton, D. *Macromol. Rapid Commun.* **2014**, *35*, 422−430.

Crossland, E. J. W.; Nedelcu, M.; Ducati, C.; Ludwigs, S.; Hillmyer, M. A.; Steiner, U.; Snaith, H. J. *Nano Lett.* **2009**, *9*, 2813−2819.

Cuthbert, T. J.; Harrison, T. D.; Ragogna, P. J.; Gillies, E. R. *J. Mater. Chem. B* **2016**, *4*, 4872−4883.

Davidock, D. A.; Hillmyer, M. A.; Lodge, T. P. *Macromolecules* **2003**, *36*, 4682−4685.

Ding, S.; Tang, H.; Radosz, M.; Shen, Y. *J. Polym. Sci. A: Polym. Chem.* **2004**, *42*, 5794−5801.

Dobbelin, M.; Jovanovski, V.; Llarena, I.; Marfil, L. J. C.; Cabanero, G.; Rodriguez, J.; Mecerreyes, D. *Polym. Chem.* **2011**, *2*, 1275−1278.

Dong, K.; Liu, X.; Dong, H.; Zhang, X.; Zhang, S. *Chem. Rev.* **2017**, *117*, 6636−6695.

Drzal, P. L.; Halasa, A. F.; Kofinas, P. *Polymer* **2000**, *41*, 4671−4677.

Elabd, Y. A.; Hickner, M. A. *Macromolecules* **2011**, *44*, 1−11.

Epps, T. H.; Bailey, T. S.; Waletzko, R.; Bates, F. S. *Macromolecules* **2003**, *36*, 2873−2881.

Epps, T. H.; Cochran, E. W.; Bailey, T. S.; Waletzko, R. S.; Hardy, C. M.; Bates, F. S. *Macromolecules* **2004**, *37*, 8325−8341.

Estager, J.; Holbrey, J. D.; Swadz´ba-Kwas´ny, M. *Chem. Soc. Rev.* **2014**, *43*, 847−886.

Fan, W.; Wang, L.; Zheng, S. *Macromolecules* **2009**, *42*, 327−336.

Fetters, L. J.; Lohse, D. J.; Richter, D.; Witten, T. A.; Zirkel, A. *Macromolecules* **1994**, *27*, 4639−4647.

Floudas, G.; Vazaiou, B.; Schipper, F.; Ulrich, R.; Wiesner, U.; Iatrou, H.; Hadjichristidis, N. *Macromolecules* **2001**, *34*, 2947−2957.

Förster, S.; Timmann, A.; Konrad, M.; Schellbach, C.; Meyer, A.; Funari, S. S.; Mulvaney, P.; Knott, R. *J. Phys. Chem. B* **2005**, *109*, 1347−1360.

Fukushima, T.; Kosaka, A.; Yamamoto, Y.; Aimiya, T.; Notazawa, S.; Takigawa, T.; Inabe, T.; Aida, T. *Small* **2006**, *2*, 554−560.

Gao, R.; Wang, D.; Heflin, J. R.; Long, T. E. *J. Mater. Chem.* **2012**, *22*, 13473−13476.

Gohy, J.; Zhao, Y. *Chem. Soc. Rev.* **2013**, *42*, 7117−7129.

Greaves, T. L.; Drummond, C. J. *Chem. Rev.* **2015**, *115*, 11379−11448.

Green, M. D.; Choi, J.-H.; Winey, K. I.; Long, T. E. *Macromolecules* **2012**, *45*, 4749−4757.

Green, M. D.; Long, T. E. *J. Macromol. Sci. C: Polym. Rev.* **2009**, *49*, 291−314.

Green, M. D.; Wan, D.; Hemp, S. T.; Choi, J.-H.; Winey, K. I.; Heflin, J. R.; Long, T. E. *Polymer* **2012**, *53*, 3677−3686.

Green, O.; Grubjesic, S.; Lee, S.; Firestone, M. A. *J. Macromol. Sci. C: Polym. Rev.* **2009**, *49*, 339−360.

Gu, Y.; Timothy P. Lodge, T. P. *Macromolecules* **2011**, *44*, 1732−1736.

Guo, C.; Bailey, T. S. *Soft Matter* **2010,** *6*, 4807−4818.

Hadjichristidis, N.; Pitsikalis, M.; Iatrou, H. *Adv. Polym. Sci.* **2005**, *189*, 1−124.

Hailes, R. L. N.; Oliver, A. M.; Gwyther, J.; Whittell, G. R.; Manners, I. *Chem. Soc. Rev.* **2016**, *45*, 5358−5407.

Hajduk, D. A.; Gruner, S. M.; Rangarajan, P.; Register, R. A.; Fetters, L. J.; Honeker, C.; Albalak, R. J.; Thomas, E. L. *Macromolecules* **1994**, *27*, 490−501.

Hajduk, D. A.; Harper, P. E.; Gruner, S. M.; Honeker, C. C.; Kim, G.; Thomas, E. L.; *Macromolecules* **1994**, *27*, 4063−4075.

Hajduk, D. A.; Takenouchi, H.; Hillmyer, M. A.; Bates, F. S.; Vigild, M. E.; Almdal, K. *Macromolecules* **1997**, *30*, 3788−3795.

Hamley, I. W.; O'Driscoll, B. M. D.; Lotze, G.; Moulton, C.; Allgaier, J.; Frielinghaus, H. *Macromol. Rapid Commun.* **2009**, *30*, 2141−2146.

Han, G. L.; Xu, P. Y.; Zhou, K.; Zhang, Q. G.; Zhu, A. M.; Liu. Q. L. *J. Membr. Sci.* **2014**, *464*, 72−79.

Hardya, C. G.; Zhang, J.; Yan, Y.; Ren, L.; Tang, C. *Prog. Polym. Sci.* **2014**, *39*, 1742−1796.

He, H.; Averick, S.; Roth, E.; Luebke, D.; Nulwala, H.; Matyjaszewski, K. *Polymer* **2014**, *55*, 3330−3338.

He, H.; Luebke, D.; Nulwala, H.; Matyjaszewski, K. *Macromolecules* **2014**, *47*, 6601−6609.

He, H.; Zhong, M.; Adzima, B.; Luebke, D.; Nulwala, H.; Matyjaszewski, K. *J. Am. Chem. Soc.* **2013**, *135*, 4227−4230.

He, H.; Zhong, M.; Luebke, D.; Nulwala, H.; Matyjaszewski, K. *J. Polym. Sci. A: Polym. Chem.* **2014**, *52*, 2175−2184.

He, X.; Yang, W.; Pei, X. *Macromolecules* **2008**, *41*, 4615−4621.

Hillmyer, M. A.; Bates, F. S.; Almdal, K.; Mortensen, K.; Ryan, A. J.; Fairclough, J. P. A. *Science* **1996,** *271*, 976−978.

Ho, H. A.; Leclerc, M. *J. Am. Chem. Soc.* **2003**, *125*, 4412−4413.

Hu, H.; Yuan, W.; Zhao, H.; Baker, G. L. *J. Polym. Sci. A: Polym. Chem.* **2014**, *52*, 121−127.

Jaeger, W.; Bohrisch, J.; Laschewsky, A. *Prog. Polym. Sci.* **2010**, *35*, 511−577.

Jangu, C.; Wang, J. H.; Wang, D.; Fahs, G.; Heflin, J. R.; Moore, R. B.; Colby, R. H.; Long, T. E. *J. Mater. Chem. C* **2015**, *3*, 3891−3901.

Jangu, C.; Wang, J. H.; Wang, D.; Sharick, S.; Heflin, J. R.; Winey, K. I.; Colby, R. H.; Long, T. E. *Macromol. Chem. Phys.* **2014**, *215*, 1319−1331.

Jo, Y-D.; Park, K-S.; Ahn, J-H.; Ihm, S-K. *Eur. Polym. J.* **1996,** *32*, 967−972.

Karjalainen, E.; Chenna, N.; Laurinm¨aki, P.; Butcher, S. J.; Tenhu, H. *Polym. Chem.* **2013**, *4*, 1014−1024.

Karjalainen, E.; Izquierdo, D. F.; Marti-Centelles, V.; Luis, S. V.; Tenhu, H.; Garcia-Verdugo. E. *Polym. Chem.* **2014**, *5*, 1437−1446.

Kim, H.; Park, S.; Hinsberg, W. *Chem. Rev.* **2010**, *110*, 146−177.

Kim, J. K.; Han, C. D. *Adv. Polym. Sci.* **2010**, *231*, 77−145.

Kim, J. K.; Yang, S. Y.; Lee, Y.; Kim, Y. *Prog. Polym. Sci.* **2010**, *35*, 1325−1349.

Kinning, D. J.; Thomas, E. L. *Macromolecules* **1984**, *17*, 1712−1718.

Kohno, Y.; Cowan, M. G.; Masuda, M.; Bhowmick, I.; Shores, M. P.; Gin, D. L.; Noble, R. D. *Chem. Commun.* **2014**, *50*, 6633−6636.

Lee, S.; Bluemle, M. J.; Bates, F. S. *Science* **2010**, *330*, 349−353.

Lee, Y.; Gomez, E. D. *Macromolecules* **2015**, *48*, 7385−7395.

Lei, Z.; Dai, C.; Chen, B. *Chem. Rev.* **2014**, *114*, 1289−1326.

Li, J.; Liang, J.; Wu, W.; Zhang, S.; Zhang, K.; Zhou, H. *New J. Chem.* **2014**, *38*, 2508−2513.

Li, L.; Schulte, L.; Clausen, L. D.; Hansen, K. M.; Jonsson, G. E.; Ndoni, S. *ACS Nano* **2011**, *5*, 7754−7766.

Li, X.; Iocozzia, J.; Chen, Y.; Zhao, S.; Cui, X.; Wang, W.; Yu, H.; Lin, S.; Lin, Z. *Angew. Chem. Int. Ed.* **2018**, *57*, 2046−2070.

Lipic, P. M.; Bates, F. S.; Matsen, M. W. *J. Polym. Sci. B Polym. Phys.* **1999**, *37*, 2229−2238.

Liu, S.; Xu, T. *Macromolecules* **2016**, *49*, 6075−6083.

Long, S.; Wan, F.; Yang, W.; Guo, H.; He, X.; Ren, J.; Gao, J. *J. Appl. Polym. Sci.* **2013**, *130*, 2680−2687.

Lu, J.; Yan, F.; Texter, J. *Prog. Polym. Sci.* **2009**, *34*, 431−448. (d) Anderson, E.; Long, T. *Polymer* **2010**, *51*, 2447−2454.

Luo, M.; Epps, T. H. III. *Macromolecules* **2013**, *46*, 7567−7579.

Lynd, N. A.; Hillmyer, M. A. *Macromolecules* **2005**, *38*, 8803−8810.

Mahmood, S.; Li, T.; Xu, B.; Guo, Y.; Zhang, S. *Asian J. Org. Chem.* **2017**, *6*, 768−774.

Mai, Y.; Eisenberg, A. *Chem. Soc. Rev.* **2012**, *41*, 5969−5985.

Marcilla, R.; Curri, M. L.; Cozzoli, P. D.; Mart´ınez, M. T.; Loinaz, I.; Grande, H.; Pomposo, J. A.; Mecerreyes, D. *Small* **2006**, *2*, 507−512.

Margaretta, E.; Fahs, G. B.; Inglefield, D. L.; Jangu, C.; Wang, D.; Heflin, J. R.; Moore, R. B.; Long, T. E. *ACS Appl. Mater. Interfaces* **2016**, *8*, 1280−1288.

Mastroianni, S. E.; Patterson, J. P.; O'Reilly, R. K.; Epps, T. H. *Soft Matter*, **2013**, *9*, 10146−10154.

Maton, C.; De Vos, N.; Stevens, C. V. *Chem. Soc. Rev.* **2013**, *42*, 5963−5977.

Matsen, M. W.; Bates, F. S. *J. Chem. Phys.* **1997**, *106*, 2436−2448.

Matsen, M. W.; Bates, F. S. *J. Polym. Sci. B Polym. Phys.* **1997**, *35*, 945−952.

Matsen, M. W.; Bates, F. S. *Macromolecules* **1996**, *29*, 7641−7644.

Matsen, M. W. *J. Phys. Condens. Matter* **2002**, *14*, R21−R47.

Matsen, M. W. *Phys. Rev. Lett.* **2007**, *99*, 148304-1−148304-4.

Matsushita, Y.; Mori, K.; Saguchi, R.; Nakao, Y.; Noda, I.; Nagasawaid, M. *Macromolecules* **1990**, *23*, 4313−4316.

Mecerreyes, D. *Prog. Polym. Sci.* **2011**, *36*, 1629−1648.

Meek, K. M.; Elabd, Y. A. *J. Mater. Chem. A* **2015**, *3*, 24187−24194.

Meek, K. M.; Sharick, S.; Ye, Y.; Winey, K. I.; Elabd, Y. A. *Macromolecules* **2015**, *48*, 4850−4862.

Moad, G. *ACS Symp. Ser.* **2015**, *1187*, 211−246.

Mori, H.; Yahagi, M.; Endo, T. *Macromolecules* **2009**, *42*, 8082−8092.

Nam, W.; Kim, H. J.; Kim, S. H.; Ho, R. Y. N.; Valentine, J. S. *Inorg. Chem.* **1996**, *35*, 1045−1049.

Nguyen, P. T.; Wiesenauer, E. F.; Gin, D. L.; Noble, R. D. *J. Membr. Sci.* **2013**, *430*, 312−320.

Nishimura, N.; Ohno, H. *Polymer* **2014**, *55*, 3289−3297.

Nunes, S. P. *Macromolecules* **2016**, *49*, 2905−2916.

Nykaza, J. R.; Ye, Y.; Nelson, R. L.; Jackson, A. C.; Beyer, F. L.; Davis, E. M.; Page, K.; Sharick, S.; Winey, K. I.; Elabd, Y. A. *Soft Matter* **2016**, *12*, 1133−1144.

Oh, J. Y.; Chi, W. S.; Lee, J. H.; Kim, J. H.; Kang, S. W. *Ind. Eng. Chem. Res.* **2013**, *52*, 9607−9611.

Oh, J.; Kuk, J.; Lee, T.; Ye, J.; Paik, H.-J.; Lee, H. W.; Chang, T. *ACS Macro Lett.* **2017**, *6*, 758−761.

Ohno, H., Ito, K. *Chem. Lett.* **1998**, *27*, 751−752.

Ohno, H., Yoshizawa, M., Ogihara, W. *Electrochim. Acta* **2004**, *50*, 255−261.

Osada, I.; de Vries, H.; Scrosati, B.; Passerini, S. *Angew. Chem. Int. Ed.* **2016**, *55*, 500−513.

Päch, M.; Zehm, D.; Lange, M.; Dambowsky, I.; Weiss, J.; Laschewsky, A. *J. Am. Chem. Soc.* **2010**, *132*, 8757−8765.

Patil, N. M.; Sasaki, T.; Bhanage, B. M. *ACS Sustainable Chem. Eng.* **2016**, *4*, 429−436.

Patil, N. M.; Sasaki, T.; Bhanage, B. M. *RSC Adv.* **2016**, *6*, 52347−52352.

Plechkova, N. V.; Seddon, K. R. *Chem. Soc. Rev.* **2008**, *37*, 123−150.

Punniyamurthy, T.; Bhatia, B.; Iqbal, J. *J. Org. Chem.* **1994**, *59*, 850−853.

Punniyamurthy, T.; Karla, S. J. S.; Iqbal, J. *Tetrahedron Lett.* **1994**, *35*, 2959−2960.

Qian, W.; Texter, J.; Yan, F. *Chem. Soc. Rev.* **2017**, *46*, 1124−1159.

Qiao, Y.; Ma, W.; Theyssen, N.; Chen, C.; Hou, Z. *Chem. Rev.* **2017**, *117*, 6881−6928.

Rao, A. H. N.; Kim, H.-J.; Namb, S.; Kim, T.-H. *Polymer* **2013**, *54*. 6918−6928.

Rao, A. H. N.; Kim, H.-J.; Namb, S.; Kim, T.-H. *Int. J. Hydrogen Energy* **2014**, *39*, 5919−5930.

Rao, A. H. N.; Thankamony, R. L.; Kim, H.-J.; Namb, S.; Kim, T.-H. *Polymer* **2013**, *54*, 111−119.

Ricks-Laskoski, H. L.; Snow, A. W. *J. Am. Chem. Soc.* **2006**, *128*, 12402−12403.

Riduan, S. N.; Zhang, Y. *Chem. Soc. Rev.* **2013**, *42*, 9055−9070.

Romulus, J.; Henssler, J. T.; Weck, M. *Macromolecules* **2014**, *47*, 5437−5449.

Ryu, I. H.; Kim, Y. J.; Jung, Y. S.; Lim, J. S.; Ross, C. A.; Son, J. G. *ACS Appl. Mater. Interfaces* **2017**, *9*, 17427−17434.

Sanoja, G. E.; Popere, B. C.; Beckingham, B. S.; Evans, C. M.; Lynd, N. A.; Segalman, R. A. *Macromolecules* **2016**, *49*, 2216−2223.

Santos, E.; Albo, J.; Irabien, A.; *RSC Adv.* **2014**, *4*, 40008−40018.

Satapathy, A;. Gadge, S. T.; Kusumawati, E. N.; Harada, K.; Sasaki, T.; Nishio-Hamane, D.; Bhanage, B. M. *Catal. Lett.* **2015**, *145*, 824−833.

Scalfani, V. F.; Bailey, T. S. *Chem. Mater.* **2010,** *22*, 5992−6000.

Scalfani, V. F.; Bailey, T. S. *Macromolecules* **2011,** *44*, 6557−6567.

Scalfani, V. F.; Wiesenauer, E. F.; Ekblad, J. R.; Edwards, J. P.; Gin, D. L.; Bailey, T. S. *Macromolecules* **2012**, *45*, 4262−4276.

Schenkel, M. R.; Zhao, R.; Robertson, L. A.; Wiesenauer, B. R.; Clark, N. A.; Gin, D. L. *Liq. Cryst.* **2013**, *40*, 1067−1081.

Schneider, Y.; Modestino, M. A.; McCulloch, B. L.; Hoarfrost, M. L.; Hess, R. W.; Segalman, R. A. *Macromolecules* **2013**, *46*, 1543−1548.

Serpell, C. J.; Cookson, J.; Thompson, A. L.; Brown, C. M.; Beer, P. D. *Dalton Trans.* **2013**, *42*, 1385−1393.

Shaplov, A. S.; Ponkratov, D. O.; Vygodskii, Y. S. *Polym. Sci. Ser. B.* **2016**, *58*, 73−142.

Sharma, V. B.; Jain, S. L.; Sain, B. *J. Mol. Catal. A: Chem.* **2005,** *227*, 47−49.

Shi, Z.; May, A. W.; Kohno, Y.; Bailey, T. S.; Gin, D. L. *J. Polym. Sci. A: Polym. Chem.* **2017**, *55*, 2961−2965.

Shi, Z.; Newell, B. S.; Bailey, T. S.; Gin, D. L. *Polymer* **2014**, *55*, 6664−6671.

Strandman, S.; Zhu, X. X. *Prog. Polym. Sci.* **2015**, *42*, 154−176.

Stancik, C. M.; Lavoie, A. R.; Achurra, P. A.; Waymouth, R. M.; Gast, A. P. *Langmuir* **2004**, *20*, 8975−8987.

Stancik, C. M.; Lavoie, A. R.; Schutz, J.; Achurra, P. A.; Lindner, P.; Gast, A. P.; Waymouth, R. M. *Langmuir* **2004**, *20*, 596−605.

Sudre, G.; Inceoglu, S.; Cotanda, P.; Balsara, N. P. *Macromolecules* **2013**, *46*, 1519−1527.

Sun, X.; Luo, H.; Dai, S. *Chem. Rev.* **2012**, *112*, 2100−2128.

Tang, J.; Tang, H.; Sun, W.; Radosz, M.; Shen, Y. *J. Polym. Sci. A: Polym. Chem.* **2005**, *43*, 5477−5489.

Texter, J.; Vasantha, V. A.; Crombez, R.; Maniglia, R.; Slater, L.; Mourey, T. *Macromol. Rapid Commun.* **2012**, *33*, 69−74.

Tome, L. C.; Marrucho, I. M. *Chem. Soc. Rev.* **2016**, *45*, 2785−2824.

Tritschler, U.; Pearce, S.; Gwyther, J.; Whittell, G. R.; Manners, I. *Macromolecules* **2017**, *50*, 3439−3463.

Vijayakrishna, K.; Jewrajka, S. K.; Ruiz, A.; Marcilla, R.; Pomposo, J. A.; Mecerreyes, D.; Taton, D.; Gnanou, Y. *Macromolecules* **2008**, *41*, 6299−6308**.**

Vygodskii, Y.; Shaplov, A.; Lozinskaya, E.; Lyssenko, K.; Golovanov, D.; Malyshkina, I.; Gavrilova, N.; Buchmeiser, M. *Macromol. Chem. Phys.* **2008**, *209*, 40−51.

Wang, Z.; Wang, J.; Li, J.; Feng, M.; Zou, G.; Huang, X. *Chem. Commun.* **2015**, *51*, 3094−3097.

Weber, R. L.; Ye, Y.; Schmitt, A. L.; Banik, S. M.; Elabd, Y. A.; Mahanthappa, M. K. *Macromolecules* **2011**, *44*, 5727−5735.

Weingrtner, H. *Angew. Chem. Int. Ed.* **2008**, *47*, 654−670.

Widin, J. M.; Kim, M.; Schmitt, A. K.; Han, E.; Gopalan, P.; Mahanthappa, M. K. *Macromolecules* **2013**, *46*, 4472−4480.

Wiesenauer, E. F.; Edwards, J. P.; Scalfani, V. F.; Bailey, T. S.; Gin, D. L. *Macromolecules* **2011**, *44*, 5075−5078.

Wiesenauer, E. F.; Nguyen, P. T.; Newell, B. S.; Bailey, T. S.; Noble, R. D.; Gin, D. L. *Soft Matter* **2013**, *9*, 7923−7927.

Wijayasekara, D. B.; Cowan, M. G.; Lewis, J. T.; Gin, D. L.; Noble, R. D.; Bailey, T. S. *J. Membr. Sci.* **2016**, *511*, 170−179.

Wijayasekara, D. B.; Huang, T.; Richardson, J. M.; Knauss, D. M.; Bailey, T. S. *Macromolecules* **2016**, *49*, 595−608.

Xia, J.; Matyjaszewski, K. *Macromolecules* **2011**, *30*, 7697−7700.

Yang, Q.; Zhang, Z.; Sun, X.; Hu, Y.; Xing, H.; Dai, S. *Chem. Soc. Rev.* **2018**, *47*, 2020−2064.

Ye, Y.; Sharick, S.; Davis, E. M.; Winey, K. I.; Elabd, Y. A. *ACS Macro Lett.* **2013**, *2*, 575−580.

Yoshida, Y.; Saito, G.; in *Ionic Liquids: Theory, Properties, New Approaches*; Kokorin, A., ed.; InTech, 2011. 723−739.

Young, W.; Kuan, W.; Epps, T. H. III. *J. Polym. Sci. B: Polym. Phys.* **2014**, *52*, 1−16.

Yuan, J.; Antonietti, M. *Polymer* **2011**, *52*, 1469−1482.

Yuan, J.; Mecerreyes, D.; Antonietti, M. *Prog. Polym. Sci.* **2013**, *38*, 1009−1036.

Zekoll, S.; Marriner-Edwards, C.; Hekselman, A. K. O.; Kasemchainan, J.; Kuss, C.; Armstrong, D. E. J.; Cai, D.; Wallace, R. J.; Richter, F. H.; Thijssen, J. H. J.; Bruce, P. G. *Energy Environ. Sci.* **2018**, *11*, 185−201.

Zeng, S.; Zhang, X.; Bai, L.; Zhang, X.; Wang, H.; Wang, J.; Bao, D.; Li, M.; Liu, X.; Zhang, S. *Chem. Rev.* **2017**, *117*, 9625−9673.

Zhang, Q.; Shreeve, J. M. *Chem. Rev.* **2014**, *114*, 10527−10574.

Zhao, D.; Fei, Z.; Ang, W. H.; Dyson, P. J. *Small* **2006**, *2*, 879−883.

Zhao, H.; Foss, F. W. Jr.; Breslow, R. *J. Am. Chem. Soc.* **2013**, *130*, 12590−12591.

Zhou, J.; Whittell, G. R.; Manners, I. *Macromolecules* **2014**, *47*, 3529−3543.